DESIGN OF INSECT-SCALE FLAPPING WING VEHICLES

A thesis submitted to The University of Manchester for the degree of
Doctor of Philosophy
in the Faculty of Engineering and Physical Sciences

2015

Mostafa Ramadan Ahmed Nabawy

School of Mechanical, Aerospace and Civil Engineering

Contents

Word count: 66818

Figures

Tables

Nomenclature

a	:	circle radius for Joukowski transformation (m)
A	:	coefficient of the particular solution
ALR	:	actuator length ratio
AR	:	single wing aspect ratio
b	:	actuator width (m)
B	:	non-dimensional effective radius (R_{ef}/R)
c	:	chord (m)
$\bar{c}$	:	mean chord (m)
c_v	:	viscous damping coefficient (N.sec.m^{-2})
C_D	:	wing steady drag coefficient
C_{D_i}	:	wing induced drag coefficient
$C_{D_{pro}}$	:	wing profile drag coefficient
C_{D0}	:	wing drag coefficient at zero angle of attack
C_l	:	local wing lift coefficient
$C_{l,\,free}$	:	lift coefficient due to free circulation
$C_{l\alpha,2d}$	:	2d-aerofoil lift curve slope (deg^{-1})
C_L	:	wing steady lift coefficient
$C_{L,p}$	:	potential lift coefficient of Polhamus model
$C_{L,v}$	:	vortex lift coefficient of Polhamus model
$C_{L\alpha,3d}$	:	3d-wing lift curve slope (deg^{-1})
C_N	:	normal force coefficient
$\hat{C}_N$	:	amplitude of the normal force coefficient

$C_{P_{pro}}$	:	profile power coefficient
C_{rot}	:	rotational force coefficient
C_T	:	translational lift constant
C_{Th}	:	thrust coefficient
C_{α_g}	:	equivalent angle of attack correction term
C_ϕ	:	flapping angle variation control parameter
C_θ	:	pitching angle variation control parameter
d_{31}	:	piezoelectric constant ($m.V^{-1}$)
D	:	drag force (N)
D_3	:	electric displacement in 3-direction ($Pa.m.V^{-1}$)
$D_{ij}(x)$	:	i^{th} - j^{th} element of the actuator dynamic matrix
DL	:	disk loading ($N.m^{-2}$)
e	:	inviscid wing *span efficiency*
E	:	edge correction
E_3	:	electric field in 3-direction ($Volt.\ m^{-1}$)
f	:	flapping frequency (Hz)
$f(x,t)$	:	external force per unit length ($N.m^{-1}$)
f_a	:	anti-resonant frequency (Hz)
f_r	:	resonant frequency (Hz)
f_1, f_2	:	half-power point frequencies (Hz)
F	:	force (N)
F_b	:	actuator blocking force (N)
FM	:	*Figure of Merit*
G	:	gear/transmission ratio
GN	:	*Glide Number*
h	:	thickness (m)
I	:	area moment of inertia of the composite cross section (m^4)
I_{wing}	:	mass moment of inertia of the wing ($kg.m^2$)
J	:	advance ratio

J_1	:	ratio of chord wise component of the wing tip flow velocity due to translation and revolution
k	:	overall induced power factor, *k*-factor
k^2	:	electromechanical coupling factor, EMCF
k_{31}	:	piezoelectric material electromechanical coupling coefficient
k_{ind}	:	induced power factor due to non-uniform downwash effect
k_{per}	:	induced power factor due to wake periodicity effect
k_{flap}	:	induced power factor due to effective flapping disk area effect
K_D	:	damping constant
K_i	:	derivative of the induced drag coefficient with respect to the square of the lift coefficient in Polhamus model
K_P	:	potential lift constant of Polhamus model
K_V	:	vortex lift constant of Polhamus model
l	:	actuator length (m)
l_T	:	output gear radius (m)
L	:	lift force (N)
$\overline{L}$	:	mean flapping cycle lift force (N)
$\dot{m}$	:	mass flow rate (kg.sec^{-1})
m	:	number of wing stations solved
m_{acts}	:	actuators mass (kg)
m_{bats}	:	batteries mass (kg)
m_{other}	:	other systems mass (kg)
m_{total}	:	total vehicle mass (kg)
m_{wing}	:	single wing effective mass (kg)
$m_{w,a}$	:	wing aerodynamic inertia (kg)
$m_{w,s}$	:	wing structural inertia (kg)
MA	:	Mechanical Advantage
N_b	:	number of blades
p	:	beta function parameter
P_{ideal}	:	minimum induced power (W)
P_{ind}	:	induced power (W)

P^*	:	specific aerodynamic power ($W.kg^{-1}$)
PF	:	*Power Factor*
PTT	:	PZT Total Thickness (m)
q	:	beta function parameter
Q	:	electric charge (C)
r	:	radial distance (m)
r_{mw}	:	wing structure inertia radius of gyration (m)
$r_{mw,a}$	:	wing aerodynamic inertia radius of gyration (m)
r_n	:	frequency ratio
$\hat{r}$	:	non-dimensional wing radial position (r/R)
$\hat{r}_1$	:	non-dimensional radius of first moment of wing area (r_1/R)
$\hat{r}_2$	:	non-dimensional radius of second moment of wing area (r_2/R)
$\hat{r}_3$	:	non-dimensional radius of third moment of wing area (r_3/R)
R	:	wing length (m)
R_{ef}	:	effective disk radius (m)
R_i	:	inner wing (root) radial distance (m)
R_o	:	outer wing (tip) radial distance (m)
Re	:	Reynolds number
S_d	:	disk area (m^2)
s_{11}	:	elastic compliance (1/Pa)
S_1	:	piezoelectric strain in 1-dirction
S_{ij}	:	i^{th} - j^{th} element of the actuator static matrix
t	:	time (sec)
$T_n(t)$	:	time solution function
T_1	:	piezoelectric stress in 1-dirction (Pa)
U	:	velocity ($m.sec^{-1}$)
$\dot{v}_n$	:	first derivative of the normal velocity component of the chord relative to air ($m.sec^{-2}$)
V	:	voltage (Volt)
w	:	induced downwash velocity ($m.sec^{-1}$)
W	:	weight (N)
x, y, z	:	Cartesian axes (m)

$\hat{x}_o$	:	non-dimensional position of the wing pitching spanwise axis
$X_n(x)$	:	mode shape
$\bar{y}$	:	neutral axis position (m)
Y	:	Young's modulus (Pa)

Greek

α	:	angle of attack (deg.)
α_e	:	effective angle of attack (deg.)
$\alpha_{e,opt}$	:	optimum effective angle of attack (deg.)
α_{eq}	:	equivalent angle of attack (deg.)
α_g	:	geometric angle of attack (deg.)
α_i	:	induced angle of attack (deg.)
α_p	:	piezoelectric actuator configuration parameter
α_{stall}	:	angle of attack at which stall occurs (deg.)
β	:	beta function distribution
χ	:	phase lag angle (deg.)
δ	:	transverse deflection (m)
δ_D	:	*Dirac delta* function
ε_{33}^T	:	permittivity at constant stress ($F.m^{-1}$)
ϕ	:	flapping angle amplitude (deg.)
Φ	:	peak to peak flapping stroke angle (deg.)
φ	:	angular position in circle plane of Joukowski transformation (deg.)
γ	:	non-dimensional spanwise circulation
Γ	:	spanwise circulation ($m^2.sec^{-1}$)
Γ_{free}	:	circulation of the free vortex ($m^2.sec^{-1}$)
η_a	:	aerodynamic efficiency
κ	:	wave number
λ	:	inflow ratio
μ	:	wing characteristic coefficient in the lifting line formulation

μ_{act}	:	mass fraction of single actuator
μ_{acts}	:	mass fraction of two actuators
μ_{bats}	:	mass fraction of batteries
μ_{other}	:	mass fraction of the systems components other than batteries and actuators
μ_{wing}	:	mass fraction of single wing
Λ	:	wing sweep angle (deg.)
θ	:	wing pitching angle (deg.)
ϑ	:	coefficient of the particular solution
ρ	:	density ($kg.m^{-3}$)
ρA	:	mass per unit length ($kg.m^{-1}$)
σ	:	stroke plane angle (deg.)
Ω	:	angular velocity ($rad.sec^{-1}$)
τ	:	radius in circle plane of Joukowski transformation (m)
υ	:	mode shape coefficient
ω	:	frequency (Hz)
ξ	:	location in circle plane of Joukowski transformation (m)
ψ	:	angular parameter used to define position along the wing (deg.)
ζ	:	damping ratio

Subscripts

1	:	denotes length direction for piezoelectric actuator
3	:	denotes thickness direction for piezoelectric actuator
act	:	actuator
e	:	elastic
ef	:	effective
eq	:	equivalent
max	:	maximum (amplitude) value
n	:	indicates n^{th} mode shape
rot	:	rotational aerodynamic component
p	:	PZT

tip	:	at wing tip

Superscripts

·,··	:	first and second derivatives with respect to time
',''	:	first and second derivatives with respect to length

Abbreviations

BDC	:	Bottom Dead Centre
BEMT	:	Blade Element Momentum Theory
CFD	:	Computational Fluid Dynamics
CoG	:	Centre of Gravity
DARPA	:	Defence Advanced Research Projects Agency
DOF	:	Degree of Freedom
DPIV	:	Digital Particle Image Velocimetry
EMCC	:	Electromechanical Coupling Coefficient
EMCF	:	Electromechanical Coupling Factor
FEA	:	Finite Element Analysis
FEM	:	Finite Element Method
LEV	:	Leading-Edge Vortex
Li-Po	:	Lithium Polymer
LLT	:	Lifting Line Theory
LLT_{hw}	:	Lifting Line Theory for hovering wings
MAV	:	Micro Air Vehicle
Mid	:	Mid halfstroke
NAV	:	Nano Air vehicle
PZT	:	Lead Zirconate Titanate (stands for piezoelectric)
Re	:	Reynolds number
RPM	:	Revolutions Per Minute
TDC	:	Top Dead Centre
UAV	:	Unmanned Air Vehicle
VTOL	:	Vertical Take Off and Landing

Abstract

Design of Insect-Scale Flapping Wing Vehicles

Mostafa Ramadan Ahmed Nabawy
The University of Manchester Doctor of Philosophy 29/1/2015

This thesis contributes to the state of the art in integrated design of insect-scale piezoelectric actuated flapping wing vehicles through the development of novel theoretical models for flapping wing aerodynamics and piezoelectric actuator dynamics, and integration of these models into a closed form design process.

A comprehensive literature review of available engineered designs of miniature rotary and flapping wing vehicles is provided. A novel taxonomy based on wing and actuator kinematics is proposed as an effective means of classifying the large variation of vehicle configurations currently under development. The most successful insect-scale vehicles developed to date have used piezoelectric actuation, system resonance for motion amplification, and passive wing pitching.

A novel analytical treatment is proposed to quantify induced power losses in normal hover that accounts for the effects of non uniform downwash, wake periodicity and effective flapping disc area. Two different quasi-steady aerodynamic modelling approaches are undertaken, one based on blade element analysis and one based on lifting line theory. Both approaches are explicitly linked to the underlying flow physics and, unlike a number of competing approaches, do not require empirical data. Models have been successfully validated against experimental and numerical data from the literature. These models have allowed improved insight into the role of the wing leading-edge vortex in lift augmentation and quantification of the comparative contributions of induced and profile drag for insect-like wings in hover.

Theoretical aerodynamic analysis has been used to identify a theoretical solution for the optimum planform for a flapping wing in terms of chord and twist as a function of span. It is shown that an untwisted elliptical planform minimises profile power, whereas a more highly tapered design such as that found on a hummingbird minimises induced power. Aero-optimum wing kinematics for hovering are also assessed. It is shown that for efficient flight the flapping velocity should be constant whereas for maximum effectiveness the flapping velocity should be sinusoidal. For both cases, the wing pitching at stroke reversal should be as rapid as possible.

A dynamic electromechanical model of piezoelectric bending actuators has been developed and validated against data obtained from experiments undertaken as part of this thesis. An expression for the electromechanical coupling factor (EMCF) is extracted from the analytical model and is used to understand the influence of actuator design variables on actuator performance. It is found that the variation in EMCF with design variables is similar for both static and dynamic operation, however for light damping the dynamic EMCF will typically be an order of magnitude greater than for static operation.

Theoretical contributions to aerodynamic and electromechanical modelling are integrated into a low order design method for propulsion system sizing. The method is unique in that aside from mass fraction estimation, the underlying models are fully physics based. The transparency of the design method provides the designer with clear insight into effects of changing core design variables such as the maximum flapping amplitude, wing mass, transmission ratio, piezoelectric characteristics on the overall design solution. Whilst the wing mass is only around 10% of the actuator mass, the effective wing mass is 16 times the effective actuator mass for a typical transmission ratio of 10 and hence the wing mass dominates the inertial contribution to the system dynamics. For optimum aerodynamic effectiveness and efficiency it is important to achieve high flapping amplitudes, however this is typically limited by the maximum allowable field strength of the piezoelectric material used in the actuator.

Declaration

No portion of the work referred to in the thesis has been submitted in support of an application for another degree or qualification of this or any other university or other institute of learning.

Copyright Statement

Dedication

TO ALYA & BASMA

MOSTAFA

2015

Acknowledgements

First and foremost I wish to express my deepest gratitude and sincere thanks to my supervisor **Dr William Crowther** for his instructive supervision, continuous guidance, valuable instructions and offering of all facilities. You have devoted your intellectual energies and high sense of profession in the supervision of this thesis. Without your creative thinking, valuable suggestions and constructive criticism, the fulfillment of this work would have been extremely difficult. I am thankful to your caring and concern, and faith in me throughout this project journey. I have learned a great deal and gained valuable experience.

I owe much to my lady **Basma**. Through her love, support, encouragement and most importantly patience, I have been able to complete this long mission. She has taken care of me, lilo and all our life aspects without complaining, just so I can focus on completing my study. I cannot even imagine my life without you by my side. Thank You Basbousa.

Whatever I say or write, I will never be able to express my deep feelings and profound gratitude to my mother **Prof Mona Nosseir**. You have raised me with a love of science, you have always believed in me, and you have never stopped to support and encourage me. Thank you for your patience throughout all the years. I am forever grateful. Thank You Mameya.

I must thank the **School of MACE** for the MACE PhD Award which funded my PhD project. I also thank **Prof Hector Iacovides** and the fluid research group for partially funding my conferences expenses.

I would like to acknowledge two inspiring figures in my life, **Prof Mokhtar ElNomrossy** and **Prof Mohamed Madbouli Abdelrahman**. They have laid my aerospace scientific foundations; without their indefinite support and valuable guidance, I would have never reached to this place.

I owe much to **Prof Ibrahim Badran** who I had the chance to know when I was looking for supplementary funding sources for my PhD. From the first moment, I found him a wonderful person and a great scientist who is always willing to support. Indeed, he persuaded **El Masry Foundation for Community Services** to partially support my living costs during the first year of my studies here. I am in complete admiration of your great personality; you are an inspiration to any young researcher.

I must thank **all my teachers** throughout the years from KG to University stage. It has been like a building and every one of you has added a brick and now it is time to add one more brick. I hope I will be always able to lighten your faces.

A very special thank you goes to **Khris** for teaching me everything here in Manchester, for doing me all the SolidWorks models I want, for the nice times we spent together, and for our true friendship. Another special thank you goes to **Gareth** for our rich cultural discussions, for always inviting me to his lovely house in Manchester and to his family house in Wales, for mountain biking, for training me RC piloting and for toping up my laundry account, and most importantly for saving my life in my Wales canoe disaster. A final special thank you goes to **Bilal**, I will never forget our ‘Kasdouras’ together; you are a wonderful person and a true friend. Thank you so much guys for the great time together; my life at Manchester was made enjoyable mainly due to you.

I would like to express my great thanks to my colleague and dear friend **Haithem Taha** for the inspiring and valuable discussions we had on flapping flight aerodynamics. I would also like to thank **Andrew Kennaugh** for the help in building the piezoelectric actuators measurement setup. A special thank you goes to my friend **Alberto Llopis Pascual** for his generous help in presenting a paper on my behalf in the 32nd AIAA

aerodynamic conference. Thanks are due to my colleague and dear friend **Islam ElQatary** for his support and help especially in handling all my administrative paper work in Cairo University throughout my period of study here.

Thanks are due to my colleagues and friends in the **UAV Research Group**: **Ben**, **Alberto**, **Ola**, **James**, **Alex**, **Nick**, **Brad**, **Shalini**, **Giru** and **Tobi**. Thank you guys for the nice memories especially our football matches, breakfasts, lunches and dinners, laser tagging, cinemas and pool games.

Last but not least, thanks to my grandmother **Aleya**, my wonderful aunts **Wafaa and Hanaa,** and to **all my family** who have been supporting me ever since, standing beside me and seeking my success. I love you. I hope I would fulfil your ambitions.

Mostafa R A Nabawy
The University of Manchester
2015

1

Introduction

This chapter defines aim, objectives and outline of this thesis.

1.1 Background

In aeronautical engineering, scale and scientific passion are inversely proportional. This is demonstrated by the development of unmanned air vehicles (UAVs) in the last two decades, where the miniaturisation challenge has gone from ‘mini’ to ‘micro’ then to ‘nano’ and now to ‘pico’. Whilst there is no clear definition of the boundaries between these classes, the naming progress is obviously encouraging smaller and smaller platforms. This passion towards smaller air vehicles is not only because of being a new frontier to human scientific knowledge but also because of our rapidly progressing life demands that involve missions in geometrically constrained areas. The first concept that will approach one's mind when considering tiny sized air vehicles is ‘insects’. This does not necessitate that they are the best solution, but they are definitely a proven solution that is copious in nature. Indeed Insect-like flapping flight is nowadays a very interesting research topic lying at the interface between biology and engineering. Whilst biologists are probably more concerned with understanding the principles of insects flying behaviour, engineers are trying to cast this understanding into design models that would develop this class of bio-inspired vehicles. However, unlike fixed and rotary wing vehicles, insect-like vehicles are still in their infancy with little known, not just about the higher level understanding of the optimality of their designs, but even about the basic fundamental requirements for a successful operation.

Many insect-like hover-capable designs employing different concepts have been introduced within the last fifteen years, each achieving success to a certain limit. However, the last four years, in particular, witnessed the presentation of breathtaking designs that can be considered important milestones within the development history of these vehicles, Figure 1.1. In 2011, the ‘Nano-Hummingbird’ was introduced, representing a successful palm-size flapping wing vehicle capable of controlled hovering flight. In 2013, the pneumatic and electric automation company Festo presented its ‘Bionic-Insect’. Whilst having a relatively large size (wing span of 63 cm), the dragonfly-like vehicle was able to demonstrate full active control of wing pitch, flapping amplitude and frequency. The year 2013 also witnessed the first controlled liftoff for the Harvard ‘Microrobotic-Fly’ which is a tether powered piezoelectric actuated insect-scale flapping wing vehicle design. The present work will consider

vehicles similar to this latter design and will contribute to their development through the presentation of generic toolsets for their preliminary design.

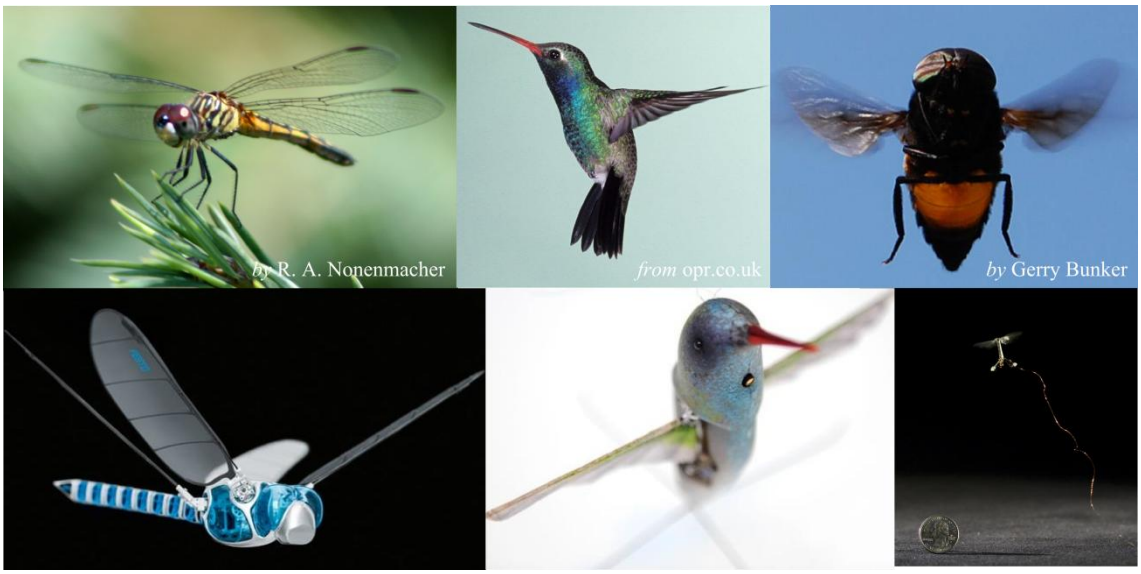

Figure 1.1 Examples of the latest successful demonstrators of insect-like flapping wing air vehicles along with their biological counterparts. From left to right are the Festo 'Bionic-Insect', the AeroVironment 'Nano-Hummingbird' and the Harvard 'Microrobotic-Fly'. These vehicles, in the shown order, represent increasing degrees of miniaturisation; however, they also demonstrate decreasing levels of control authority. More details of these designs will be provided in Chapter 2; engineered insect images taken from [42], [40] and [99] respectively.

1.2 Aim

The overall aim of this thesis is defined as

To contribute to the state of the art in integrated design of insect-scale piezoelectric actuated flapping wing vehicles through the development of theoretical models for flapping wing aerodynamics and piezoelectric actuator dynamics, and integration of these models into a closed form design process.

1.3 Objectives and Thesis Outline

- Provide a thorough review of the available design concepts, system components and development challenges facing insect-like flapping wing vehicles (Chapter 2).

- Develop theoretical models to evaluate the efficiency of lift production of insect-like flapping flight based on the *induced power factor* and the *figure of merit* measures (Chapter 3).
- Introduce a generic, transparent and compact model for evaluation of the aerodynamics of insect-like flapping wings in hovering flight (Chapter 4).
- Provide a theoretical argument for attributing the observed lift enhancement in revolving/flapping wings, particularly the role of the leading-edge vortex in lift production (Chapter 4).
- Develop a quasi-steady lifting line theory and evaluate the drag breakdown for insect-like hovering flight (Chapter 5).
- Identify the optimum hovering wing planform and investigate the aerodynamic performance of other hovering wing planforms driven by broader multidisciplinary engineering or evolutionary constraints (Chapter 6).
- Identify optimum flapping wing kinematics against aerodynamic criteria of effectiveness measured in terms of maximum lift, and efficiency measured in terms of minimum power for a given amount of lift (Chapter 7).
- Provide explicit and compact analytical expressions for lift and power of a hovering wing that enable exploration of a rich kinematic design space (Chapter 7).
- Develop a comprehensive analytical model of the electromechanical behaviour of piezoelectric bending actuators in dynamic operations (Chapter 8).
- Analyse the electromechanical coupling performance of piezoelectric actuators and identify their optimum configurations and best material properties (Chapter 8).
- Develop a multi-physics design process capturing the electrical, mechanical and aerodynamic domains of the system for physical sizing of piezoelectric bending actuators for insect-scale flapping wing vehicles (Chapter 9).
- Assess the feasible design space for insect-scale flapping wing vehicles in terms of identifying the most influential design variables, and understanding the best feasible design space for the piezoelectric type of propulsion (Chapter 9).
- Summarise the main research outputs and their implications to the fields of insect flight aerodynamics, piezoelectric actuation dynamics and design of insect-scale flapping wing vehicles (Chapter 10).
- Recommend routes for further research within the different disciplines involved (Chapter 10).

2

Towards an Insect-Scale Air Vehicle: A Review of Design Concepts, System Components and Development Challenges

This chapter provides a detailed assessment of existing hover capable micro air vehicle (MAV) and nano air vehicle (NAV) designs. The aim is to provide a thorough review of the available design concepts and to identify areas in which further effort is needed to advance the state of the art. The core of this chapter consists of four main sections discussing the different available design concepts. The first section discusses rotary wing MAVs. The second section discusses flapping wing vehicles driven by rotary actuators. The third section discusses flapping wing vehicles driven by reciprocating actuators. The fourth section provides a detailed assessment of the main subsystems constituting flapping wing vehicles driven by reciprocating piezoelectric actuators. Because of the breadth of each of the four sections, a summary is provided at the end of each section highlighting the strengths and weaknesses of the presented concepts.

2.1 Introduction

In 1997, the Defence Advanced Research Projects Agency (DARPA) launched a pilot study for the design of micro air vehicles with a maximum dimension of no more than 15 cm, take-off weight of less than 200 g, a range of 10 km, maximum velocities over 13 m/s, and can operate for more than 20 minutes [1,2,3]. In 2005, DARPA once again pushed the limits by announcing the program for nano air vehicles or NAVs. The requirement this time was an air vehicle with a maximum dimension of no more than 10 cm, take-off weight of less than 10 g, able to fly 1 km or more besides its capability for VTOL (Vertical Take Off and Landing) [3,4]. Whilst the previous MAV and NAV design specifications are not based on specific physical reasons, they provide a useful reference to define the engineering challenge. Birds and insects offer proven platforms satisfying these specifications; thus, it was not surprising to see the huge interest directed towards flapping flight to inspire a solution for this new challenge. Indeed, this opened a new frontier for aeronautical engineering and many design concepts has been presented within the last 15 years to achieve such purpose. It is thus necessary to review what has been proposed, define strengths and weaknesses, extract ideas for development and identify potential directions for future designs.

Driven by civilian and military objectives, the main mission usually assigned to MAVs and NAVs is to perform surveillance and monitoring missions in geometrically constrained areas such as building, caves and tunnels. This requires a small size vehicle, capable of hovering and low speed flight, highly manoeuvrable, amongst other things [1]. Fixed wing air vehicles are not agile enough for indoor missions and are unable of sustained hovering [5,6]. Thus, rotary and flapping wing air vehicles are considered more able to satisfy the target specifications.

This chapter is concerned with reviewing designs for insect-scale flapping wing air vehicles capable of hovering flight. This means that developments in fixed wing MAVs and larger scale flapping wing vehicles of bird size [7] are not considered. The chapter will provide a quick review on rotary wings MAVs; however, the main focus will be towards recent developments of flapping MAVs. Whilst there are a few assessments for some specific flapping wing designs [3,8-12], a detailed, coherent and consistent work that attempts to review the state of the art for hover capable MAV and NAV designs is still missing. Thus, the objectives of this chapter are: (1) provide taxonomy for

categorising existing relevant designs. (2) Discuss exiting designs in terms of configuration layout and achieved flight performance. (3) Provide comprehensive discussion on the primary systems of insect-scale vehicles including aspects of their prototyping and implementation. (4) Summarise the current state of the art of these vehicles, identifying current challenges, and directions for development.

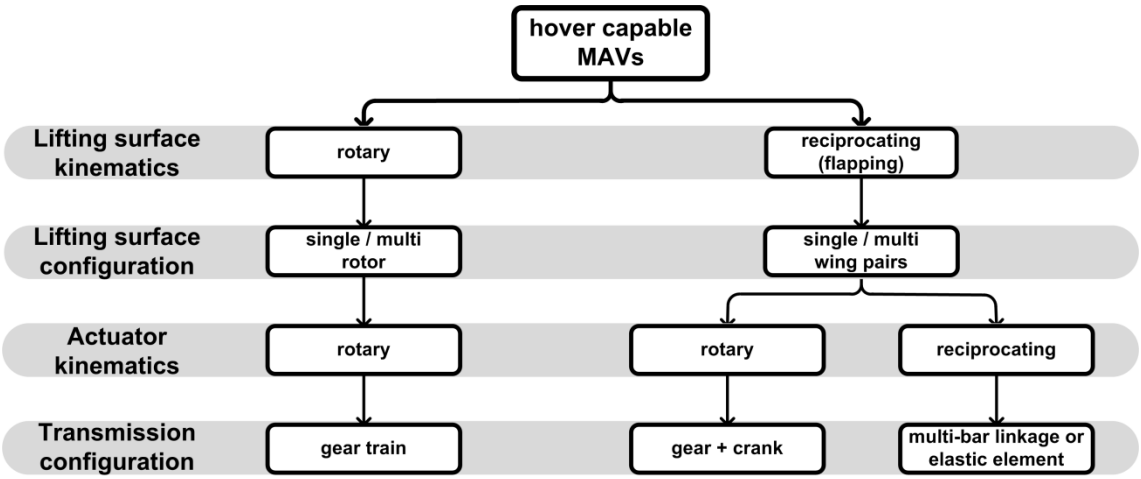

Figure 2.1 Taxonomy of hover capable micro air vehicles based on lifting surface and actuator kinematics.

In order to provide a coherent framework for discussing the different approaches to achieving hovering flight with a small scale vehicle, a simple taxonomy is defined based on the kinematics of the surfaces producing lift and the actuator providing the motive power, Figure 2.1. The principle division is between rotary wings and reciprocating (flapping) wings. However, there are two important technological distinctives between reciprocating wings driven by a rotary actuator and reciprocating wings driven by a reciprocating actuator. Firstly, for rotary actuation some form of gear and crank transmission system is required, whereas for reciprocating actuation some form of multi-bar linkage is required. This has impact on manufacturing requirements for the given scale and frequency required. Secondly, there is a natural technology choice for rotary actuation in the form of an electric motor, whereas for reciprocating actuation the choice is not clear cut. For high force, low amplitude, high frequency applications piezoelectric actuators are a natural choice, whereas for higher amplitude lower frequency applications, electromagnetic actuators are well suited. As a higher level distinction between rotary and reciprocating kinematics, reciprocating systems can utilise system resonance to amplify the displacement output of the actuator whereas

rotary systems cannot. This is particularly important for piezoelectric actuators where the maximum actuator displacement is typically very small compared to the required wing displacement. Note that whilst exploitation of resonance provides significant performance benefits, it introduces significant design complexity in that the design of actuator is highly coupled to the design of the vehicle wing and transmission as will be addressed in Chapter 9 of this thesis.

Section 2.2 will review the current state of the art in rotary wing MAVs. This will be followed in Section 2.3 by a review of palm-size flapping wing MAVs actuated by rotary motors. Section 2.4 will then present a detailed review of insect-scale flapping wing NAVs exploiting resonance for flapping motion amplification. These designs are discussed in light of their actuator configuration which can be a solenoid, a rotary motor or a piezoelectric bending actuator. Because this thesis is concerned with resonant piezoelectric actuated vehicles, Section 2.5 of this chapter will put more light on the main subsystems constituting these vehicles including energy sources, power electronics board, piezoelectric actuators, mechanical transmission and wings.

2.2 Rotary Wing MAV Designs

2.2.1 Motor actuated designs

2.2.1.1 Coaxial configurations

Whilst there are some concerns on the aerodynamic efficiency due to rotors wake interaction, most of the presented rotary wing designs at the MAV scale are of the coaxial configuration. This configuration allows reduction in rotors net size, ease of handling, structure simplicity and the exclusion of the tail rotor allows all the power to be devoted for providing useful lift [13].

An early attempt in this class was the ‘MICOR’ (Micro Coaxial Rotorcraft), Figure 2.2a, developed at the University of Maryland in 2003 [13]. The design had a mass of approximately 100 g. The used rotors had a solidity ratio of 0.119, a chord of 1 cm and a length of 7 cm. Power was provided from 17 g 6-V WES-Technik coreless DC motor with a maximum power output of 8.52 W. Lateral control was not implemented, however each rotor was driven by a separate motor to allow different rotational speeds for yaw control. The vehicle flew using onboard installed power along with open loop differential yaw control and using a nylon string for guidance. Although designed for 17

minutes of endurance, only 3 minutes were achieved which was reported to be due to a higher than expected current draw from the three 430 mAh, 3-V $LiMnO_2$ batteries. Reported motor efficiency was 60% and the best measured rotor figure of merit (*FM*) for a single rotor was 0.42.

Another design in this category is the ‘µFR’ (Micro Flying Robot) developed by Seiko Epson Corporation in 2003 [14]. The ‘µFR’ was powered by ultrasonic motors and was balanced in air by means of a stabilizing mechanism that uses a linear actuator [15]. The ‘µFR’ rotor diameter was 13 cm and had a mass of 8.9 g [14]. Though the ‘µFR’ was radio-controlled, it relied on power from an external battery via a power tether (i.e. umbilical power). In 2004, the company released the ‘µFR-II’ with on-board lithium-polymer (Li-Po) battery, Figure 2.2b. A new gyro-sensor that is one-fifth the weight of its predecessor was included, and lift was increased by 30% through the introduction of more powerful ultra-thin ultrasonic motors as well as newly designed rotors [14,15]. The ‘µFR-II’ had a rotor diameter of 13.6 cm and a mass of 12.3 g. It was able to show flight endurance of 3 minutes.

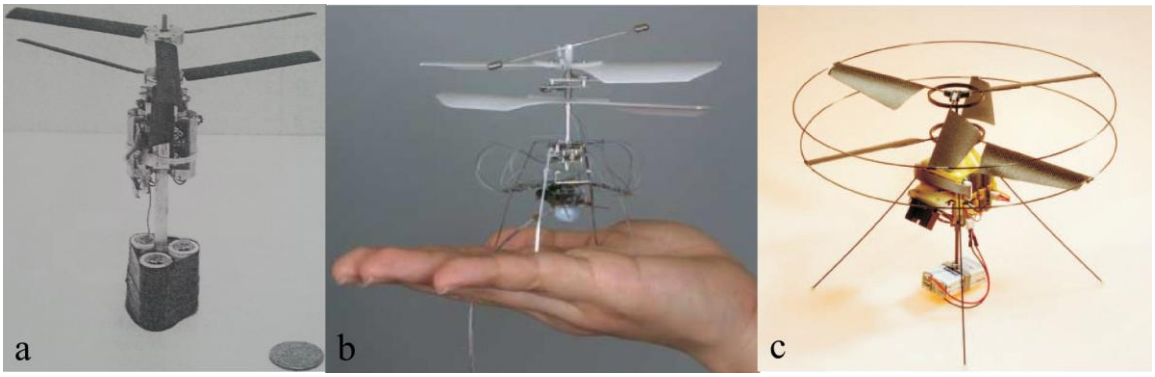

Figure 2.2 Coaxial rotary MAV designs. (a) The University of Maryland ‘MICOR’; image taken from [13]. (b) Seiko Epson ‘µFR-II’; image taken from [14]. (c) ETH Zurich ‘Coax’; image taken from [16].

The last design to be discussed in this category is the ‘CoaX’, Figure 2.2c, developed at ETH Zurich in 2006 [16]. The design objective was to achieve up to 40% thrust margin and nearly 20 minutes flight while respecting the initial design requirements constrained by a maximum mass of 200 g and 30 cm diameter. Centre of gravity (CoG) shifting was used to control the lateral motion, and a separate motor was used for each rotor to achieve yaw control. Brushless sensorless motors with a mass of 12 g using a dedicated speed controller along with a 4:1 reduction gear were used. A 70

g, 900 mAh Li-Po battery powered the system. ‘CoaX’ was reported to hover without any external control for short moments.

2.2.1.2 Quad-rotor configurations

Quad-rotors or rotorcraft with four lifting rotors have recently attracted special attention within the UAV community particularly from a control and stability perspective. Control is achieved by varying the RPM and/or collective pitch angle of the different rotors allowing variation of the magnitude and direction of the vehicle thrust vector. Many successful designs have been introduced within the 0.5 to 1 metre-scale; however, fewer designs have been demonstrated within the NAV scale. Here, only NAV-scale quad-rotors will be discussed. In 2013, hobby companies started to present some small-scale designs such as the ‘Hubsan Q4’ [17], Figure 2.3. This design measures approximately 5 cm x 5 cm, has a mass of around 11.5 g and can fly for about 5 minutes.

Figure 2.3 The ‘Hubsan Q4’ nano quad-copter; image taken from [17].

From academia, the only NAV-scale quad-rotor design presented was the ‘Mesicopter’, Figure 2.4, developed at Stanford University around the year 2000 [18-20]. It is a battery powered system that was only able to demonstrate thrust production but not free flights. Two prototypes were developed, an initial prototype of a maximum take-off weight of about 3 g operated through an external power supply and a second battery powered prototype with a maximum take-off weight of 10 to 15 g. The prototypes used 325 mg DC motors from RMB Switzerland of efficiencies up to 67%. Motor control electronics have been replicated using small components to achieve a board weight of much less than 1 g.

Figure 2.4 'Mesicopter' quad-copter rotary NAV design developed at Stanford University. (a) and (b) Initial prototypes. (c) Four rotor lift test. All images taken from [19].

A set of analysis, design, and fabrication methods were applied to investigate the feasibility of the very small rotorcraft. The aerodynamic design of the rotor system was presented in details based on 2D Navier-Stokes analysis of the rotor sections combined with blade element analysis for 3D nonlinear optimisation of the rotors. Two rotor geometries were examined, the first was a 1.5 cm diameter rotor whereas the second was 2.2 cm diameter rotor designed for four times the thrust. However, the manufactured rotor section shapes did not well approximate the initially designed sections mainly due to less precise manufacturing at this scale. Stability, control and power systems aspects of the design were considered in a general discussion fashion without demonstrating their implementation. The 'Mesicopter' did not demonstrate free flight; however, single rotor and four rotors tests on a pivoted arm constraining the motion to a single degree of freedom were conducted, Figure 2.4c. Thrust measurements of the rotors showed maximum thrusts of about 80% of the predicted values which according to the developers opinion indicates that, apart from the manufacturing differences between the built rotors and the intended design, the aerodynamic design approach was appropriate at this scale.

2.2.1.3 Single main rotor/tail rotor configurations

Although large scale rotorcraft are usually designed in a conventional main rotor/tail rotor configuration and despite that some hobby rotary MAVs including the 6.9 g 'Pixelito' are provided in this configuration, almost no notable MAV designs in this configuration have been presented from academia. This is usually attributed to the additional mechanical complexity from the tail rotor drive system [13]; however, this configuration provides good aerodynamic efficiency as well as good controllability and

manoeuvrability characteristics. A successful MAV example in this category is the 'PD-100 Black Hornet', Figure 2.5. The 'Black Hornet' development started in April 2008 and several prototypes and technology demonstrators were produced; however, serial production was established in early 2012 [21]. The system is considered the world's first operational complete nano-system and is currently in service with international units [22]. The 'Black Hornet' has a rotor span of 12 cm, a mass of 16 g including a steerable EO camera (pan/tilt). It can achieve maximum speeds of 10 m/s, and has endurance up to 25 minutes. It has a digital data link, range 1000 m Line-of-Sight, GPS navigation or visual navigation through video.

Figure 2.5 The 'PD-100 Black Hornet' conventional rotorcraft MAV design; images taken from [21].

2.2.1.4 Winged seed configurations

Robotic samara, or winged seed resembles one of nature's fliers, the seed of the Maple tree [23], Figure 2.6a. These vehicles achieve continuous rotation making use of the available thrust force from a propeller attached to their bodies (see Figures 2.6b and 2.6c), and in the event of motor failure the vehicles should gently auto-rotate back to the ground. Advantages over traditional micro-scaled VTOL configurations include efficient autorotation and mechanical simplicity; however, there is a clear disadvantage in that fuselage and attached sensors are constrained to rotate with the main rotor.

A group from the University of Maryland considered this configuration in depth and developed three robotic samaras [24-27]; Samara I and II are shown in Figure 2.6b and Samara III is shown in Figure 2.6c. These robotic Samaras were developed based on an iterative design process which produced an order of 100 vehicles. The maximum dimension of Samara I was 27 cm, and had a total mass of 75 g. Its flight duration was about 20 minutes with a 25 g, 480 mAh 7.4V two-cell Li-Po battery. Samara II was a smaller version designed and constructed in a similar fashion to Samara I. The total

mass was 38 g, the maximum dimension was 18 cm and could fly for around 10 minutes. The smallest of the robotic samaras was the Samara III which had a maximum dimension of 75 mm and a total mass of 9.5 g. It was powered by a 60 mAh 3.4 V single-cell Li-Po battery and had a maximum flight time of around 2 minutes. Due to compactness issues, the Samara III had only a passive flap hinge and did not have servo control collective pitch, which reduced control only to the vertical axis.

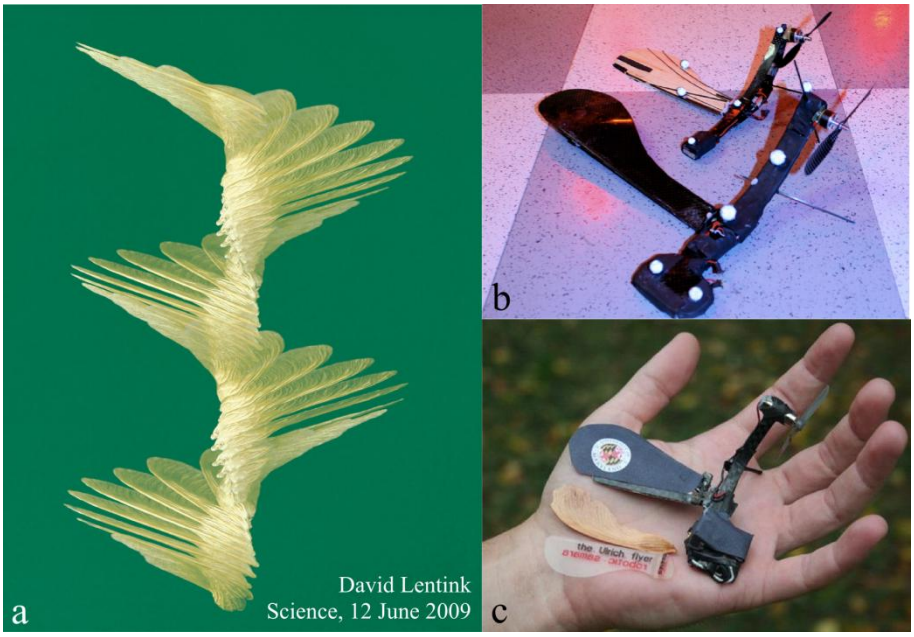

Figure 2.6 (a) The flight path of a maple seed visualized in a composite multiflash photograph; cover photo of Science, June 2009. Winged seed rotating MAV designs: (b) The University of Maryland Samara I and II; image taken from [26]. (c) The University of Maryland Samara III; image taken from [25].

2.2.1.5 Other configurations

In this sub-section other possible rotary configurations are highlighted. The first configuration is from the Konkuk University and was developed in 2004 [28], Figure 2.7a. The system was composed of an electronic motor, a rotor with two blades, two passive anti-torque vanes, two active anti-torque vanes, and a directional control surface. The reported total mass was less than 130 g and the motor used produced sufficient thrust at 1900 rpm with a total current of 1.67 A. The battery capacity was 340 mAh. The anti-torque control surfaces were designed to produce a torque of 270 g.cm in hover conditions; these surfaces were 8 cm long, and attached at 3.2 cm below

the rotor blade. The vehicle was designed for a flight time of 8.4 minutes, and maximum reported duration was 5 minutes.

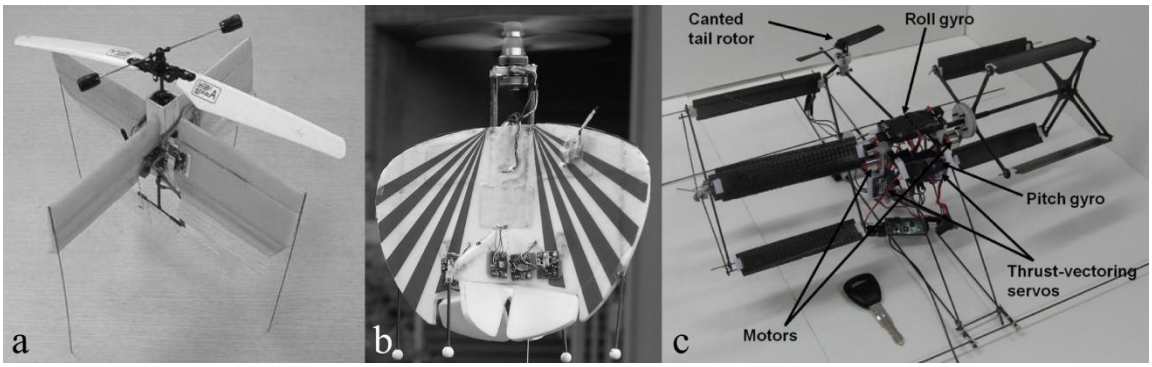

Figure 2.7 Other rotary wing MAV designs. (a) Konkuk University design; image taken from [28]. (b) Arizona/ISAE design; image taken from [29]. (c) The University of Maryland cyclorotor; image taken from [30].

In 2008 a team from the University of Arizona and the ISAE of France presented a tilt-body, tail-sitter VTOL MAV concept [29], Figure 2.7b. The design is based on a contra-rotating propeller-motor electric propulsion system where detailed design/analysis was conducted regarding the aerodynamic and propulsion characteristics. The takeoff weight was 180 g. Each propeller was powered by a separate motor. This system was assembled by using off-the-shelf brushless outrunners MPJetAC22/4-60D with Phoenix-25 electric speed controllers. Propellers used were APC with a 14 cm diameter and 11.4 cm pitch. The distance between propellers was 1.7 cm. The airframe had a Zimmerman wing planform with 30 cm wingspan and wing area of 488 cm^2. Power required was 80 W, and the used battery was a 3-cell Li-Po battery with 740 mAh capacity. Two fins with rudders provided roll and yaw stabilisation, whereas two elevons provided pitch and yaw control. Demonstrations of hover, sustained vertical climbs, and transition to and from a level flight were conducted using manual control from a pilot.

The Cycloidal-rotor or cyclorotor is another possible rotary wing MAV concept, e.g. that developed by the University of Maryland [30-32], Figure 2.7c. Here, the blade span is parallel to the rotation axis and the pitch angle of each blade is varied cyclically such that the blade is at a positive incidence at top and bottom halves of the azimuth cycle [30]. The amplitude and phase variations of the cyclic blade pitch is employed to change the magnitude and direction of the net thrust vector for control purposes. The

design shown in Figure 2.7c is a twin cyclocopter capable of stable hovering and has a mass of 215 g and a blade span of 15.24 cm. Several study aspects were conducted on this concept including aerodynamic and PIV measurements as well as investigations to improve the performance through studying the effects of the geometric and kinematics design variables. These parametric investigations showed possible significant improvement in the cyclorotor performance and the final efficiency was found to be comparable to that of a conventional micro rotor at the same scale: The power loading of the optimised cyclorotor was higher than that of a conventional micro-scale rotor when compared at the same disk loading [30] and the *FM* was 0.4 [32].

2.2.2 Piezoelectric actuated rotary wing design

There has been an attempt to replace the rotary wing motor with a reciprocating piezoelectric actuator in a concept referred to as 'Flapping Wing Rotor' from the University of Cranfield in 2011 [33]. Theoretical study, numerical modelling, and experiments were undertaken. It is essentially a 'piezofan' design (see section 2.4.2.1) but with the wings attached in a rotor fashion. Excitation of the piezoelectric actuator at resonance in the flapping axis leads to a thrust force that rotates the two wings. A prototype was manufactured and tested, Figure 2.8. This prototype was made of a piezoelectric actuator, a shaft, and a pair of flapping wings connected at the two ends of the actuator in axial symmetry about the shaft. The piezoelectric actuator used in the test model was the commercially available THUNDER TH-8R of dimension 13.7 × 6.3 cm. The wing was made of four beams supporting a polymer thin foil skin with a length of 9 cm and a maximum chord of 3 cm.

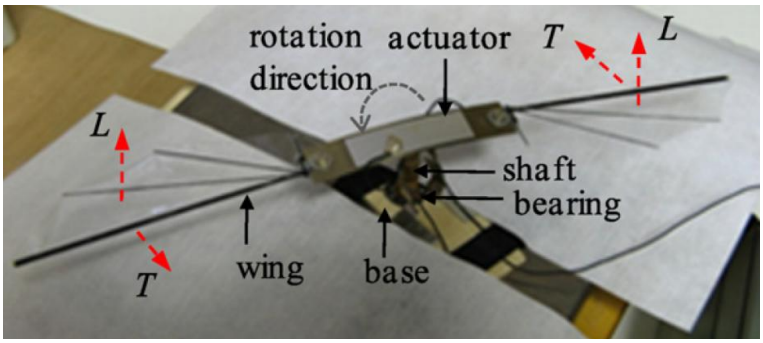

Figure 2.8 Cranfield University flapping wing rotor actuated with a piezoelectric actuator; image taken from [33].

The dynamic behaviour of the model was analysed using FEM. The aerodynamic forces were modelled based on Theodorsen theory as well as using CFD numerical simulations. To validate their theoretical and numerical analysis, an experiment of the test model was carried out through which the total force produced by the flapping wing rotor including the aerodynamic and inertia forces has been measured. The comparison showed a good agreement between the experimental and analytical results. Flight tests were not reported.

2.2.3 Summary of rotary wing MAV designs

This sub-section provides a summary of the presented rotary wing MAVs. Design data are presented in Table 2.1.

Table 2.1 Comparison of the main characteristics of rotary wing MAVs. Designs are presented in a chronological order.

Design	Year[1]	Source	Configuration	Mass (g)	Rotor diameter (cm)	Endurance (min)	Power Source	Features
Mesicopter	2000	Academia	Planar-Multirotor	3	1.5	NA	Tether power	**N**o free flight
MICOR	2003	Academia	Coaxial	103	15.24	3	Three 430 mAh $LiMnO_2$	**O**pen loop differential yaw
µFR II	2004	Industry	Coaxial	12.3	13.6	3	LiPo	**G**yro sensor / linear actuator for stability / 32-bit RISC microcontroller
Konkok	2004-2006	Academia	Hybrid	130	NA	5	340 mAh LiPo	**G**yro for anti-torque stability / Yaw directional control surface
CoaX	2006	Academia	Coaxial	200	30	Short moments	900 mAh LiPo	**L**ateral control using CoG shifting / differential yaw
Arizona /ISAE	2008	Academia	Hybrid	180	14	NA	740 mAh LiPo	**F**ins with rudders for roll & yaw stability / Elevons for pitch & yaw stability
Samara I	~2009	Academia	Samara	75	27*	20	480 mAh LiPo	**S**ervo control of collective pitch / Propeller control of rotation rate / Indoor close loop control
Samara III	~2010	Academia	Samara	9.5	7.5*	2	60 mAh LiPo	**N**o servo control of collective pitch / Passive flap hinge
Black Hornet	2008-2012	Industry	Conventional	16	12	25	NA	**G**PS and Visual navigations / Digital data link
Hubsan Q4	2013	Industry	Planar-Multirotor	11.5	3	5	100 mAh LiPo	**6** axis flight control system with adjustable gyro sensitivity

[1] based on most significant publication, * based on maximum dimension

In summary, the development of rotary wing vehicles at the micro scale started only a decade ago and it seems that achieving relatively long endurance remains the main

challenge. However, despite some concerns regarding the achieved flight performance, most micro rotary wing vehicles succeeded in demonstrating free flight.

Most of the vehicles presented did not achieve the flight endurance they were designed for. It is common to find groups reporting this issue and usually reasoning it to low aerodynamic efficiency at this scale as well as failure to accurately predict performance of batteries. Reported *FM* values are around 0.4 and can reach 0.6 in best cases; this is mainly attributed to profile drag which is higher at low Reynolds number (more discussions on the *FM* will be presented in Section 3.4.2). This motivates further research to enhance the aerodynamic efficiency as well as improve power sources characteristics. However, electric power source development is driven mainly by electronic consumers and is not considered in this thesis.

Designs presented from industry were generally more successful compared to those from academia. A very impressive design is the Black Hornet that is now the world first operational MAV in service; its considerably improved endurance given the small size and weight as well as its control and guidance systems represent an important milestone in the development timeline of MAVs.

Many of the possible rotary configurations were demonstrated successfully including coaxial, main rotor/tail rotor, quad rotor, rotary seed and hybrid designs. No significant contributions at the micro scale were presented in the tandem or ducted coaxial configurations. Most probably compactness issues limit the former while complexity issues limit the latter.

The ‘Mesicopter’ and the ‘Hubsan Q4’ designs were the only presented demonstrators at the insect-scale. Both are in the quad-rotor configuration. Whilst the ‘Mesicopter’ did not achieve free flight, the ‘Hubsan Q4’ is now attracting much attention from the hobby community.

2.3 Flapping Wing MAV Designs with Rotary Actuation

2.3.1 Two wing designs

This sub-section will discuss designs having a single pair of flapping wings as the lift generating surfaces. For completeness, a number of traditional ornithopter designs with a horizontal tail surface which are primary designed for forward flight are included. These vehicles are unable to achieve sustained controlled hover, however since in principle they can meet the thrust ≥ weight requirement they are considered as in scope.

Whilst elastic powered model ornithopters have been in existence for many years, the first electrically powered ornithopter to fly was the ‘Microbat’ developed by Caltech and Aerovironment in 1998 [34,35], Figure 2.9a and 2.9b. Four transmission designs were considered, Figure 2.9c, from which configuration C was built, Figure 2.9d.

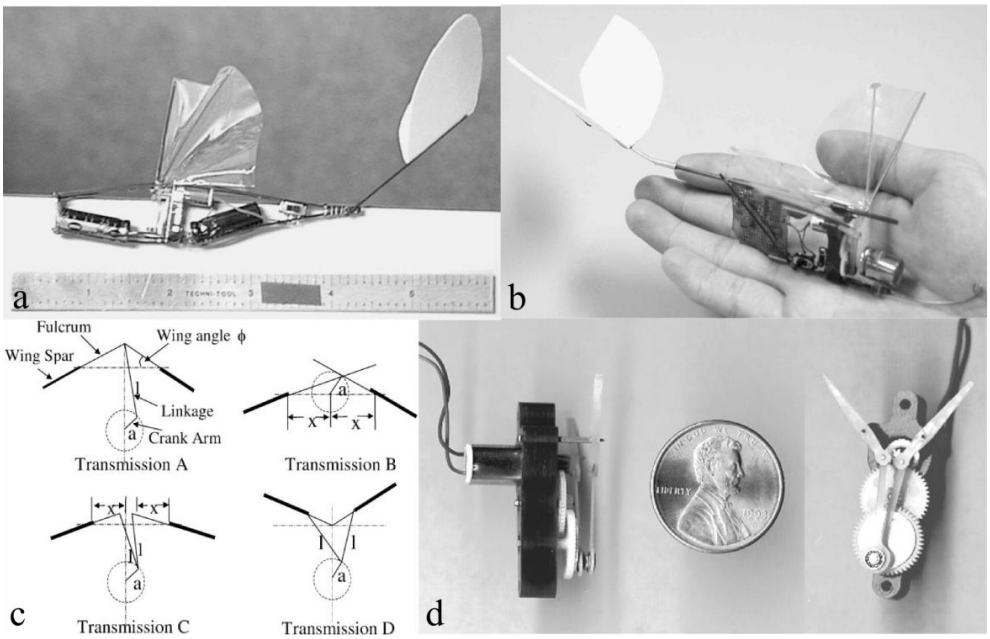

Figure 2.9 The two ‘Microbat’ versions: (a) super capacitor-powered, (b) battery-powered. (c) Various transmission designs for the ‘Microbat’ MAV developed at Caltech. (d) The fabricated transmission system. All images are taken from [34].

Motive power was provided by a 1.5 W DC motor via a gear box with transmission ratio of 22:1. With no wings attached a flapping frequency of 42 Hz was achieved. The operational frequency with wings on was 30 Hz. Two variants of the vehicle were developed, one powered by a super capacitor and one by a battery. The super capacitor variant, Figure 2.9a, had two 1 F super capacitors, an overall weight of 6.5 g and flew for 9 seconds. The battery powered variant used a 3.5 g Sanyo 50 mAh NiCd N-50 battery, which was the lightest battery commercially available at the time. A DC to DC converter weighing 1.9 g was used to step up the nominal battery voltage of 1 V to the 4-6 V required by the motor. The battery variant, Figure 2.9b, had an overall weight of 10.5 g and flew for 18 seconds.

A design similar to the ‘Microbat’ was presented by a group from the Tamkang University in Taiwan around 2006 [36], Figure 2.10a. The wing skin was made from PVDF (polyvinylidene fluoride), with the objective of using the skin to sense

aerodynamic forces as part of a control system. The transmission system used a four bar linkage system that allowed variable phase lag between each wing. The wing span was 28 cm and the all up weight was 11 g. Motive power has been provided by a DC motor via a 27:1 reduction gear box. Flight control was via 2 channel radio control (tail angle, motor rpm). A flight duration of 10 seconds over a distance of 40 m was reported. In a later attempt [37], a second prototype produced with improved manufacturing methods and a reduced wing span of 22 cm reduced the vehicle mass to 6 g and increased the flight endurance to last over 6 minutes.

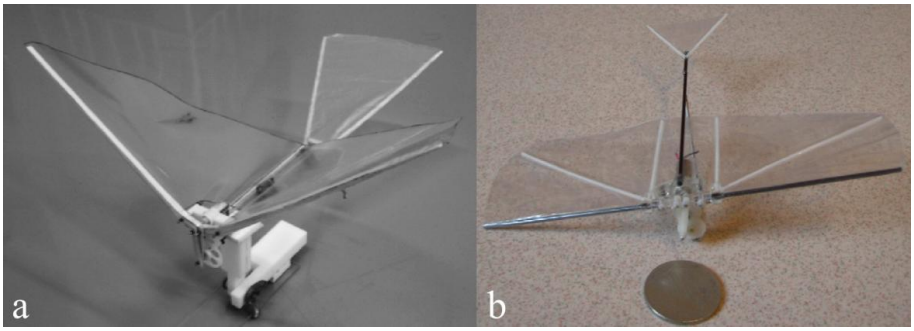

Figure 2.10 (a) MAV with PVDF sensors from the Tamkang University; image taken from [36]. (b) MAV from Chung Hua University; image taken from [38].

Tsai and Fu from Chung Hua University in Taiwan presented a further Microbat-like design in 2007 [38], Figure 2.10b. The vehicle weighed 8 g, had a wing span of 15 cm and an aspect ratio of 3. The aerodynamic surfaces were sized and arranged based on statistical data from previous designs. Power was provided by a 2 g DC motor with an output speed of 28,000 rpm. The battery used was a single cell Li-H battery weighing 1.5 g. The transmission system used a 18:1 reduction gear followed by a four bar crank. Flapping frequency was around 26 Hz and the total flapping angle was 73 degrees. A flight distance of 8 m was reported.

The ‘Proxdynamics’ ornithopter introduced in 2007 [39], Figure 2.11a, is similar in configuration to the preliminary described ‘Microbat’ configuration but at a significantly reduced all up weight of 1.1 g. The vehicle had a span of 10 cm, and a length of 8.5 cm. It used a 3.2 mm diameter coreless DC motor and an 8 mAh Li-Po battery. The ornithopter was set to fly in circles with the speed and height being controlled, and flight time was around 1 minute.

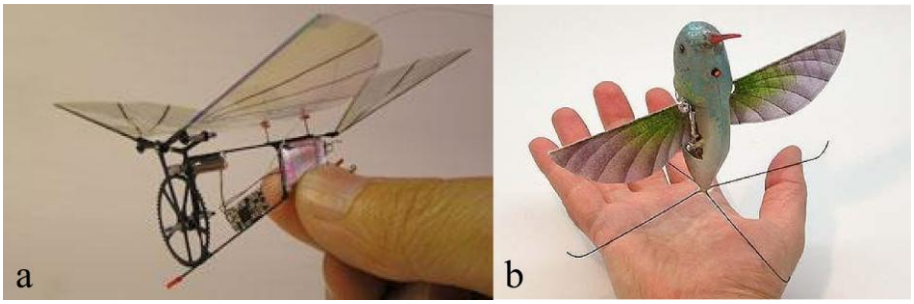

Figure 2.11 (a) The Proxdynamics ornithopter; image taken from [39]. (b) AeroVironment 'Nano-Hummingbird'; image taken from [40].

A significant technological leap was provided by the AeroVironment 'Nano-Hummingbird' introduced in 2009 [40], Figure 2.11b. The full technical details of this vehicle are not published, however it can be surmised that each wing was independently actuated in flapping and twist axes in order to provide 6 degree of freedom control of the vehicle in hover. The wing span was 16 cm and the all up weight was 19 g. A hover endurance of 8 minutes is quoted. Controlled transition from hover to forward flight at 5 m/s and back to hover was demonstrated.

2.3.2 Four wing designs

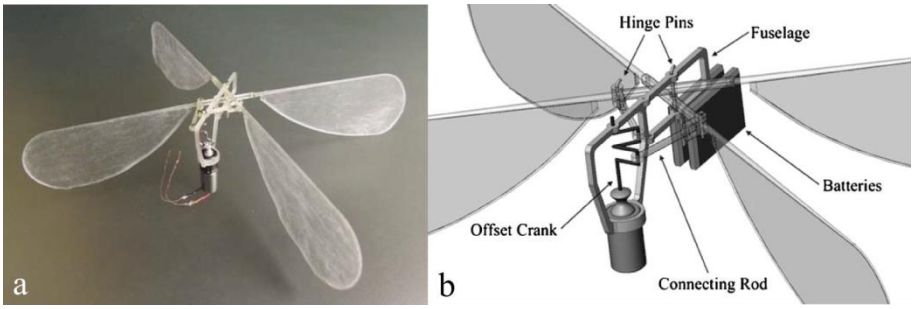

Figure 2.12 (a) The Cornell University four wing ornithopter, and (b) the ornithopter detailed mechanism; image taken from [41].

Few designs have been presented recently in a four wing configuration similar to a dragon fly, and can be considered as analogous to quad rotor designs. A first example is the design presented by Ritcher and Lipson from Cornell University in 2010 [41], Figure 2.12a. The vehicle had a mass of 3.89 g, and demonstrated an 85 seconds untethered hovering flight. Experimentation with several wing designs were carried, and the finally chosen wings were 8 cm long with a maximum chord length of 3 cm. The wings alone were flapped at approximately 30 Hz through an angle of 110 degrees using

a GM15 motor available from Solarbotics with 25:1 gear reduction. A fuselage was designed to carry the motor, crank, and wing hinge, Figure 2.12b. The vehicle was first tested using a tether power source and was able to lift up to 1.5 g of payload, which is roughly equivalent to the mass of the two 10 mAh Li-Po batteries required for flight.

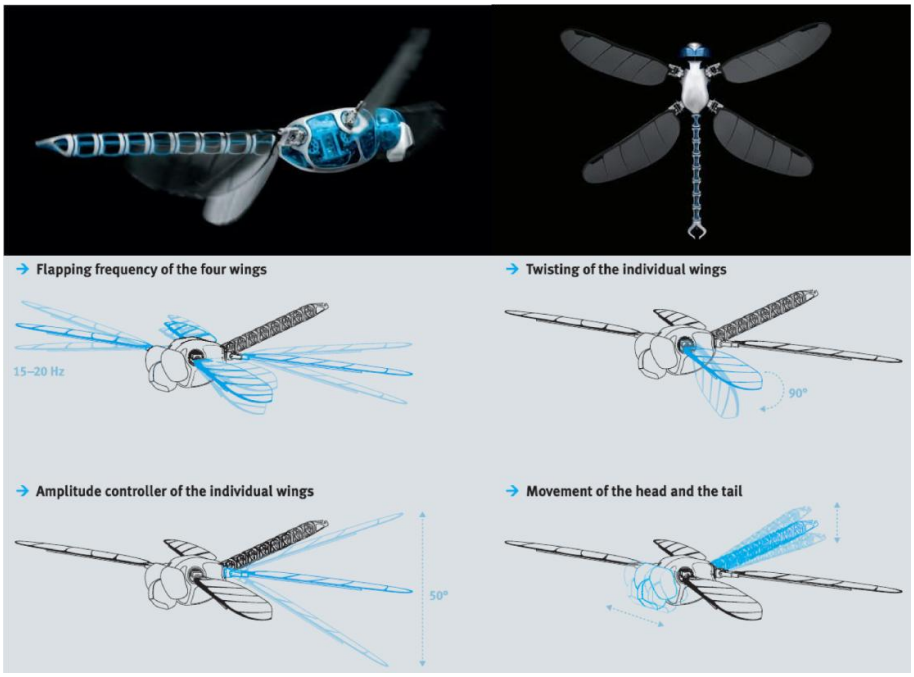

Figure 2.13 The ‘Bionic-Insect’ from Festo; image taken from [42].

Festo in 2013 presented a dragonfly-like vehicle named the ‘Bionic-Insect’ [42], Figure 2.13. The vehicle had a relatively large wingspan of 63 cm; however, it is a successful demonstrator inspired from insects that deserves reporting. The body length was 44 cm and the vehicle had a mass of 175 g. Each of the four wings can achieve control of the flapping frequency, flapping amplitude, and wing pitching motion allowing superior control of the magnitude and direction of thrust force of each wing. The flapping frequency was adjustable between 15 and 20 Hz. Wings can be turned from horizontal to vertical using servo motors that can pitch the wing by up to 90 degrees, see Figure 2.13. Four servo motors at the wing junctions controlled the flapping amplitudes through a linear movement at the wing root allowing the integrated crank mechanism to change the angle between approximately 80 and 130 degrees. Additional degrees of freedom were added in the head and tail through four flexible muscles made of nitinol. By allowing an electric current through this shape memory alloys, they act as ultra-light actuators able to move the head horizontally and the tail

vertically. The vehicle used one brushless motor powered by two 7.6 V Li-Po batteries, and was able to demonstrate free flight.

2.3.3 Clap and fling wing designs

This sub-section will discuss designs with wings employing the clap and fling mechanism as described by Weis-Fogh [43]. Note that inclusion of clap and fling as a specific category of vehicles is because there are a number of designs that can be conveniently grouped under this heading. Clap and fling of itself does not provide significant novelty over other ornithopter designs described previously. An earlier design relying on this mechanism is the 'Mentor' MAV developed by Advanced Subsonics Inc., the University of Toronto and SRI International in 2002 [44]. Two flying prototypes were built, Figures 2.14a and b, one with an internal combustion engine and another with an electric motor. Both had a drive train to reduce the high rpm rotary shaft motion to lower-frequency flapping oscillation as well as a programmable logic board for stabilisation.

The internal combustion engine prototype had a mass of 580 g and wings of 35.5 cm span actuated at a nominal frequency of 30 Hz. The MAV was controlled with four independently actuated fins of approximately the same size as the flapping wings. Although designed to achieve up to 6 minutes of hovering flight, an endurance of around 1 minute was only achieved. The electric-powered version had a mass of 440 g and the wings were identical to those used for the engine prototype, except that the stiffness was reduced and this was argued to be for greater aerodynamic efficiency. The flapping frequency was approximately 30 Hz and power was delivered from a brushless electric motor driving a gearbox connected to a rotary to oscillatory transmission. A battery pack of eight 600 mAh Ni-Cd cells was used allowing hovering flights of around 20 seconds.

Another design in this category is the 'Delfly-Micro' from the Delft University of Technology [45] introduced in the year 2008, Figure 2.14c. The 'Delfly-Micro' is the result of two miniaturisation steps of a single design based on two successful previous versions, namely the Delfly I and Delfly II [9,45]. Here only the 'Delfly-Micro' is discussed because it represents the lower bound of the miniaturisation process implemented on this concept. It had a 10 cm wingspan, a mass of 3.07 g and flapped its wings at 30 Hz. It carried a video camera fully controllable by radio. Control was achieved by the tail section. A DC electric motor drove the four wings through a gear

reduction and a linkage system. Wing pitching was obtained by tailored stiffness of spar reinforced membrane wings. The ‘Delfly-Micro’ demonstrated slow moving and near hovering flight up to 3 minutes using a 30 mAh Li-Po battery.

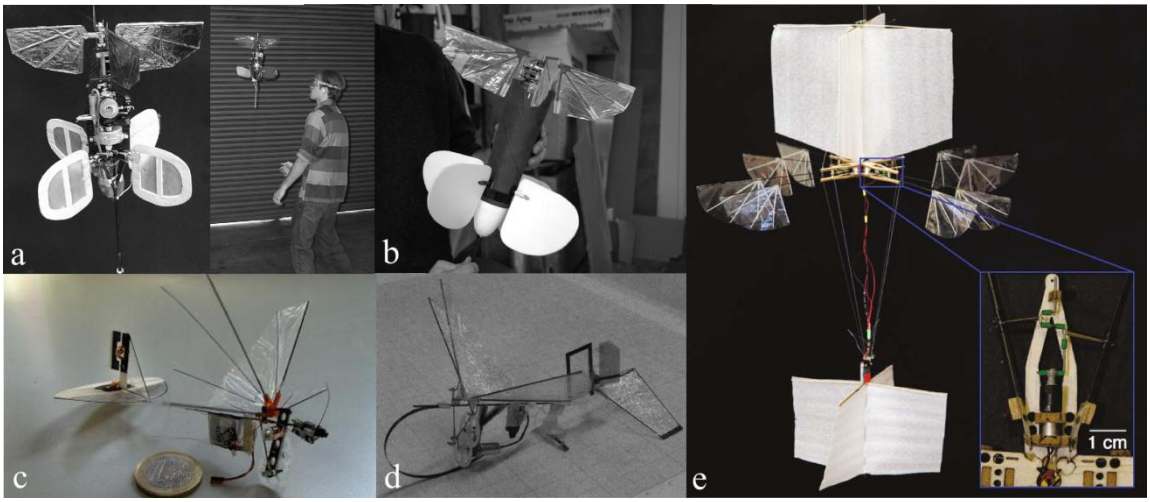

Figure 2.14 Clap and fling designs. (a) and (b) The ‘Mentor’ MAV with internal combustion and electric propulsions respectively; images taken from [44]. (c) The ‘Delfly-Micro’; image taken from [45]. (d) The Fukuoka Institute of Technology MAV; image taken from [46]. (e) The Cornell University MAV; image taken from [47].

A design developed by Kawamura Laboratory, Fukuoka Institute of Technology was proposed in 2008 [46], Figure 2.14d. The vehicle had a 10 cm wingspan, a mass of 2.3 g, and the hovering flapping frequency was 35 Hz. A DC motor connected to a reduction gearbox was used, and a linkage based four-bar mechanism was designed so that the two pair of wings claps at the peak and bottom of the stroke. The prototype was reported to be capable of free flight using a tail with control surfaces.

The last design presented within this group is the unique MAV shown in Figure 2.14e developed at Cornell University in 2010 [47]. The design is a combination of the ‘four wing’ and ‘clap and fling’ configurations. The vehicle had an all up mass of 24 g. Four pairs of wings were used and each wing pair was actuated by a separate 1.2 g geared (25:1) DC pager motor. The motor was connected to a crankshaft, which was connected to the wings with connecting rods and ball joints. Motors were powered in parallel using two 3.1 g, 3.7 V, 90 mAh Li-Po batteries. Top and bottom sails to provide stability were used. Flight testing operating conditions were measured to be 6.5 V at 1.07 A to generate a total lift of 25 g for 33 seconds of flight.

2.3.4 Non-Conventional designs

The designs presented in this sub-section are unique in either their configuration and/or their thrust generation concept. The first design is from the Naval Postgraduate School (NPS) that used flapping wings for propulsion whilst generating lift by a stationary non-flapping wing [12]. A clapping flapping style was demonstrated through flapping with constant spanwise amplitude rather than flapping as insects or birds around the wing root. Because the flapping wings draw air in with a suction effect, it was argued that delay of flow separation is evident and the vehicle can recover from stall and gain control back quickly [48,12]. Several wind tunnel test models were prototyped to test the concept leading to a few generations of radio controlled MAVs. The third generation model is shown in Figure 2.15a. It had a 25 cm span and a mass of 13 g. The flight speed ranged between 2 and 5 m/s, where the maximum flight speed was clearly limited by the maximum achievable frequency of 40 Hz. The speed was controlled by trimming the pitch of the flapping wings pre-flight, and the altitude was controlled by varying the flapping rate [7]. The MAV demonstrated extended controlled forward flight for 15 min on a rechargeable battery [12]; however, the concept is not well suited to steady hovering.

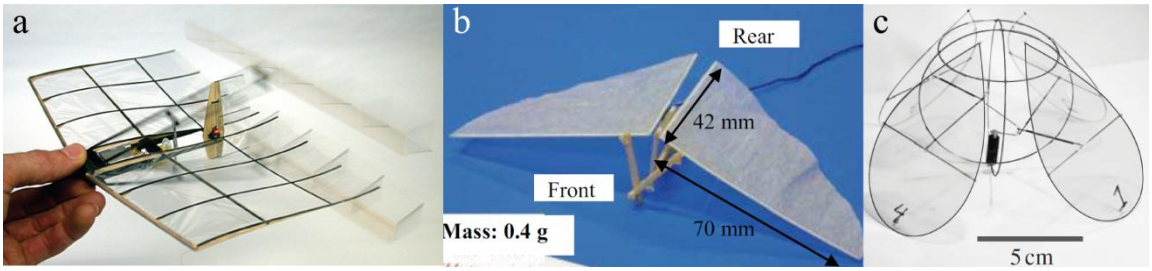

Figure 2.15 Non conventional designs. (a) Naval Postgraduate school concept third generation model; image taken from [48]. (b) Butterfly-type ornithopter (BTO) prototype developed at the University of Tokyo; image taken from [49]. (c) Jellyfish like MAV; image taken from [50].

The second design presented here has neither a tail nor flight control devices. This concept was studied at the University of Tokyo to mimic butterfly flight in 2005[49], Figure 2.15b. The rubber band actuated vehicle was referred to as Butterfly-type ornithopter 'BTO'; it had a 14 cm wing span and a mass of 400 mg. The flapping frequency was adjusted by the rubber band thickness and length. The wings were flapped at 10 Hz by a steel wire crank and linkages with a stroke angle that varies from

–24 to 50 degrees. Because it has no continuous power source; the BTO demonstrated flight for about 3 seconds.

The last concept discussed here was presented in early 2014. The unique concept employed an electric motor for actuation but flapped its wings in a jellyfish like motion [50], Figure 2.15c. The total vehicle mass was 2.1 g and the wings were 8 cm in length. It used a 1.1 g GM15 Solarbotic motor powered through a tether. The motor was positioned at the bottom of the vehicle driving a crankshaft that is connected to the wings through low friction Teflon junctions. The employed kinematics were such that each pair of wings leads the other by a quarter period. A voltage of 5.5 V to the motor allowed a 19 Hz flapping frequency sufficient to support the vehicle weight. The model was used to study stability in hovering without the need for additional aerodynamic surfaces or feedback control; it was also used to demonstrate the enhancement of aerodynamic force generation due to wing bending.

2.3.5 Summary of flapping wing MAV designs with rotary actuation

Here, a summary of the presented rotary actuated flapping wing MAVs is provided, and these MAV data are presented in Table 2.2. In summary, having achieved sufficient thrust, improving flight endurance seems to be the biggest next challenge. Reducing weight, improving aerodynamic design and enhancing power systems performance are the major drivers. Academia has presented more designs than industry; however, the designs presented from industry were generally more successful including Aeronvironment ‘Nano-Hummingbird’ and Festo ‘Bionic-Insect’. Similar to rotary wing concepts, the designs within this group that employ a four wing configuration use these wings for lift generation as well as for stability and control whilst the designs employing two wings, apart from the BTO, have a tail for stabilisation and possible control.

Almost all of the developed designs within this category employ the same transmission mechanism concept; i.e. a motor is connected to a reduction gear box which in turn drives a four bar linkage mechanism for flapping motion generation. All these designs relied on conventional mechanical elements, such as gears and sliders, which are known to have unfavourable scaling of surface effects as the size is reduced. Therefore, the employed mechanisms are suitable for the palm sized vehicles but are not suitable for application to an insect-scale flapping wing NAV design. Flapping frequency varied between 20 to 40 Hz. With the exception of the two designs presented

from industry, all the designs within this category employed passive pitching of the wing.

Table 2.2 Comparison of the main characteristics of flapping wing MAVs with rotary actuation. Designs are presented in a chronological order.

Design	Year[1]	Source	Configuration	Mass (g)	Span (cm)	Endu-rance (sec.)	Frequency (Hz)	Hover capable	Features
Microbat I	1998-2000	Academia + Industry	2 wings	6.5	15.24	9	30	NA	**P**owered by super capacitor
Microbat II	1998-2000	Academia + Industry	2 wings	10.5	15.24	18	30	NA	**B**attery powered
Mentor I	2002	Academia	Clap& Fling	580	35.5	> 60	30	Yes	**I**C Engine
Mentor II	2002	Academia	Clap& Fling	440	35.5	> 20	30	Yes	**E**lectric motor
NPS	2005	Academia	Non-Conventional	13	25	900	40	No	**F**lapping biplane for propulsion / Fixed wing for lift / Flow separation control
BTO	2005	Academia	Non-Conventional	0.4	14	3	10	No	**R**ubber band / No flight control
Tamkang	~2006	Academia	2 wings	10.7	28	10	NA	NA	**P**VDF sensors / Wet etching for construction
Chang Hua	~2007	Academia	2 wings	8	15	NA	25.58	NA	**A**chieved 8 m range
Prox-dynamics	2007	Industry	2 wings	1.1	10	< 60	NA	NA	**1** Channel radio control for motor
Fukuaka	2008	Academia	Clap& Fling	2.3	10	NA	35	NA	-
Delfly Micro	2008	Academia	Clap& Fling	3.07	10	Up to 180	30	Near hover	**C**amera payload / RC
Cornell I (van Breugel)	2007-2010	Academia	Clap& Fling + 4 wings	24	45	33	NA	Yes	-
Nano Humming bird	2009-2011	Industry	2 wings	19	16	> 480	NA	Precision hovering	**A**ctive wing pitching
Cornell II (Ritcher)	2010	Academia	4 wings	3.89	~16	85	30	Yes	**3**D printing demonstrator
Festo	2013	Industry	4 wings	175	63	NA	15-20	NA	**A**ctive control of wing pitch, flapping frequency and amplitude

[1] based on most significant publication

2.4 Flapping Wing MAV Designs with Reciprocating Actuation

2.4.1 Solenoid and motor actuated designs

2.4.1.1 The University of Tokyo Micro-robot

Following the initial vision of Flynn [51], work in micro-robotic flight was started in 1993 by a group in the University of Tokyo based on the concept of a vehicle with an external skeleton similar to that of an insect [52]. A large scale model consisting of plastic plates, springs and solenoids was used to demonstrate the concept, as well as several micro-sized models with micro-fabricated wing structures. The wings were

actuated via a solenoid excited at the system natural frequency. Conventional methods were used for calculating aerodynamic forces generated on the wings, based on aerodynamics of high Reynolds number flows [53]. Experiments in what they argued low Reynolds number flows (Re ~ 386,000) were conducted, and it was found that the aerodynamic forces were underestimated when using conventional aerodynamics. This result was thus used to explain that the actual vertical component of the aerodynamic force generated from the wings would be larger than the weight of the flying micro-robot.

Although, the work developed at the University of Tokyo may seem basic, it can be considered of importance at its time. It revealed a lot of preliminary facts about micro-robotic flappers that represented a starting point for further developments. Their major two finding were: (1) the ability to use the system resonance to generate the required large amplitude flapping motion. (2) Aerodynamic forces calculation at this scale should be revisited.

2.4.1.2 The Delft University ring-type resonator

Bolsman *et al*. from TU Delft investigated the application of ring type structures as the basis for flapping MAVs [54-56]. The inertia, stiffness and dimensions of the ring can be changed to tune the resonant frequency of the coupled system to a specific frequency value. Freedom in wing coupling options, absence of the need for a support structure, and space in the centre of the ring to place the actuator were all reported benefits of the proposed setting.

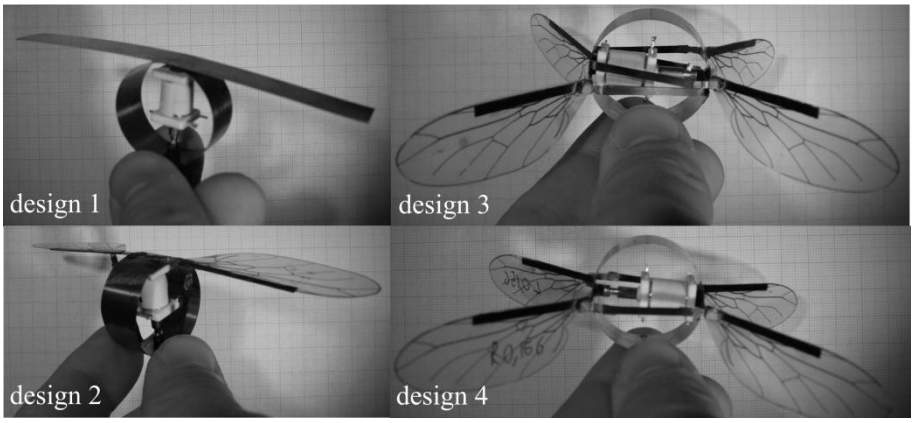

Figure 2.16 The four designs of the ring-type resonator from TU Delft; images taken from [54].

Four structures were initially proposed to study the concept of ring type resonators. These structures were dynamically analysed using both multi-body as well as FEMs, and then built and tested [54], Figure 2.16. The first design had wings crudely manufactured from a bending beam, and rigidly coupled to the ring centre and thus the main mode of amplitude amplification was the wings bending. The structure was driven by a solenoid actuator within the ring, with the direction of actuation set perpendicular to the wingspan. The second design had the actuator connected in the same manner but used struts to connect the opposite side of the ring to the wings; thus, the connection served as flexures for the main mode of amplification. The third design is an extension of the second but the number of wings was doubled to four. The main benefit of this setup was the positioning of the wings along a horizontal stroke plane more suitable for hovering flight. The struts of this design interfered with each other; thus a fourth design was presented where two struts were removed. Large amplitude deflections were obtained from designs 3 and 4 at resonant frequencies of 28 and 24 Hz respectively. However due to differences in strut topology, the wings in design 4 moved half that of those in design 3 with same ring motion. Thus, design 3 was chosen as the preferred concept.

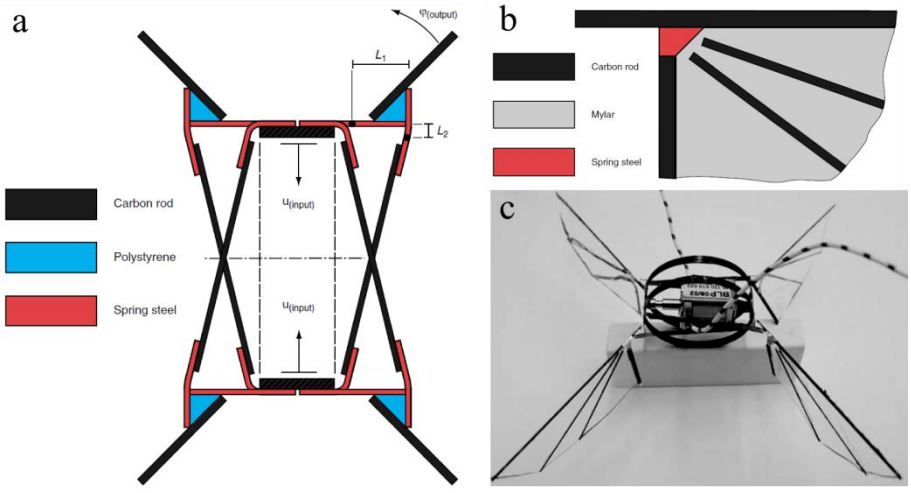

Figure 2.17 The implemented ring-type resonator design from TU Delft. (a) Schematic of the amplification mechanism. (b) Schematic of the wing design. (c) The final prototype including rings, actuator, amplification mechanism and wings. All images are taken from [55].

In a later demonstration [55,56], design 3 was employed but with two parallel carbon fibre ring strips connected with a crossbar, Figure 2.17. The actuator had a maximum stroke of 6 mm, the ring diameter was 30 mm, and the transmission ratio was

7.85 based on appropriate choice of the L_1 and L_2 dimensions in Figure 2.17a. The wings were analysed using a quasi-steady model, then realised with the construction shown in Figure 2.17b. A flexible section made of spring steel was used as a hinge to allow passive wing pitching. The wing planform was based on the shape of the hummingbird wing with a length of 50 mm and a mean chord of 16.75 mm. The whole structure with the two rings, the amplification mechanism, the actuator and the wings is shown in Figure 2.17c. The maximum flapping amplitude at resonance was found to be 34 degrees. The structure was driven at its resonant state close to 27 Hz with a 12 V sinusoidal signal applied to the solenoid. A thrust of 0.9 g was achieved which is more than the weight of the system without actuator by a factor of 1.28. Thus, further amendments on the design are necessary to achieve the required force production.

2.4.1.3 The Carnegie Mellon University Flapper

A group at the Carnegie Mellon University presented a simple motor-driven design capable of producing thrust greater than weight, and torques suitable for flight control in 2013-2014 [57-60]. The design used an elastic element (helical spring) placed in parallel with the motor output shaft. The system resonance frequency can be set by varying the elastic element spring constant. This is different to the majority of piezoelectric actuated designs (Section 2.4.2) where the system stiffness is set by the actuator stiffness.

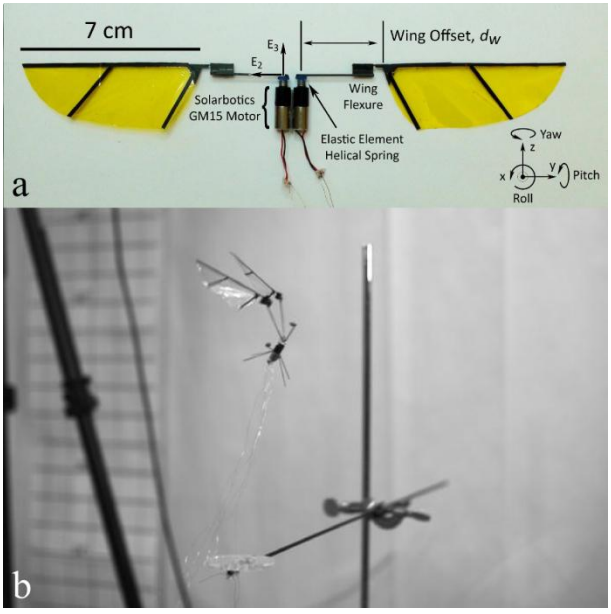

Figure 2.18 The Carnegie Mellon University resonant motor driven flapping wing MAV. (a) The prototype; image taken from [57]. (b) Liftoff the MAV; image taken from [60].

The design as shown in Figure 2.18 is composed of the driving motors, elastic elements, and wings. Two brushed GM15 Solarbotics DC motors driving a 25:1 planetary gearbox were used. The motors were operated with a reciprocating motion rather than continuous rotation like most other rotary motor designs. The flapping motion was driven by a sinusoidal input voltage defined by a frequency, amplitude and bias. Roll authority is obtained by difference in voltage amplitude between motors whilst pitch authority is achieved through the bias voltage. This control philosophy is similar to that used by the Harvard group for the Split Actuator Microrobotic Bee as will be discussed in Section 2.4.2.5. The wing length was 7 cm and the maximum chord was 2.6 cm. Wing pitching was passively achieved through a rotational flexure. The vehicle mass was 2.7 g without a battery, sensors, and additional electronics.

The effect of varying wing offset and elastic element stiffness was examined experimentally with a series of prototypes. A dynamic model was developed, and compared to the experimental results. A desired operating frequency of 10 Hz was defined based on the maximum lift measured experimentally; note that this frequency was slightly beyond the flapping resonance of 7 Hz. The highest lift for the least input power was produced from an elastic element of stiffness of 2.8e3 mN.mm/rad and a wing offset of 38 mm. The system was able to achieve a lift-to-weight ratio of 1.4, and a tethered prototype showed successful liftoff, Figure 2.18b.

2.4.2 Piezoelectric actuated designs

2.4.2.1 Piezofan configuration designs

Recently, some proposals for a so-called ‘piezofan’ configuration for the aerodynamic force generation within flapping wing NAVs have been presented. Whilst these designs lack mechanical maturity compared to other efforts, the work has prompted some useful analytical contributions for actuator dynamics of NAVs. A piezofan configuration couples a piezoelectric bending actuator directly attached to a flexible wing as shown in Figure 2.19. Flexibility of the wing allows relatively large wing flapping motions to be obtained from small piezoelectric actuator displacements without use of a dedicated transmission mechanism.

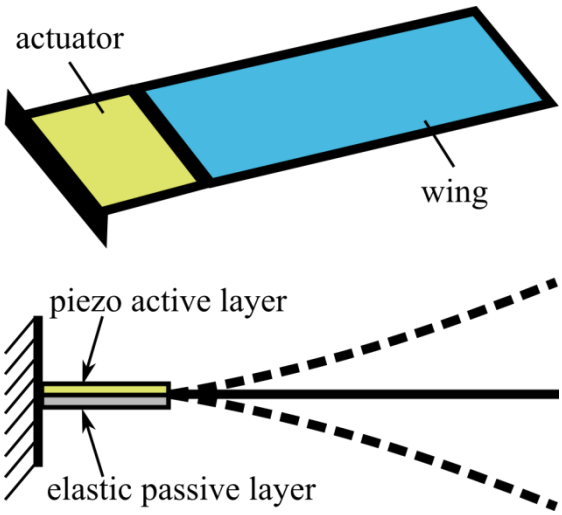

Figure 2.19 Piezofan flapping-wing configuration.

Chung *et al*. [61] used two piezofans in parallel, driven by two sinusoidal voltages with dissimilar phase to control the flapping and pitching motions of the wing. A flexible wing formed by a pair of carbon fibre wing spars and polymer skin attached to two piezoelectric actuators as shown in Figure 2.20 has been demonstrated. High speed digital cameras were used to characterise the motion of the wing and FEA. The system was able to generate a range of wing flap and twist behaviour by adjustment of the actuators drive signals.

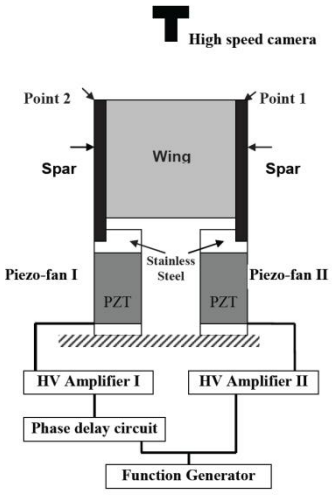

Figure 2.20 Coupled piezoelectric fans with the attached wing arrangement by Chung *et al*. [61]. The phase delay between the driving voltages applied to the coupled piezoelectric fans plays an important role in the control of the flapping and pitching motions of the wing. Image taken from [61].

Later in another study, Chung *et al*. [62] studied only the actuation element of piezofan configurations. The fundamental resonant frequencies of the unimorphs were calculated by a linear analytical method as well as a FEA and these compared favourably with experimental measurements. The free tip deflection at quasi-static operation and the vibration amplitude at dynamic operation of the unimorphs were experimentally measured. The main output was a proposed form of design optimisation using the Strouhal number to select the best unimorph configuration for flapping wing MAV applications (this point will be reconsidered in Chapter 8).

Mukherjee and Ganguli [63] used an energy method by Mahmoodi and Jalili [64] to describe the actuator non-linear equations of motion of a flapping wing which is actuated from the root by a unimorph in the piezofan configuration similar to the one shown in Figure 2.19. An aerodynamic model based on modified strip theory developed by DeLaurier [65] was used to obtain the aerodynamic forces. The main outcome of the work was the integration of two existing models describing the actuator and aerodynamic behaviours of the system. In later studies, they considered the beam twisting motion [66] and compared the performance of unimorphs using different materials of PZT-5H and PZN-7%PT [67].

2.4.2.2 Vanderbilt University designs

Early attempts to realise centimetre-scale flapping wing MAVs based on resonant piezoelectric actuators were presented by a group at Vanderbilt University [68,69] around the year 2002. The idea of designing the right and left wings with slightly different resonant frequency to have differential control of wing amplitude for rolling has been also proposed. Three piezoelectric actuated flexure-based mechanisms that convert the linear output of unimorph piezoelectric actuators into single degree of freedom (DOF) flapping movement were developed. These designs are shown in Figure 2.21.

The first prototype was a four-bar design with the fuselage and wings made from carbon fibre, Figure 2.21a. The total mass was 5.5 g and the resonant frequency was 20 Hz. Angular output was about 30 degrees generated using a sinusoidal input of 180 V. The second prototype was a four-bar design with a clamshell configuration instead of the fuselage, Figure 2.21b. In this design, the output linkage was attached to a second unimorph to increase angular output. The wing was made from a carbon fibre spar and a thin polymer membrane. The design total mass was 22.8 g and resonated at 18 Hz.

Angular output was about 50 degrees generated using a sinusoidal input of 180 V. The third prototype was a five-bar linkage design integrating three orthogonal unimorphs actuators, two moving laterally and one moving vertically, Figure 2.21c. This design had a wing span of 15 cm and a total mass of 7 g; it resonated at 20.5 Hz to produce a 30 degrees wing root motion. More details on the transmission mechanisms will be presented in Section 2.5.5.

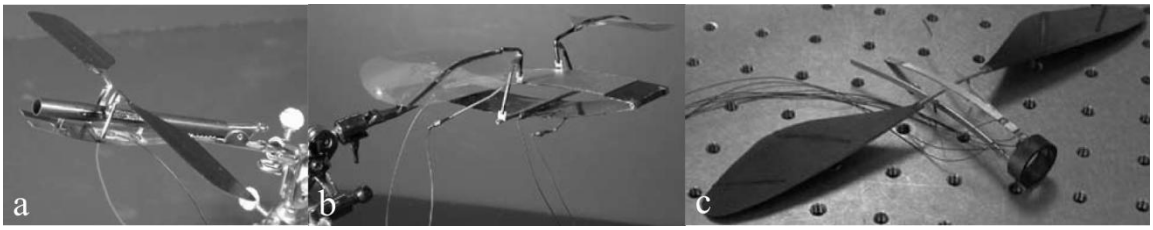

Figure 2.21 Three different bench-top design concepts of resonant piezoelectric actuated flapping MAVs proposed by the group in Vanderbilt University. (a) Four-bar design, (b) four-bar design with a clamshell, and (c) five-bar design. All images are taken from [69].

The work can be judged as a very good attempt at its time (1998-2002) to demonstrate the concept of resonant piezoelectric actuated flapping wing operation using bench-top designs. However, these designs were relatively big, did not show to work independently in any free flight testing and no further work was published later.

2.4.2.3 The U.C. Berkeley Micromechanical Flying Insect (MFI)

A group at U.C. Berkeley made significant efforts between the years 2000 and 2007 to develop a robotic insect with independent control on flapping and pitching motions [10,70-76]. They developed the so-called 'Micromechanical Flying Insect' (MFI) which is a 25 mm wing span resonating piezoelectric actuated flapping wing NAV. A first generation of bench-top models was developed that showed a lift per wing of 506 μN at 160 Hz. However, this lift was marginal given a target weight of 100 mg. Thus, a second generation with refinements to the MFI design increased the wing beat frequency to 275 Hz and lift per wing to 1400 μN. This was achieved by operating with pitching angle amplitude of 45 degrees and flapping angle amplitude of 40 degrees using pure sinusoidal drive. The resonant frequency was increased by reducing the wing inertia using carbon fibre spar wings instead of polyimide tubing. The piezoelectric actuator stiffness was also doubled. An image as well as a schematic of the refined design is shown in Figure 2.22.

The MFI design was actuated by two piezoelectric bending actuators providing an unloaded displacement amplitude of 250 μm and blocking force amplitude of 60 mN [10,77]. Two stages of mechanical amplification followed by a differential element were used to convert the actuator motion into wing flapping and pitching. The first stage was a slider crank to convert the actuator linear displacement into an angular input to the second stage of amplification. This second stage was a four bar mechanism designed for a nominal amplification of 6:1, providing a 60 degrees output motion from a maximum input of 10 degrees. The actual achieved maximum output motion was 40 degrees. The two planar four bars were then coupled into a spherical five-bar differential element to produce the insect wing hinge effect. The differential element role was to convert the angle difference between the four bars into wing pitching, such that an input 22 degree angle difference allows a 45 degrees wing pitching [10].

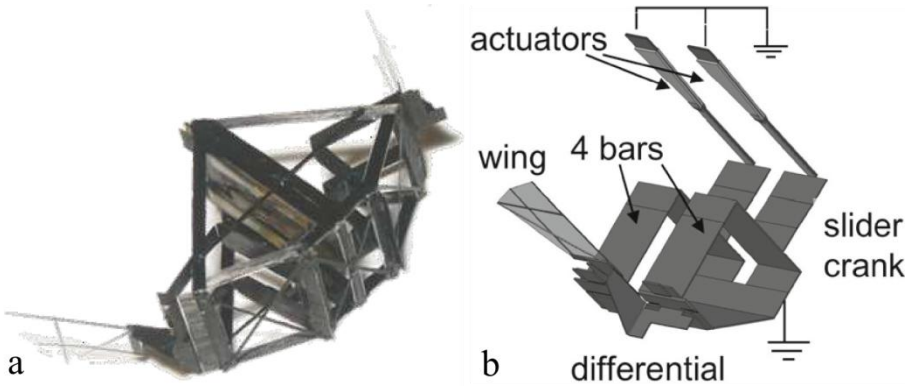

Figure 2.22 The second version of the MFI, (a) the prototype and (b) a schematic of the system components; images taken from [10] and [76].

A very simple blade element model for wing aerodynamic characteristics was used. Predicted results were found to be less than the measured [76]. It was shown that a sinusoidal waveform produces close to maximal lift, however significantly improved wing performance could be achieved using non-sinusoidal actuator drives. In practice the non-sinusoidal motions were unobtainable due to actuator limitations. This group has also done extensive work in the fabrication, testing and analysis of piezoelectric actuators [77-82].

The transmission mechanisms developed for the MFI can be judged as complicated and have not been proven in flight demonstration. Also the size of the mechanism is large with respect to the wing size. However, the mechanism is relatively of light weight

and a vehicle thrust to weight ratio more than 2 was obtained (note that the weight does not include the power system). It was reported that: '*wing inertial and aerodynamic coupling effects dominated the available actuator control effort, making independent control difficult to achieve*' [10, p. 221].

2.4.2.4 The Konkuk University flapping device

A group from Konkuk University in Korea introduced an insect-inspired piezoelectric actuated flapping device around the year 2005 [83-85], Figure 2.23. The flapper employed the clap and fling mechanism for aerodynamic force generation. The motion amplification mechanism was a 4-bar linkage system, and the device used a simply supported unimorph piezoelectric composite actuator.

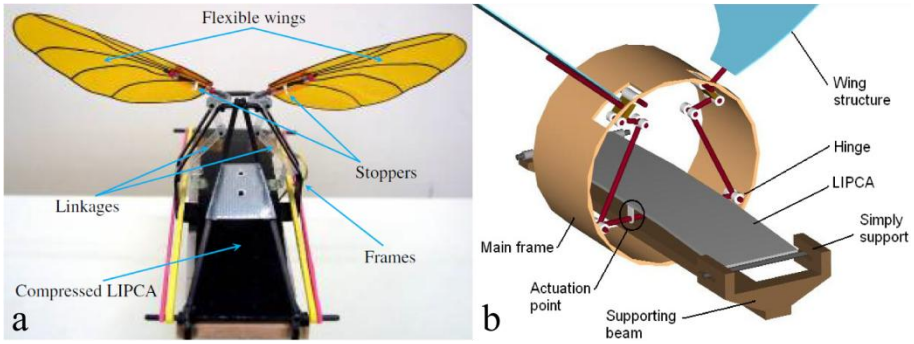

Figure 2.23 The Konkuk University flapping device, (a) real prototype, (b) concept schematic. Note that the actuator is in a simply supported configuration; images taken from [83] and [85].

The developed flapper had a device length of 10 cm, width of 12.5 cm, height of 6.5 cm, wing length of 5.7 cm and an all up mass of 10.38 g. Materials such as balsa wood, acrylic sheet, kapton film, carbon rod and carbon/epoxy composites were used to fabricate the components of the flapper including four-bar linkage systems, hinges, wings, stoppers and supporting frame. The wing shape and vein pattern were mimicked from wings of horse botfly. Passive wing pitching was employed whilst the pitching angle was limited by the shape of an adjustable stopper installed at the rotational axis of the wing. The actuator performance was improved by applying pre-compression of around 10 N (using rubber band), Figure 2.23a. The flapping angle amplitude was 55 degrees with actuator pre-compressing compared to 45 degrees without. This increase in flapping angle corresponded to a 19% increase in the measured aerodynamic force.

Tests to identify the aerodynamic flapping performance of the flapper were conducted both in the air and in a vacuum chamber to measure total vertical force and vertical inertia force. Wing kinematics were examined using high-speed video. The operating point was at a resonance flapping frequency of 9 Hz and an actuator peak to peak voltage of 300 V.

2.4.2.5 The Harvard Microrobotic Fly (HMF)

The 'Harvard Microrobotic Fly' (HMF) has been under development by a group in Harvard University since 2007 [3,8,10,11,86-89]. This group built on earlier experience developed at U.C. Berkeley. The group has made a major contribution to development of manufacturing techniques for insect-scale flapping wing vehicles. A 60 mg, 15 mm wing length propulsion system (actuator + transmission mechanism + wings, Figures 2.24a and 2.24b) externally powered through a tether was developed and was able to produce thrust to weight ratios greater than one, Figure 2.24c.

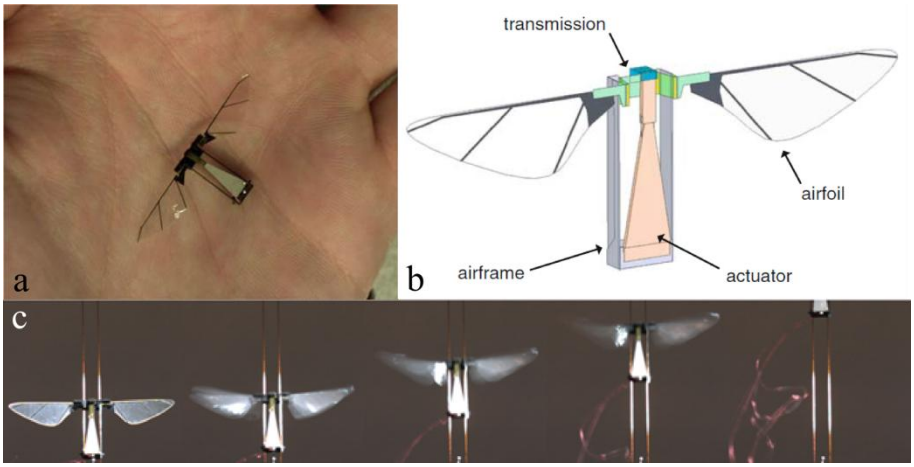

Figure 2.24 The Harvard Microrobotic Fly (HMF). The figures in (a) and (b) show the first prototype of the 60 mg HMF and all its system elements. The figure in (c) shows the HMF first successful vertical tethered flight but in the presence of rail guides. All images are taken from [10] and [88].

The design relied on a central power actuator for generating the flapping motion whilst pitching was achieved passively. The wings were rigid with a flexure hinge at the base of the wing at the interface between the wing and the transmission. Joint stops were used to limit pitch amplitude.

The design was evaluated through a series of sequential tests. To start with, the wings were driven in an open loop fashion at the flapping resonant frequency (110 Hz)

and the wing motion was observed with a high-speed camera. Secondly, thrust was measured using a custom single-axis force transducer. The average thrust-to-weight was approximately 2:1. Finally, a demonstration of constrained takeoff was performed through use of guide wires, as shown in Figure 2.24c. None of these demonstrations included onboard power, sensors, or used any form of automatic control. A later demonstrator with a reduced mass of 56 mg achieved thrust-to-weight ratio up to 3.6:1 [90,91], and one degree of freedom altitude control was investigated.

A second configuration referred to as 'RoboBee' was derived from the original HMF, Figure 2.25a. The new design included two additional smaller control actuators at the base of each wing [92]. The design demonstrated the ability to generate yaw torque through introduction of lateral asymmetry in stroke amplitude. This model was also used to perform experiments with stroke plane deviation as an alternative method for torque generation [93]. The extra actuators increased the mass of the original vehicle to 130 mg. Refinements in construction lead to a lighter prototype of 83 mg, Figure 2.25b, that was capable of liftoff with tether power and was able to demonstrate open loop control [94].

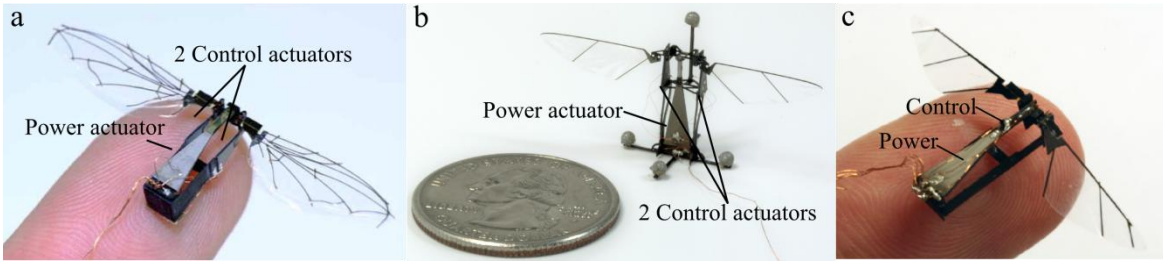

Figure 2.25 (a) The second iteration of the HMF named RoboBee. Two main modifications were incorporated: two control actuators were added as well as a new wing design with bio-inspired venation pattern; image taken from [92]. (b) A lighter version of the Robobee used for free flight experiments, including retroreflective markers for motion tracking; image taken from [94]. (c) Another iteration on the Robobee design implementing a hybrid actuator for power and control; image taken from [95].

A further iteration of the previous concept merged the power and control actuators to create a hybrid power-control actuator [95,96]. The hybrid 2 DOF actuator consisted of one large actuator to supply flapping power and a smaller actuator to serve as a control input, Figure 2.25c. Note that the control actuator vibrates in an orthogonal plane to that of the primary power actuator. This design removed the redundancy of the previous design, and right and left wings stroke amplitude cannot be modified

independently as the stroke amplitude of one wing cannot be reduced without simultaneously increasing the amplitude of the second wing [96].

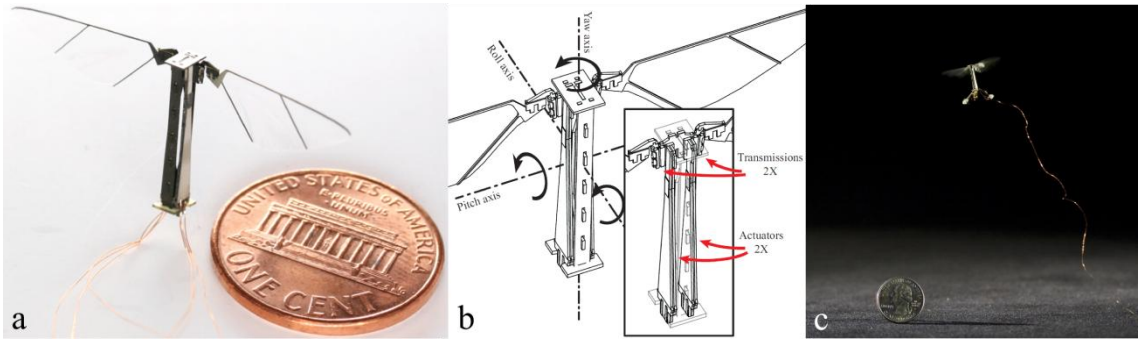

Figure 2.26 (a) The Split Actuator Microrobotic Bee from the Harvard group. (b) A schematic of the Split Actuator Microrobotic Bee thorax design; images taken from [97]. (c) The Split Actuator Microrobotic Bee in tethered controlled flight; image taken from [99].

The most recent iteration presented in 2012-2013 from the Harvard group is called the 'Split Actuator Microrobotic Bee' (SAMB), Figure 2.26. The SAMB design can be considered a substantial milestone in the development time line of insect-scale NAVs as it provides the first demonstration of free controlled flight but still using tether power [97-99]. Position and attitude measurements were obtained via optical tracking of markers on the vehicle. Thrust modulation was achieved by changing the flapping amplitude rather than changing the frequency which is constrained to the system resonance value. The vehicle was able to demonstrate motion modulation of both wings and produced roll, pitch and yaw torques. Wing dynamics were typically about an order of magnitude faster than body dynamics; thus, variations in average parameters over the entire stroke were sufficient to generate mean body torques [98]. Thus: (a) rotation of mean flapping stroke angle for both wings produces a pitch torque. This was achieved practically by applying an offset (bias) voltage to the input signal to actuators. (b) Differential stroke amplitude for each wing produces a roll torque, and was achieved by applying a differential voltage to the actuators. (c) Difference in the drag force on the wing during up and down strokes due to different wing velocities in the two half strokes produces a yaw torque. This was achieved by varying the cycle period that is occupied by the up stroke.

These control actions were achieved mainly because the main power actuator was split into two separate actuators able to independently drive each wing. The shape of each split actuator was such the base is half of the original HMF actuator: 1.75 mm

versus 3.5 mm; nevertheless, each actuator had sufficient power density to drive the load on a single wing. The overall mass of the two actuators was 22% more than the single original HMF actuator [97]. This lead to an 80 mg vehicle capable of producing 1.36 mN which is almost a 2:1 thrust to weight ratio [98]. The vehicle had a wing span of 3 cm and the wing planform was based on the aspect ratio and area distribution of hoverfly. Excitation was sinusoidal at a frequency near the resonance frequency of the coupled actuator-transmission-wing system of 120 Hz [98]. The measured power consumption was 19 mW. The peak to peak flapping amplitude was 110 degrees.

In parallel with the vehicle development work, the Harvard group has also made several contributions to supporting techniques including blade element theory for the aerodynamic characterisation [100], power electronics board design [101-103], piezoelectric actuators [77, 104], flexure joints design [105], and vision sensors for free flight control [106].

2.4.3 Summary of flapping wing MAV designs with reciprocating actuation

This sub-section will provide a summary of the presented flapping wing MAVs employing reciprocating actuation elements. These MAVs data are presented in Table 2.3, and Figure 2.27a provides a wing span versus mass plot. It should be remembered that all the designs presented in this category include only the propulsion system (actuator(s) + transmission mechanism + wings) without any energy source (battery) or power electronics boards. In Table 2.3, the flapping frequency and amplitude are provided; to gather these two characteristics in a more meaningful parameter, the mean wing tip velocity is calculated and plotted in Figure 2.27b. This velocity is based on the approximate formula $V_{tip}= 2\times\phi\times f\times span$, where ϕ is the flapping amplitude, f is the frequency.

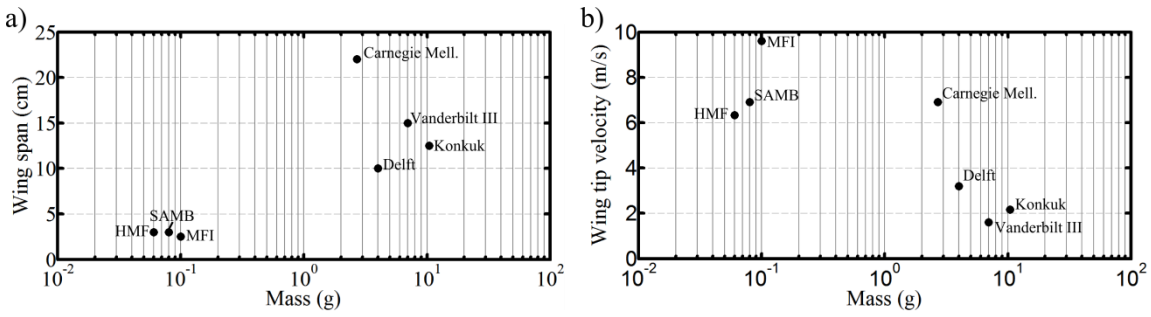

Figure 2.27 Semi-log plots of the main characteristics of flapping wing MAVs with reciprocating actuation. (a) Wing span versus mass. (b) Mean wing tip velocity versus mass.

Table 2.3 Comparison of the main characteristics of flapping wing MAVs with reciprocating actuation. Designs are arranged according to being a bench-top demonstrator.

Design	Year	Actuator type	Bench-top	Wing Pitch	Mass (g)	Span[1] (cm)	Flap angle[2] (deg)	Freq. (Hz)	T/W	Tether Flight	Features
Vanderbilt I	1999 - 2002	piezo	Yes	passive	5.5	NA	15	20	NA	No	**F**our bar design
Vanderbilt II	1999 - 2002	piezo	Yes	passive	22.8	NA	25	18	NA	No	**F**our bar with calm shell / second unimorph to increase flapping angle
Vanderbilt III	1999 - 2002	piezo	Yes	passive	7	15	15	20.5	NA	No	**F**ive bar linkage / three orthogonal unimorphs: 2 lateral and 1 vertical
MFI	2000 - 2007	piezo	Yes	active	0.1	2.5	40	275	2.8	No	**C**omplex design for flapping & pitch control: Two stage amplification followed by differential element
Konkuk	2005	piezo	Yes	passive	10.38	12.5	55	9	<<1	No	**S**imply supported actuator / Four bar linkage mechanism / Clap and fling
Delft ring resonator	2008 - 2009	solenoid	Yes	passive	NA (goal 4 g)	~10	34	27	<1	No	**F**our wings / ring structure
HMF	2007 - 2011	piezo	No	passive	0.06	3	>50	110	~2	Yes (guide rails)	**A**n improved design iteration achieved L/W of 3.6 for a mass of 0.056 g
RoboBee	2009 - 2012	piezo	No	passive	0.083	4	NA	NA	>1	Yes (guide rails)	**O**ne power actuator / Additional control actuator per wing
SAMB	2012 - 2013	piezo	No	passive	0.08	3	55	120	~2	Yes	**O**ne actuator per wing / amplitude modulation for control / first controlled liftoff
Carnegie Mellon	2013	motor	No	passive	2.7	22	Up to 90	10	1.2 (up to 1.4)	Yes	**O**ne motor per wing / Most simple amplification mechanism

[1] Span is based on wing tip to tip distance. [2]Flapping angle represents half the peak to peak flapping stroke angle.

Figure 2.28 shows the characteristic length versus mass of the sub 30 cm characteristic length MAVs discussed in this chapter. Several simple points are clear from the figure: (1) rotary MAVs are the heaviest followed by flapping MAVs with a rotary actuation. (2) Bench-top flapping demonstrators with reciprocating actuation are clustered within the same zone as flapping vehicles with rotary actuation. (3) The MFI, HMF and SAMB (i.e. non bench-top designs) are within a different lower mass and shorter characteristic length zone; nevertheless, no on board power was integrated on these designs. (4) Most designs from rotary wing and flapping wing with rotary

actuation categories are clustered around mass values of 10 g and characteristic length of 15 cm.

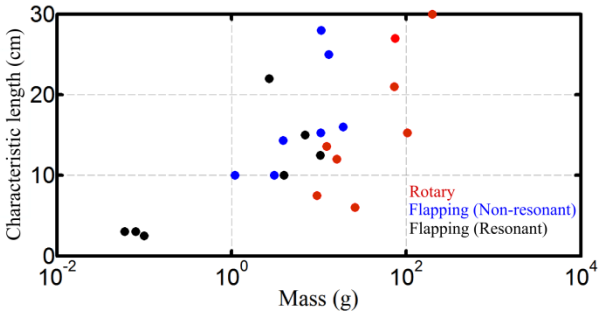

Figure 2.28 Semi-log plot of characteristic length versus mass of the sub 30 cm characteristic length MAVs discussed in Chapter 2.

In summary of the presented literature for flapping wing MAVs with reciprocating actuation:

1. Despite the success achieved within the years 2013 and 2014 that witnessed the first liftoff for both piezoelectric and motor actuated resonant flapping vehicles, extensive further research not just in secondary disciplines but rather in fundamental topics is required to achieve configurations with acceptable flight performance. Most of the wing planforms used were based on mimicking insect species wings. Actuators and motors were usually chosen based on market availability or were manufactured based on available facilities. Advances in both systems modelling and manufacturing should relieve these constraints to some extent in the future.
2. Unlike rotary wing and rotary actuated flapping wing MAVs, All MAVs in this category were presented from academia without any significant contribution from industry.
3. The current piezoelectric actuated vehicles do not yet show integrated sensing and control, or onboard power and electronics. The development of these elements (which some efforts have started recently) represents a future challenge to have a fully functioning air vehicle.
4. All designs in this category do not include a tail; thus, the wings must produce 3 DOF of control torques as well as thrust for weight support. The use of four wings instead of two simplifies the control strategy in that differential thrust can be used

to provide pitch and roll authority (like a quad-rotor). The Delft bench-top model was the only design presented in a four wing configuration.

5. All piezoelectric actuated designs employed the actuator in a cantilever mode except the Konkuk University design which employed a simply supported configuration.
6. All designs within this category were operated at the frequency of the first bending mode to achieve the maximum possible amplification at resonance.
7. Reliance on passive wing pitching is sufficient to achieve successful flapping flight. This reduces mechanical complexity of the system and minimises actuation requirements. However, the wing pitch dynamics should be considered through proper sizing of the wing hinge flexures and end stops as well as careful attention to the wing stiffness distribution.
8. Minimal actuation is a key element for a successful design; aiming to achieve active control on both flapping and pitching wing motions is not necessary. On the other hand, reliance on only one power actuator for flapping motion generation of both wings as demonstrated by the initial HMF was not enough to achieve a sustained controlled flight. The latest successful demonstrators capable of controlled tethered flight including the Harvard SAMB and the Carnegie Mellon University flapper implemented two actuators (one per wing).
9. Rigid wings without many of the aeroelastic features of insect wings appear to be sufficient for successful flapping wing vehicles as demonstrated by the Harvard SAMB and the Carnegie Mellon University flapper. The degree to which use of non-rigid elastic wings within engineering designs would improve the system performance is still an open question.
10. The system frequency increases with decreasing the size as witnessed in insects. Also, the wing tip velocity significantly increases with decrease in mass and size.
11. Despite significant recent advances in motor development, piezoelectric actuators are the most suitable solution for insect-scale vehicles at the moment. However, it is worth noting that all piezoelectric actuators require relatively high voltages around 300 to 400 peak to peak voltages (as in the Vanderbilt and Konkuk designs) whereas motor designs require modest voltages (judged from the Delft and Carnegie Mellon designs). This high voltage put a tough requirement on the power electronic circuit board for piezoelectric actuated vehicles.

12. Unlike piezoelectric actuated systems, the resonant frequency for motor actuated reciprocating systems can be chosen as desired because the system elastic element is not a property of the actuator itself; this allows more flexibility in the design.
13. Exploitation of resonance to achieve increased flapping amplitudes and improve the electromechanical coupling of the actuation (as will be detailed in Chapter 8) are substantial benefits of the designs presented in this section. However, this constrains the operation frequency to a single value (the resonance value), which means frequency cannot be used as a control variable. This leaves amplitude modulation as the only remaining control option.

2.5 Propulsion Sub-Systems of Piezoelectric Actuated Flapping Wing NAVs

2.5.1 Overview

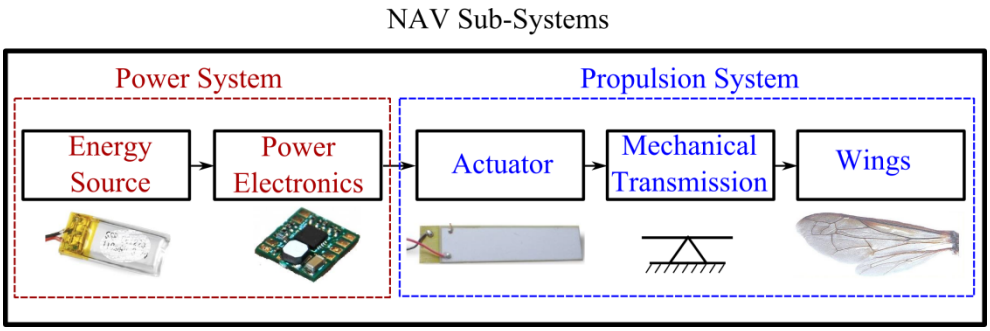

Figure 2.29 Piezoelectric actuated flapping wing NAV propulsion subsystems.

This section provides a detailed description of the subsystems involved to create a propulsion system for a piezoelectric actuated insect-scale NAV. Following the component description presented in [89], there are five primary subsystems involved, Figure 2.29. The first is the electrical energy source (which is typically a battery or possibly a super capacitor). The second is the power electronics board which regulates the flow of electrical power from source to actuator. Piezoelectric actuators pose two challenges for power electronics board: (1) conversion of low voltage DC to high voltage AC, and (2) recovery of substantial unused energy at the end of the cycle due to the actuator's low electromechanical coupling factor. The third subsystem is the piezoelectric actuator element which is responsible for conversion of the input electric power to output mechanical power. The fourth subsystem is the transmission, which serves as a mechanical transformer in the drive train between actuator and the

aerodynamic effectors (wings), and is responsible for conversion of relatively small actuator linear motion into large flapping angles. The final subsystem of the vehicle includes the wings which are responsible for the generation of the required aerodynamic forces and moments for successful operation.

The following sub-sections will discuss in more details the progress achieved by all the previously mentioned research groups within the development of the pointed subsystems. Greatest attention will be directed towards the actuator, mechanical transmission and wing subsystems as they represent the technologically imperative aspect of the design in the sense that a tethered version can be demonstrated with these three subsystems only.

2.5.2 Energy source

Provision of a suitable electric energy source for NAVs is a significant challenge because the NAV application is outside current commercial boundaries; hence batteries of the required voltage and capacity are not available. Note that although fuel cells are anticipated to have higher energy densities compared to batteries, they can be discounted on the basis that the technology does not scale well to small capacity units. At the present moment, it is apparent that Li-Po batteries are the only well developed commercially available technology that can be used for NAV energy source. There are commercially available sub-gram Li-Po batteries of approximately 0.35 g [107]; however, the energy densities of these batteries are low compared to larger batteries currently produced in larger quantities. Toy, robotic and communication industries continue to push the lower bounds of battery technology in terms of high energy density at small scale, and improved manufacturing as well as use of new materials may allow smaller batteries with better energy densities to become feasible in the near future.

Since air vehicles are relatively power intense applications, both battery specific power and specific energy need to be considered as part of the battery selection process. However, the properties of battery capacity de-rating depend heavily on the battery design and manufacturing parameters. As a result, it is difficult to estimate battery performance without a specific battery in mind. Stux and Swider-Lyons provided a survey of commercial small lithium polymer batteries of masses between 0.8 to 5 g [108]. Figure 2.30 shows a Ragone plot made from the Li-Po battery discharge data they investigated. The Ragone plot shows how battery specific energy trades with specific power at different discharge rates. The underlying trend is an inverse relationship: as

energy density is increased, specific power decreases. The study was carried out in 2007; however, it seems that no significant advances in batteries have happened and hence their result remains relevant.

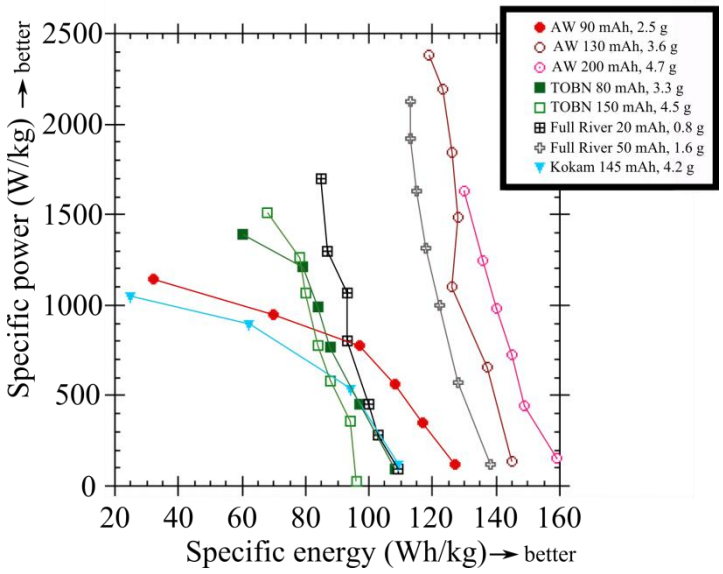

Figure 2.30 Ragone plot for the Li-Po batteries according to the batteries discharge data at different c-rates. AW stands for Atomic Workshop. Figure redrawn from [108].

Fearing and Wood [10] defined the requirements for a power source for a vehicle weighing around 100 mg to be a mass of 50 mg and power density of 600 W/kg. Li-Po batteries achieve the power density requirement; however, the 50 mg size is still about an order of magnitude smaller than what is commercially available.

2.5.3 Power electronics board

The power electronics function is to convert the constant, low input voltage from the battery (usually around 3.7 V) into a time-varying, high-voltage signal (amplitude around 200 V) to power the piezoelectric actuator. The output signal may also need to be unipolar (i.e. only positive or only negative) in order to avoid depolarisation of the piezoelectric layers [78,89]. Furthermore because of the low electromechanical coupling efficiency of piezoelectric actuators, a requirement for the power electronics board is to recover the actuator unused energy for use in following cycles [89].

Steltz *et al*. [81] explored three different high voltage generation methods including boost converter, transformer method and hybrid converter with the latter being realised. They demonstrated a miniature voltage converter and a drive stage with no energy

recovery which had a length of 25 mm, width of 14 mm and weighed approximately 427 mg.

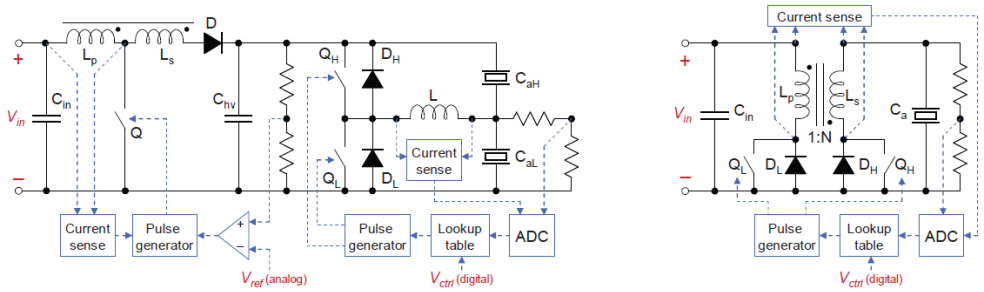

Figure 2.31 Example of dual stage (left) and single stage (right) circuit topologies suitable for driving piezoelectric actuators developed by the Harvard group. The dual stage topology has a tapped inductor boost as the conversion stage (for voltage step up), and a switching amplifier as the drive stage (for alternating waveform generation). C_{aH} and C_{aL} represent piezoelectric layers of a triple layer actuator. The single stage topology has a bidirectional flyback converter to simultaneously step up the voltage and generate an alternating signal. C_a represents a unimorph or a single layer of a triple layer actuator. In both cases, an A/D converter monitors the actuator voltage to be adjusted by modulating the semiconductor switches. Figure and description are taken from [102].

A significant contribution in this field was presented recently by the Harvard group which provided theoretical and practical solutions for high-voltage drive circuits [101-103], Figure 2.31. Circuit implementation was investigated using either a dual-stage design or a single stage design. A dual-stage design includes a conversion stage to step up the low input voltage and a drive stage to use the conversion stage output for generating a time-varying drive signal. This design has more components and higher weight, but allows the high-voltage to be shared by the different actuators. On the other hand, a single-stage design simultaneously steps up the voltage and generates the time-varying drive signal. This design has a lighter weight but output cannot be shared. Thus, the number and type of actuators within the flapper will influence the selection of the drive method.

Several attempts were undertaken by the Harvard group to realise these circuit topologies. Their first implementation used conventionally packaged discrete components and custom-wound bobbin cores on a flex substrate [101], Figure 2.32a. The result was a dual-stage design weighing 90 mg (40 mg conversion stage and 50 mg drive stage) whereas the single-stage circuit weighed 60 mg without any control functionality. Later, a further weight reduction in these circuits was achieved making use of laser micro-machined magnetic components along with chip-scale high-voltage

components. Several demonstrations for the inductor boost converter configuration (conversion stage) were presented, the lightest of which weighed only 20 mg, Figure 2.32b. However, it should be noted that for all the presented designs, control functionality for increasing circuit efficiency remained external; thus an increase in the weight of the final board is anticipated. Additional details on the components of the implemented designs as well as the experimental results for power electronic circuits can be found in references [102] and [103].

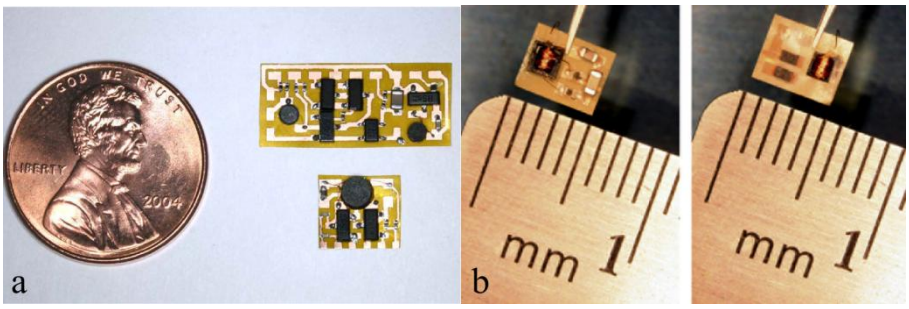

Figure 2.32 The Harvard group power electronic circuits for micro-robotic applications. (a) First implementation of the piezoelectric drive circuits; image taken from [101]. (b) The front and back views of the 20 mg tapped inductor boost converter that can allow a further reduction of the circuit weight; image taken from [103].

2.5.4 Piezoelectric actuators

Piezoelectric bending actuators are a class of actuators designed to utilise the inverse piezoelectric effect to convert input electric energy to output mechanical energy [109-111], and are attractive for insect-scale flapping vehicles application for several reasons: (1) they have high power density at small scales. (2) They have simple geometries and their materials are commercially available. (3) They offer robust mechanical performance. (4) From a scaling perspective, the resonant frequency will increase as size is reduced in a similar manner to what is observed in real insects. On the other hand, piezoelectric actuators have drawbacks including: (1) low fracture toughness. (2) Low electromechanical coupling factor which increases the energy recovery demand on the power electronic circuit board. (3) They require high operating voltages which require voltage conversion circuits with high step up ratios.

There are other possible actuator technologies that might be suitable for wing flapping motion actuation at this scale subject to further research. Karpelson *et al*. [109] provided a review of the actuation options for flapping wing vehicles. An analysis was

conducted based on simple assumptions to allow a system-level optimisation for comparing the different actuator possibilities. They considered electrostatic, thermal, piezoelectric cantilever, shape memory alloy (SMA) and dielectric elastomers actuator categories. Their results showed that electrostatic actuators are of low output energy, but have high operating frequencies. To the contrary, thermal and SMA actuators achieved the requirements for force and displacement; however, they have low operating frequencies owing to the heating and cooling of the active material. Piezoelectric and dielectric elastomer actuator categories were found to achieve the actuation requirements for the insect-scale flapping wing vehicle application.

In a similar attempt, Petricca *et al*. [110] provided a useful quality comparison for both linear and rotational actuators. Linear actuators included piezoelectric ceramics, shape memory alloys (SMA), magnetostrictor, solenoid and dielectric elastomers. Piezoelectric ceramics and magnetostrictor were described as having excellent performance except for the high operation voltages required for operation. SMAs were described as having excellent performance except for their frequency range and poor fatigue life (the previous points are in accordance with Karpelson *et al*. analysis [109]). Solenoids have high strain but low energy density (this was demonstrated by the Delft ring resonator design). Dielectric elastomers are very good candidates with respect to both force and displacement output; however, they are a new technology that is not widely available. On the other hand, rotary actuators as electric motors are efficient, reliable and versatile but there are significant issues in scaling the technology to insect scale application. Nevertheless, future developments may bring suitable candidates; the Carnegie Mellon University flapper was a promising step towards this goal.

Now considering piezoelectric actuator configurations and manufacturing. The group at Vanderbilt University (Section 2.4.2.2) used piezoelectric unimorph actuators (unimorph has one passive elastic layer and one active piezoelectric layer). The Konkuk university flapper (Section 2.4.2.4) used a unimorph actuator immersed in Glass/Epoxy layups, Figure 2.33a. This actuator was designed based on a laminate plate theory model for stacked actuators [112]. The choice of unimorph is not surprising given its simple structure, ease of manufacture and improved reliability compared to other piezoelectric bending actuator [78]. The U.C. Berkeley group started working with unimorphs [78]; then, they developed a composite triple layer piezoelectric actuator with S-glass extension based on a laminate plate theory model [77]. This actuator configuration was used in the second version of the Microrobotic Flying Insect (Section 2.4.2.3) and was

also used (with different dimensions) within the various designs of the Harvard group, Figure 2.33b.

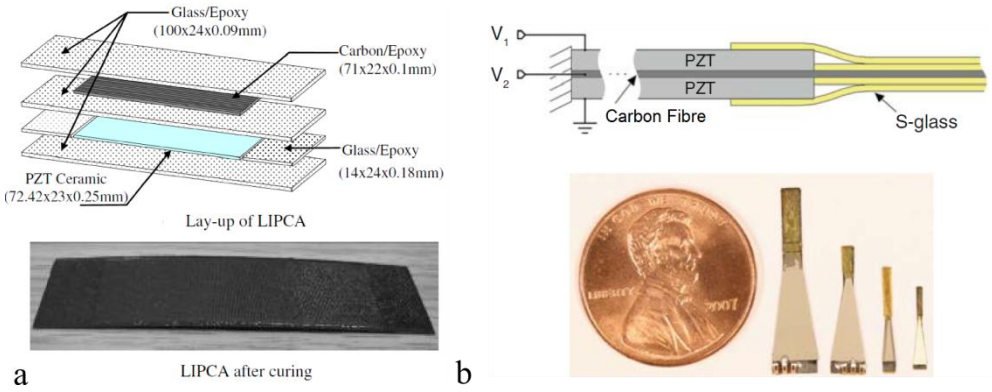

Figure 2.33 The different piezoelectric actuators employed for insect-scale NAV designs. (a) The LIPCA unimorph used by the Konkuk University group; image taken from [85]. (b) Composite piezoelectric actuator cross section as well as example actuators at multiple scales developed for the U.C. Berkley and Harvard group designs; image taken from [10].

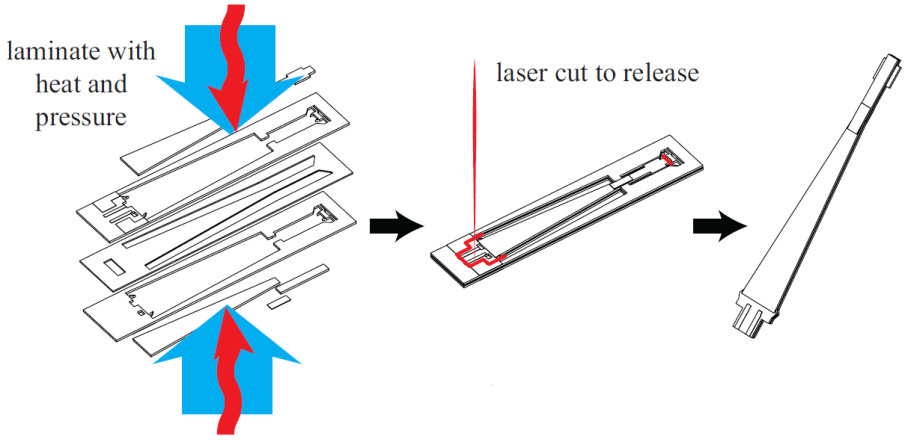

Figure 2.34 Piezoelectric actuator fabrication process employed in the SAMB design prototyping. Heat and pressure are used to laminate the parts together with the adhesive being the epoxy resin in the carbon fibre middle layer; laser cutting is then used to release the actuator; image and description are taken from [97].

In terms of prototyping, the Harvard group employed several techniques for their actuator manufacturing. Their first attempts to manufacture the actuators were based on stacking the actuator layers manually and using an opaque vacuum-bagged setup; thus perfect alignment of the layers was not guaranteed [77,97]. However, their latest process used within the development of the SAMB achieved more convenient results using the heated weight press and pin alignment process [97]. In this process, all layers of the actuator had alignment pin holes for alignment assurance during the heat press

and cure process for bonding the layers together. The actuator was then laser cut and released. This fabrication technique is illustrated in Figure 2.34.

2.5.5 Mechanical transmission

The transmission mechanism is the intermediate linkage between the actuator and the wing which in some studies is called the 'thorax' as similar to that of insects [86-88]. This mechanical amplification system matches the actuator to the wing and converts the small actuator motions to large angular wing motions. The amplification is usually called the *transmission ratio* and is directly analogous to a *gear ratio* for an equivalent rotary system connected via a gear box. Here, the role of the transmission mechanism is only towards the generation of the flapping motion with a large wing stroke, and it is assumed that there is an independent wing hinge to allow the passive pitching motion.

Several considerations should be accounted when designing or choosing the transmission mechanism configuration. These considerations include: (1) the geometry and weight constraints on the insect-scale vehicle. (2) Durability and fatigue resistance given the high flapping rates. (3) The required amount of force and displacement to be transmitted and thus the required transmission ratio. (4) Easiness in manufacturing. Note that conventional mechanical elements such as gears, links and sliders have unfavourable scaling characteristics as the size is reduced; thus, alternative solutions are required.

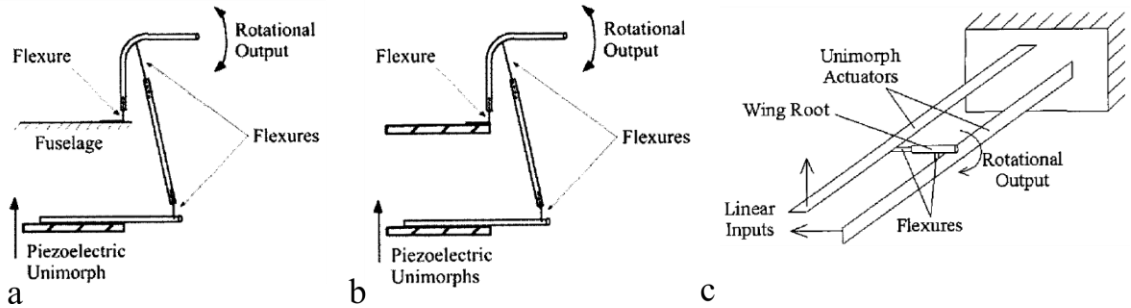

Figure 2.35 The three different transmission mechanisms proposed by the group in Vanderbilt University. (a) The four bar design. Excitation of the unimorph at resonance produces high flapping rotational output. (b) The four-bar design with a clamshell. Its operation is similar to the first concept, however the output link is connected to a second unimorph to increase angular output. (c) The five-bar design with orthogonal unimorphs moving laterally and vertically for flapping rotational output to the flexures. All images are taken from [69].

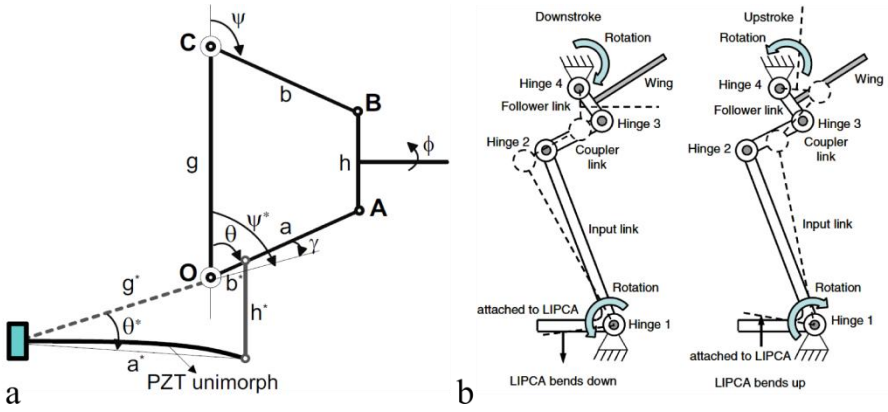

Figure 2.36 (a) Four-bar design proposal for the initial design of the U.C. Berkeley 'MFI'; image taken from [71]. The Konkuk university 4-bar linkage system working principle; image taken from [85].

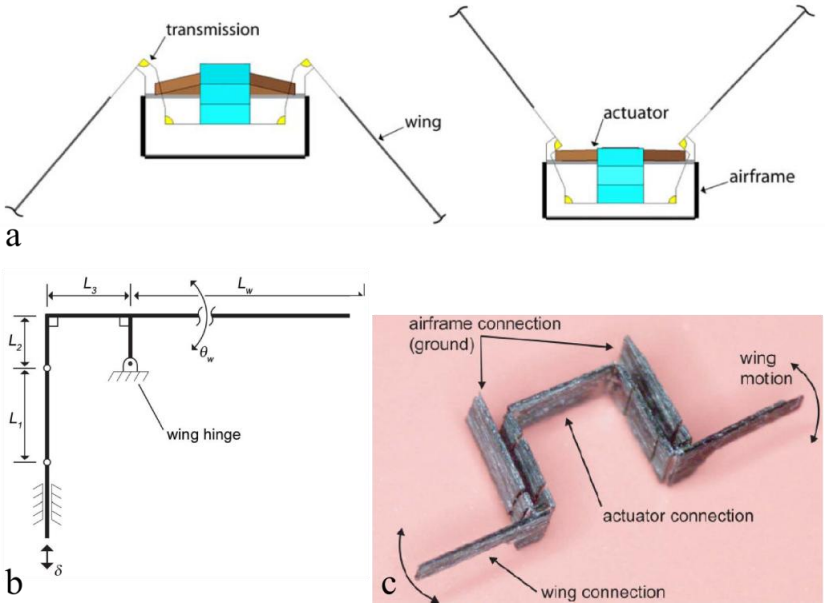

Figure 2.37 The HMF transmission mechanism. (a) Flexure-based transmission; image taken from [88]. (b) Motion generation concept relying on the ratio between the lengths of the different arm parts to amplify the input actuator linear displacements, δ, to large angular flapping motions; image taken from [87]. (c) Fabricated transmission mechanism; image taken from [86].

Several solutions have been presented by the different groups for the transmission mechanisms. Three different transmission mechanisms were used by the Vanderbilt University group to generate the required flapping motion and are shown in Figure 2.35. Note that the actual systems were previously shown in Figure 2.21. Figure 2.36a shows a diagram illustrating the four bar mechanism representing the main flapping motion generator in the initial MFI mechanism. Figure 2.36b shows the Kunkok University flapper four bar linkage system working principle. The flexure based transmission

mechanism developed by the Harvard group for the HMF is shown in Figure 2.37. It relies on choosing the optimal arm lengths with respect to the wing hinge (Figure 2.37b) to produce large wing flapping motions.

Considering manufacturing, the U.C. Berkley and the Harvard groups have attempted several attractive prototyping solutions. The first solution was so-called 'smart composite microstructures', and relied on laser micromachining and lamination process [113]. Another solution was so-called 'pop-up book MEMS', the concept is similar to an unopened pop-up book where mechanism links reside on multiple interconnected layers to reduce interference and to allow folding of three dimensional assemblies [114]. In a later contribution, the technique was extended to include other features such as pick-and-place components, scaffold-assisted assembly, increased material variety and integrated actuation [115]. The fabrication of the transmission mechanism of the SAMB vehicle [97] partially benefited from the previous method through using the assembly scaffold concept to assist in folding up the transmission mechanism; however, the other assembly steps were done by free hand, Figure 2.38.

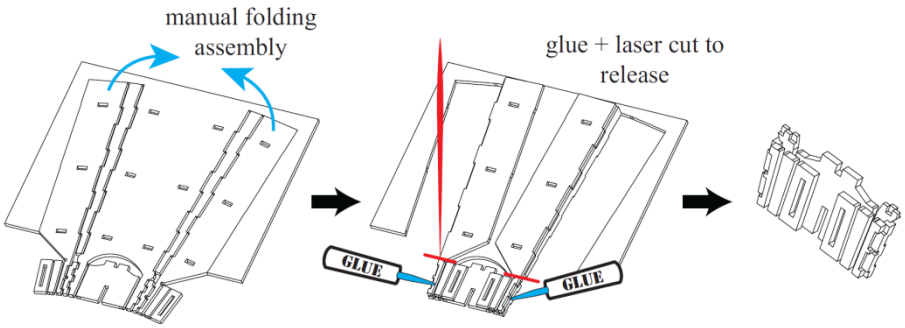

Figure 2.38 Transmission mechanism fabrication process employed in the SAMB design prototyping. Transmission fabrication includes an auxiliary structure for precision folding; image taken from [97].

2.5.6 Wings

Wings are responsible for generating the required aerodynamic forces and moments for flight. Figure 2.39 shows the wings prototyped by the different groups. The first set of wings in Figure 2.39 is the one used by the Vanderbilt University group. These wings were unique in that the pitching motion was generated using wing flexibility and not a flexural hinge [69]. The main target was to develop wings with passive dynamic properties that provide maximum lift and/or efficiency. This was allowed by tuning the

ratio of the frequencies of the first mode of wing bending to the first mode of wing twisting. They called the ratio of the first mode of bending to torsion the ‘wing frequency ratio’. In doing so, it was assumed that the two modes are reasonably decoupled. A wing-testing rig was built to measure the generated lift by each wing and the corresponding expended mechanical power. Different wings were examined with wing frequency ratios ranging from 0.5 to 2.5. It was found that a wing frequency ratio of one produces the maximum lift, while, the wing frequency ratio of two produces higher lift to power ratio (which was used as a measure of efficiency).

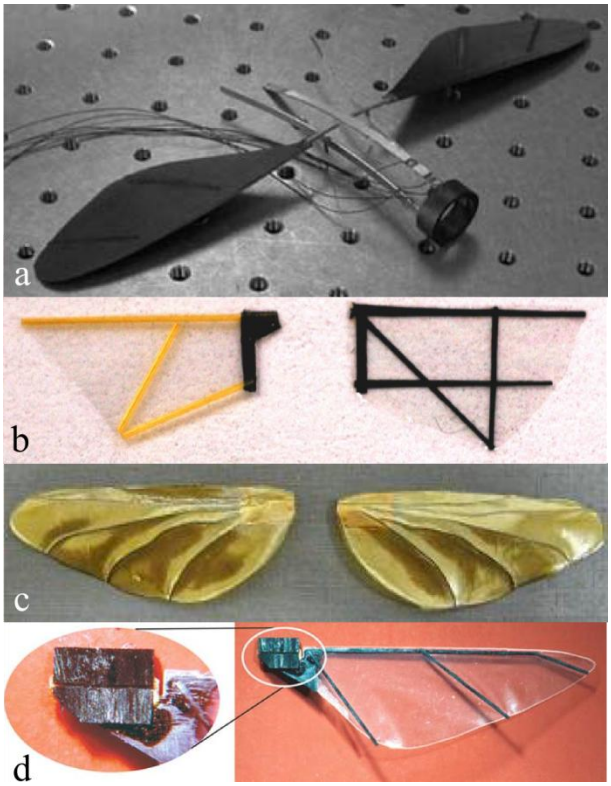

Figure 2.39 The different wings used within the different NAVs. (a) Vanderbilt University wings, image taken from [69]. The MFI wings; left: initial wing, right: improved wing; image taken from [76]. The Konkuk University wings; image taken from [85]. The HMF wing with the wing pitching hinge; image taken from [10].

Figures 2.39b, 2.39c and 2.39d show the wings used for the U.C. Berkeley MFI, the Konkuk University flapper, and the HMF respectively. The wings of the MFI and HMF were made from thin film membrane and acquired their rigidity over the expected range of flight forces due to the carbon veins. The wing pitching motion of the Konkuk University flapper and the HMF was achieved passively through flexural hinges and joint stops to ensure that the pitching rotation does not exceed the required angle.

Various methods exist for the manufacture of flapping NAV wings. The most common method of constructing these wings is spanning a membrane by a rod type structure. The membrane is usually a stretched high strength mylar film. The stiffening structure is usually made of unidirectional carbon rods of various cross sections. Wings constructed in this way are usually reported to have excellent strength-to-weight ratio. This method has been applied to the MFI, HMF and SAMB wings.

The method implemented by the Konkuk university group to fabricate their wings used carbon/epoxy fibres and kapton film 30 μm in thickness [85]. The carbon/epoxy fibres were arranged on the kapton film to mimic the wing vein structure. The whole structure was then vacuum bagged and cured in an autoclave at high temperature (177 ^{o}C) to melt the epoxy resin serving as the glue between carbon fibres and kapton film. After cooling the artificial wings were slightly deformed due to thermal effect.

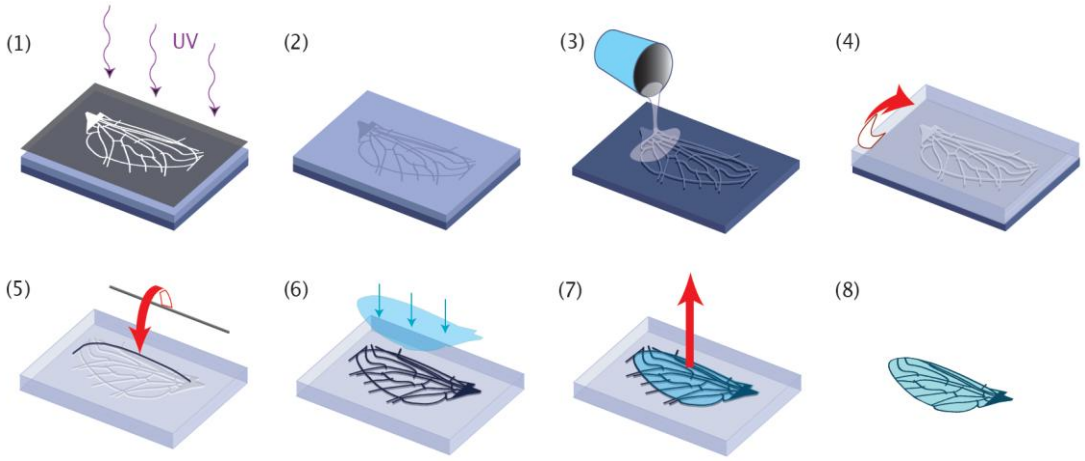

Figure 2.40 Wing fabrication process, using photolithography [116]. (1) A wing transparency is put on a Silicon wafer spin-coated with photoresist, and then exposed to UV light. (2) The unexposed photoresist is cleared with a solvent, and the wafer is silanized. (3) Polydimethylsiloxane is then poured. (4) The mold is removed from the wafer and silanized. (5) Carbon fibre veins are arranged within the mold channels. (6) A membrane is put on top, and the assembly is cured. (7) and (8) The wing is released, and tidied up. Image and description are taken from [116].

Figure 2.40 shows another method for constructing wings using a membrane and a vein like stiffening structure proposed by the Harvard group [116]. Here, the advantage is to produce planar insect-like wings with non-straight spars, and achieve more controllability on the wing stiffness. In a later contribution, Tanaka and Wood fabricated polymer corrugated wing mimicking the morphological features of a hoverfly wing [11, 117], Figure 2.41. Here, veins and membranes are simultaneously prototyped

within a single process using a bottom rigid (Silicon) mold and a top compliant (PDMS: Polydimethylsiloxane) mold. The molds were produced using a custom high resolution laser machining system (more details of the mold production process can be found in [117]). The molds were then used to form a thermosetting resign from which the wing is produced.

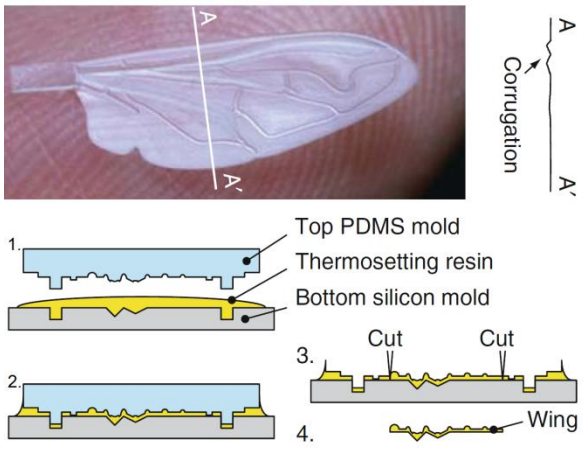

Figure 2.41 Wing fabrication process of a polymer corrugated wing; image taken from [11].

It should be mentioned that it is currently unknown how exactly morphological features such as veins and corrugation affect flight. Whether these features of insect wings are due to bio-material limitations or are an indicator of beneficial performance is yet unknown for sure. However, Luo and Sun [118] conducted a CFD analysis on different insect wings and showed that the aerodynamic forces generated from corrugated and flat plat candidates are approximately the same because the corrugation scale is much smaller than the separated flow region or the leading-edge vortex (LEV) size. Moreover, it evident that a rigid flat plate wing, as that used on the HMF or SAMB, is sufficient to guarantee successful flight.

Considering the flexure-based wing hinge responsible for generating the wing pitching motion, Tanaka *et al*. [11] from the Harvard group showed the fabrication process of a wing hinge made from carbon fibre plates and a polyimide hinge, Figure 2.42. Composite sheets were laser cut from carbon fibre reinforced prepregs and then laminated with a thin sheet of polyimide. The resulting composite was then laser cut and laminated to a second carbon fibre sheet.

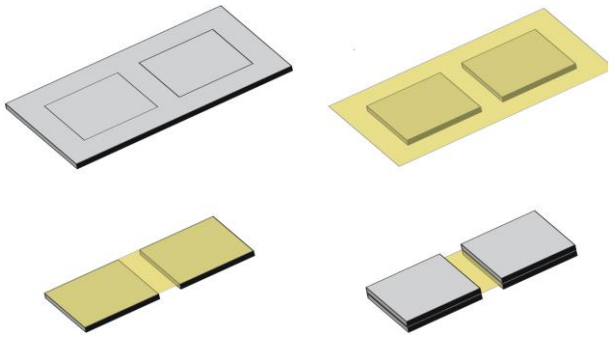

Figure 2.42 Wing hinge made of carbon fibre rigid plates and polyimide layer; image taken from [11].

2.5.7 Summary of propulsion sub-systems of piezoelectric actuated flapping wing vehicles

Section 2.5 discussed the five main sub-systems of piezoelectric actuated flapping wing vehicles. In summary:

1. The biggest barrier facing insect-scale vehicles is availability of electrical power sources with high power and energy density.
2. Several attempts have been presented to produce miniature power electronics board for insect-scale flapping wing vehicles. A board mass of 60 mg was achieved but without including any control or charge recovery functionalities.
3. Actuation options have been assessed by different groups; whilst electric motors are more efficient at larger scales, the piezoelectric option was usually recommended for flapping wing vehicles at the very tiny scale of insects. Unimorphs and triple layer actuator configurations were the most implemented actuators within the proposed designs mainly for their relatively simple structure, ease of manufacturing and robust mechanical performance.
4. Conventional mechanical elements, such as gears and sliders suffer from unfavourable scaling characteristics due to surface effects as the size is miniaturised. Therefore, these elements probably do not offer a scalable technology path to the insect-scale flapping wing vehicle design.
5. The complexity of the mechanisms used for the transmission systems of the piezoelectric actuated NAVs is different from one design to another. However, most of them can be described as relatively complex and present a significant fraction of the vehicle weight. Main constraints on the design of these mechanisms

include weight, fatigue resistance, simplicity of fabrication and achieving maximum stroke amplitudes.

6. Various methods for wing manufacturing have been presented. The most common implemented method is that of reinforcing a membrane by stiff rod type structures. Recently, some efforts have been directed towards developing fabrication methods for creating wings that can exactly mimic insect wings. This can allow the control of mechanical and stiffness characteristics of the wings; however, these wings do not seem to provide superior aerodynamic characteristics that can be beneficial for flight performance.
7. Considering all subsystems, it is apparent that low aerodynamic efficiency, low electromechanical coupling factors of piezoelectric bending actuators, and relatively inefficient systems for storing and releasing energy are the most significant factors hindering the development of efficient miniature robotic flying machines.
8. If the historical research development towards the creation of an insect-scale flapping wing NAV is traced, it can be easily observed that the experience gained over the years converged to designs that rely on: (1) piezoelectric actuation. (2) Resonant mechanisms for flapping motion amplification. (3) Simple mechanical transmission designs to avoid excess weight and complexity. (4) Passive wing pitching for less mechanical complexity and reduced system mass.
9. Further scientific progress is required in the following areas: (1) low-Reynolds-number aerodynamics modelling; (2) lightweight and biologically inspired multifunctional materials and structures; (3) improved understanding of actuation performance; (4) miniaturised power sources of high energy density; (5) suitable flight navigation and control algorithms; (6) miniaturised power, navigation and control electronic boards; and (7) system engineering tools for easy, fast and inexpensive prototyping.

3

Efficiency of Lift Production in Hovering Flapping Flight[1]

Any arbitrary shaped flat surface placed at an angle to the stream of air will produce a lift force. The goal of good aerodynamic design is to identify wing shapes that create a given amount of lift with the minimum amount of power expenditure, that is, the wing is aerodynamically efficient. This chapter is concerned with minimising induced power, which is the power directly attributed to lift production. The actuator disc theory provides a simple momentum based model for the interaction of a revolving (rotary) or flapping wing with a surrounding fluid based on the assumption that the wing induces a uniform downwash velocity over the area swept by the wing. This assumption is consistent with minimisation of the induced power, however in reality, the downwash is not uniform and the induced drag and hence induced power is increased. The ratio of actual induced power to minimum ideal induced power for a given thrust is known as the induced power factor, k. This chapter provides a first principles approach to determining k to provide improved understanding of the aerodynamic performance of a range of different insects, and to provide support for the development of engineering tools for optimisation of the wing planforms and kinematics of insect scale flapping wing vehicles. Whilst the chapter is focussed on a so-called correction to the ideal induced power, this correction may be as high as a factor of two and hence forms a fundamental part of the aerodynamic treatment to follow in subsequent chapters.

[1] This chapter is based on the publication: Nabawy MRA, Crowther WJ. 2014 On the quasi-steady aerodynamics of normal hovering flight part I: the induced power factor. *J. R. Soc. Interface* **11**: 20131196 (doi 10.1098/rsif.2013.1196)

3.1 Introduction

Within the actuator disk theory, the induced power factor, *k*, is a measure used to estimate the efficiency of an oscillatory or rotary wing through comparing the actual induced power required to produce a given lift (usually called thrust for rotors) with the minimum possible induced power required to produce that lift [119-121]. Thus, a unity *k* value represents the ideal minimum condition. An analytical approach to determining the induced power factor for hovering flight was provided by Ellington [122], who used a combined modified actuator disc and vortex theory to give so-called temporal and spatial corrections for the induced power. He showed that each correction is around 10% giving an overall *k* value between 1.15 and 1.2. The temporal correction is related to tip losses, while the spatial correction accounts for non-uniformities over the ideal actuator disk. Later, Sunada and Ellington [123] proposed a more sophisticated method for the evaluation of *k* in which they modelled flapping forces with the added masses of vortex wake sheets. This analysis gave normal hovering *k* values between 1.2 and 1.4 for the different species investigated.

More recently, a significant amount of work on flapping animals has been undertaken with the aim of identifying wing inviscid span efficiency (inverse of induced power factor [120,121]) in forward flight through experiments [119,124-129]. The downwash velocity distribution was measured using Digital Particle Image Velocimetry (DPIV) techniques. These measurements were then used within the actuator disk theory framework to define the real lift and induced power values. Comparison with ideal conditions then allowed the evaluation of the induced power factor and hence flapping wing inviscid span efficiency. Henningsson and Bomphrey [124] obtained a maximum span efficiency within the flapping cycle of forward flying locusts of 0.79 and an average span efficiency value of 0.53, implying *k* values of 1.27 and 1.89 respectively. Also, Henningsson and Bomphrey [125] assessed the span efficiency of six hawkmoth species flying tethered in a wind tunnel. The obtained average span efficiencies for the moths ranged from 0.31 to 0.6; equivalent to *k* values ranging from 1.67 to 3.23. Most recently, Henningsson *et al.* [126] found the average span efficiencies of swifts over the measured speed range to be 0.62 and 0.41 for flapping and gliding flights respectively.

Muijres *et al*. [127,128] performed similar measurements on bats and pied flycatchers; however, they used a hovering induced power factor expression to evaluate

the *k* values at different speeds. For bats, they obtained an average *k* value throughout the measured speed range of 1.25. Average *k* values between 1.1 and 1.25 were obtained for pied flycatchers. Also, Johansson *et al*. [129] followed the same methodology in [127] and [128] and obtained an average *k* value of 1.61 for flying beetles. All the previous measurements show that: (1) the early *k* estimate of 1.2 that was usually used for animal wings needs revision [125]; (2) the value of the induced power factor in flapping flight is generally high, thus is significant for accurate evaluation of the aerodynamics.

The aim of this chapter is to provide a transparent analytical treatment to capture the different aerodynamic effects influencing a real flapping wing in normal hovering flight using the single parameter, *k*. It builds upon previous analytical treatments through accounting for contributions to *k* due to both wing shape and flapping kinematics. The following section develops a model for the induced power losses in normal hovering due to non uniform downwash velocity distribution, wake periodicity and finite flapping amplitude. Section 3.3 demonstrates the validity of the approach by providing a comparison of model results with experiments in the literature; an evaluation of the induced power factor in normal hover for eight insects is then provided. In Section 3.4, the developed model is used to understand the effect of Reynolds number on induced power factor, and then the figure of merit is comprehensively analysed for insect-like hovering flight. Section 3.5 provides the main conclusions from this chapter.

3.2 Contributions to the Induced Power Factor

3.2.1 Analytical model for induced power losses

The method for modelling normal hovering flapping flight proposed here is based on the method of Stepniewski and Keys [130] for evaluation of the induced power factor of hovering rotors, with appropriate modifications applied to represent flapping flight. The flapping wing system is approximated by an actuator disk of area S_d. The mass flow rate, $\dot{m}$, of air through the disk is

$$\dot{m} = \int_{S_d} \rho w dS_d \,, \tag{3.1}$$

where ρ is the air density and w is the downwash velocity. For normal hovering flapping flight, the effective disk area is the area of sectors swept out by both flapping wings and is given by [122,131]

$$S_d = \Phi R^2, \tag{3.2}$$

where Φ is the flapping stroke angle and R is the wing length. Equation 3.2 may appear inconsistent with the use of a circular actuator area for non flapping wings. However, it can be argued that the flapping case is sufficiently different to other modes of flight that a different definition of the actuator disc area must be used. In particular, the wake dimensions for flapping flight must be influenced by the stroke angle, Φ, and vorticity is known to be created only at the interface between the wing and the fluid. Thus, it is more appropriate to define S_d as the area over which the wings actually impart downward momentum to the air [122]. Following Equation 3.2, an elementary disk area will be

$$dS_d = 2\Phi r dr, \tag{3.3}$$

and substitution into (3.1) gives

$$\dot{m} = \int_0^{R_{ef}} \rho w(r) 2\Phi r dr, \tag{3.4}$$

Note that the upper bound of the above integration is changed to the effective radius, R_{ef}, to account for the aerodynamic phenomena occurring at the outer rim of the disk reducing its lift generating effectiveness in that region generating so called tip losses due to the wake discreteness and periodicity. The generated lift force, L, (usually called thrust for rotors) from the actuator disk is equal to the rate of change of downward momentum, which is obtained by multiplying the mass flow rate by the eventual downward velocity, which is equal to twice the induced velocity at the disk

$$L = 4\Phi\rho \int_0^{R_{ef}} \left(w(r)\right)^2 r dr. \tag{3.5}$$

The above expression can be written as

$$L = 4\Phi R^2 \rho \int_0^B \left(w(\hat{r})\right)^2 \hat{r} d\hat{r}\,, \tag{3.6}$$

where $\hat{r} = r/R$ and B is the non-dimensional effective radius (R_{ef} /R).The corresponding induced power will be

$$P_{ind} = 4\Phi R^2 \rho \int_0^B \left(w(\hat{r})\right)^3 \hat{r} d\hat{r}\,. \tag{3.7}$$

On the other hand, if a constant downwash velocity distribution is achieved, there are no tip losses, and the wings sweep the maximum possible disk area (i.e. $S_d = \pi R^2$), the ideal lift produced is

$$L_{ideal} = 2\pi R^2 \rho w^2\,, \tag{3.8}$$

and

$$P_{ideal} = 2\pi R^2 \rho w^3\,. \tag{3.9}$$

The induced power factor, k, is obtained as the quotient P_{ind}/P_{ideal}, where the uniform ideal downwash velocity required within the ideal power expression (Equation 3.9) is obtained by equating Equations 3.6 and 3.8. This leads to an induced power factor of

$$k = \frac{P_{ind}}{P_{ideal}} = k_{ind} k_{per} k_{flap}\,, \tag{3.10}$$

where

$$k_{ind} = \frac{2\int_0^1 \left(w(\hat{r})\right)^3 \hat{r} d\hat{r}}{\left(\sqrt{2\int_0^1 \left(w(\hat{r})\right)^2 \hat{r} d\hat{r}}\right)^3}\,, \tag{3.11}$$

$$k_{per} = \frac{1}{B} = \frac{R}{R_{ef}}\,, \tag{3.12}$$

$$k_{flap} = \sqrt{\frac{\pi}{\Phi}}\,. \tag{3.13}$$

The first contributor to the overall induced power factor expression, k_{ind}, considers the effect of non-uniform downwash distribution. A discussion is provided on the effect

of chord distribution, advance ratio and root offset on this term in the following section. The second contributor to the overall k considers wake periodicity losses and is referred to as k_{per}. It will be discussed in the context of its derivation from the 'finite number of blades' concept from rotary wing aerodynamics as well as its derivation from Ellington's temporal correction. Finally, the term k_{flap} is based on simple geometric considerations and will be discussed briefly at the end. The three sources of inefficiency are schematically represented in Figure 3.1.

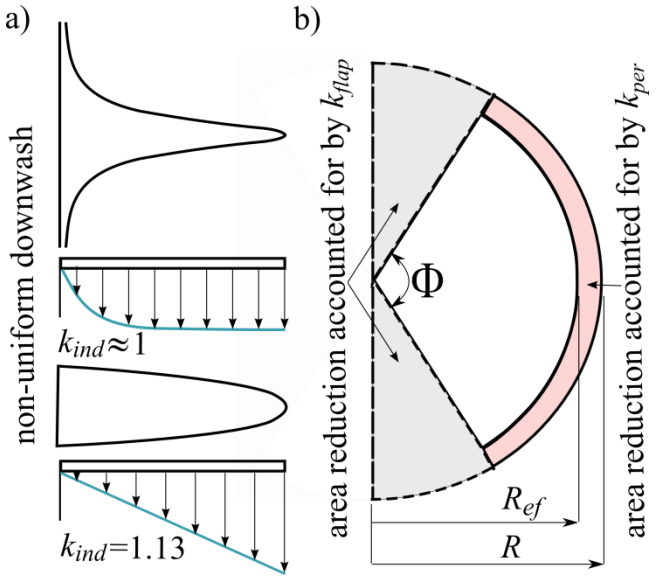

Figure 3.1 A schematic of the three sources of inefficiency within flapping normal hovering flight. (a) The non-uniform downwash effect. For illustration, an untwisted optimal wing planform (which will be later discussed in Chapter 6) whose downwash distribution is almost constant in typical hovering is shown; also shown is an untwisted wing planform whose chord varies as a half-ellipse along the wing length giving a linear downwash distribution in typical hovering. The method to obtain the downwash distribution is discussed in Section 3.2.2. (b) Both the effective flapping disk area and wake periodicity effects for a single wing.

3.2.2 Non-uniform downwash velocity effect

In this section, the effect of non-uniform downwash velocity is discussed. Equation 3.11 can be used to evaluate k_{ind} if the induced downwash velocity distribution over the wing is known. Here, an analytical method based on lifting line blade models is proposed. Sane [132] presented a lifting line blade model for hovering flapping wings, however, the model relied on empirical experimental data; hence, measurements are still required for the calculation. Leishman provided a generic formulation of the lifting line problem [133, Ch. 14]. Also, Ansari *et al.* [1] discussed lifting line models in the context of

insect-like flapping wings. However, in the latter two references, generic formulas were provided without complete details of the method (Note that more discussions on these contributions to the lifting line theory will be provided in Chapter 5). Here, a more general formulation of the lifting line problem will be presented.

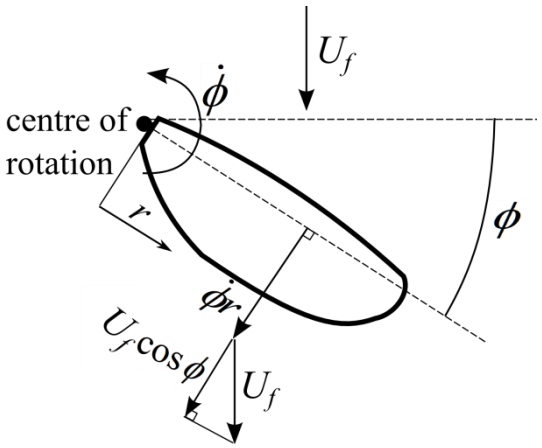

Figure 3.2 Sectional flow velocities of a flapping wing with an additional translational constant velocity component.

As a starting point, the velocity distribution, $U(r)$, on the wing must be defined. The more general case of a wing moving with an angular velocity, $\dot{\phi}$, and additionally experiencing a constant free stream velocity component, U_f, parallel to the flapping plane is shown in Figure 3.2. For this case, the sectional flow velocity at a station r from the centre of rotation is given by [134]

$$U(r) = \dot{\phi}r + U_f \cos\phi, \tag{3.14}$$

where ϕ is flapping angle amplitude. The wing tip angular flapping velocity will be given the name, U_{tip}

$$U_{tip} = \dot{\phi}R. \tag{3.15}$$

J_1 is defined as the ratio of the chord wise components of the wing tip flow velocity due to translation and revolution [134]

$$J_1 = \frac{U_f \cos\phi}{U_{tip}}. \tag{3.16}$$

Therefore, over one flapping cycle, J_1 will vary between - J and J [134], where J is the advance ratio given by

$$J = \frac{U_f}{|U_{tip}|}. \tag{3.17}$$

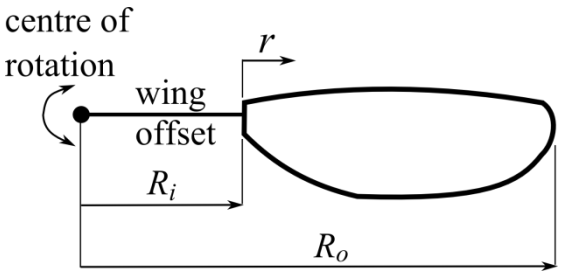

Figure 3.3 A schematic of a flapping wing offset.

Practically, the definition of the advance ratio is useful for studying the wing root offset effect on the aerodynamic characteristics of normal hovering wings (See Figure 3.3). The main effect of the wing offset is to change the wing velocity to

$$U(r) = \dot{\phi}(r + R_i) = \dot{\phi}r + \dot{\phi}R_i, \tag{3.18}$$

where R_i is the inner wing (root) radial distance. Comparing Equations 3.14 and 3.18, it can be concluded that the wing offset leads to a constant velocity contribution added to the linear varying velocity; hence, in effect it can be treated in same manner as advance ratio, where J_1 is defined here as

$$J_1 = \frac{\dot{\phi}R_i}{\dot{\phi}R} = \frac{R_i}{R} = \frac{R_i}{R_o - R_i}. \tag{3.19}$$

The wing offset will have an additional effect on the induced power factor as a root cut out that reduces the effective disk area; however, to maintain simplicity this effect will not be considered here.

Now, the wing can be modelled as a vortex of strength $\Gamma(r)$ bound to the aerodynamic centre and the lift per unit span can be obtained using the Kutta-Joukowski theorem as [133]

$$dL(r) = \rho U(r)\Gamma(r)dr = \frac{1}{2}\rho(U(r))^2 c(r)drC_{l\alpha,2d}(\alpha_g - \alpha_i), \tag{3.20}$$

where c is the chord, $C_{l\alpha,2d}$ is the 2d-aerofoil lift curve slope, α_g is the geometric angle of attack and α_i is the induced angle of attack. Hence, $\Gamma(r)$, is obtained as

$$\Gamma(r) = \frac{1}{2} c(r) C_{l\alpha,2d} \left(U(r)\alpha_g - w(r) \right). \tag{3.21}$$

The distribution of the induced downwash velocity along the wing length, $w(r)$, can be obtained by applying the Biot-Savart law to the vortex wake produced by the wing [135-137]

$$w(\breve{r}) = \frac{1}{4\pi} \int_{-R}^{R} \frac{d\Gamma}{dr} \frac{dr}{\breve{r} - r}, \tag{3.22}$$

where $\breve{r}$ is the selected wing location at which the downwash velocity is required, and r is the location of vortices causing the downwash [136]. In the above relations, a wing location can be substituted with [135,136]

$$r = -R\cos\psi, \tag{3.23}$$

where ψ is now used to define position along the wing. Also, the vortex strength, $\Gamma(r)$, is written in a non-dimensional form as [135-137]

$$\gamma = \frac{\Gamma(r)}{2RU(r)} = 2\sum_{m=1}^{\infty} a_m \sin m\psi, \tag{3.24}$$

hence,

$$\Gamma(r) = 4RU(r)\sum_{m=1}^{\infty} a_m \sin m\psi. \tag{3.25}$$

Substituting the velocity distribution of Equation 3.14 (making use of Equations 3.16 and 3.23) into the equation for circulation (3.25) leads to

$$\Gamma(r) = 4U_{tip}R\left(J_1\left(\sum_{m=1}^{\infty} a_m \sin m\psi \right) - \left(\sum_{m=1}^{\infty} a_m \cos\psi \sin m\psi \right) \right). \tag{3.26}$$

Substituting Equation 3.26 into Equation 3.22 and performing integration making use of the available Glauert integrals [138] leads to the following expression for the downwash

$$w(r) = U_{tip}\left(\left(J_1\sum_{m=1}^{\infty} m a_m \frac{\sin m\psi}{\sin\psi}\right) - \left(\sum_{m=1}^{\infty} m a_m \frac{\cos\psi \sin m\psi}{\sin\psi} + a_m \cos m\psi\right)\right). \quad (3.27)$$

The a_m coefficients can be obtained using the well-known lifting line technique by equating Equations 3.21 and 3.26 making use of Equations 3.14 and 3.27, leading to

$$\mu\alpha_g\left(J_1 \sin\psi - \sin\psi\cos\psi\right) = J_1\sum_{m=1}^{\infty} a_m \sin\psi \sin m\psi - \sum_{m=1}^{\infty} a_m \sin\psi\cos\psi \sin m\psi + \mu\left(J_1\sum_{m=1}^{\infty} m a_m \sin m\psi - \left(\sum_{m=1}^{\infty} a_m \sin\psi \cos m\psi + m a_m \cos\psi \sin m\psi\right)\right), \quad (3.28)$$

where $\mu = c(r)C_{l\alpha,2d}/8R$. For the 2d lift curve slope, $C_{l\alpha,2d}$, either the experimental (0.09 deg^{-1}) or the theoretical value (2π rad^{-1} = 0.11 deg^{-1}) for a flat plate can be used. Calculated values of k_{ind} are relatively insensitive to lift curve slope value and it is usual practice to use the experimental value. In this study, a value of 0.09 deg^{-1} will be used which is based on the experimental work at typical insects Reynolds numbers of Okamoto *et al.* [139]. Owing to the symmetry of load distribution, only the odd terms of m are considered. Following the conventional lifting line solution procedure, the series is truncated at a convenient number of terms and the above equation is satisfied at a number of wing stations resulting in a set of simultaneous linear equations. This set is solved for the a_m coefficients and hence the downwash distribution is obtained. In the limit when J_1 approaches infinity, the well known monoplane fixed wing equations are obtained, whilst if J_1 is zero, the typical normal hovering case is simulated. Therefore, the above equations represent a more general formulation of the lifting line problem. It should be noted that the k_{ind} value is sensitive to the chord distribution and advance ratio. Therefore, k_{ind} depends on the wing morphology (through chord distribution) and kinematics (through advance ratio). Further discussion of these effects will be provided in the following sections of this chapter.

3.2.3 Tip loss effect due to wake periodicity

It is well known that lifting line blade models are unable to fully capture the flow structure at the blade/wing tip (a discussion on this point is provided by Johnson in [Ch. 10, 140] and by Sane in [132]). There are a number of options for correction for corrected tip effects ranging from simple tip loss factors to a complete lifting surface

theory analysis of the aerodynamics. For the present work, a tip loss factor approach that models the loss as an effective reduction in wing span is adopted.

Prandtl provided a solution for a tip loss correction for a rotor with finite number of blades. He showed that when accounting for tip loss due to wake periodicity, the effective blade radius, R_{ef}, is given by [133,140]

$$B = \frac{R_{ef}}{R} = 1 - \left(\left(\frac{2 \ln 2}{N_b} \right) \frac{\lambda}{\sqrt{1+\lambda^2}} \right), \tag{3.29}$$

where N_b is the number of blades and λ is the inflow ratio. Although this formula was originally developed for rotors with finite number of blades, Sane [132] showed that it can be used within the context of flapping flight, suggesting a value of 2 for N_b to simulate a complete wing cycle and a value of 1 for a single up or down stroke. For a hovering case, λ is the ratio of the induced downwash velocity to the wing tip velocity and can be evaluated using the simple model [130,133]

$$\lambda = \sqrt{\frac{C_{Th}}{2}}, \tag{3.30}$$

where C_{Th} is the thrust coefficient defined as

$$C_{Th} = \frac{DL}{\rho U_{tip}^2}, \tag{3.31}$$

where DL is disk loading obtained as the quotient of the thrust (≡weight) to the effective disk area, and the tip velocity can be evaluated from the mean value expression

$$U_{tip} = \dot{\phi} R \cong 2\Phi f R. \tag{3.32}$$

A different tip loss model is provided by Ellington, where a temporal correction is applied to the Rankine-Froude theory to account for wake periodicity [122]. Ellington stated that his model compares well with hovering helicopters. It will be shown in the results section that the two methods are in very good numerical agreement. Nevertheless, Ellington also added that his method provides a more satisfying physical and conceptual description of the flapping problem; hence, it will be presented here in some detail. The expression for the temporal correction is given as [122]

$$k_{per,Ellington} = 1 + 0.079 s^2, \tag{3.33}$$

where s is the so-called 'spacing parameter', which for a normal hovering case with a horizontal stroke plane is given by [122]

$$s^2 = \frac{2\pi W}{\rho n^2 f^2 \left(\Phi R^2\right)^2}, \tag{3.34}$$

where W is the insect weight, f is the wing beat frequency and n is the frequency of lift impulses per wing beat frequency. It takes a value of 2 in normal hovering as the two wing strokes provide weight support and takes a value of 1 if only one wing stroke provides weight support. Therefore, the number of lift impulses per wing beat frequency of Ellington's model is analogous to the number of blades of the rotor model.

3.2.4 Finite flapping amplitude effect

The last contributor to the overall induced power factor expression, k_{flap}, considers losses associated with the reduction of effective disk area for flapping stroke angles less than 180 degrees. Hence, this reduction in the effective disk area will cause further increase in the disk loading and higher induced velocity compared to that given by the simple momentum theory leading to a third contributor to the overall induced power factor. It is named k_{flap} as it is an induced power loss specific to flapping wings only.

3.3 Results

3.3.1 Comparison with experiments

In this section, the model for induced power factor proposed above is tested against available experimental measurements from the literature. First, the model is compared to the experimental study of Dickson and Dickinson [134] in which they have investigated the effect of advance ratio on the aerodynamics of revolving wings. A wing with R=0.25m, AR=4.2 and a non-dimensional radius of the first moment of wing area of 0.59 was used. Experimental measurements of lift and drag coefficients were provided for a range of kinematics corresponding to J_1 ranging from -0.5 to 0.5. One of the main conclusions was that the lift coefficient decreases with the increase in J_1. Here, the same experimental conditions are used within the proposed model for calculating the downwash velocity distribution, which was then used within Eqn. 3.11 to evaluate k_{ind},

and this was repeated for the different J_1 values of the experiment. The wing chord distribution was defined based on the beta function proposed by Ellington [141] (this function will be presented in the next section).

Results for the variation of k_{ind} over the J_1 range of the experiment ($-0.5 < J_1 < 0.5$) are shown in Figure 3.4. On the basis that by definition the lift coefficient decreases with the increase of the *k*-factor, the obtained results provide qualitative agreement with the experimental observations of Dickson and Dickinson.

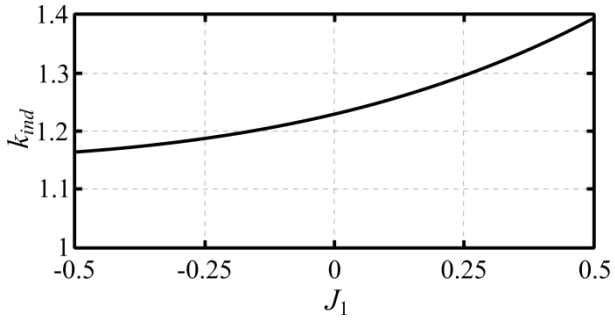

Figure 3.4 The variation of k_{ind} with J_1 for a wing shape and kinematics similar to that experimentally measured by Dickson and Dickinson [134].

Second, the induced power factor variation shown in Figure 3.4 is compared to results from the low Rossby number hypothesis of Lentink and Dickinson [142]. The Rossby number is a non-dimensional number that is used to quantify the centripetal and Coriolis accelerations, and for a revolving wing is the ratio of the wing radius of gyration to the chord. Lentink and Dickinson measured the force coefficients for a fruit fly like wing model at different values of the Rossby number, and concluded that the lift coefficient decreases with increasing the Rossby number (see Figure 6 of [142]). The way they increased the Rossby number was by elongating the robot arm (wing root offset). As discussed in Section 3.2.2, this way can be seen as increasing the wing tip velocity ratio J_1 as described in Equations 3.18 and 3.19 (In line with this is the later explanation given by Harbig *et al*. [143] where they showed that the Rossby number can be written in terms of $1+J$). Thus in conclusion of Lentink and Dickinson measurements, increasing the wing tip velocity ratio will increase the Rossby number which in turn leads to lower lift coefficient values. Therefore again the results shown in Figure 3.4 provides qualitative agreement with these findings.

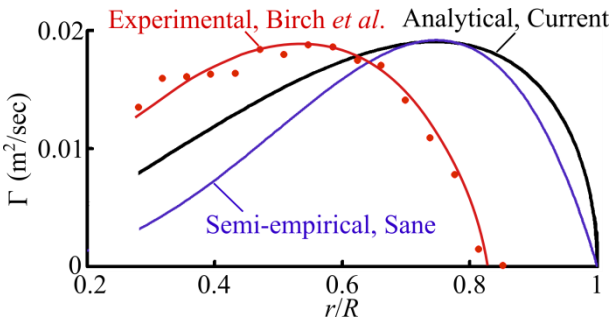

Figure 3.5 Circulation around the revolving fruit fly wing model in a typical hovering condition ($J_1 = 0$). The circles are the experimental results digitised from Figure 2 of [144]; a best fit line is drawn for the experimental data to which the lifting line model is compared. The semi-empirical treatment by Sane as presented in Figure 3b of [132] is also included for comparison.

Finally, the lifting line model is compared with results from Birch *et al*. [144] who used DPIV to measure the circulation around a revolving model fruit fly wing with a mean chord of 7 cm [132] in a typical hovering condition ($J_1 = 0$). Since the wing has a planform shape of a fruit fly wing, the real fruit fly *AR* of 3.015 and non-dimensional radius of the first moment of wing area of 0.55 (Table 3.1) are used to define the chord distribution based on the beta function. The measurements were performed with the wing set at a 45 degrees geometric angle of attack and revolved with a wing tip velocity of 0.26 m/sec. The circulation distribution at the same experimental conditions is calculated using the lifting line model and the result is compared with the experiment, Figure 3.5. On the same figure, the semi-empirical treatment of Sane [132] for the same experiment is included for comparison. The important aspect with regards to the induced power factor evaluation method presented here is to compare the shape of variation of circulation. Excellent agreement between the analytical model and the experiment for the shape of variation is evident from the rate of decay of circulation towards zero. Note that the lifting line model assumes a totally homogeneous system and does not include a tip loss effect as a result of wake periodicity; hence, prediction of the effective wing tip location is not an explicit output of the model. As will be shown in the next section, for a revolving fruit fly wing, a value of *B* (inverse of k_{per}) of 0.87 is obtained which is in a very good agreement with the experimental results.

3.3.2 Induced power factor values

In this section, the value of the different contributors to the induced power factor for eight insects in normal hovering with $J_1 = 0$ will be presented. Table 1 shows weight, morphological and kinematic data of the eight insects taken from Sun and Du [145].

Note that these data were collected by Sun and Du from the most relevant study for each insect.

Table 3.1 Weight, morphological and kinematic parameters of hovering insects [145].

Insect	mass (mg)	R (mm)	$\bar{c}$ (mm)	$\hat{r}_1$	f (Hz)	Φ (deg.)
Fruit fly (FF)	0.72	2.02	0.67	0.55	254	150
Bumble bee (BB)	175	13.2	4.02	0.49	155	116
Hawkmoth (HM)	1648	51.9	18.26	0.46	26.3	121
Honey bee (HB)	101.9	9.8	3.08	0.5	197	131
Cranefly (CF)	11.4	12.7	2.38	0.56	45.5	123
Hoverfly (HF)	27.3	9.3	2.2	0.52	160	90
Dronefly (DF)	68.4	11.4	3.19	0.48	157	109
Ladybird (LB)	34.4	11.2	3.23	0.47	54	177

In this evaluation, the chord distribution for the different insects was defined based on the method proposed by Ellington [141]. For many insect wings, Ellington found that the chord distribution is accurately described to within 5% of the measured values using a beta function as [141]

$$c(r) = \bar{c}\left(\frac{\hat{r}^{\,p-1}(1-\hat{r})^{q-1}}{\beta(p,q)} \right), \tag{3.35}$$

where

$$\beta(p,q) = \int_0^1 \hat{r}^{\,p-1}(1-\hat{r})^{q-1} d\hat{r}\,, \tag{3.36}$$

with the beta function parameters chosen as

$$p = \hat{r}_1\left(\frac{\hat{r}_1(1-\hat{r}_1)}{\hat{r}_2^2 - \hat{r}_1^2} - 1 \right),\ q = p\,\frac{(1-\hat{r}_1)}{\hat{r}_1}\,, \tag{3.37}$$

where $\hat{r}_1$ and $\hat{r}_2$ are the non-dimensional radii of first and second moments of wing area respectively. For insect wings, Ellington found a strong correlation between the second and first radii of moments of wing area as [141]

$$\hat{r}_2 = 0.929\left(\hat{r}_1\right)^{0.732}. \tag{3.38}$$

Table 3.2 Calculated contributions to the induced power factor, k.

Insect	k_{ind}	k_{per} (Eqn. 3.12 & 3.29 with $S_d = \pi R^2$)	k_{flap}	$k_{ind}\, k_{per}\, k_{flap}$	$k_{per,Ellington}$ (Eqn. 3.33)
Fruit fly	1.21	1.14	1.10	1.51	1.11
Bumble bee	1.17	1.10	1.25	1.61	1.07
Hawkmoth	1.14	1.12	1.22	1.55	1.09
Honey bee	1.18	1.10	1.17	1.52	1.07
Cranefly	1.24	1.09	1.21	1.63	1.06
Hoverfly	1.20	1.10	1.41	1.88	1.07
Dronefly	1.16	1.09	1.29	1.63	1.06
Ladybird	1.15	1.12	1.01	1.30	1.09
mean ± s.d.	1.18 ± 0.034	1.1 ± 0.02	1.21 ± 0.12	1.58 ± 0.16	1.07 ± 0.02

Table 3.2 shows the hovering values of k_{ind}, k_{per} and k_{flap} calculated using the procedure presented in Section 3.2 for the eight insect species based on their data provided in Table 3.1. Also the variation of k_{ind}, k_{per} and k_{flap} with the relevant variables is shown in Figure 3.6. The mean value of k_{ind} for the eight insects is 1.18. Values of k_{per} associated with wake periodicity are presented for normal hovering with two active wing strokes. The first calculation is based on the rotor expression (Equation 3.12 and 3.29) using an effective disk area of $S_d = \pi R^2$ to calculate the disk loading. This method is more appropriate for revolving wings that is usually employed for experimental measurements of insect wings [142,146,147] where the wing sweeps the actuator disk area in a propeller fashion. The second calculation of k_{per} is based on Ellington's expression (Equation 2.33). It has slightly lower values than that obtained using the rotor expression, however, the two calculation results are in obvious agreement and their values are usually around 1.1. The ladybird has a value of k_{flap} almost equal to unity, the hoverfly has a k_{flap} value of 1.41 whereas other insects k_{flap} values are clustered around 1.2. Generally, values of k_{flap} represent the major contributor to the total k for most insects. The large variation in k_{flap} might be expected on the basis that it is driven primarily by the maximum wing flapping amplitude, which will vary between different insect body arrangements. Finally, Table 3.2 shows values of the overall k that accounts for all three effects. These k values range between 1.5 and 1.6 except for the hoverfly that has the largest k with a value close to 1.9 and the ladybird that has the smallest k of a value of 1.3. The difference in the hoverfly and ladybird k values is mainly due to differences in k_{flap}.

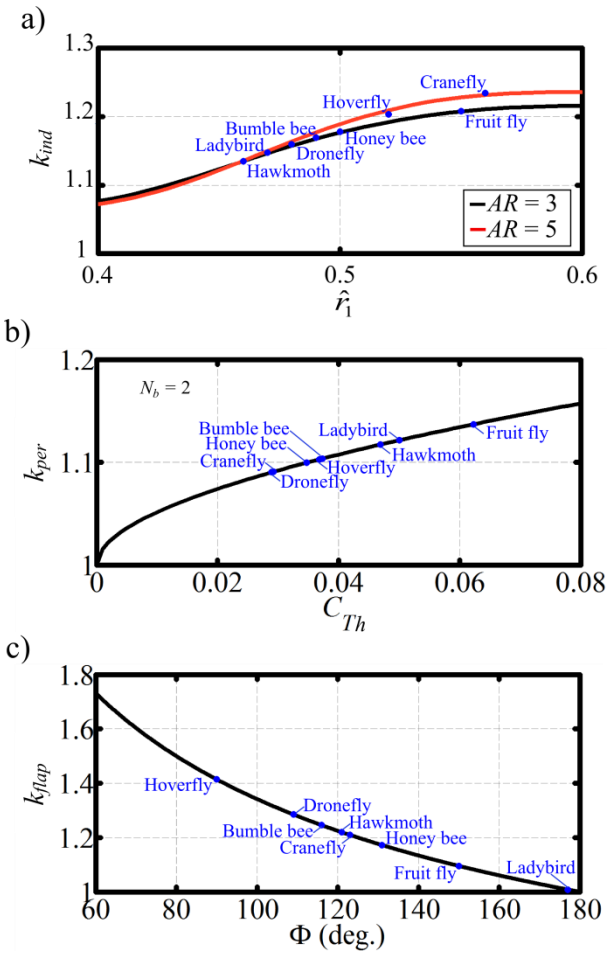

Figure 3.6 (a) Variation of the induced power factor due to non-uniform downwash effect with wing morphology. (b) Variation of the induced power factor due to wake periodicity with the thrust coefficient. (c) Variation of the induced power factor due to effective flapping disk area with the peak to peak flapping stroke angle.

3.4 Applications and Discussion

3.4.1 Reynolds number effect on the induced power factor

There is currently some evidence that suggests that hovering flapping wing flows at insect scale are largely independent of Reynolds number. This is consistent with the experimental observations that show that the net force vector at high angles of attack is normal to the wing surface indicating dominance of pressure forces at these low Reynolds numbers and the relative lack of influence of viscous forces [142,146,148,149]. In their experimental study, Lentink and Dickinson [142] tested the aerodynamics of a fruit fly wing model at three Reynolds numbers using the same kinematics, but using fluids of different viscosities. They found that the lift–drag coefficient polars did not change much and almost no dependence on Reynolds number

over the range they measured (100< Re <14,000) was demonstrated. Similarly, Sane and Dickinson [150, p. 1094] reported that their measured forces might not be crucially dependent on viscosity, stating that '*Both viscid and inviscid models show reasonable agreement with forces measured on our apparatus using identical kinematics*'.

Building on the previous, a proposed analytical manipulation that would explain the variation of the induced power factor with Reynolds number is presented. This will be achieved using the analytical expression of the induced power factor due to wake periodicity provided by Ellington (Equation 3.33). Here, a rearrangement of Equation 3.34 is proposed for the spacing parameter as follows

$$s^2 = \left(\frac{2\pi W}{\rho}\right)\left(\frac{1}{AR^2}\right)\left(\frac{1}{(2\Phi f R\bar{c})^2}\right) = \left(\frac{2\pi W}{\rho}\right)\left(\frac{1}{AR^2}\right)\left(\frac{1}{\nu^2 \mathrm{Re}^2}\right), \tag{3.39}$$

where AR is a single wing aspect ratio, $2\Phi fR$ is the mean wing tip speed, $\bar{c}$ is the mean chord, ν is the air kinematic viscosity and Re is the Reynolds number based on the wing tip speed [151]. In the above equation, the kinematic viscosity was enforced into the expression to obtain the Reynolds number. This means that the main parameter controlling the Reynolds number is the wing speed and chord, while the viscosity has no effect. However, this can be accepted at typical insects Reynolds numbers due to the minor role of viscosity on the aerodynamic characteristics of flapping wings discussed previously.

With other contributors to k being fixed (i.e. k_{flap} and k_{ind}) and following Spedding and McArthur [120], an inviscid wing span efficiency due to wake periodicity can be defined as the inverse of the induced power factor due to the same effect as

$$e_{per} = \frac{1}{k_{per,Ellington}}. \tag{3.40}$$

Figure 3.7 shows the effect of varying the Reynolds number on the value of this wing span efficiency for a fruit fly wing, with the mass and aspect ratio taken from Table 3.1. For Reynolds numbers above ~ 100, the span efficiency is effectively independent of Reynolds number, whereas below this value, the efficiency drops increasingly rapidly towards zero. This is in good agreement with the experimental observations of Lentink and Dickinson [142].

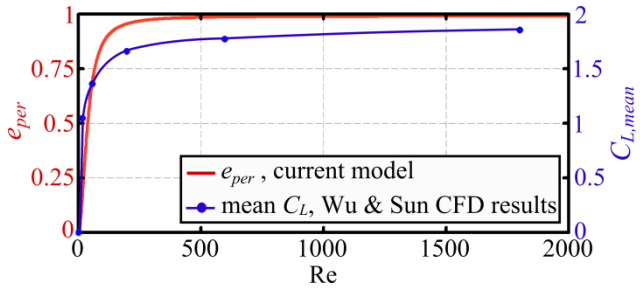

Figure 3.7 Variation of the wing span efficiency due to wake periodicity effect with Reynolds number for the fruit fly. The mean lift coefficient variation with Reynolds number adopted from [152] is included for comparison.

For comparison, Figure 3.7 also shows mean flapping cycle lift coefficient as a function of Reynolds number from CFD results of Wu and Sun [152]. Although the quantities presented on Figure 3.6 are different, the span efficiency will directly influence the lift coefficient values attained during a flapping cycle, hence, allowing a meaningful comparison of the shape of variation.

3.4.2 Figure of Merit

Not all aerodynamic losses are due to induced effects; other sources as skin friction and pressure drag of the wing should be included in the assessment of flapping flight aerodynamic efficiency. The figure of merit, *FM*, is defined as the ratio of the ideal power to hover to the actual power required including all possible sources responsible for this actual power; it is written as [133,140]

$$FM = \frac{\frac{C_{Th}^{3/2}}{\sqrt{2}}}{\frac{kC_{Th}^{3/2}}{\sqrt{2}} + C_{P_{pro}}}. \tag{3.41}$$

The numerator of the above expression is the ideal induced power coefficient given by the momentum theory representing the minimum possible power level. The first term in the denominator is the actual induced power coefficient that accounts for the previously discussed non-ideal induced effects through the factor, *k*. The second term of the denominator, $C_{P_{pro}}$, is the profile power coefficient. Note that if profile effects are ignored, the figure of merit returns to the reciprocal of the induced power factor and become analogous to the inviscid span efficiency.

It is useful at this point to consider the values of *FM* for rotary platforms. In practice, *FM* values for rotary wings range between 0.7 and 0.8 and in some cases can approach 0.82 [133]. However, the previous values are for full-scale helicopters and it is more appropriate to consider *FM* values for rotors at the micro-scale; herein some of the figures found in the literature are reported. Leishman [133, Ch. 6] provided experimental data gauging the performance of a small rotating wing MAV with a 3 inch radius rotor representing a convenient platform for comparison. For this rotor, the estimated value of the profile drag coefficient was 0.035 based on low Reynolds number airfoil data and the induced power factor, *k*, was given a value of 1.75 based on the asymptotic value of the measured *FM* curve. Thus, these values lead to a maximum *FM* of 0.5 which represents a lower hovering performance compared to large rotors. Ramasamy *et al.* [153] conducted rotor performance measurements on a similar two bladed rotor with a radius of 86 mm and a uniform chord of 19 mm giving a blade aspect ratio of 3.7. They confirmed the low aerodynamic efficiency the rotor had with an average *FM* of about 0.5. However it is noteworthy to mention that this experiment was conducted at blade tip chord Reynolds number around 50,000 where the flow turbulence is expected to affect the aerodynamic characteristics as opposed to insects that generally fly in a laminar world of Reynolds number below 10,000 [154]. The highest measured *FM* by Bohorquez *et al.* [13] for a single rotor configuration of the MICOR MAV (see Section 2.2.1.1) at a rotor tip Reynolds number of 25,000 was 0.42. They also showed that profile drag accounts for 45% of the losses as opposed to 30% in full-scale helicopters. Other hover performance measurements of rotors at the micro-scale showed maximum *FM* values between 0.4 and 0.6 [155,156].

Lentink *et al.* [9] compared what they called ‘hover efficacy’ of both a flapping and a rotary fruit fly wing model at typical Reynolds numbers of insect operation using the experimental results from reference [142]. The important aspect of this comparison is that the two different motions (i.e. rotary and flapping) are compared at the same Reynolds number for the same wing within one experiment. Through the comparison of aerodynamic power and inertial power loss, they suggested that helicopter-like MAVs but fitted with insect-like wings can be significantly, up to a factor 4, more energy efficient than flapping insect-like MAVs.

Ellington [151] conducted a useful analysis on some hovering insects including the ladybird, cranefly, hoverfly, dronefly, honey bee and bumble bee to evaluate their efficiency using a measure similar to the figure of merit. However, this measure was

referred to as the aerodynamic efficiency and was given the symbol, η_a (the aerodynamic efficiency was defined as the minimum power required to hover divided by the actually expended aerodynamic power). In this analysis, Ellington evaluated the induced power based on his own model [122]. He estimated the profile drag coefficient using the expression obtained from wind tunnel measurements of some insect wings at high angles of attack: $C_{D_{pro}} = 7/\sqrt{\mathrm{Re}}$. The obtained mean values for $C_{D_{pro}}$ ranged between 0.14 and 0.35 leading to profile power values of similar magnitude as induced power values. Thus, the aerodynamic efficiency, η_a, values ranged between 0.35 and 0.55. Ellington described these aerodynamic efficiency levels as being '*not bad*' considering the enhanced profile power for wings operating at high angles of attack and low Reynolds numbers. Note that Ellington analysis will be critically reinvestigated again in Chapter 5 in light of its comparison to the results from a developed lifting line theory for hovering flight.

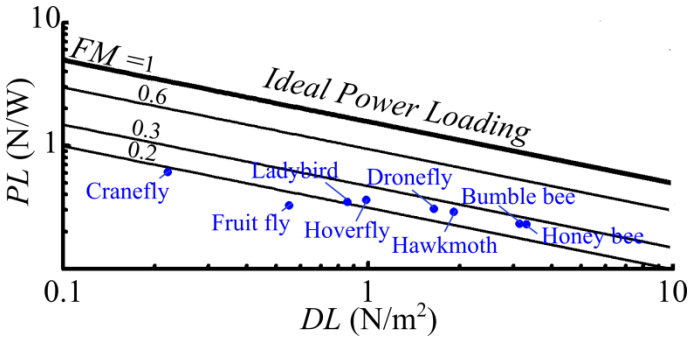

Figure 3.8 Figure of Merit values for eight hovering insects. Power loading is calculated from Sun and Du [145] CFD results.

Now to provide more accurate estimates for the *FM*, the values of power loading for the eight hovering insects are calculated from the CFD results of Sun and Du [145] and are plotted in Figure 3.8 for each insect against its corresponding ideal disk loading based on insect data in Table 3.1. On the same plot, power loading values following the momentum theory for different values of *FM* are plotted based on [133]

$$PL = \frac{\sqrt{2\rho FM}}{\sqrt{DL}}. \tag{3.42}$$

The eight insects show *FM* values ranging between 0.15 (as for fruit fly) and 0.28 (as for honey bee) representing very low aerodynamic efficiency levels. As will be shown in Chapter 4, the tangential skin friction force for insect-like flows can be neglected and only pressure and induced drag components are sufficient to account for the total aerodynamic power budget. If only the induced component is considered, then the *FM* value would be around 0.6 (based on mean value of overall *k* in Table 3.2 and using the expression: 1/*k*). However, the *FM* values in Figure 3.8 are considerably lower demonstrating the significant role of pressure drag towards the obtained aerodynamic efficiency which is consistent with the high angle of attack operation nature of flapping insects. This pressure drag contribution affects to a great extent the degree of efficiency attained, leading to considerably low efficiency measures compared to micro-scale rotors which typically operate at low angles of attack. Note that the relative contribution of pressure and induced components to the overall drag of insect-like hovering flight will be reinvestigated comprehensively in Chapter 5.

It is noteworthy at this point to address that the figure of merit should be used with considerable care as a comparative measure between two wing configurations when they are also compared at the same disk loading. Here comes the role of the power loading as a useful measure that should be used in conjunction with the previous measures to gauge the aerodynamic efficiency [131,133]. The power loading is defined as the quotient of thrust to power (hence analogous to a propulsive efficiency) and it decreases rapidly with increasing the disk loading. Therefore, a hovering configuration with a low disk loading will require relatively low power per unit of thrust produced and might be judged as more efficient, even if the figure of merit is of low value. To illustrate this point, the case of cranefly and honey bee shown on Figure 3.8 are compared. The cranefly has a *FM* value of 0.18 while the honey bee has a *FM* value of 0.28; nevertheless, the power loading of the cranefly is higher than the honey bee case due to its lower disk loading and hence can be regarded as a more efficient platform. This consideration should also apply when comparing flapping and rotary platforms where in some cases a flapping platform can have higher power loading despite of the lower *FM*. Yet, an important point to remember is that power loading suffers from being a dimensional quantity providing an absolute measure of efficiency, whilst both the induced power factor and the figure of merit are non-dimensional quantities providing relative measures of the efficiency.

3.5 Chapter Conclusions

This chapter has provided an analytical treatment of a flapping wing to capture the different aerodynamic effects influencing normal hovering flight in terms of the induced power factor. A number of non-ideal but physical effects that should be accounted when designing and/or analysing a hovering flapping wing are discussed comprehensively, including the effects of: non-uniform downwash velocity distribution, wake periodicity tip losses and effective flapping disk area. A novel method that combines actuator disk and lifting line blade theories is proposed to handle the effect of non-uniform downwash distribution taking into consideration the possible effect of advance ratio on the aerodynamic characteristics of the wing. The developed model has been validated against results from the literature and good agreement with experimental investigations on the effect of advance ratio on the aerodynamics of a revolving fruit fly wing has been obtained. A very good agreement has also been found between the results of the proposed model and experimental measurements of the circulation distribution on a revolving fruit fly wing at zero advance ratio. Different methodologies for the evaluation of the tip losses are presented and analysed. This allowed an investigation on the variation of normal hovering flapping wings induced power factor with Reynolds number.

Specific conclusions for the evaluated induced power factor for eight hovering insect cases at zero advance ratio are as follows:

1. Contributions to the induced power factor: The non-uniform downwash effect leads to k values ranging between 1.14 and 1.24; wake periodicity have been evaluated using two approaches where the two calculation results are around 1.1; losses due to effective flapping disk area lead to k around 1.2.
2. Overall induced power factor: values of the total k accounting for all three discussed effects range from 1.3 for the ladybird and 1.88 for the hoverfly and are most clustered between 1.5 and 1.6 for the remaining species. Losses due to reduction in effective actuation area from flapping stroke angle values less than π represent the major contributor to the overall k for most insects.

Specific conclusions for achieving ideal values of the hovering induced power factor (i.e k=1) are as follows:

1. The contribution to *k* arising from the non-uniform downwash effect is found to depend on both the wing chord distribution and the advance ratio. Thus, for a given advance ratio this effect can be eliminated through appropriate choice of the wing chord distribution. (The optimum hovering chord distribution for zero advance ratio, representing the typical hovering case which is of most interest, will be presented in Chapter 6).
2. The wake periodicity contribution to *k* can be minimised through having lower disk loading values. Additionally, it is confirmed from the different wake periodicity models that normal hovering in which the two wing strokes provide weight support is more efficient than asymmetric strokes along an inclined stroke plane in which mainly one wing stroke provides the weight support.
3. The effective flapping disk contribution to *k* can be controlled through the kinematic parameters: (a) stroke plane angle and (b) flapping stroke angle. Obviously, to minimise k_{flap} to unity, a horizontal stroke plane (i.e normal hovering) should be employed and a flapping stroke angle of 180 degrees should be used.

The figure of merit of eight hovering insects was estimated and the following specific conclusions were obtained:

1. It is found that the figure of merit attained values ranging from 0.15 to 0.28 for the eight insects considered suggesting very low aerodynamic efficiency levels for insect-like hovering flight.
2. The effect of the pressure drag component on the efficiency levels is discussed showing a significant contribution to the efficiency levels obtained due to the high angles of attack operation in hovering flapping flight.

4

A Quasi-Steady Aerodynamic Model of Normal Hovering Flight[2]

This chapter provides a compact and transparent model for the quasi-steady aerodynamics of normal hovering flight. A generic analytical methodology for evaluating the steady translational force coefficients of flapping wings in normal hover and its validation against available experimental data is discussed. The coefficient expressions are then implemented within a quasi-steady blade element model for the analysis of several hovering insects. Generated aerodynamic forces and expended aerodynamic power are calculated and validated against other existing aerodynamic modelling methodologies including CFD simulations. The analytical model is then compared with two other possible analytical approaches to aero-modelling of wings with a leading-edge vortex (LEV). Similarities and differences between the models are identified and results of the three approaches are compared to available experimental data. This allows a reassessment of the role of the LEV in lift augmentation of revolving/flapping wings.

[2] Significant sections of this chapter are based on the publication: Nabawy MRA, Crowther WJ. 2014 On the quasi-steady aerodynamics of normal hovering flight part II: model implementation and evaluation. *J. R. Soc. Interface* **11**: 20131197 (doi 10.1098/rsif.2013.1197)

4.1 Introduction

There have been several attempts to construct sophisticated analytical models for the aerodynamics of insect flight such as those developed by Minotti [157] and Ansari *et al*. [158,159]. Another class of aerodynamic models representing a medium cost, medium fidelity treatment is based on the unsteady vortex lattice method as developed by Fritz and Long [160] and Roccia *et al*. [161]. However, the simpler so-called 'semi-empirical' quasi-steady models [1] are generally more widely used because they are relatively fast, offer insight into the generated forces and allow the comparison between different types of wing morphologies and kinematics. These models require the use of experimental data for the flapping translational force coefficients within the model. Hence their applicability is dependent on the availability of experimental data, such as those presented by Dickinson *et al*. [162] and by Usherwood and Ellington [146,147].

Examples of semi-empirical quasi-steady models are provided by Walker and Westneat [163], Sane and Dickinson [150], Berman and Wang [164], Whitney and Wood [100] and Khan and Agrawal [165]. The main physical assumption in these models is that the flapping wing instantaneous aerodynamic forces are equivalent to the forces generated during the wing steady motion at the same instantaneous velocity and angle of attack [166]. These models start with a definition of wing kinematics from which the angle of attack and the incident velocity in the wing frame of reference are obtained. The lift and drag forces acting on the wing due to its flapping translation are then calculated using the available experimental data on flapping translational force coefficients. Finally, force components due to wing rotation as well as the non-circulatory added mass effects are usually added. The success of a quasi-steady aerodynamic model is based primarily on the availability of appropriate flapping translational force coefficients from experimental data. However, quality experimental data are limited to a few specific geometries and test cases, and force coefficients can show considerable change with variations in the wing shape [167].

In contrast to analytical models, CFD models have the benefit of providing detailed information on both the generated aerodynamic forces and the structure of the wake and surrounding fluid. However, from an interpretation point of view, it is generally difficult to separate the contributions of the various fluid dynamic mechanisms to force generation [1] and as a result these models may not provide insight appropriate to

engineering design or insect physiological analysis. CFD models are also computationally expensive meaning that they are of limited use as part of optimisation studies. Example CFD models include those developed by Liu *et al*. [168] to study a hawkmoth wing in hover, Ramamurti and Sandberg [169] for a fruit fly wing as well as the comprehensive CFD studies of different insect wings developed by Sun and his group [145,152,170,171].

The aim of this chapter is to develop and validate a generic, transparent and compact modelling treatment for representing the aerodynamics of insect-like flapping wings in hover. The main intended use of the resulting model is in the preliminary engineering design of insect-scale flapping wing vehicles; however, the model can also be used to support quantitative studies of insect physiology. A fundamental aspect of the model is its ability to be generic through accounting for different aerodynamic effects related to flapping flight including, for example, the influence of wing shape and kinematics on the aerodynamic characteristics. It allows wider application of 'semi-empirical' quasi-steady models as it removes constraints imposed by the availability of experimental data, allowing flexible analysis, design and optimisation of hovering flapping wings.

4.2. Flapping Wing Analytical Model

4.2.1 Wing morphology

The modelling process begins with definition of the wing shape in terms of chord distribution as a function of span. Here, the procedure proposed by Ellington [141] is used to define the chord distribution through a beta function representation. This representation provides a compact analytical description of wing shape using just three variables: wing length, mean chord and the non-dimensional radial location of the wing centre of area. Details of this method were provided in Section 3.3.2 and hence will not be repeated here.

4.2.2 Wing kinematics

The wing kinematics are defined using the axis systems shown in Figure 4.1. The reference axis system is (x_0, y_0, z_0) with the x_0-axis taken parallel to the earth surface. Kinematics of the wing are defined by Euler rotations relative to the reference axis

system. These rotations govern the stroke-plane angle, σ (Figure 4.1a), wing flapping angle, ϕ (Figure 4.1b) and wing pitching (varying incidence) angle, θ (Figure 4.1c).

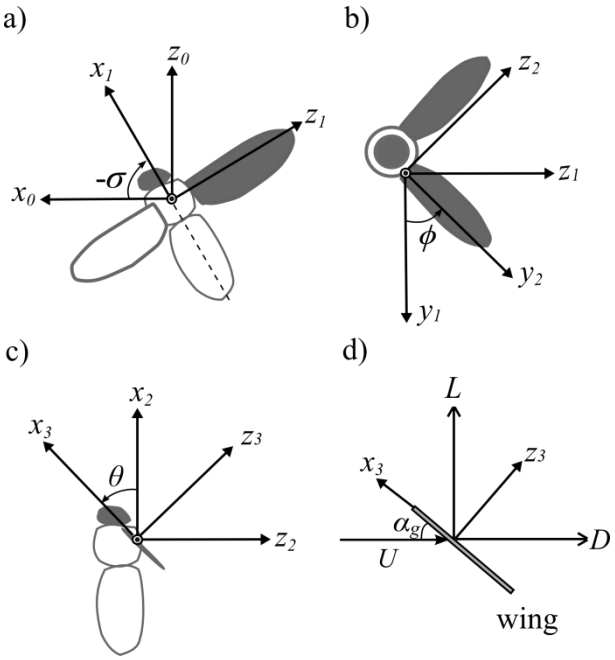

Figure 4.1 Axis systems. (a) Stroke plane axes, for clarity, x_1 and x_2 are aligned with the body axis. (b) Flapping axes. (c) Pitching axes. (d) Lift-Drag frame.

In normal hovering, most insects use symmetrical half strokes and horizontal stroke plane (σ of -90 degrees) [1,167]. Maximum angular deviation from the stroke plane is typically small (less than 15 degrees, see Figure 6 in [171] and Figure 1 in [172]) and it is common to assume that the motion is planar [1,8,165,167]. Therefore, the required kinematic angles to be defined are the flapping angle, ϕ, and the pitching angle, θ. The angles $\phi(t)$ and $\theta(t)$ are defined here using representations as those given by Berman and Wang [164]. However, their parametric expressions are reduced to simpler expressions more compatible with the current work as follows

$$\phi(t) = \frac{\phi_{\max}}{\sin^{-1} C_\phi}\left(\sin^{-1}\left[C_\phi \cos(2\pi f t)\right]\right), \tag{4.1}$$

$$\theta(t) = \frac{\theta_{\max}}{\tanh C_\theta}\left(-\tanh\left[C_\theta \cos(2\pi f t + \chi)\right]\right), \tag{4.2}$$

where $\phi_{\max}$ is the flapping angle amplitude, $\theta_{\max}$ is the pitching angle amplitude and f is the flapping frequency. The parameters C_ϕ and C_θ are used to control the shape of

flapping and pitching cycles respectively where $0 < C_\phi < 1$ and $0 < C_\theta < \infty$ [164]. In the limit where $C_\phi \rightarrow 0$, $\phi(t)$ becomes sinusoidal, and when C_ϕ approaches 1, $\phi(t)$ becomes a triangular waveform as shown in Figure 4.2a. On the other hand, as C_θ approaches 0, $\theta(t)$ becomes sinusoidal while as C_θ tends to ∞, $\theta(t)$ becomes rectangular as shown in Figure 4.2b. The phase lag angle, χ, controls the pitching timing through the flapping cycle and is 90 degrees for the symmetric case. Note that, a comprehensive investigation into the optimisation of kinematics for different aerodynamic objectives will be presented in Chapter 7.

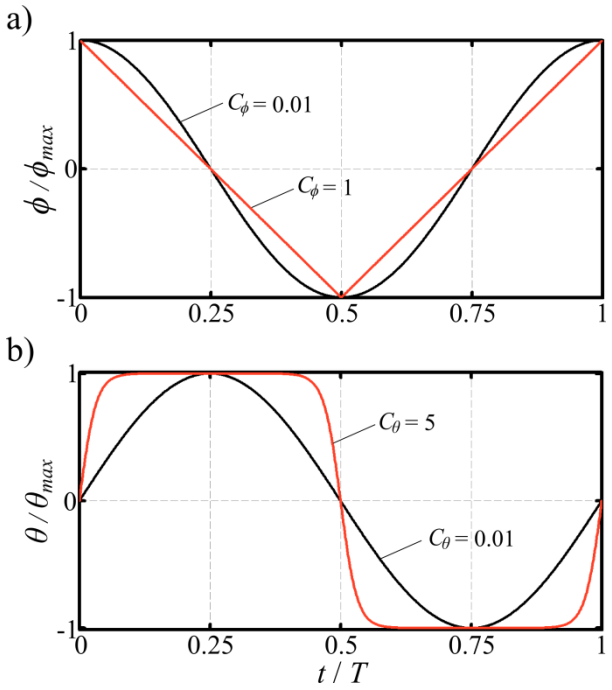

Figure 4.2 Kinematics model for symmetric normal hovering, (a) Flapping angle, $\phi(t)$ and (b) pitching angle, $\theta(t)$. The parameters C_ϕ and C_θ are used to control the shape of flapping and pitching cycles.

Once the kinematics of the wing are defined, the instantaneous angular velocity in the wing frame is derived. The linear velocity vector, *U*, is then obtained by cross multiplication of the angular velocity vector and the position vector in the wing frame [100]. The wing geometric angle of attack, α_g, defined as the angle between the zero lift line and the instantaneous velocity vector (Figure 4.1d) in the *x*-*z* plane, is obtained as

$$\alpha_g = \arctan 2(-U_{z_3}, U_{x_3}). \tag{4.3}$$

The instantaneous lift and drag force components on each wing strip are expressed as

$$\begin{aligned} dL &= \frac{1}{2}\rho\|U(r)\|^2 C_L(\alpha_g)c(r)dr \text{ and} \\ dD &= \frac{1}{2}\rho\|U(r)\|^2 C_D(\alpha_g)c(r)dr, \end{aligned} \tag{4.4}$$

where ρ is the density, c is the chord, while, C_L and C_D are the flapping wing translational lift and drag coefficients which will be discussed comprehensively in next section.

4.2.3 Aerodynamics

4.2.3.1 Modelling principles

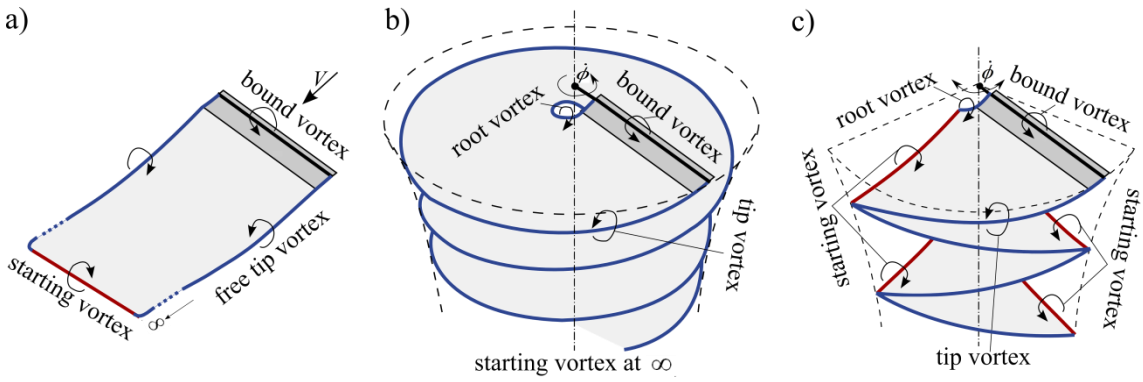

Figure 4.3 Illustration of an idealised conception of the vortex wakes from the three principal wing motions used for practical lift generation: (a) Parallel translating. (b) Revolving. (c) Flapping. For flapping motion, it is assumed that wing rotation at the beginning and end of each half stroke occurs instantaneously and the angular velocity is constant through each half stroke such that the starting and stopping vortices are coincident. In practice, the flapping wake structure is significantly less stable than the wakes for translating and rotating motion due to self induced velocities and thus represents the most idealised case of the three wakes shown.

Previous experimental work conducted on flapping wings has included experiments on model insect wings in parallel translation motion as well as revolving and flapping translations. These three possible wing motions are shown schematically in Figure 4.3 with an idealised conception of their associated vortex structures. An objective of this diagram is to show that whilst the three wing motions lead to quite different wake structures, the fundamental building blocks of the wake are similar and hence it should be anticipated that an aerodynamic theory for the flapping case can built from modification of existing components developed for translating and revolving flight. It

has been observed in experimental studies that at small angles of attack the wing lift coefficients are almost the same for all three wing motions (see Figure 12 in [146], Figure 1 in [9] and Figure 7 in [173]). However, once the wing enters the high angles of attack region, the lift coefficients of parallel translating wings drop significantly due to wing stall. On the other hand, revolving and flapping wings do not exhibit classical abrupt stall characteristics and the lift coefficient tends to increase up to a maximum value at around 45 degrees. The reason for this is typically attributed to the formation of a leading-edge vortex (LEV) on the top surface of the wing [146,174,175]. This LEV has stable characteristics and is often continuously attached during the flapping cycle. Section 4.4 will comprehensively discuss the possible methods to theoretically model the LEV, and will provide a theoretical argument for attributing the observed lift enhancement and in particular the role of the LEV in lift production.

4.2.3.2 Translational aerodynamic force coefficients

The current study considers a very simple aerodynamic model for the translational aerodynamic force on a flapping wing based on a normal force as a function of angle of attack [8,134]

$$C_N(\alpha_g) = \hat{C}_N \sin\alpha_g, \tag{4.5}$$

where $\hat{C}_N$ is the magnitude of the normal force coefficient at 90 degrees angle of attack, which will depend primarily on Reynolds number and wing shape [164,176]. Resolving the normal force in the lift and drag directions gives

$$\begin{aligned} C_L(\alpha_g) &= \hat{C}_N \sin\alpha_g \cos\alpha_g = \tfrac{1}{2}\hat{C}_N \sin 2\alpha_g \text{ and} \\ C_D(\alpha_g) &= \hat{C}_N \sin^2\alpha_g . \end{aligned} \tag{4.6}$$

This model is based on the following assumptions:

(1) Absence of classical wing stall; i.e. the wing undergoes a 3d flapping translation where the leading edge vortex is stable and does not grow with time. Because there is no new vorticity generated at the leading edge, no additional vorticity is generated at the trailing edge and the wing satisfies the Kutta condition at angles beyond which classical stall would occur for parallel translating wings [148]. This means that the lift is a continuous function of angle of attack.

(2) The wing is an infinitesimally thin flat plate, and hence there is no chordwise component to the integrated surface pressure force.

(3) The chordwise tangential force due to skin friction is negligible compared to the integrated surface pressure force acting normal to the wing chord.

(4) The magnitude of the normal pressure force is proportional to the projected wing chord perpendicular to the flow direction [134].

Because of assumption 4, the current model will be named as the 'normal force' model. Additionally, it is understood that assumption 1 (absence of classical wing stall) will become invalid at angles of attack approaching 90 degrees where from a symmetry argument, there must be a separation at both the leading and trailing edges, and hence the Kutta condition cannot be satisfied.

Experiments on model insect wings and CFD simulations [134,177] have shown that the above model provides a close approximation of the measured translational steady lift coefficient and is widely used for modelling lift for insect physiology and engineering studies [100,164,176]. Within this community, it is customary to present the model as

$$C_L(\alpha_g) = C_T \sin 2\alpha_g, \tag{4.7}$$

where C_T is referred to as the translational lift constant and is equal to half the peak normal force coefficient.

A value for translational lift constant loosely based on a method used by Hewes [178] is obtained as follows. Taking the limit of Equation 4.7 in the vicinity of small angles of attack gives

$$C_L = (C_T 2)\alpha_g . \tag{4.8}$$

Hence,

$$C_T = \tfrac{1}{2} C_{L\alpha,3d}, \tag{4.9}$$

where, $C_{L\alpha,3d}$ is the three dimensional wing lift curve slope at small angles of attack. For a given wing shape, the wing lift curve slope can be obtained using an appropriate wing theory and hence an expression for C_T can be obtained. A suitable way for the evaluation of the three dimensional wing lift curve slope is to use Prandtl lifting line theory [179,180]

$$C_{L\alpha,3d} = \frac{C_{l\alpha,2d}}{E + \frac{kC_{l\alpha,2d}}{\pi AR}}. \tag{4.10}$$

The above lifting line expression gives good results for aspect ratios above 3 [137], hence can be applied to most insect wings, which have aspect ratios ranging between 3 and 5 [141]. An important aspect of the above relation is that it accounts for the influence of the vorticity in the wake on the wing lift curve slope [144,175,181]. Note that the experimental values of the lift coefficient, used within 'semi-empirical' quasi-steady aerodynamic models, are calculated based on the linear velocity at the radius of second moment of area for the wing. This allows the obtained lift coefficient values to be compared directly with those from wings in parallel translation motion [146,148]. These experiments were also performed under stationary conditions (i.e. the wing is moved at a constant angular velocity with fixed angle of attack). Therefore, stationary aerodynamic treatments are valid and the above expression for evaluation of the 3d wing lift curve slope is appropriate.

An expression for the steady lift coefficient due to translation is thus obtained by substituting Equations 4.9 and 4.10 into Equation 4.7, giving

$$C_L(\alpha_g) = \left(\frac{C_{l\alpha,2d}}{E + \frac{kC_{l\alpha,2d}}{\pi AR}} \right) \sin\alpha_g \cos\alpha_g = \left(\frac{0.5C_{l\alpha,2d}}{E + \frac{kC_{l\alpha,2d}}{\pi AR}} \right) \sin 2\alpha_g . \tag{4.11}$$

Note that, the above expression is consistent with the un-stalled, high angle of attack 2d airfoil lift coefficient expression, $C_l = \frac{C_{l\alpha,2d}}{2} \sin 2\alpha = C_{l\alpha,2d} \sin\alpha \cos\alpha$, usually used in helicopter and fixed wing aerodynamics [182,183].

As discussed in Chapter 3, the two dimensional aerofoil lift curve slope, $C_{l\alpha,2d}$, has a theoretical value of 2π rad^{-1} (0.11 deg^{-1}) for a flat plate. However, Spedding and McArthur [120] showed experimentally that this value reduces at the low Reynolds number at which insects operate. Okamoto *et al*. [139,184] have shown that for a flat plate wing at typical insects Reynolds numbers, the lift curve slope takes a value of 0.09 deg^{-1}; hence, this value will be used here. The parameter E is the edge correction proposed by Jones [185] for the lifting line theory and is evaluated as the quotient of the wing semi perimeter to its length [185,186] (a discussion on this parameter will be

provided in Chapter 5 as well). The aspect ratio, *AR*, is based on the span of a single wing, [100,145,158,164] on the assumption that the lift and hence bound circulation drops to zero at the inboard edge of the wing and there is no carry-over of lift to the opposite wing. The parameter *k* is the '*k*-factor' included to correct for the difference in efficiency between assumed ideal uniform downwash distribution and real downwash distribution [120,127,187,188]. In this chapter, the *k*-factor required within Equation 4.11 will be estimated using the induced power factor expression of hovering actuator disc models [127,188]. The induced power factor of normal hovering flight was discussed comprehensively in Chapter 3 and was analytically expressed in terms of three contributors accounting for the non-uniform downwash velocity distribution, tip losses and effective flapping disk area.

Once the lift coefficient is obtained, the steady translational drag coefficient can be obtained from Equation 4.6 using trigonometry, with the assumption that the tangential friction force is zero

$$C_D(\alpha_g) = C_L \tan\alpha_g = 2C_T \sin^2 \alpha_g \,. \tag{4.12}$$

The above relation will underestimate the drag coefficient at very low angles of attack where skin friction contributes to the drag. However, during hover, flapping wings typically operate at relatively higher angles of attack (between 25 and 45 degrees) where the model accuracy is good [146]; this point is further highlighted in Appendix A.

4.2.3.3 Non Translational coefficients

At the end of every half stroke, the flapping wing pitches about a spanwise axis and there has been an argument that rotational forces exist as a function of this instantaneous rotation rate [150,162]. These forces are usually modelled using the quasi-steady treatment for the case of small-amplitude flutter on thin rigid wings [150] and it is therefore necessary to make an assumption that the theory holds true for large angles of attack. Given this, the rotational component of the total aerodynamic force is then defined using the Kutta-Joukowski equation and the instantaneous circulation due to wing rotation as follows

$$\Gamma_{rot} = C_{rot}\Omega c^2 \,, \tag{4.13}$$

$$dF_{rot} = \rho U \Gamma_{rot} dr \,, \tag{4.14}$$

where Ω is the wing angular velocity around a spanwise axis at $\hat{x}_o$ and the rotational coefficient, C_{rot}, is given by

$$C_{rot} = \pi(0.75 - \hat{x}_o), \tag{4.15}$$

where $\hat{x}_o$ varies from 0 to 1 and is usually taken as 0.25 [189]. It should be noted that for symmetric hovering half strokes (which is the main concern of this work), the forces due to rotation effects sum to zero and therefore can be ignored [100,150]. Nevertheless, rotational effects are believed to have an important role in control and manoeuvrability [146].

The final class of aerodynamic force considered is non circulatory and forces in this class are referred to as 'added mass' forces. These are the forces that results from accelerating or decelerating the neighbouring air mass surrounding the wing due to flapping motion. They are usually modelled as [150,163,164]

$$dF_{a.m} = \left(\rho\pi \left(\frac{c}{2} \right)^2 dr \right) \dot{v}_n . \tag{4.16}$$

The outer bracket in the above equation is the mass of air surrounding a wing element, while $\dot{v}_n$ is the first derivative of the normal velocity component of the chord relative to air. However, once again, for symmetrical half-strokes, the net added mass force is zero [1,134,150,176].

4.3 Model Results

4.3.1 Comparison with experimental results of revolving wings

The force coefficients modelled in the present work are three dimensional steady coefficients that account for the downwash effect on the aerodynamic characteristics. In this section, Equations 4.11 and 4.12 are used to calculate the variation of the lift and drag coefficients with geometric angle of attack for hawkmoth and bumble bee wings and results are compared with the measured steady force coefficients from revolving wing experiments of Usherwood and Ellington [146,147]. These experiments were performed at Reynolds numbers similar to those experienced by the actual insect with (single) wing aspect ratios of 2.83 and 3.16 for the hawkmoth and the bumble bee

respectively. Here, these aspect ratio values are used as well as the revolving wing k values (i.e $k=k_{ind}k_{per}$) evaluated in Chapter 3 giving a k value of 1.27 for the hawkmoth and 1.29 for the bumble bee. Also lift and drag coefficients are evaluated for the case of fruit fly wing using a revolving wing k value of 1.37 (see Table 4.1). The results are compared with the experimental data of Lentink and Dickinson [142] who provided revolving wing data at similar Reynolds number experienced by the actual insect (Re =110).

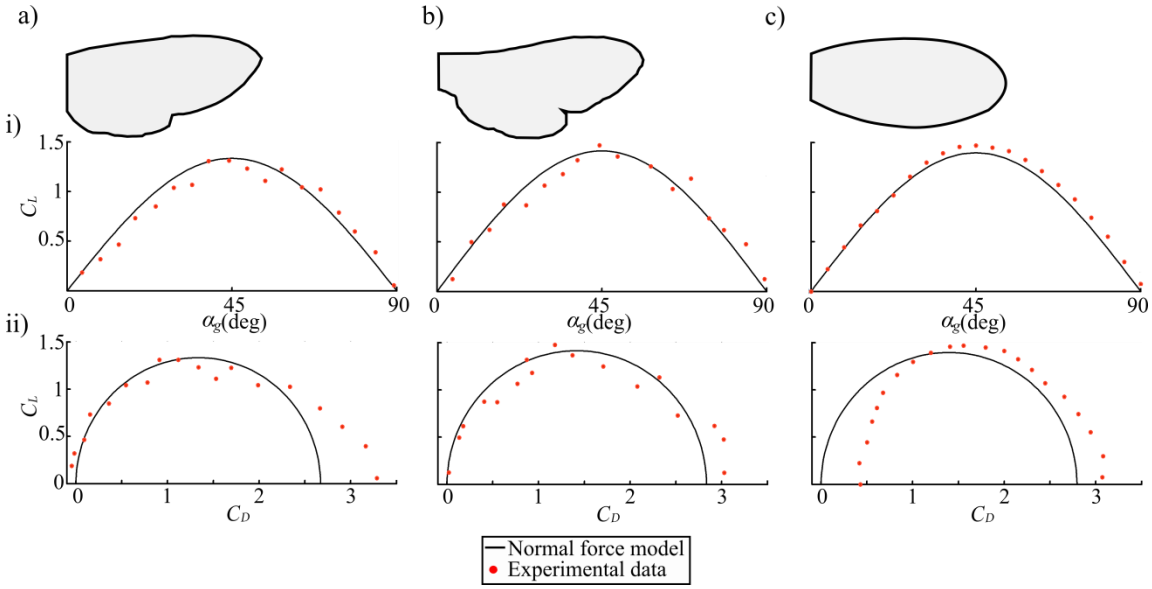

Figure 4.4 Lift coefficient variation with (i) angle of attack and (ii) drag coefficient. Results evaluated using the current model are compared to available experimental measurements for (a) hawkmoth; experimental data digitised from Figure 6 of [146], (b) bumble bee; experimental data digitised from Figure 7 of [147] and (c) fruit fly; experimental data digitised from Figure 7 of [142].

Figure 4.4 compares the calculated lift coefficient variation for the entire range of geometric angles of attack as well as the calculated drag polars against the experimental data. There are two aspects to the fit between theory and experiment that need to be considered. First, the degree to which the form of the data fits the model, and second the agreement between predicted and measured amplitude. The agreement between the model and experiments with respect to either the fit or the amplitude is good, though the agreement is better for lift than for drag. Given that the flow topology is different at 90 degrees angle of attack for the reasons discussed in Section 4.2.3.2, some sort of discrepancy at very high angles of attack is not unexpected. In terms of the impact of the model discrepancy, it should be noted that most insect wings operate at mid-stroke

angle of attack range between 25 and 45 degrees (see Table 4.2), and in this range there is very good fit between the model and data. The fruit fly data has a drag offset, and a possible remedy, as proposed by Dickson and Dickinson [134], is to add a constant representing the drag coefficient at zero lift. However, it is noteworthy to mention that Usherwood and Ellington [146,147] and Lentink and Dickinson [142] measurements at higher Reynolds number (Re ~ $O(10^3)$ to $O(10^4)$) did not show any existence of this drag offset.

4.3.2 Comparison with previous flapping wing aerodynamic models

Table 3.1 of Chapter 3 provided the morphological and kinematic data of eight hovering insects taken from Sun and Du [145] against which the current model will be validated. Here, a wing is divided into 50 evenly spaced wing strips in the spanwise direction and a wing flapping period is divided into 500 evenly spaced time steps. Aerodynamic forces on each strip are integrated along the wing length and averaged over the flapping period. For evaluation of the aerodynamic power consumed during the flapping cycle the energetic cost to the hovering insect is assumed to be given by the time-averaged mechanical power output, where power can be positive or negative. This approach is consistent with that used by Sun and Du [145] to determine the net aerodynamic power. A specific power, P^*, is then obtained as power divided by the total mass. Accounting for negative power assumes that mechanical energy can be stored and released when the wing does positive work. This method of accounting also means that inertial power cancels out and thus can be ignored (see Figure 10 of [145]). It is noteworthy to mention that Sun and Du demonstrated the minor contribution of the wing rotational power component compared to the wing translational power component. Thus rotational power was neglected in their aerodynamic power evaluation.

Table 2 shows the values of k_{ind}, k_{per} and k_{flap} accounting for the non-uniform downwash velocity distribution, tip losses due to wake periodicity, and effective flapping disk area respectively. They are calculated using the procedure presented in Chapter 3 for eight insect species based on their data provided in Table 3.1. These values are repeated here as they will be used within the analysis of the obtained results.

Table 4.1 Contributions to the induced power factor, *k*.

Insect	k_{ind}	k_{per}	k_{flap}	$k_{ind}\,k_{per}$	$k_{ind}\,k_{per}\,k_{flap}$
Fruit fly (FF)	1.21	1.14	1.10	1.37	1.51
Bumble bee (BB)	1.17	1.10	1.25	1.29	1.61
Hawkmoth (HM)	1.14	1.12	1.22	1.27	1.55
Honey bee (HB)	1.18	1.10	1.17	1.30	1.52
Cranefly (CF)	1.24	1.09	1.21	1.35	1.63
Hoverfly (HF)	1.20	1.10	1.41	1.33	1.88
Dronefly (DF)	1.16	1.09	1.29	1.26	1.63
Ladybird (LB)	1.15	1.12	1.01	1.29	1.30

Results from the quasi-steady blade element implementation are now compared with CFD results from Sun and Du [145] as well as the quasi-steady blade element model of Berman and Wang [164]. Both simulations used a horizontal stroke plane, symmetrical half strokes, a sinusoidal variation of flapping angle (corresponding to $C_\phi \rightarrow 0$) and a trapezoidal like variation of the pitching angle with a time interval over which rotation lasts of about 25% of the flapping cycle duration. This corresponds to a value of 5 for C_θ in the current model. The mid-stroke geometric angle of attack, $\alpha_{g,mid}$, used by Sun and Du in their calculations are given in Table 4.2. Vertical force to weight ratio as well as specific power results from the current model compared to other models are shown in Table 4.2. The vertical force is defined as the magnitude of the z-component of the total force produced by a pair of wings in the reference frame (x_0, y_0, z_0) and is the force used for weight support ($\bar{L}/W = F_{z0}/W$).

Table 4.2 Comparison between current model and that of CFD by Sun and Du [145] and quasi-steady model of Berman and Wang [164].

Insect	Current model		CFD, Sun & Du [145]			Quasi-steady, Berman & Wang [164]
	$\bar{L}/W$	P^* (W.kg^{-1})	$\alpha_{g,mid}$ (deg.)	$\bar{L}/W$	P^* (W.kg^{-1})	$\bar{L}/W$
Fruit fly	0.98	26	44	1	30	1.003
Bumble bee	1.06	43	28	1	42	0.95
Hawkmoth	0.92	30	32	1	33	1.15
Honey bee	1.1	43	25	1	41	-
Cranefly	1.3	18	30	1	16	-
Hoverfly	1	25	29	1	27	-
Dronefly	1.2	37	26	1	32	-
Ladybird	0.96	30	43	1	28	-

The results in Table 4.2 show very good agreement with CFD results for weight support and power consumption for the eight insects. It should be remembered that Sun and Du developed their simulation model to obtain the value of $\alpha_{g,mid}$ (supplied in Table 4.2) that would enable weight support. Hence, all their $\bar{L}/W$ ratios are almost 1. In the current model their $\alpha_{g,mid}$ values are used to calculate $\bar{L}/W$. The current model correctly predicts near unity values of $\bar{L}/W$, but with a small underestimation in the hawkmoth and an overestimation in the cranefly and dronefly. The above results demonstrate that the proposed model is able to obtain usefully accurate results for a wide range of insects with different wing shapes and with different operating conditions. Table 4.2 also shows results from the quasi-steady blade element model developed by Berman and Wang which was limited to the analysis of only three insect for which experimental data are present. Additionally, Berman and Wang represented all wing planform shapes as a half ellipse; the model implemented here represents the wing planform shape using the more convenient beta representation.

An Important feature of the proposed model is its transparency, in that it provides greater insight into how the different problem parameters affect the solution; hence allowing improved understanding of the flapping problem. As an example, results shown in Figure 4.5 allow assessment of how each of the three effects included within k affects the calculated aerodynamics (in terms of the weight support ratio). The fruit fly represents a case where k_{ind} and k_{per} are the main contributors to k, while the hoverfly represents a case where the k_{flap} effect is the most significant. Figure 4.5 also shows the importance of accounting for k in aerodynamic calculations, as assuming an ideal case (k =1) can lead to significant overestimation of the generated force (e.g. 23% for the hoverfly case).

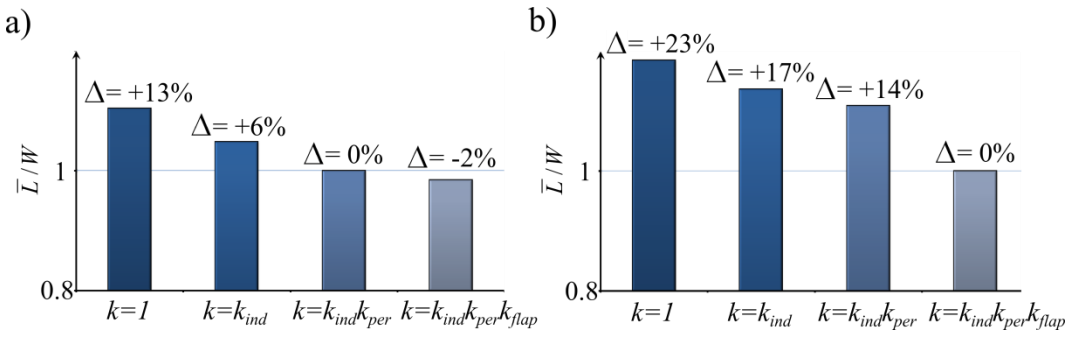

Figure 4.5 Effect of accounting different contributors to k on the weight support calculation for (a) fruit fly and (b) hoverfly. In both figures, Δ represents the percentage difference in value between calculated $\bar{L}/W$ and unity.

4.4 The Role of the Leading-Edge Vortex in Lift Augmentation

4.4.1 Overview

As introduced in Section 4.2.3.1, a leading-edge vortex (LEV) is known to form on thin wings with moderate aspect ratio (~3), steadily revolving at high angles of attack and low Reynolds number of $O(10^4)$ or lower, Figure 4.6. The LEV is stable in that its location remains fixed near the leading edge and it does not grow with time; this allows the flow over the upper surface of the wing to separate at the leading edge but then reattach before the trailing edge, Figure 4.6a. A wing with a stable LEV is thus able to satisfy the Kutta condition at the trailing edge at angles of attack beyond which classical stall would occur for wings where no LEV is present, and consequently a substantial enhancement of the wing lift coefficient is achieved [148].

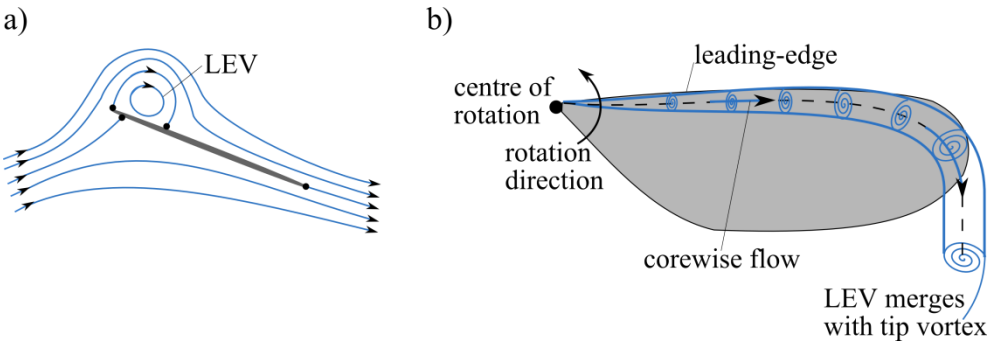

Figure 4.6 (a) A sectional view schematic showing the simplest valid LEV structure for a cylindrical vortex. The LEV is stable at high angles of attack with flow reattachment on the upper surface and satisfaction of the Kutta condition at trailing edge. The black dots represent stagnation points. (b) An idealised top view schematic illustrating a conical LEV topology for a steadily revolving wing with a focus at the root. This topology has been observed at Reynolds numbers of $O(10^3$ to $10^4)$ [174].

There has been substantial research within the last two decades directed at understanding the aerodynamic characteristics of revolving and flapping wings at Reynolds numbers relevant to insect flight. Some of these studies [174,175,181] performed flow visualisation to identify the flow topology and determine possible causes for the stability of the LEV, whilst others measured the generated forces for different wing morphologies and kinematics [134,142,146,147]. The identified LEV topologies were shown to vary from a conical form with a substantial spanwise flow at the vortex core (as that observed on model hawkmoth wings at Reynolds number from 10^3 to 10^4 [174], Figure 4.6b) to a more of a cylindrical form with a substantially

weaker corewise vortex flow (as that observed on fruit fly and thrip wings at Reynolds number of the order 10^2 and 10^1 [175,190]). However, these differences in the LEV flow topologies were not reflected in differences in the measured lift coefficients, which showed remarkable similarity [147,148,154].

The similarity of the lift coefficients despite differences in flow topology suggests that the LEV is playing a role that is independent of its shape and thus motivates the reassessment of the exact role of the LEV in lift augmentation. Is the LEV increasing the lift by directly increasing circulation at a given angle of attack? Or is it acting as a flow control mechanism that prevents or delays stall at high angles of attack? A clear answer to the above questions is of importance because it affects the selection of the analytical approach through which the problem should be handled.

This section will provide an objective review of two different possible approaches to aero-modelling of wings with a LEV and compare them with the current 'normal force' model. Similarities and differences between the models are identified and results of the three approaches are compared to available experimental data.

4.4.2 Comparison with the potential flow model

Following the work of Saffman and Sheffield [191], Huang and Chow [192] and Pitt-Ford and Babinsky [6], the model considered here is based on inviscid, incompressible and irrotational 2d potential flow over a flat plate with an embedded free vortex. This model is based on the well-known Joukowski transformation approach where the flow is mapped from a circle of radius a to a flat plate with a chord length of $4a$ inclined at an angle of attack α to the free stream, U. A free vortex element is included with a circulation Γ_{free} located at $\xi = \tau e^{i\varphi}$ in the circle plane where τ is the radius and φ is the angle with respect to origin. An image vortex of equal but opposite sign to Γ_{free} is located at the inverse square point and a second vortex of equal circulation to Γ_{free} is located at the circle centre; thus, the circulations of image vortices cancel [6]. The Kutta condition is satisfied by equating the velocity to zero at $\xi = a$. The magnitude of the bound circulation is thus obtained as [6]

$$\Gamma = 4\pi a U \sin\alpha + \Gamma_{free}\frac{2a(a-\tau\cos\varphi)}{\tau^2 - 2a\tau\cos\varphi + a^2}. \qquad (4.17)$$

The first term of the right hand side of Equation 4.17 is the well known result for the bound circulation of a flat plate at incidence whereas the second term accounts for the

circulation added by the free vortex (LEV) located at $\xi = \tau e^{i\varphi}$. The lift coefficient is thus obtained from Equation 4.17 as

$$C_l = \frac{\Gamma}{2aU} = 2\pi \sin\alpha + C_{l,\,free}\,\frac{2\left(1-(\tau/a)\cos\varphi\right)}{(\tau/a)^2 - 2(\tau/a)\cos\varphi + 1}, \tag{4.18}$$

where

$$C_{l,\,free} = \frac{\Gamma_{free}}{2aU}. \tag{4.19}$$

The effect of the addition of a free vortex in the above results can be referred to as a '*flap effect*' as the second term represents an additional constant increment in circulation at all angles of attack. For more details, see the discussion on the different wing lift augmentation effects in Appendix B. Now, for a given chord, U and α, Equation 4.18 becomes one equation in three unknowns (C_l, Γ_{free} and ζ); thus cannot be used without further input to evaluate the lift, so either additional information or experimental data (as in [6]) needs to be used to define some of the unknown parameters. Here, a hypothesis is made that a non-zero value of Γ_{free} is required to capture the high lift effect of the LEV. Thus, let $\Gamma_{free} = 0$; if the calculated lift values are less than experimental values, then the hypothesis is true whereas if the calculated lift is equal to or more than the experimental values, then the hypothesis is false. For $\Gamma_{free} = 0$ the lift coefficient returns to the flat plate formula, i.e. $C_l = C_{l\alpha,2d}\sin\alpha = 2\pi\sin\alpha$. This formula will be evaluated against experimental results of 3d wings, hence it is necessary to use the 3d wing lift curve slope, $C_{L\alpha,3d}$, that accounts for the downwash effect.

Note that in the potential flow model, it is the *lift* that is proportional to $\sin\alpha$ rather than the normal force. This leads to increasing divergence between the potential flow and normal force models as the angle of attack approaches 90 degrees.

4.4.3 Comparison with the leading edge suction analogy

The conical LEV created on laminar revolving/flapping wings is similar in form to that observed over delta wings at subsonic speeds and high angles of attack. The leading edge suction analogy was originally proposed by Polhamus for delta wings [193], and due to the similarities in the flow structure between delta wings and flapping wings, the leading edge suction analogy has usually been considered as a possible aerodynamic treatment for the flapping problem (see reviews by Sane [148], Ansari *et al*. [1] and

Taha *et al*. [167]) and the model has been adopted by a number of researchers [194-196] to tackle the flapping wing problem. In this section, Polhamus model will be thoroughly analysed in the light of its application to revolving/flapping wing aerodynamics modelling.

The leading edge suction analogy is based on an assumption, substantiated from experiments, that the flow external to the LEV passes around the vortex and reattaches to the wing upper surface. It is formulated on the basis that the leading edge flow separation that creates the LEV causes a loss of the leading edge suction and the lift is thus comprised of two components: the first is the potential flow lift with zero leading edge suction. The second is a vortex lift equivalent to the leading-edge suction associated with the potential flow. Polhamus did not provide a theoretical proof of his analogy concept; however, it proved useful in estimating force coefficients on delta wings. The model is expressed as follows [193]

$$C_L = K_P \sin\alpha_g \cos^2\alpha_g + \left(K_P - K_P^2 K_i\right)\frac{1}{\cos\Lambda}\sin^2\alpha_g \cos\alpha_g , \tag{4.20}$$

where K_P is the wing lift curve slope at small angles of attack, Λ is the wing sweep angle and K_i is the derivative of the induced drag coefficient with respect to the square of the lift coefficient. Thus, Equation 4.20 can be written as

$$C_L = \underbrace{C_{L\alpha,3d} \sin\alpha_g \cos^2\alpha_g}_{\text{Potential lift term, } C_{L,p}} + \underbrace{\left(C_{L\alpha,3d} - \frac{kC_{L\alpha,3d}^2}{\pi AR}\right)\frac{1}{\cos\Lambda}\sin^2\alpha_g \cos\alpha_g}_{\text{Vortex lift, } C_{L,v} = \text{ leading edge suction}} , \tag{4.21}$$

Assuming a non-swept wing which is consistent with insect wings, the above relation has almost the same shape of variation with angle of attack as the sin $2\alpha_g$ relation. This is shown in Figure 4.7a where each of the two relation plots is normalised by its maximum (amplitude) value. Next, in order to compare the amplitudes, Equation 4.21 is rearranged as

$$C_L = \left(C_{L\alpha,3d} \sin\alpha_g \cos\alpha_g\right)\underbrace{\left(\cos\alpha_g + \left(1 - \frac{kC_{L\alpha,3d}}{\pi AR}\right)\sin\alpha_g\right)}_{K_{Polhamus}} . \tag{4.22}$$

Note that the first bracket in the above expression is the 'normal force' model. The second bracket represents an additional term multiplied to the proposed lift coefficient relation of the 'normal force' model which will be named $K_{Polhamus}$. Figure 4.7b illustrates the variation of this term with the wing aspect ratio. In this illustration and without losing generality, the parameter k was assigned a unity value and the angle of attack is taken as 45 degrees to represent the condition of maximum C_L value.

The implications of the results in Figure 4.7b are: first, the value of the $K_{Polhamus}$ term is of the order of unity. From this we can conclude that the Polhamus model is matching quantitatively with the normal force model. Second, the term $K_{Polhamus}$ has a slightly higher value than unity. This is to be expected as Polhamus did not take into account the effect of the vortex flow on the attached flow [195], hence would over-predict the lift. Third, the term $K_{Polhamus}$ increases with the increase in aspect ratio. Once again this is expected as the Polhamus model is known to increasingly over-predict the wing lift coefficient as the wing aspect ratio increases. Polhamus obtained very good agreement for his model with delta wing experimental data of aspect ratios up to 1.5; however, for an aspect ratio of two, lower experimental lift coefficient values were evident (see discussion of [193]). Therefore, for the range of insect wing aspect ratios, the Polhamus model is expected to over predict the lift. It should be noted that the values of angle of attack and k used for the result in Figure 4.7b lead to maximum values of $K_{Polhamus}$; hence, the maximum deviation case is considered. Furthermore, the values of $K_{Polhamus}$ are only weakly sensitive to the angle of attack and/or k values; hence, the conclusions derived here may be considered as general results.

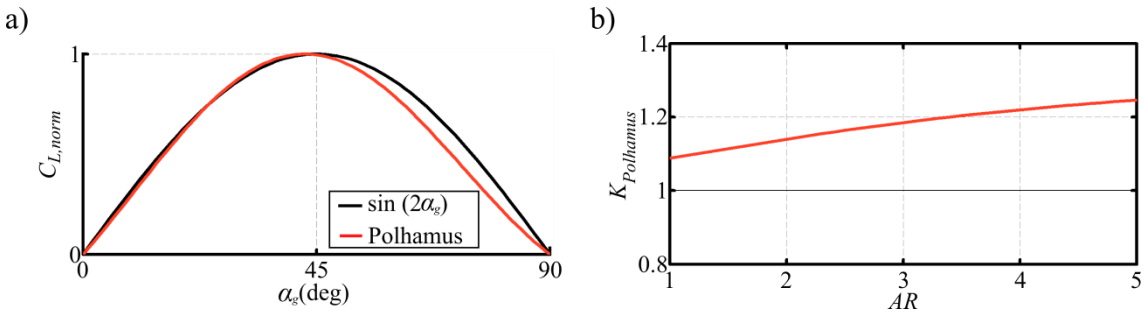

Figure 4.7 (a) Comparison of the shape of variation of the Polhamus and the sin 2α relation. Each plot is normalised by its amplitude value. (b) $K_{Polhamus}$ variation with the wing aspect ratio for a unity k-factor at 45 degrees angle of attack using the extended lifting line model [137].

4.4.4 Models evaluation and discussion

Figure 4.8 compares the calculated lift coefficient variation for the first quadrant of geometric angle of attack. When reviewing the data in Figure 4.8 it should be noted that for normal hovering flight the typical values for the mid-stroke angles vary between 25 and 45 degrees (see Table 4.2) and therefore particular attention should be focussed on the degree of correlation in this angle of attack range.

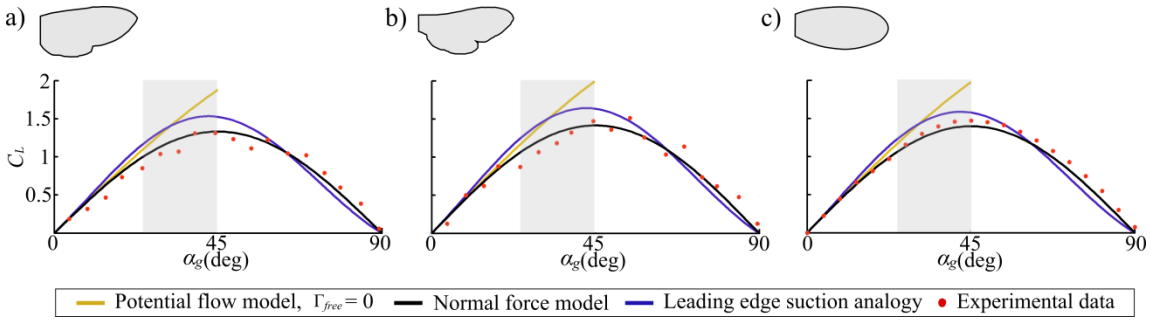

Figure 4.8 Lift coefficient variation with geometric angle of attack using three different models. Owing to the failure in capturing the lift symmetry, the potential flow model results are only shown up to an angle of attack of 45 degrees. Models results are compared to available experimental measurements for (a) hawkmoth; experimental data taken from Figure 6 of [146], (b) bumble bee; experimental data taken from Figure 7 of [147] and (c) fruit fly; experimental data taken from Figure 7 of [142]. Gray band represents typical angle of attack values within the mid-strokes of normal hovering insect flight.

The potential flow model results shown in Figure 4.8 fail to capture the lift symmetry about the 45 degrees angle of attack and continue to increase to a maximum value at 90 degrees where the lift is known to vanish. However, it offers good evaluation of lift up to around 25 degrees angle of attack after which it starts to over-predict the measurement data. Despite these concerns, the important result here is that by setting Γ_{free} to zero, the model *over-predicted* the lift coefficient. Hence the $\sin\alpha_g$ term alone in Equation 4.18 is more than sufficient to estimate the lift value, and additional circulation from the leading-edge vortex is not required to predict the observed lift coefficient values.

The normal force model provides the best fit with respect to both the shape of variation and the amplitude. Note that the normal force model is simply the potential flow model multiplied by $\cos\alpha_g$ with the leading-edge vortex strength set to zero. At very small angles of attack the normal force model thus reduces to the well-known lift expression $C_L \approx C_{L\alpha,3d} \sin\alpha_g \approx C_{L\alpha,3d}\alpha_g$. At very high angles of attack the

multiplication by $\cos\alpha_g$ allows the lift to tend to zero at 90 degrees angle of attack as required by basic geometric considerations.

The leading edge suction analogy provides a fair fit with respect to the shape of variation of lift against α_g; however, it overestimates the lift magnitudes up to an α_g value around 60° and then starts to underestimate it. It is noteworthy that the potential lift component of the leading edge suction analogy, $C_{L,p}$, is a further attenuation of the potential lift, i.e. $C_{L,p}$ = Equation 4.11 × $\cos\alpha_g$. The $\cos^2\alpha_g$ in the $C_{L,p}$ term was explained by Polhamus to arise from the assumption of a Kutta-type flow condition at the leading edge [197]. However, the application of a Kutta condition at the leading edge was shown to be mathematically invalid by Saffman and Sheffield [191]. This attenuation of the potential lift was compensated for by the addition of vortex lift, $C_{L,v}$; hence allowing recovery of the total lift coefficient value. The total lift coefficient of the leading edge suction analogy for the angles of attack between 0 and 45 degrees angle of attack can be regarded as effectively having a higher lift curve slope compared to the 'normal force' model (for more details see Appendix B).

Based on the presented comparison, the normal force model is the most accurate model over the whole first quadrant of angle of attack. It is also the simplest of the models and does not explicitly include any aerodynamic force contribution from the LEV. Hence, the LEV does not have a direct effect on lift by increasing circulation or generating increased local suction; rather, it has an indirect effect on high lift by preventing flow separation in the same manner as a '*slat*' in classical aerodynamics.

4.5 Chapter Conclusions

A generic, transparent and compact model for the design and/or analysis of rigid flapping wings in hover has been presented. The model is generic in that it can be applied to wings of arbitrary planform geometry following arbitrary kinematic cycles, and is transparent in that the model parameters are clearly linked to attributes of the flow physics. The model is compact in the sense that relatively modest computational effort is required for solution compared to higher order models such as those based on CFD, and hence the model is suitable for use as part of preliminary engineering design and optimisation of flapping wings.

The modelling capability provides an improvement in the state of the art in that relevant aerodynamic model parameters are obtained by analytical means from geometry and kinematic information alone; aerodynamic data from experiments or higher order models is not required. The model is implemented using a quasi-steady blade element framework with parametric control of both wing chord distribution and wing kinematics.

The developed model has been validated against experimental and numerical results from the literature with the following outcomes:

1. Comparison of the calculated steady force coefficients with available experimental data for revolving hawkmoth, bumble bee and fruit fly model wings shows good agreement with respect to both the shape of variation of the force coefficients with incidence as well as the magnitude.
2. Comparison of the calculated aerodynamic forces and consumed power with available numerical CFD simulations for eight insect cases shows good agreement.

The validated model is used to evaluate the relative impact of different contributors to the induced power factor for the hoverfly and fruit fly. It is shown that assumption of an ideal induced power factor (k=1) for a hoverfly leads to a 23% overestimation of the generated force due to flapping.

The developed so-called ‘normal force’ model was compared to other analytical models including the potential flow model with an embedded vortex and the Polhamus leading edge suction analogy. The potential flow model provides its best correlation to the experimental measurements when the embedded vortex strength is set to zero. For this case, good matching results are evident just up to a 25 degrees geometric angle of attack. Moreover, this model does not allow lift coefficient symmetry around the 45 degrees angle of attack. To the contrary, the lift coefficient increases up to 90 degrees geometric angle of attack where the lift is known to vanish. On the other hand, the Polhamus leading edge suction analogy shows an acceptable agreement with respect to the shape of variation of lift coefficient over the full range of incidence up to 90 degrees geometric angle of attack. However, the magnitude of the lift coefficient is always higher than experimental values particularly in the expected range of operation of normal hoverers. This was shown to be consistent with the expected overestimation in the lift coefficient values by the Polhamus analogy for typical insect wing aspect ratios.

In conclusion, of the three models evaluated, the ‘normal force’ model provides the best correlation with measured lift values from steadily revolving wings experiencing a LEV, despite the fact that it does not account for additional circulation due to the LEV as in the potential flow model, or account for a vortex lift (suction) component as in the Polhamus model. This shows that it is unnecessary to add a specific lift contribution from the LEV to explain the high lift generated in the experimental results and thus the hypothesis that the LEV eliminates wing stall in a similar manner to a ‘*slat effect*’ in classical aerodynamics is the simplest sufficient theoretical explanation for the observed behaviour.

5

A Quasi-Steady Lifting Line Theory for Insect-Like Hovering Flight

In this chapter, a novel lifting line formulation is presented for the quasi-steady aerodynamic evaluation of insect-like wings in hovering flight. The approach represents an alternative route for accurate estimation of aerodynamic forces and provides quantitative information on the relative contribution of induced and profile drag components associated with lift production for insect-like wings in hover. The main adaptation to the original Lifting Line Theory (LLT) is the use of an equivalent angle of attack, which enables capture of the steady non-linear aerodynamics at high angles of attack whilst preserving the essential linear aspects of the original LLT. A simple methodology to include other non-ideal induced effects due to wake periodicity and effective actuator disc area within the lifting line theory is included in the model. Low Reynolds number effects as well as the edge velocity correction required to account for different wing planform shapes are also incorporated through modification of the 2d lift curve slope. The model is successfully validated against measurements from revolving wing experiments and high order CFD simulations.

5.1 Introduction

The classical lifting line theory (LLT), developed by Prandtl a century ago provided the first satisfactory analytical treatment for the evaluation of the aerodynamics of a finite wing [198-200]. The LLT laid the foundation for understanding the aerodynamics of flight, and is still widely used today to provide accurate predictions of the lift and induced drag for 3d wings [201,202]. The solutions delivered by the LLT are closed form and they are many orders of magnitude faster to evaluate compared to higher order computational methods. They are also able to provide deep insight into how different wing parameters affect the aerodynamic performance [201].

The physical foundation of the LLT is based on Prandtl's hypothesis that the lift of a finite wing is reduced compared to the lift of an infinite wing due to the change of the local flow direction induced by the free vortices in the wake. The Kutta-Joukowski theorem can then be applied at each wing section, which is assumed to behave as a 2d wing at a modified angle of attack referred to as the *effective angle of attack*. This concept led Prandtl to his well-known linear equation governing the circulation on a finite lifting surface, which will be formally introduced in Section 5.2.2. Because the obtained governing equation is of an integro-differential type, there exists no unique mathematical procedure to solve it, and throughout the past century different mathematical methods have been proposed to handle the problem [203]. The most well-known solution methodology is that presented by Glauert [135] who provided a solution in the form of an infinite Fourier sine series with the series coefficients obtained from the collocation method.

Whilst the LLT is usually used for the aerodynamic modelling of high aspect ratio, planar, fixed wings in steady flows, the long reach of Prandtl's insight is demonstrated through the various adaptations presented over the years that have enabled much broader applicability of his original model. With few alterations, the LLT has been successfully used to predict the aerodynamics of a wide variety of lifting surfaces under a wide variety of flow conditions. Jones [185] proposed a simple correction for the LLT which he showed could bring the lifting line result into close agreement with the lifting surface result over an extended range of wing aspect ratio, hence improving accuracy of the LLT for low aspect ratio wings. Phillips and Snyder [204] extended the lifting line formulation so that it can be used for non-planar wings with arbitrary camber, sweep

and dihedral. Sclavounos [205] developed an unsteady lifting line treatment for wings of large aspect ratio undergoing time-harmonic oscillations where he showed in the zero-frequency limit that it reduces to the Prandtl's lifting line theory, whilst for high frequencies it tends to the two-dimensional strip theory. Mehrle [206] extended Multhopp's quadrature method to the calculation of the circulation of cyclic periodic lifting systems, e.g. for wings operating in swirling flow. Anderson [207] proposed a numerical iterative lifting line treatment that uses look-up tables of the sectional lift as a function of effective angle of attack for the use within flight conditions such as spins and high angles of attack manoeuvres.

The LLT has also been adopted for the evaluation of the aerodynamics of wings prescribing rotary and flapping motions. Conlisk [208] discussed the implementation of the LLT for rotary wings in hover, and highlighted the importance of accounting for the effect of the linear velocity variation along the blade on the bound circulation distribution. Leishman [133, Ch. 14] provided a generic formulation of the LLT for rotary wing motions; whereas, Johnson [140, Ch. 10] discussed the importance of adopting corrections to the LLT to handle specific rotary wing aerodynamic phenomenon such as wake periodicity.

Lifting line formulations very similar to that of fixed wings have been used in references [121,209] for the mathematical modelling of the avian flight power curve. Philips *et al*. [210] presented a LLT for forward flapping flight in which some unsteady flow effects were accounted for through the use of a 3d model of the vortex wake to evaluate the unsteadiness to a first order. For a review of lifting line models for flapping wings in forward flight, the reader is referred to reference [211].

For hovering flapping flight, two significant contributions have been presented. The first is by Sane [132] who proposed a semi-empirical lifting line blade model for hovering insects to investigate the mean induced flow over their bodies. However, the model relied on experimental data; hence, measurements are still required as inputs to the calculation. The second contribution was by Ansari *et al*. [1] who reviewed the use of lifting line blade theory based on the Glauert solution [135] in the context of insect-like flapping wings: a general description of the model was provided and some results for the variation of the mean lift with flapping frequency and wing shape were presented. However, their model relied on a linear aerodynamic representation which would significantly over-estimate the lift and induced drag at high angles of attack

where insects are known to operate. Additionally, other relevant aerodynamic phenomena such as wake periodicity were not included.

The aim of this chapter is to provide a convenient theoretical treatment for evaluating the aerodynamics of insect-like wings in the translational phase of the flapping cycle. This work builds on the foundation laid in Chapters 3 and 4 which establishes a compact transparent formulation for the quasi-steady aerodynamics of hovering. The contribution of this chapter lies in the novel reformulation of the LLT for application to estimating the translational forces for hovering wings and the subsequent insight that this brings to the flow physics. In particular, the modelling approach allows unique insight into the relative contribution of induced and profile drag for flapping wings; something that is currently missing in the available literature. Whilst the present contribution only considers quasi-steady effects, there is a logical path to include rotational and added mass effects as model extensions using the method discussed in Section 4.2.3.3 that would enable capturing aerodynamic time history effects if required.

5.2 The Lifting Line Model

5.2.1 Basic assumptions

The lifting line theory assumes a fluid that is incompressible and inviscid. Compressibility effects are negligible for application areas of interest. With regard to viscous effects, recent experimental measurements [142] have demonstrated that insect-like flapping wing aerodynamics depends only very weakly on Reynolds number (see Section 3.4.1), and numerical studies [169] demonstrated that the flows are well modelled by the inviscid Euler equations. Nevertheless, and following the general practice within the LLT, the Reynolds number effect is taken into account in the two dimensional properties of the wing section represented through the section lift curve slope.

The wing is assumed to be an infinitesimally thin and un-cambered rigid flat plate with zero spanwise twist and zero sweep. Wing twist about a spanwise axis can be included as an alteration to the wing geometric angle of attack.

The lifting line theory is valid as long as the Kutta condition is satisfied, and in general this will be the case if there is an absence of classical wing stall [201]. For the current problem, the formation of a leading-edge vortex (LEV) on the wing top surface

prevents classical wing stall as discussed comprehensively in the previous chapter: the LEV is stable in the sense that it does not shed as the wing motion progresses, and allows the flow over the upper surface of the wing to separate at the leading edge but subsequently reattach upstream of the trailing edge. The Kutta condition is therefore established at the trailing edge at angles of attack beyond which classical stall would occur for wings where no LEV is present [148,212,213].

Other secondary aerodynamic effects from wing pronation and supination as well as the wing-wing interactions (clap-and-fling) are not included in the current model. Thus the current modelling treatment is consistent with the well known 'revolving wing' concept which captures the quasi-steady aerodynamics between stroke reversals.

5.2.2 LLT fundamental equations

The wing is modelled as a vortex of strength $\Gamma(r)$ bound to the aerodynamic centre. The goal is to determine $\Gamma(r)$ as a function of the wing geometric properties. The Kutta-Joukowski theorem is used to obtain the lift per unit span [133,135]

$$dL(r) = \rho U(r)\Gamma(r)dr = \frac{1}{2}\rho\left(U(r)\right)^2 c(r)drC_{l\alpha,2d}\left(\alpha_g - \alpha_i(r)\right), \tag{5.1}$$

where ρ is the air density, $U(r)$ is the sectional flow speed along the wing length, r is wing radial position measured from the wing root, c is the chord, $C_{l\alpha,2d}$ is the 2d-aerofoil lift curve slope, α_g is the wing geometric angle of attack and α_i is the induced angle of attack. Thus $\Gamma(r)$ is obtained as

$$\Gamma(r) = \frac{1}{2}c(r)C_{l\alpha,2d}\left(U(r)\alpha_g - w(r)\right), \tag{5.2}$$

where $w(r)$ is the induced downwash velocity distribution along the wing length determined by [135]

$$w(\breve{r}) = \frac{1}{4\pi}\int_{-R}^{R}\frac{d\Gamma}{dr}\frac{dr}{\breve{r}-r}, \tag{5.3}$$

where $\breve{r}$ is the wing station at which the downwash is calculated, and r is the location of vortices responsible for the downwash.

Equation 5.2 represents Prandtl's fundamental lifting line equation. Note that Equation 5.2 was already introduced in Chapter 3 where it was sufficient to calculate

the shape of the downwash distribution and thus the value of k_{ind}. However, to apply it for the calculation of lift and induced drag coefficients of insect-like wings in hover, it is rewritten here as

$$\Gamma(r) = \frac{1}{2} c(r) C_{l\alpha,2d,ef} \left(V(r)\alpha_{eq} - w_{ef}(r) \right). \tag{5.4}$$

The above equation represents the basis for the developed lifting line theory for hovering wings which, in the present work, will be referred to as LLT_{hw}. Three main adaptations are introduced in Equation 5.4. These correct for (1) non-linear aerodynamics of the lift curve, (2) non-ideal induced downwash effects, and (3) planform effects on the 2d lift curve slope. Each of these corrections is now considered in detail.

5.2.3 Adapting the LLT for non-linear aerodynamics

The primary adaptation introduced here to the classical LLT is the introduction of the concept '*equivalent angle of attack*' to account for non-linearity in the wing lift curve. This *equivalent angle*, α_{eq}, is defined as *the geometric angle of attack within the linear aerodynamic representation that will provide the same lift coefficient of the 3d wing within a non-linear aerodynamic representation*. The original LLT formulation assumes a linear lift curve for the wing; i.e. the 3d wing lift coefficient is proportional to the geometric angle of attack

$$C_L \propto \alpha_g . \tag{5.5}$$

However, for an insect-like wing in hover, the lift coefficient increases to a maximum at a geometric angle of attack of 45 degrees and then decreases back to zero at a 90 degrees angle of attack. As discussed in Chapter 4, it has been shown that this behaviour can be adequately represented by the trigonometric relationship

$$C_L \propto \sin\alpha_g \cos\alpha_g . \tag{5.6}$$

Experiments on revolving and flapping wings [134] show that despite its simplicity the function $\sin\alpha_g \cos\alpha_g$ provides an excellent representation of the variation of the measured steady lift coefficient with geometric angle of attack. The physical foundation of the $\sin\alpha_g \cos\alpha_g$ variation is based on the assumption that pressure forces dominate

over skin friction forces for this type of flow, hence the magnitude of the normal force is proportional to $\sin\alpha_g$ (see Chapter 4 for more details on the physical foundations). By comparison of Equations 5.5 and 5.6, an equivalent angle of attack expression can be derived as

$$\alpha_{eq} = C_{\alpha_g}\alpha_g\,, \tag{5.7}$$

where

$$C_{\alpha_g} = \sin\alpha_g \cos\alpha_g / \alpha_g\,. \tag{5.8}$$

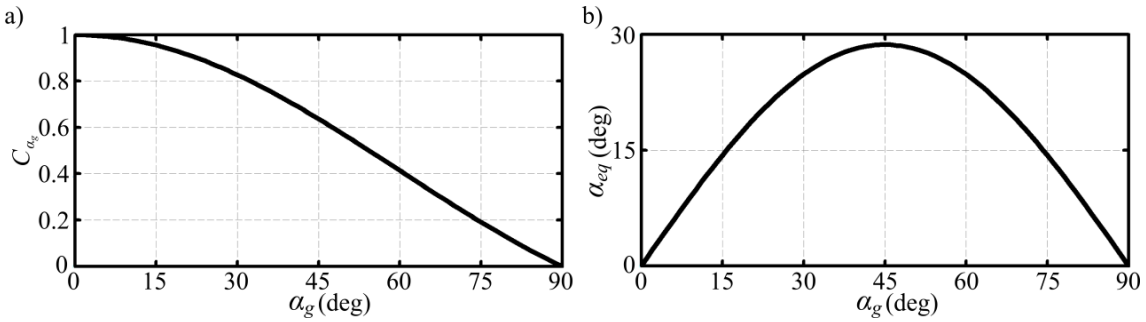

Figure 5.1 Variation of (a) the correction term, and (b) the equivalent angle attack against the geometric angle of attack.

Figure 5.1 shows the correction term, C_{α_g}, and the equivalent angle of attack variations against the geometric angle attack. The maximum lift coefficient at a 45 degrees geometric angle of attack is achieved with a 29 degrees equivalent geometric angle of attack within the linear aerodynamics representation. At small angles of attack ($\alpha_g \leq 15^\circ$), the equivalent angle of attack is almost equal to the geometric angle of attack meaning that the LLT_{hw} converges to the original LLT at low angles of attack. On the other hand, at very high angles of attack ($\alpha_g \to 90^\circ$) the equivalent angle of attack reduces back towards zero as required by basic geometric considerations.

By applying the above adaptation within the LLT expressions, the quasi-steady non-linear lift curve behaviour essential to the insect-like flapping wing problem is well captured. An important aspect of this proposed technique is that no alterations to the fundamental LLT equations are required, and the underlying physics of the LLT is well preserved. Whilst the concept of the equivalent angle of attack is quite simple and

appears as an obvious approach to handle the problem, it has not been attempted before either within the context of hovering insect-like wing problem or within any other non-linear aerodynamic treatment of a lifting surface. The proposed adaptation has some similarities with the well known Prandtl-Glauert compressibility transformation [207] which allows solution of compressible flow problems using incompressible-flow calculation methods. The proposed LLT transformation allows solution of non-linear aerodynamic problems using linear aerodynamic calculation methods by applying linear aerodynamic methodologies to non-linear aerodynamic cases. It is believed that the proposed technique also opens the door for solution of other 3d lifting surface problems with non-linear aerodynamic behaviour.

5.2.4 Adapting the LLT for non-ideal induced downwash effects

The second adaptation applied here is to account for non-ideal but physical effects that influence the downwash magnitude of the wing, including wake periodicity and effective flapping disk area. These effects are absent for fixed wings but must be considered for flapping wings as shown in Chapter 3. In Chapter 3, a more formal derivation of these effects based on the method of Stepniewski and Keys [130] was presented. Here an alternative route, but with the same end outcome, to the modelling of wake periodicity and effective flapping disk area effects is presented.

Consider the actuator disk theory expression for the induced velocity magnitude in hover

$$w = k_{ind}\sqrt{\frac{L}{2\rho S_{d,ef}}}\,, \tag{5.9}$$

where k_{ind} accounts for the non-uniformity in the downwash and is already accounted for in the lifting line formulation. However, the other two effects (i.e. wake periodicity and effective flapping disk area) associated with flapping flight which are directly related to the downwash need to be included in the lifting line formulation. Here, these effects are explained through their effect on the effective disk area, $S_{d,ef}$. For flapping flight, the disk area is defined as [122]

$$S_{d,\,flap} = 2\phi R^2\,, \tag{5.10}$$

where ϕ is the amplitude of the flapping stroke angle; however, to obtain an expression for $S_{d,ef}$, a further modification is implemented as

$$S_{d,ef} = 2\phi R_{ef}^2 . \tag{5.11}$$

The correction of R to R_{ef} is to account for the aerodynamic phenomena of wing tip losses due to discreteness and periodicity in the wake (see Figure 3.1). Now, by simple factorisation, the downwash expression (Equation 5.9) can be written as

$$w = k_{ind}\sqrt{\frac{L}{2\rho S_{d,ef}}} = k_{ind}\sqrt{\frac{L}{2\rho\pi R^2(2\phi/\pi)B^2}} = k_{ind}k_{per}k_{flap}\sqrt{\frac{L}{2\rho\pi R^2}} , \tag{5.12}$$

where,

$$k_{per} = \frac{1}{B} = \frac{R}{R_{ef}} , \tag{5.13}$$

$$k_{flap} = \sqrt{\frac{\pi}{2\phi}} . \tag{5.14}$$

Which are consistent with the results obtained in Section 3.2.1. That is, the overall downwash magnitude is increased due to the additional factor $k_{per}k_{flap}$ compared to the case with no assumed wake periodicity effects and with the wing sweeping the whole circular disk area, i.e. $R = R_{ef}$ and $2\phi = \pi$. Thus, from this simple momentum theory analysis, it can be seen that in the presence of these additional non-ideal effects a flapping wing has an overall induced velocity increased by the factor $k_{per}k_{flap}$. This lead to the development of the effective downwash definition in Equation 5.4 to account for these effects

$$w_{ef}(\breve{r}) = \frac{k_{per}k_{flap}}{4\pi}\int_{-R}^{R}\frac{d\Gamma}{dr}\frac{dr}{\breve{r}-r} . \tag{5.15}$$

In Chapter 3, numerical evaluations of the k_{per} and the k_{flap} parameters were presented for eight insect species. It was found that the value of k_{per} is clustered around 1.1; therefore without losing generality, this value will be used throughout this chapter. On the other hand, the value of k_{flap} varies considerably between different insects and thus insect specific values must be used.

5.2.5 Correcting the 2d aerofoil lift curve slope

The final amendment to the LLT presented here is based on a well known correction to the 2d aerofoil lift curve slope originally proposed by Jones and usually referred to as the Jones edge-velocity correction [136,185,186]. Jones incorporated his correction into the 2d aerofoil lift curve slope leading to the concept of the effective 2d lift curve slope [186]

$$C_{l\alpha,2d,ef} = \frac{C_{l\alpha,2d}}{E}, \tag{5.16}$$

where E is the Jones correction evaluated as the ratio of the wing semi-perimeter to the wing length. Thus the effective lift curve slope can be dealt with as a characteristic of the wing planform as well as the wing section [186]. This correction is most pronounced for wings with low aspect ratios, and as discussed in Section 5.1 Jones showed that by applying his correction the LLT becomes capable of capturing low aspect ratio effects.

Following Ellington [141], the wing chord distribution is defined through a beta function representation as discussed in Section 3.3.2. Insect wings typically have aspect ratios ranging from 2.5 to 6 [141,214], thus for the low aspect ratio cases the Jones correction is relevant. Figure 5.2 shows the variation of the Jones correction factor, E, for different combinations of the wing aspect ratio ($AR = R/\bar{c}$) and area centroid location.

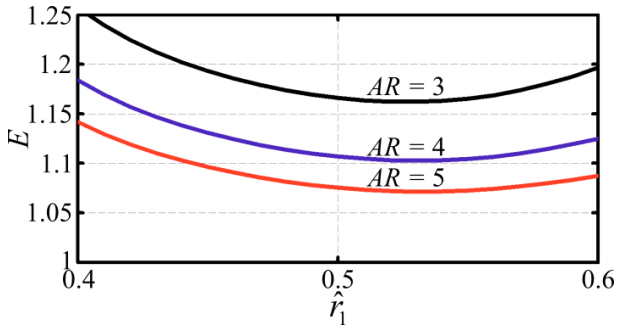

Figure 5.2 Variation of the Jones edge correction factor, E, for different combinations of wing aspect ratio and area centroid location. The wing planform is represented through the beta formulation for $\hat{r}_1$ values from 0.4 to 0.6 which is representative of the range found in nature. In this illustration, the wing is symmetric about the mid-chord.

The remaining unknown in Equation 2.16 is the 2d aerofoil lift curve slope, $C_{l\alpha,2d}$. As shown in previous chapters, for a flat plate at low Reynolds numbers, experimental

evidence suggests that $C_{l\alpha,2d}$ is less than the theoretical value of 2π and can be given a value of 0.09 deg^{-1} = 5.15 rad^{-1} [137,139,184,195].

5.2.6 Solution methodology

Having introduced the essential adaptations to the LLT, Equation 5.4 is now solved using the well-known Glauert method [1,135]. First, the wing spanwise location is substituted with [135]

$$r = -R\cos\psi\,, \tag{5.17}$$

where ψ is a generic parameter used to define position along the wing. Given the symmetry of the problem, only the starboard wing is considered and thus ψ varies from 0 to $\pi/2$. The circulation, $\Gamma(r)$, is then expressed as a sine Fourier series as [135]

$$\Gamma(r) = 4RU(r)\sum_{m=1}^{\infty} a_m \sin m\psi\,, \tag{5.18}$$

where the velocity along the wing length is given by the linear variation

$$U(r) = \dot{\phi}r = -\dot{\phi}R\cos\psi = -U_{tip}\cos\psi\,. \tag{5.19}$$

Substituting Equation 5.18 into Equation 5.15 and integration using the Glauert integrals [138,1] leads to an expression for the effective downwash as a function of the radial position

$$w_{ef}(r) = -k_{per}k_{flap}U_{tip}\sum_{m=1}^{\infty}\left(ma_m\frac{\cos\psi\sin m\psi}{\sin\psi}\psi + a_m\cos m\psi\right). \tag{5.20}$$

The a_m coefficients in the above equation can be obtained using the Glauert approach by equating Equations 5.4 and 5.18 leading to

$$\begin{aligned}\mu_{ef}\alpha_{eq}\sin\psi\cos\psi = {} & \sum_{m=1}^{\infty} a_m \sin\psi\cos\psi\sin m\psi + \\ & \mu_{ef}k_{per}k_{flap}\sum_{m=1}^{\infty}\left(a_m\sin\psi\cos m\psi + ma_m\cos\psi\sin m\psi\right)\end{aligned}\,, \tag{5.21}$$

where

$$\mu_{ef} = \frac{c(r)C_{l\alpha,2d,ef}}{8R}. \tag{5.22}$$

Note that the above expressions are similar to those presented in Section 3.2.2; however, the effect of advance ratio is removed and the corrections introduced in this chapter are added. Again following the conventional lifting line solution approach, only the odd terms of m are considered due to problem symmetry. The series is then truncated to a finite series and the a_m coefficients are obtained by solving the set of simultaneous linear equations obtained from satisfying Equation 5.21 at a convenient number of wing stations equal to the number of terms in the series. Finally, the lift and induced drag forces can be obtained from

$$L = 2\int_0^R \rho U(r)\Gamma(r)dr, \tag{5.23}$$

$$D_i = 2\int_0^R \rho w_{ef}(r)\Gamma(r)dr. \tag{5.24}$$

Thus, the lift and induced drag coefficients are obtained as

$$C_L = \frac{2L}{\rho U_{tip}^2 \hat{r}_2^2 (2R\bar{c})}, \tag{5.25}$$

$$C_{D_i} = \frac{2D_i}{\rho U_{tip}^2 \hat{r}_2^2 (2R\bar{c})}. \tag{5.26}$$

Note that in the above equations, the lift and drag forces are non-dimensionalised using the dynamic pressure at the wing radius of the second moment of wing area.

5.3 Results and Discussion

5.3.1 Comparison with revolving wing experimental measurements

The revolving wing experiment was introduced in Section 4.3.1 as a well-known measurement technique employed for insect wing aerodynamic characterisation [142,146,147,215-218]. The wing is rotated in the fashion of a simple propeller blade to simulate a continuous down (or up) stroke that excludes the effects that occur at stroke reversal such as wing flipping and wing-wing interactions. In this section, the developed LLT_{hw} is compared to available experimental measurements from revolving wing experiments. Because there are no measurements available for induced drag, only lift

coefficient data will be compared here. Although revolving wing experiments have been conducted for different species, the wings used in each case are in close morphological similarity. Thus, the available data does not allow a full validation of the LLT_{hw} against a wide range of planforms. In what follows the LLT_{hw} is compared to three sets of available experimental data for an insect, a bird and a hummingbird. It is worth mentioning that compared to Chapter 4 results, two more experimental results of revolving wings are presented here. This is just to show further possible comparisons and it should be mentioned that the LLT_{hw} results compares well to the previously demonstrated revolving wing experiments including the bumble bee and fruit fly.

Table 5.1 Morphological parameters of revolving wings.

Wing	*AR*	$\hat{r}_2$	$\hat{r}_1$ (Eqn. 3.38)	Reynolds number
Hawkmoth [146]	2.83	0.511	0.44	8,071
Pigeon [216]	3.21	0.512	0.443	54,000
Hummingbird [218]	4.06	0.499	0.43	9,800

Usherwood and Ellington [146] provided steady lift coefficient measurements against the geometric angle of attack for a hawkmoth model wing. Later, Usherwood [216] provided similar measurements for pigeon wings at higher Reynolds number. Recently, Kruyt *et al*. [218] provided measurements for hummingbird wings which they argue are more precise than previous measurements [e.g. 217]. Note that the hummingbird case is based on measuring a real wing; thus, wing compliance is not fully controlled especially at very high angles of attack [218] and thus the geometric angle of attack has significant uncertainty. Nevertheless, this test case remains useful for comparison against the developed LLT_{hw} especially in the normal operation range of angles of attack (i.e $\alpha_g < 45^{\circ}$). The morphological parameters of these three wings are provided in Table 5.1; these parameters were used as inputs within the LLT_{hw} to calculate the lift coefficient variation with the geometric angle of attack and results are compared in Figure 5.3. Within the calculation of the three cases, the value of k_{per} was set to 1.1 whereas by definition the k_{flap} for a revolving wing is unity.

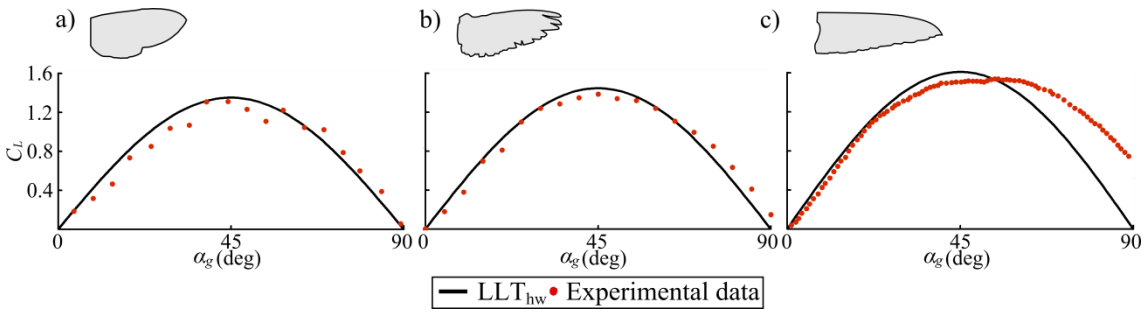

Figure 5.3 Lift coefficient variation with geometric angle of attack. Results evaluated using the LLT_{hw} are compared to available experimental measurements for (a) hawkmoth; experimental data adapted from Figure 6 of reference [146], (b) pigeon; experimental data adapted from Figure 3A of reference [216] and (c) hummingbird; experimental data adapted from Figure 6A of reference [218]; for this case, experimental data beyond 45° are affected by the wing compliance, and the setup dynamics may have influenced the obtained measurements [218].

The results shown in Figure 5.3 show a good agreement with the experimental measurements in both form and amplitude for the three cases considered. Note that the shape of variation of the lift coefficient with angle of attack is a consequence of the proposed definition of the *equivalent angle of attack* which implicitly ensures a sin 2α shape of variation (see Figure 5.1b). Of more relevance is the good agreement in the amplitudes of the lift coefficient over the whole first quadrant of angle of attack.

Now the LLT_{hw} is used to evaluate the maximum lift coefficient amplitude (C_L at $\alpha_g = 45^\circ$) for revolving wings within a range of aspect ratios and chord distributions similar to real insect wings, Figure 5.4. As expected, the value of the maximum lift coefficient increases as the aspect ratio increases; however, this result must be considered with some caution as an increase in the wing aspect ratio also reduces the chord with respect to the LEV size [143]. Thus, the lift coefficient amplitude increase will stop at some critical point (whose prediction is beyond the capability of the current model) when the LEV size to chord ratio approaches the vortex attachment limit and stall features become significant. Another important result from Figure 5.4 is that the maximum lift coefficient value decreases as the wing area centroid is shifted towards the tip, despite the fact that having more area towards the tip produces a greater lift force, everything else being equal. Thus, whilst a higher lift force is achieved by having more area towards the tip, a higher lift coefficient is achieved in hovering flight by having more wing area towards the root.

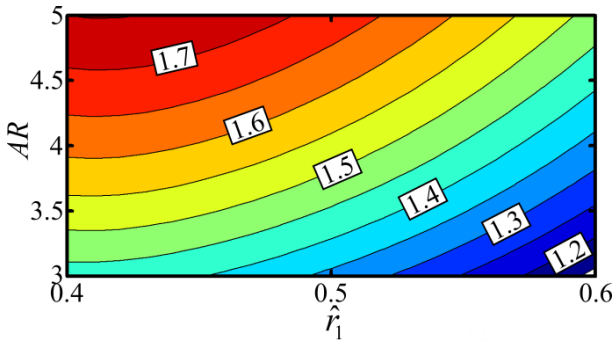

Figure 5.4 Contours of maximum lift coefficient amplitude against wing aspect ratio and wing area centroid location. The range of values for the aspect ratio and area centroid location were chosen to represent realistic limits for insect wings. In this illustration the value of k_{per} is set to 1.1 whereas k_{flap} is unity.

5.3.2 Application of the LLT_{hw} to insect wings in symmetric normal hovering flight

In this section, the LLT_{hw} is verified against the CFD results from Sun and Du [145] that provide comprehensive simulations for a variety of wing shapes operating at different conditions. In their simulations Sun and Du used a horizontal stroke plane, symmetrical half strokes and a sinusoidal-like variation of flapping angle, Figure 5.5. The geometric angle of attack was prescribed such that it takes a constant value, $\alpha_{g,mid}$, along a half stroke and then performs a smooth sinusoidal variation around stoke reversal similar to that shown in Figure 5.5. Because the flapping cycle half-strokes are symmetrical, only the variation within the down-stroke is shown. Note that the symmetry of the half-stroke also implies that the net mean forces due to rotational and added mass effects are zero [134,176,213], and only forces due to wing translation contribute to the net mean force production. Table 5.2 reviews the main aerodynamic results from Sun and Du. The mass, wing geometrical data and motion kinematic data used to obtain these results were previously presented in Table 3.1.

Table 5.2 Summary of the main aerodynamic results from the Sun and Du CFD simulations [145]. Abbreviations stand for honey bee, dronefly, bumble bee, hoverfly, cranefly, hawkmoth, ladybird and fruit fly respectively. Insects ordered by increasing angle of attack.

Insect	HB	DF	BB	HF	CF	HM	LB	FF
$\alpha_{g,mid}$ (deg.)	25	26	28	29	30	32	43	44
$\overline{L}/W$	1	1	1	1	1	1	1	1
$\overline{P}/mass$ (W.kg^{-1})	41	32	42	27	16	33	28	30

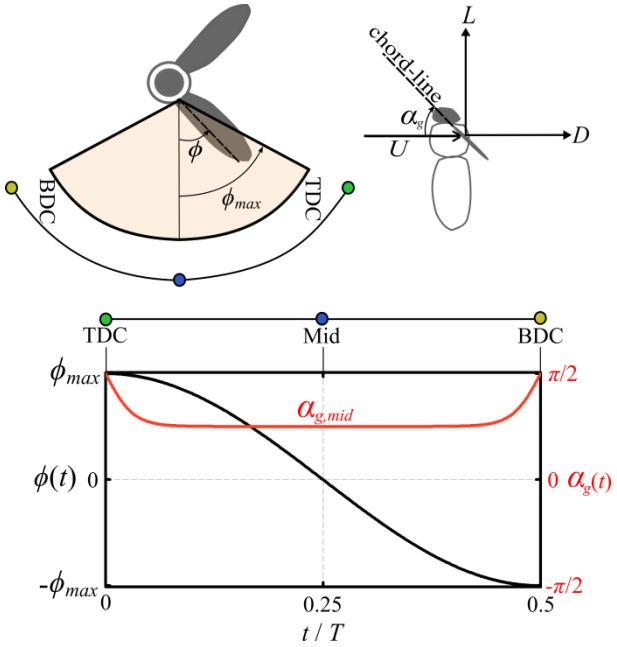

Figure 5.5 Kinematics variation similar to those employed by Sun and Du [145]. Owing to the symmetry of half-strokes, only the down-stroke period is shown. TDC is the cycle top dead centre, BDC is the cycle bottom dead centre and Mid denotes the Mid-half stroke.

The main output of the Sun and Du simulations are the calculated values of the mid-stroke geometric angle of attack, $\alpha_{g,mid}$ that would provide weight support (supplied in Table 5.2). Here, these $\alpha_{g,mid}$ values are used to calculate the mean lift force. Table 5.3 presents the mean lift to weight ratio obtained from the current lifting line theory for the different levels of adaptations employed. The purpose of showing the results for different adaptations is to demonstrate the transparency of the current framework and provide a deeper insight into how these adaptations affect the solution, thus providing more fundamental understanding of the physics of the problem. For example, results are most sensitive to the inclusion of E for wings of lower aspect ratios such as for the hawkmoth case. Also, the k_{flap} value becomes a significant effect when the flapping stroke angle is relatively low as in the hoverfly case; whereas for a case such as the ladybird where the wings scan all the possible area, this effect is negligible. However, the most significant adaption is the inclusion of the non-linear lift curve, which accounts for more than half of the overestimation in the average mean lift to weight ratio. This correction is most significant for the ladybird and the fruit fly, which have higher operating $\alpha_{g,mid}$ values and thus non-linear effects are more pronounced.

Table 5.3 Mean lift to weight ratio calculated from the LLT_{hw} for different adaptations.

Insect	Linear aero k_{per} excluded k_{flap} excluded E excluded	Nonlinear aero k_{per} excluded k_{flap} excluded E excluded	Nonlinear aero k_{per} included k_{flap} excluded E excluded	Nonlinear aero k_{per} included k_{flap} included E excluded	Nonlinear aero k_{per} included k_{flap} included E included
HB	1.53	1.34	1.29	1.20	1.11
DF	1.72	1.48	1.43	1.29	1.20
BB	1.54	1.30	1.25	1.14	1.05
HF	1.44	1.20	1.16	1.01	0.96
CF	1.71	1.40	1.36	1.27	1.22
HM	1.44	1.16	1.11	1.02	0.92
LB	1.64	1.09	1.05	1.04	0.96
FF	1.72	1.07	1.02	0.98	0.90
Average ± s.d.	1.6 ± 0.12	1.26 ± 0.15	1.21 ± 0.15	1.12 ± 0.12	1.04 ± 0.12

It can be seen from the results shown in Table 5.3 that without including any of the adaptations, the original LLT will always overestimate the lift produced with an average error of +60% for the eight insects. On the other hand, by applying the proposed adaptations, the developed LLT_{hw} formulation is able to predict the mean lift to weight ratio with an average error of 4% compared to the higher order CFD simulations, Figure 5.6a.

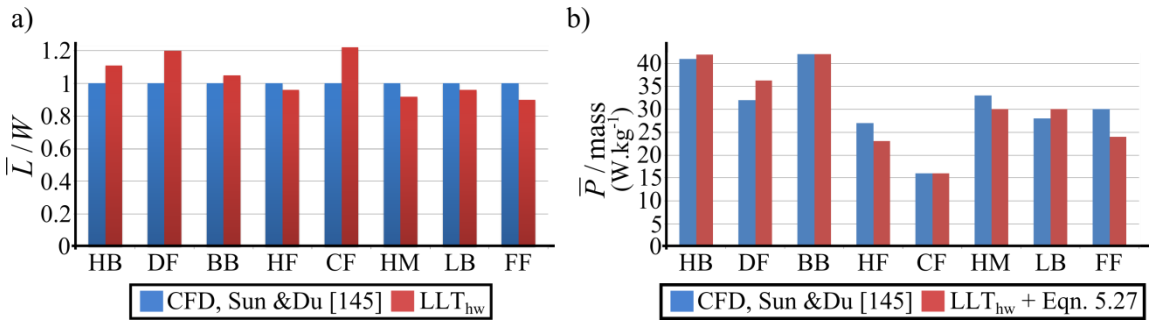

Figure 5.6 Comparison of the aerodynamic performance of eight hovering insects from the developed LLT_{hw} against CFD results from Sun and Du [145]; (a) lift to weight ratio and (b) specific aerodynamic power.

The mean lift to weight ratios obtained from the current model confirm that it is not necessary to account for unsteadiness due to the Wagner effect (indeed, most insect wing aerodynamics predictive models have neglected the Wagner effect, but see models of references [163,219,220]). Sane [148] has tackled this point comprehensively, and using the available experimental evidence he has discussed the lack of influence of the Wagner effect compared to other unsteady effects such as rotational and added mass

effects. Nevertheless, Taha *et al*. [220] showed that incorporating unsteady treatments allows better capture of the force time history near stroke reversals. Thus including an unsteady treatment for the quasi-steady models including rotational and added mass effects may improve their predictive capabilities for unsymmetrical half-strokes where rotational effects can be used for control and manoeuvrability [146,220].

The total drag comprises the induced drag and profile drag containing the effects of skin friction and pressure drag of the wings. As discussed in previous chapters, experiments on insect-like wings in simulated hovering flight showed that the skin friction component is negligible, especially at the relatively higher Reynolds numbers ($O(10^3)$ or higher) [142,146,154]. Thus, with the assumption of zero tangential friction forces, the total drag coefficient can be estimated for an infinitesimally thin flat plat using

$$C_D = C_L \tan\alpha_g , \tag{5.27}$$

which was formally introduced in Chapter 4; however, here the wing lift coefficient, C_L, will be obtained from the developed LLT_{hw}. The specific aerodynamic power expenditure for the eight insects based on Equation 5.27 is shown in Figure 5.6b, and a very good agreement is observed compared to the CFD results.

Table 5.4 Aerodynamic characteristics calculated from the current LLT_{hw}. Insects re-ordered by increasing angle of attack obtained from the LLT_{hw}.

Insect	$\alpha_{g,mid}$ (deg.)	$\bar{L}/W$	$C_L\big\|_{\alpha_{g,mid}}$	$C_{D_i}\big\|_{\alpha_{g,mid}}$	$C_D\big\|_{\alpha_{g,mid}}$	$\frac{C_L}{C_D}\big\|_{\alpha_{g,mid}}$	$\frac{C_L^{3/2}}{C_D}\big\|_{\alpha_{g,mid}}$	$\frac{C_{D_i}}{C_D}\big\|_{\alpha_{g,mid}}$	$\frac{\bar{C}_{D_i}}{\bar{C}_D}$
DF	20.5	1	0.89	0.12	0.33	2.67	2.52	0.35	0.24
HB	22	1	0.90	0.13	0.36	2.48	2.35	0.36	0.25
CF	22.5	1	1.07	0.14	0.44	2.41	2.50	0.31	0.22
BB	26	1	1.02	0.17	0.50	2.04	2.06	0.34	0.25
HF	31	1	1.19	0.22	0.72	1.66	1.82	0.31	0.24
HM	38	1	1.22	0.25	0.95	1.28	1.41	0.26	0.21
LB	45	0.96	1.47	0.26	1.47	1.00	1.21	0.17	0.14
FF	45	0.902	1.20	0.27	1.20	1.00	1.10	0.22	0.18

Predictions of the induced drag can be made directly from the developed LLT_{hw}, and Table 5.4 provides explicit analytical results of the ratio of the induced drag to the total drag. Both the mid half-stroke value as well as the mean flapping cycle value are provided for the induced to total drag ratio. In this demonstration it was more

convenient to recalculate the mid-stroke geometric angle of attack, $\alpha_{g,mid}$ that would provide weight support based on the developed LLT_{hw}. These $\alpha_{g,mid}$ values are then used to evaluate the aerodynamic quantities in Table 5.4. Note that for the cases of the fruit fly and the ladybird operation at 45 degrees geometric angle of attack leads to a slightly sub-unity value of the weight support ratio for the given kinematics and wing morphology parameters in Table 3.1. However, an alteration of the ϕ_{max} value by only a few degrees can correct for this if required.

On average for the eight insects, the induced drag is shown to contribute 22% of the total drag based on the mean cycle values and 29% of the total drag based on the mid half-stroke values (Note that the mean cycle values are directly related to the assumed motion kinematic profiles in Figure 5.5). For insects operating with high mid-stroke angles of attack (such as the ladybird and the fruit fly) this ratio decreases below 20% for the mean cycle values which is consistent with the expected prevalence of profile drag as the angle of attack increases.

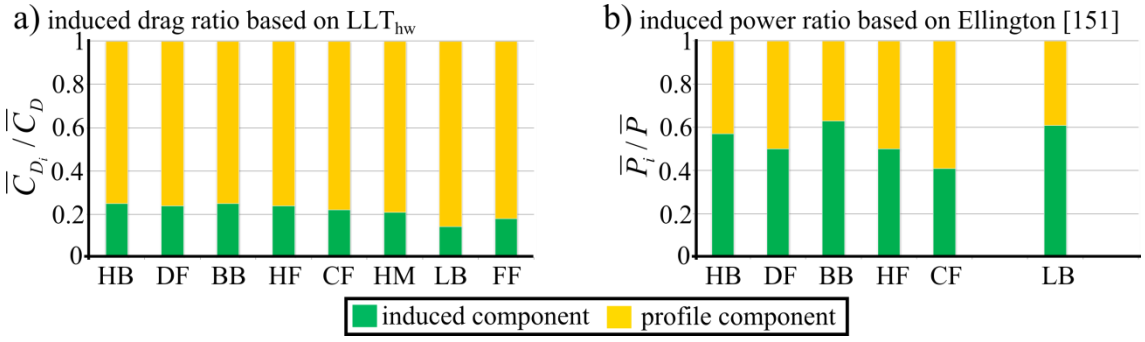

Figure 5.7 Demonstration of (a) the ratio of the induced drag to total drag based on the LLT_{hw}, and (b) the ratio of the induced power to the total aerodynamic power based on Ellington's calculations in [151].

The results in Table 5.4 show that the ratio of induced to profile component is overestimated when employing Ellington's approach [151], Figure 5.7. Ellington analysed some hovering insects including the ladybird, cranefly, hoverfly, dronefly, honey bee and bumble bee based on measured kinematics and low order methods for evaluating the aerodynamic power, Figure 5.7b. Based on an average for the considered insects, the ratio of the induced power to the total aerodynamic power was around 0.5. However, the induced power prediction in [151] was based on the Rankine-Froude estimate multiplied by the induced power factor value which had an average value of 1.15 for the considered insects, a value that was shown to be underestimating the

induced power factor of normal hovering flyers [188,221]. Furthermore, the profile power was evaluated based on a low order expression of the profile drag coefficient, $C_{D_{pro}} = 7\,\mathrm{Re}^{-1/2}$, an expression based on flow past a cylinder [222]. Whilst this expression was shown to be working at low angles of attack, it becomes unreasonable at high angles of attack.

The obtained drag results confirm that for better aerodynamic efficiency, wings should operate at lower geometric angles of attack. This can be confirmed from the two important aerodynamic performance indices: *glide number*, C_L / C_D (*GN*) and the *power factor* $C_L^{3/2} / C_D$ (*PF*) whose values generally decrease as the operational mid-stroke geometric angle of attack increases. Whilst these indices are affected by other parameters and/or variables such as those defining the wing morphology and kinematics, it is clear that the geometric angle of attack value is the parameter that has the greatest influence. The values obtained for these indices are consistent with those obtained from experimental measurements of insect-like hovering wings [142], which are very low compared to fixed wing figures mainly due to the much higher drag associated with the flapping mode of flight.

5.4 Chapter Conclusions

A novel lifting line formulation, $\mathrm{LLT_{hw}}$, has been proposed for the quasi-steady aerodynamic evaluation of insect-like wings in hovering flight. The developed modelling capability provides a framework to adapt the original LLT for hovering flight and opens the door for simplified yet accurate modelling of 3d lifting surfaces at different operating conditions. The fully theoretical framework allows accurate estimation of the aerodynamics of insect-like wings from geometry and kinematic information alone, as well as providing deeper understanding of the associated aerodynamics in terms of the induced and profile drag associated with the lift production.

The main adaptation proposed is the introduction of the concept of the equivalent angle of attack, which enables the linear aerodynamic LLT formulation to capture the steady non-linear aerodynamics of wings at high angles of attack using a simple analytical correction term. Additionally, a simplified methodology to include a number of non-ideal induced effects within the lifting line theory has been presented. These

non-ideal effects are necessary to correctly represent the flapping wing physics, including wake periodicity effects due to discreteness in the wake as well as the effective actuator disk area effect. Finally, low Reynolds number effects as well as the well-known edge velocity correction that improves the LLT performance for various wing planform shapes has been incorporated within the 2d lift curve slope value.

The developed LLT_{hw} has been validated against available measurements from revolving wing experiments for hawkmoth, pigeon and hummingbird wings, and shows very good agreement with respect to both the shape of variation of the lift coefficient with incidence as well as the magnitude. Comparison of the results obtained from the LLT_{hw} and higher order CFD simulations shows that the developed methodology can be judged as a powerful predictive tool for the preliminary evaluation of insect wing aerodynamic performance. The mean lift to weight ratio results are on average within +4% of the available CFD results for eight insect cases. The developed model has been used to assess the relative impact of the proposed adaptations on the LLT for the investigated insects. Excluding these adaptations leads on average to a 60% over estimation in the mean lift force required for weight support, and that most of this discrepancy is due to the non-linear lift curve effect. The developed model also provides explicit evaluation of the induced drag component of insect wings. It is shown that on average for the eight insects considered, the induced drag contributes 22% of the total drag based on the mean cycle values and 29% of the total drag based on the mid half-stroke values.

6

Optimum Revolving Wing Planform

In this chapter, a novel theoretical solution is introduced for the optimum planform for wings used to provide weight support by continuous or reciprocating rotation in a stationary fluid. This solution is of interest as a benchmark to which hovering wing geometries driven by broader multidisciplinary engineering or evolutionary constraints can be compared. Whilst there are some clear practical differences between continuous rotary (revolving) and reciprocating rotary (flapping) wing motions, the aerodynamic behaviour for the reciprocating rotary motion is fundamentally the same as for continuous rotation apart from wake capture and stroke reversal effects, which are of a secondary nature compared to the steady aerodynamics. For brevity and following insect flight aerodynamic literature, in this chapter wings performing continuous rotary motion or within the steady translational phase of the reciprocating rotary motion are referred to as 'revolving wings'.

6.1 Introduction

From a design perspective, it is of relevance to identify optimum wing geometries for hovering air vehicles. Additionally, there has been an argument that for flapping vehicles, it is easier modifying wing geometry than wing kinematics [223]. Yet, there have not been theoretical studies to investigate the effect of wing geometry on the flapping wing aerodynamic performance evaluated in terms of the profile and induced losses associated with lift generation. Thus, the aim of this compact chapter is to provide an assessment of the aerodynamic performance of relevant wing planforms for hovering flight. The chapter starts with driving a novel theoretical solution for the optimum hovering wing in terms of chord and twist distributions that would minimise the total aerodynamic power expenditure for a given lift. Then the effect of removing the optimum twist distribution on the aerodynamic performance is examined.

6.2 Derivation of the Optimum Planform

The optimum wing is defined as a wing that will produce a given lift for the least total power required, where the power is made up from both profile and induced components [224]; consequently, for a wing to be optimum for a given amount of lift [133]:

1- Each wing section should be operated at its optimum effective angle of attack (i.e angle of attack that allows the best lift to drag characteristic of the wing section) to minimise profile power, and

2- The downwash distribution along the wing length should be uniform to minimise the induced power.

Following steady linearised aerodynamic treatments, the local wing lift coefficient, C_l, is given by

$$C_l(r) = C_{l\alpha,2d}\left(\underbrace{\alpha_g(r) - \alpha_i(r)}_{\alpha_e(r)}\right), \tag{6.1}$$

where α_g is the geometric angle of attack, α_e is the effective angle of attack and α_i is the induced angle of attack defined as

$$\alpha_i(r) \cong w(r)/U(r), \tag{6.2}$$

where *w* is the downwash velocity, *U* is the sectional flow velocity and *r* is the distance along the span from the wing root. Note that for revolving wings the 2d airfoil lift curve slope, $C_{l\alpha,2d}$, may vary with span as the local Reynolds number varies; however, the assumption of a constant average value along the wing length does not lead to any serious loss of accuracy [133].

Consider first the optimum design of a parallel translating wing (fixed wing) for which the sectional flow velocity along the wing length is constant. For an untwisted wing, minimum profile power for a given amount of lift is achieved when there is a constant effective angle of attack along the wing length equal to the angle of attack for best lift to drag ratio of the wing section. This constraint can be achieved simultaneously with the minimum induced power condition since the constant downwash required for minimum induced power also gives a constant effective angle of attack. Thus for a practical design solution, a minimum power wing can be achieved without twist by implementing an elliptic chord distribution to give minimum induced power (constant downwash) and then adjusting the wing loading such that the lift coefficient at the design operating point is equal to the lift coefficient for best lift to drag ratio.

Consider now the optimal design of a revolving wing. Here, the sectional flow velocity along the wing takes the linear form

$$U(r) = \dot{\phi} r = \dot{\phi} R \hat{r}\ ,\ \hat{r} = \frac{r}{R} \tag{6.3}$$

where $\dot{\phi}$ is the angular velocity and *R* is the length of the wing. Given Equations 6.2 and 6.3, for a revolving wing with constant downwash distribution, the induced angle of attack is hyperbolic; or alternatively, for a constant induced angle of attack, the imposed downwash distribution must be linear. Thus to achieve minimum power for a revolving wing, it is necessary to prescribe both the wing planform and the wing twist distribution.

The design process for an optimal revolving wing is as follows. First, the minimum profile power constraint is met by specifying an appropriate geometric twist distribution, $\alpha_g(r)$, to achieve a constant optimum effective angle of attack, $\alpha_{e,opt}$, for a constant downwash [133,140]

$$\alpha_g(r) = \alpha_{e,opt} + \frac{w}{\dot{\phi} r}. \tag{6.4}$$

Next the chord distribution required to achieve the constant downwash for minimum induced power is specified in terms of the circulation distribution along the wing and the lift coefficient required for the minimum profile constraint [137]

$$c(r) = \frac{2\Gamma(r)}{C_l U(r)}. \tag{6.5}$$

In the helicopter literature [133,140], the optimum chord distribution for minimum power is derived from a simple physical interpretation based on momentum theory. This model requires a constant bound circulation to produce a uniform downwash distribution [140]. From Equation 6.5, it thus follows that the optimum chord would be of a hyperbolic shape (due to the linear velocity distribution in denominator). According to the Helmholtz theorem, this uniform circulation along the wing length leads to a single vortex of the same strength trailing from each of the wing tips. This is a significant simplification of the problem and quantitative determination of finite wing aerodynamics calls for a more accurate model. Thus, it is convenient to take the problem a step further by setting the circulation strength along the wing to an elliptic distribution which from lifting line theory is known to produce a constant downwash velocity distribution [137]. Since lift and hence bound circulation falls to zero at the inboard edge of the wing and there is no carryover of lift to the opposite wing [181,213,221], Γ(r) should vary elliptically on a single blade/wing spanning along $0 \le r \le R$. Therefore, $\Gamma(r)$ is expressed as an ellipse with the centre at *R*/2 and a major axis length of *R* as follows

$$\Gamma(\hat{r}) = \Gamma_{\max} \sqrt{1 - \left(2\left(\hat{r} - \frac{1}{2}\right)\right)^2}. \tag{6.6}$$

After simple manipulation it can be shown that

$$\Gamma(\hat{r}) = 2\Gamma_{\max} \hat{r} \sqrt{\frac{1}{\hat{r}} - 1}. \tag{6.7}$$

Substituting Equations 6.3 and 6.7 into 6.5, it can be shown that the optimal chord distribution is proportional to the expression $\sqrt{\frac{1}{\hat{r}}-1}$.Thus, the optimum chord distribution for a revolving wing can be written as

$$c(\hat{r}) = \frac{2.019\bar{c}}{\pi}\sqrt{\frac{1}{\hat{r}}-1}, \tag{6.8}$$

where $\bar{c}$ is the mean geometric chord and the factor $2.019/\pi$ preceding the above expression is obtained from satisfying the condition $\int_0^1 \frac{c(\hat{r})}{\bar{c}} d\hat{r} = 1$ [141]. This optimum chord distribution is shown in Figure 6.1 together with a number of other relevant chord distributions for reference. It is noteworthy that the obtained optimal chord distribution will only produce the minimum induced losses due to the downwash distribution effect; other non-ideal induced losses sources discussed in Chapter 3 are not function of the wing planform distribution but mainly function of wing kinematics and thus are not accounted for here.

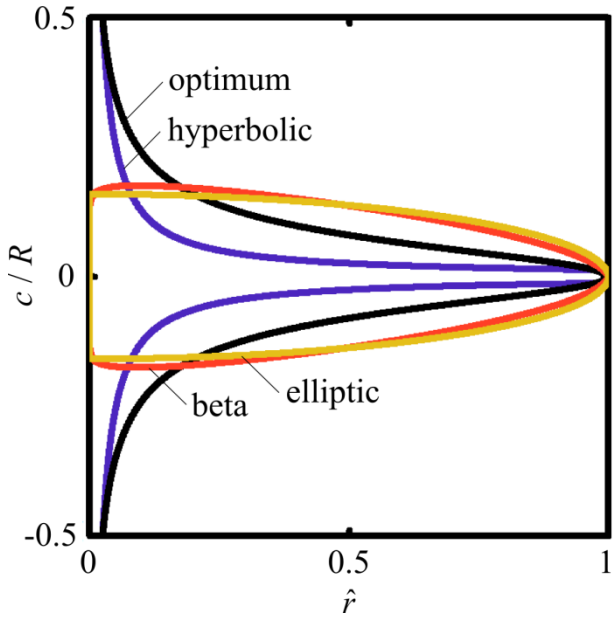

Figure 6.1 Comparison of the chord distribution for minimum power for a revolving wing against a number of reference planforms. The so-called optimum distribution (black) is the chord distribution derived in this work (Equation 6.8) and is capable of producing an elliptic circulation distribution on a revolving wing. Thus, from the lifting line theory considerations, it is able to produce a constant downwash distribution. The hyperbolic distribution (blue) produces a constant circulation distribution on a revolving wing. Within the helicopter literature, it has been referred to as the '*optimum hovering rotor*' [133,140]. The beta distribution (red) is a practical representation of an insect wing planform from biological studies [141]. In practice, it provides a good aerodynamic performance with respect to induced losses owing to the non-uniform downwash effect. The elliptic distribution (yellow) produces an elliptic circulation distribution and hence a constant downwash distribution for parallel translating wings. For untwisted revolving wings, it produces a linear downwash distribution and thus a constant induced angle of attack along the wing length. In this illustration, all wings have an aspect ratio of 4 and same length *R*.

6.3 Aerodynamic Performance of Untwisted Revolving Wing Planforms

For rotary rigid wings, it is practically feasible to implement a twist distribution along the wing length; however for a flapping wing, the forward and backward reciprocating motion implies a periodic change in sign of the implemented twist distribution which is mechanically expensive to implement, except through aeroelastic means, as in insect wings. Thus, now the effect of chord distribution only (zero twist) on the aerodynamic performance is considered. By prescribing the chord distribution only, only one of the two optimality constraints can be achieved at a time. First, the constant downwash velocity constraint (minimum induced power) is relaxed while maintaining operation at a constant optimum effective angle of attack along the wing length (minimum profile power). For an untwisted wing, a constant distribution of the effective angle of attack is

obtained when a constant induced angle of attack distribution is achieved (see Equations 6.1 and 6.2). In turn, this is obtained from a linear variation of the downwash which can be realised in hovering through the elliptic chord distribution

$$c(\hat{r}) = \frac{4\bar{c}}{\pi}\sqrt{1-\hat{r}^2}\ . \tag{6.9}$$

This shows that the elliptic chord distribution leads to a constant induced angle of attack distribution for both parallel and revolving translations; however, the constant sectional velocity distribution associated with the parallel translation motion leads in turn to a constant downwash velocity distribution and thus a unity induced power factor. On the other hand, the linear downwash distribution of the elliptic chord for a revolving wing leads to an induced power factor due to non-uniform downwash, k_{ind}, value of 1.13 (i.e. 13% more induced power compared to the ideal uniform downwash condition for a given lift [187,188]).

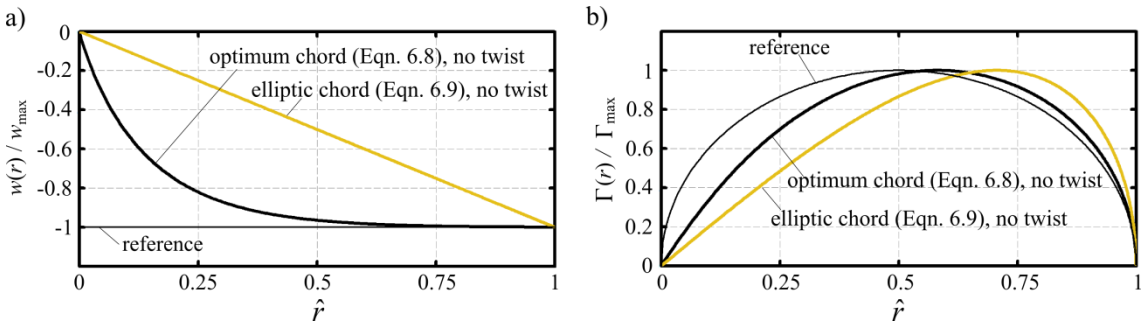

Figure 6.2 Effect of enforcing a no twist constraint on (a) downwash velocity and (b) circulation distributions for the chord distributions prescribed by Equations 6.8 and 6.9. In this illustration, the wing aspect ratio is 4 for the two chord distributions. An untwisted revolving wing with an elliptic chord distribution produces a linear downwash distribution and thus is able to produce a constant effective angle of attack distribution along the wing length. An untwisted revolving wing with the chord distribution prescribed by Equation 6.8 produces a downwash distribution very near to the constant distribution and thus is still able to significantly reduce the induced power expenditure. The optimum conditions of constant downwash and elliptic circulation distributions (obtained by prescribing both twist and chord distributions) are added to the plot to qualitatively correlate them to those of the two chords without twist. Downwash and circulation distributions are normalized using the maximum value of each distribution. Downwash and circulation distributions are evaluated based on the lifting line blade theory detailed in Section 3.2.2.

Next, if the constant effective angle of attack requirement is relaxed *and* no twist distribution is applied to the wing, it is found that the optimum chord distribution prescribed by Equation 6.8 still significantly reduces the induced power expenditure. This is shown in Figure 6.2 through plotting the downwash and circulation distributions

for this chord distribution using the lifting line blade model detailed in Chapters 3 and 5. The downwash and circulation distributions produced are very near to the constant and elliptic distributions respectively. To further demonstrate this point, Figure 6.3 shows the k_{ind} for the untwisted optimum wing planform for different aspect ratios ($AR = R/\bar{c}$) within the practical operational range. The k_{ind} values for the optimum chord shown in Figure 6.3 slightly decrease with wing aspect ratio, and have values of 1.016 or less (i.e. no more than 1.6% above the ideal uniform downwash condition). Figure 6.3 also shows the variation of k_{ind} of the elliptic chord distribution which demonstrates a very important outcome that: the k_{ind} value of the elliptic planform is independent of aspect ratio.

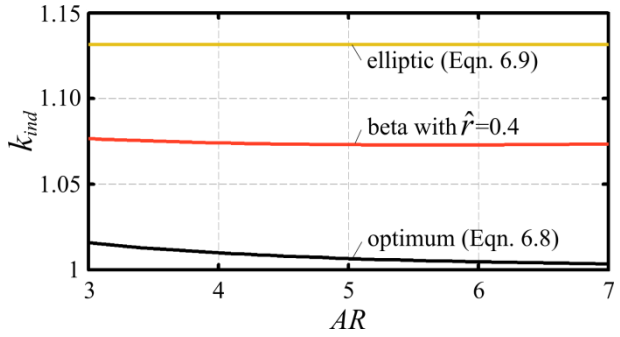

Figure 6.3 Variation of the induced power factor due to non-uniform downwash distribution with aspect ratio. All chord distributions do not employ any twist distribution. The value of k_{ind} is evaluated based on the method developed in Section 3.2.

The optimum chord distribution presented here is clearly difficult to implement due to the broad widening at the root region, and is seldom found in nature; however, it provides a useful reference point to which other less optimal but more practical chord distributions can be compared. This approach has parallels with the use of the elliptic planform as an ideal minimum induced power baseline for fixed wing design (noting that the elliptic planform itself is impractical for most applications) [188]. In a previous contribution [188] using simple optimisation technique, an 'arcsech' distribution was identified to be able to reduce the k_{ind} value to 1.036 for a wing with aspect ratio of 3 up to a k_{ind} value of 1.016 for a wing with aspect ratio of 7. Whilst an 'arcsech' distribution has less root broadening compared to a wing described by Equation 6.8, it is still judged as being impractical. As discussed in Section 3.3.2, most insect wing shapes can be accurately represented using a beta function with the non-dimensional radius of first moment of wing area varying between 40 to 60 percent of the wing length according to

the insect species [141], Figure 6.4a. The value of k_{ind} for the range between these two cases is shown in Figure 6.4b for a wing with aspect ratio of 4 (Note that k_{ind} is weakly dependent on AR as demonstrated in Figures 3.6a and 6.3).

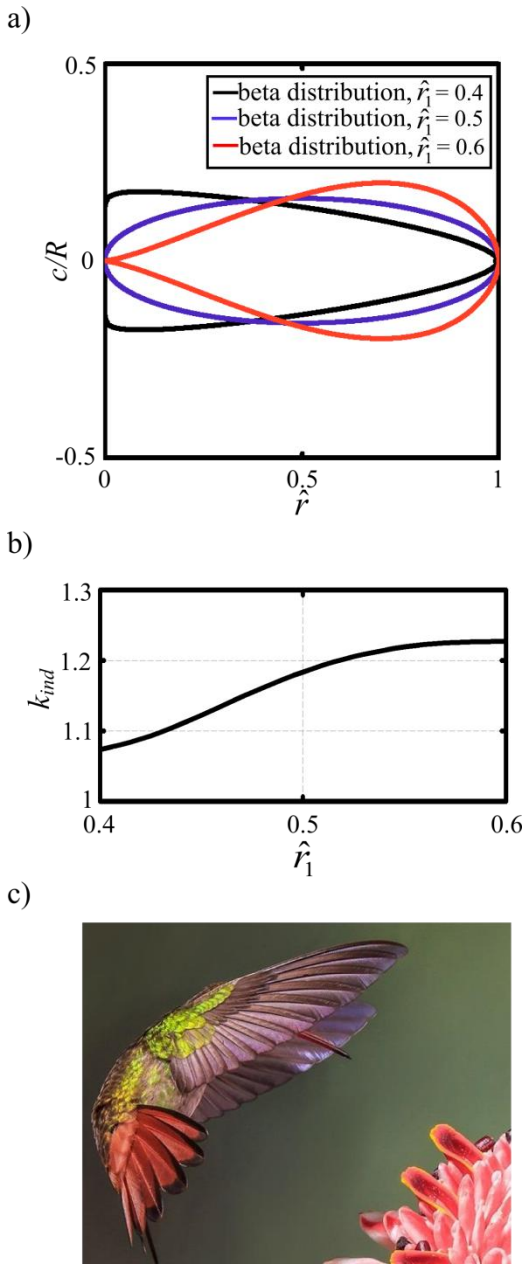

Figure 6.4 (a) Demonstration of beta chord distributions for hovering wings. (b) The induced power factor due to non-uniform downwash, k_{ind}, as a function of the non-dimensional radius of first moment of wing area. The wing aspect ratio is 4 (mid range value for insect wings) and the wing area is constant. (c) A hummingbird wing planform similar to a beta distribution chord with centre of area at 0.4R, photograph by Florian Kuster, National Geographic Your Shot.

Figure 6.4b shows that a wing whose centre of area location is at 0.4R distance from the root has the lowest k_{ind} of 1.07. This distribution is less optimal compared to

the chord distribution described by Equation 6.8, but it is more practical. Thus, the cost of increased practicality is an increase in the induced power factor which is raised to 1.07, see Figure 6.3. In reality a hummingbird wing planform is best represented by a beta distribution whose centre of area is around 40% of the wing length [217], Figure 6.4c. Thus, it can be argued that a hummingbird-like wing planform is the optimum practical wing with respect to minimisation of induced losses.

6.4 Chapter Conclusions

An optimum revolving wing planform that produces an elliptic circulation distribution has been derived. This represents a refinement to current practise in the rotary wing literature where a simplified vortex model with a bound vortex of constant circulation is employed. Additionally, useful insights into the aerodynamic performance of several untwisted revolving wing planforms are presented. It has been shown that even without applying any twist distribution the optimum chord distribution derived in this chapter produces a downwash distribution very near to the constant distribution and thus the induced power expenditure is still significantly reduced.

The optimum chord distribution requires a very broad root region presenting an implementation disadvantage that makes it difficult to realise this planform in practice. An investigation into the effect of wing shape on induced power factor of relevance to real hovering insects has been undertaken using wing shapes represented by a beta function. A wing planform, similar to that of a hummingbird, whose centre of area is at forty percent of the wing length provides the minimum k due to non-uniform downwash with a value of 1.07. Thus, it has slightly less optimal performance in terms of downwash distribution but with a more practical planform shape.

The elliptic wing has always been an attractive planform known for its minimum induced drag within the fixed wing literature. The current study has revealed the unique aerodynamic advantage of the elliptic wing when performing a revolving motion. It has been shown that for any aspect ratio an untwisted elliptic revolving wing can allow all wing sections to operate at the same optimum effective angle of attack for a minimum profile power requirement.

7

Aero-Optimum Hovering Kinematics

Hovering flight for flapping wing vehicles requires rapid and relatively complex reciprocating movement of a wing relative to a stationary surrounding fluid. This chapter will develop a compact analytical aero-kinematic model for optimisation of flapping wing kinematics against aerodynamic criteria of effectiveness and efficiency. The combined aero-kinematic model provides explicit analytical expressions for both lift and power of a hovering wing in a compact form. The model is also used to predict the required flapping frequency for a given geometry and basic aerodynamic parameters.

7.1 Introduction

Effective hovering flight requires generation of rapid wing motion relative to the stationary surrounding fluid. For helicopter-like vehicles the wing motion is generated relatively simply by continuous rotation of the wing; however, the absence of a viable continuously rotating joint in nature means hoverers have to adopt a reciprocating motion in which the direction and pitch angle of the wing must be reversed at the end of each stroke. The fundamental kinematic relations are quite simple: as the wing goes back and forth, the wing should be pitched such that the leading edge is always travelling forward and a positive angle of attack is maintained; however inclusion of non sinusoidal motion primitives makes the problem non trivial. This chapter presents a novel formulation of a parameterised analytical aero-kinematic model for hovering flapping flight that can be used in an explicit fashion to evaluate kinematics optimised for different flight performance requirements. The model is also unique in that it can make explicit prediction of the required flapping frequency from relatively basic geometric and weight information. This provides the means for low order design of insect-scale flapping wing vehicles or alternatively prediction of flapping frequency of insects from a relatively small number of basic input parameters.

Identification of optimum flapping kinematics has been the goal of a number of previous studies addressing the aerodynamic efficiency of hovering flapping flight [164,225,226]. An optimisation problem is typically formulated to identify the wing motion that minimises power expenditure for a given wing while satisfying a weight support (thrust) constraint. The aerodynamic models adopted vary from numerical CFD models solving the flow governing equations [226] to the simpler quasi-steady models [164,225]. The main objectives of these studies were typically either to understand insect flying behaviour [164] or to search for flapping motions that are aerodynamically efficient compared to steady fixed wing flight [225,226]. Some other studies have varied one or two kinematic parameters at a time to investigate the effect of these wing kinematic parameters on the aerodynamic performance [165,227] with the aerodynamic performance assessed based on average lift and average lift to drag ratio values over the flapping cycle. It is reported that lift is increased by increasing flapping frequency, increasing flapping stroke amplitude, and advancing wing pitch rotation [227], and that parameter values for maximum average lift are different to those maximising the

average lift to drag ratio [165]. These studies [165,227] omitted important aspects such as consideration of the different time shapes of variation for the Euler angles through the flapping cycle [227], or were specific for a linear aerodynamic force coefficient representation [165]. Thus despite allowing insight into the problem, a clear procedure for specification of the kinematics requirements within the engineering design of insect-scale flapping wing vehicles is yet to be defined.

In the following, two aspects of aerodynamic performance are considered: optimum kinematics for maximum effectiveness defined in terms of the maximum aerodynamic lift force that can be generated, and optimum kinematics for maximum efficiency defined based on minimising the power expenditure required to generate a given amount of lift. Section 7.2 defines the motion kinematics and the aerodynamic models upon which the developed aero-kinematic model is based. An interpretation of the developed model is presented in Section 7.3. Section 7.4 provides results in the form of efficiency and effectiveness maps as a function of motion control parameters and comparison of predicted against actual flapping frequency of a number of different insect species.

7.2 Aero-Kinematic Model

7.2.1 Kinematic motion parameterisation

The kinematics of a rigid wing flapping motion is defined explicitly by three time varying Euler rotations at the shoulder. For insect wing work it is convenient to use the rotation sequence shown in Figure 7.1. The flapping stroke angle $\phi(t)$ represents the main up and down motion of the wing with respect to the defined lateral plane of the insect. For normal hovering the stroke plane defined by the flapping motion will be horizontal with respect to gravity. Any forward or aft sweep $\varepsilon(t)$ of the wing during flapping will cause the wing to deviate from its original stroke plane, where $\varepsilon(t)$ is referred to as the stroke plane deviation angle. Finally, a rotation $\theta(t)$ is applied about the wing longitudinal axis to alter the geometric angle of attack of the wing, where $\theta(t)$ is referred to as the wing pitching angle.

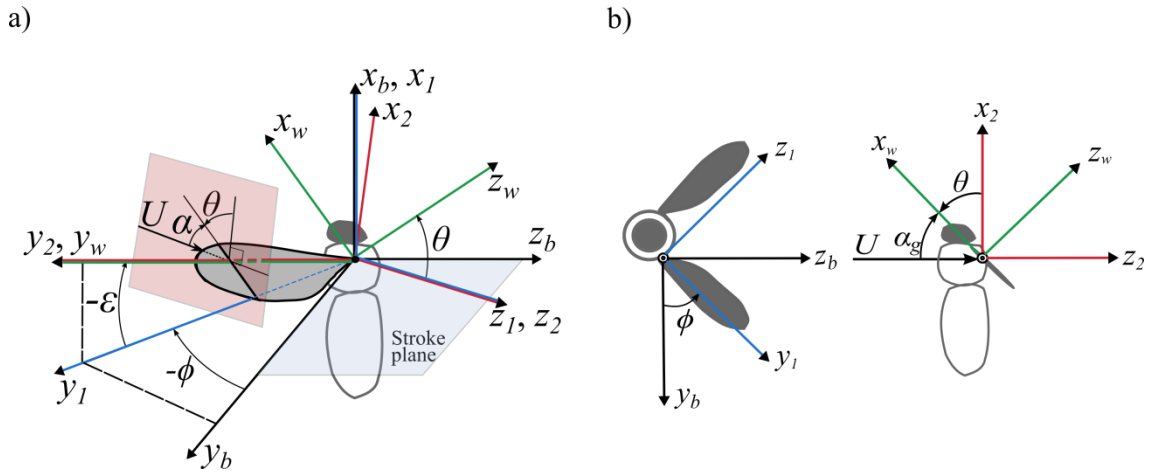

Figure 7.1 (a) The three Euler rotations from the body axes (x_b, y_b, z_b) to the wing axes (x_w, y_w, z_w). (b) For zero stroke plane deviation angle, the axis systems (x_1, y_1, z_1) and (x_2, y_2, z_2) become identical and only two Euler rotations are required from the body to the wing axes. The flapping wing kinematic motion is defined using: the flapping angle, ϕ, the stroke plane deviation angle, ε (zero for Figure 7.1b), and the wing pitching angle, θ. The angle ϕ is a rotation about x_b, the angle ε is a rotation about z_1, the angle θ is a rotation about y_2.

For the present work, angle time histories are defined using parameterisations similar to those given by Berman and Wang [164], however the number of parameters were consolidated to improve the robustness of the motion optimisation process without significant loss of model fidelity. This consolidation is based on the assumption of planar symmetric normal hovering flight in which the wing motion has symmetric half-strokes and the stroke plane deviation angle is zero, reducing the required number of motion parameters of Berman and Wang [164] model from 11 to 5. The symmetric normal hovering assumption is justified on the basis that this is a more efficient style of flapping compared to flapping with asymmetric strokes along an inclined stroke plane (for detailed discussions, see references [176,188,221]). The assumption of a planar wing motion is consistent with experimental studies visualising real insect kinematics [171,172] where it has been shown that the typical deviation angle amplitudes over the flapping cycle are small and do not make a significant contribution to the generation of primary flight forces.

Following from the above, the time variation of the flapping angle is defined as [164]

$$\phi(t) = \begin{cases} \phi_{\max} \cos(2\pi f t) & C_\phi = 0 \\ \dfrac{\phi_{\max}}{\sin^{-1} C_\phi} \left(\sin^{-1} \left[C_\phi \cos(2\pi f t) \right] \right) & 0 < C_\phi \leq 1 \end{cases}. \tag{7.1}$$

For the aerodynamic model we require the flapping velocity. This is obtained by differentiation of Equation 7.1 to give

$$\dot{\phi}(t) = \begin{cases} -2\pi f \phi_{\max} \sin(2\pi f t) & C_\phi = 0 \\ \dfrac{\phi_{\max}}{\sin^{-1} C_\phi} \left(- \dfrac{2\pi f C_\phi \sin(2\pi f t)}{\sqrt{1 - C_\phi^2 \cos(2\pi f t)^2}} \right) & 0 < C_\phi \leq 1 \end{cases}. \tag{7.2}$$

The pitching angle time variation is defined by [164]

$$\theta(t) = \begin{cases} \theta_{\max} \sin(2\pi f t) & C_\theta = 0 \\ \dfrac{\theta_{\max}}{\tanh C_\theta} \left(\tanh \left[C_\theta \sin(2\pi f t) \right] \right) & 0 < C_\theta < \infty \end{cases}. \tag{7.3}$$

The flapping and pitching motion defined in Equations 7.1 to 7.3 is controlled with five parameters ($\phi_{\max}$, $\theta_{\max}$, f, C_ϕ and C_θ), where $\phi_{\max}$ is the flapping angle amplitude, $\theta_{\max}$ is the pitching angle amplitude, f is the flapping frequency, and C_ϕ and C_θ are parameters that control the shape of variation of the flapping and pitching cycles respectively. These parameters are sufficient to simulate a range of flapping motions relevant to biological and engineering studies, and provide intuitive control parameters for evaluation of feasible engineering designs. Figure 7.2 shows range of the kinematic variations that can be simulated with the above motion parameterisation using values of C_ϕ and C_θ set to their bound values.

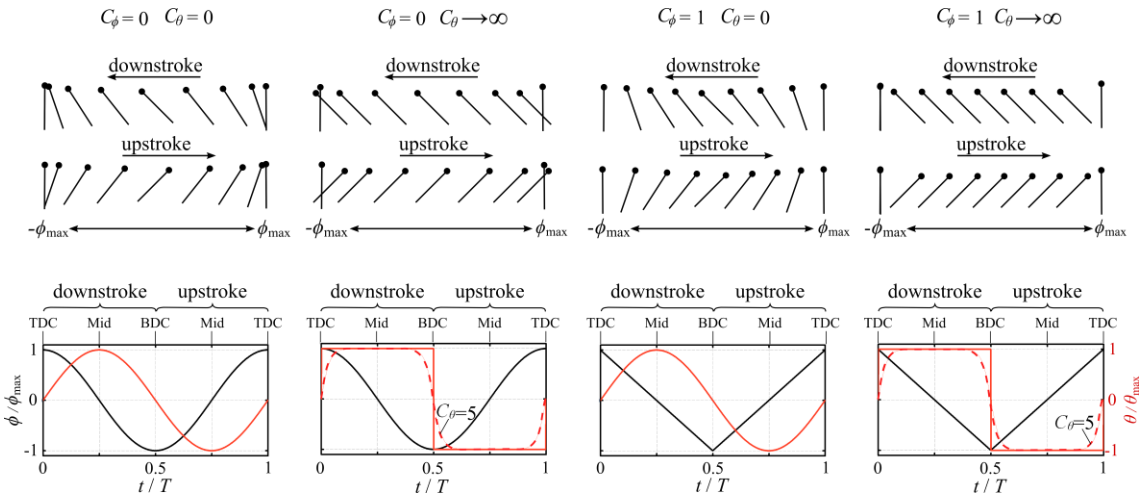

Figure 7.2 Flapping and pitching angle variations during a flapping cycle for different values of C_ϕ and C_θ. Stick diagrams of the wing motion are represented for a time interval 0.0625T. For visualisation purposes, the wing graphic is shown rotated around the mid-chord. The black dots represent the wing leading edge in the graphs. The time variation of the flapping and pitching angles is shown in black and red respectively. TDC denotes Top Dead Centre; BDC denotes Bottom Dead Centre and Mid denotes Mid half-stroke.

7.2.2 Aerodynamic model

7.2.2.1 Generic aerodynamic formulation

The aerodynamic model adopted here is based on a quasi-steady treatment. The lift and drag coefficients, C_L and C_D, of the hovering flapping wing are defined in terms of the geometric angle of attack, α_g, based on the well-established non-linear expressions introduced in Chapter 4

$$C_L(\alpha_g) = C_T \sin(2\alpha_g), \tag{7.4}$$

$$C_D(\alpha_g) = 2C_T \sin^2(\alpha_g), \tag{7.5}$$

where C_T is the translational lift coefficient which depends primarily on the wing shape and Reynolds number [176,213]. Note that Equations 7.4 and 7.5 require two assumptions: Firstly the wing has an un-cambered section with zero twist distribution along the span $\left((C_L)_{\alpha_g=0} = 0\right)$, which is likely to be valid under normal hovering conditions for most insect wings. Secondly, the skin friction drag on the wing is negligible compared to other drag components including pressure and induced drag $\left((C_D)_{\alpha_g=0} = 0\right)$, which is consistent with the experimental drag measurements of insect- as discussed in Chapter 4 and 5. For completeness, further justification for assuming a negligible C_{D0} value is included in Appendix A. The current aerodynamic model also

ignores the wake capture effect which can be important during start of the flapping cycle under some conditions [172]. However, the wing translational phase is the primary contributor to the force generation within the flapping cycle and is alone sufficient to provide weight support [146,176,213].

Here, the energetic cost for hovering is given by the time averaged power output, which can be positive or negative; hence it is assumed that mechanical energy can be stored and released when the wing does positive work. This is appropriate for most engineering designs where an elastic spring element can be used to recover the energy; though there is some debate on the degree to which this applies in nature. Nevertheless, some studies show that insects have elastic elements within the flight muscles, thorax and wing hinges that can significantly reduce the inertial power expenditure; for review of this point, the reader is referred to references [151,228]. The assumption of full elastic energy recovery as well as the employment of symmetric half-strokes leads to a zero net inertial cost; additionally, symmetric kinematics leads to zero net force components due to rotational and added mass effects [134,176,229]. Thus, relatively simple analytic formulae to describe the problem can be derived.

Given the symmetry of half-strokes, the hovering lift and power will be based on averaged values during the down-stroke phase. In the down stroke the time variation of the angle of attack can be written as

$$\alpha_g(t) = \frac{\pi}{2} - \theta(t)\,. \tag{7.6}$$

Using Equations 7.2 to 7.6, it can be shown, after some mathematical manipulation, that the average lift and power can be expressed as

$$\overline{L} = G_L \int_0^{\frac{1}{2f}} \left(\dot{\phi}(t)\right)^2 \sin(2\alpha_g(t))dt\,, \tag{7.7}$$

$$\overline{P} = G_P \int_0^{\frac{1}{2f}} \left(\dot{\phi}(t)\right)^3 \sin^2(\alpha_g(t))dt\,, \tag{7.8}$$

where

$$G_L = \rho f (R^2 \hat{r}_2^2)(2R\bar{c})(C_T)\,, \tag{7.9}$$

$$G_P = \rho f (R^3 \hat{r}_3^3)(2R\bar{c})(2C_T)\,, \tag{7.10}$$

where ρ is the air density, R is the wing length from root to tip, $\bar{c}$ is the mean geometric chord and $\hat{r}_2, \hat{r}_3$ are the non-dimensional second and third radii of moment of area of the wing.

7.2.2.2 Explicit formulae for average lift and power

Whilst the lift and power expressions in Equations 7.7 and 7.8 are relatively simple, analytic evaluation of the integrals is not trivial. Nevertheless, with mathematical effort, explicit analytical formulae can be obtained for specific kinematic profiles. These specific profiles include: (1) sinusoidal flapping and pitching angle variations (i.e. C_ϕ = C_θ = 0), and (2) rectangular pitching angle variation for any flapping angle variation (i.e. $C_\theta \to \infty$). These profiles allow simplification of the integrand in Equations 7.7 and 7.8, and instead of performing the integration numerically analytical expressions can be obtained for the average lift and power as

$$\bar{L} = \begin{cases} G_L\left(\frac{16}{3}\pi f \phi_{\max}^2 \theta_{\max}\left(Hypergeom\left[\{2\},\{\frac{3}{2},\frac{5}{2}\},-\theta_{\max}^2\right]\right)\right) & C_\phi = C_\theta = 0 \\ G_L \sin(2\alpha_g)\left(\left(\frac{C_\phi}{\sin^{-1} C_\phi}\right)^2 \frac{2\pi^2 f \phi_{\max}^2}{1+\sqrt{1-C_\phi^2}}\right) & C_\theta \to \infty \end{cases}, \qquad (7.11)$$

$$\bar{P} = \begin{cases} G_P\left(\frac{8}{3}\pi^2 f^2 \phi_{\max}^3\left(1+Hypergeom\left[\{2\},\{\frac{1}{2},\frac{5}{2}\},-\theta_{\max}^2\right]\right)\right) & C_\phi = C_\theta = 0 \\ G_P \sin^2(\alpha_g)\left(-8\pi^2 f^2 \phi_{\max}^3\left(\frac{1}{\sin^{-1} C_\phi}\right)^3\left(C_\phi\sqrt{1-C_\phi^2} - \sin^{-1}(C_\phi)\right)\right) & C_\theta \to \infty \end{cases}, \qquad (7.12)$$

where *Hypergeom* denotes the Barnes extended hypergeometric function, and can be easily implemented from commercial software libraries as Matlab® and Mathematica®. Note that for the case when $C_\theta \to \infty$, the value of α_g is constant along the half-stroke and thus is taken out of the integration. Also for this case, the lift and power expressions become singular when C_ϕ is zero; however, using a small value of C_ϕ (as 0.001) allows representative simulation of the sinusoidal flapping variation. Using the above lift equation, the frequency, f, can be calculated to satisfy a weight, W, requirement as

$$f=\begin{cases}\sqrt{\dfrac{3W}{\rho(4\phi_{\max}R\hat{r}_2)^2(2R\bar{c})(C_T)\left(\pi\theta_{\max}\left(Hypergeom\left[\{2\},\{\frac{3}{2},\frac{5}{2}\},-\theta_{\max}^2\right]\right)\right)}} & C_\phi=C_\theta=0 \\ \sqrt{\dfrac{8W\left(\sin^{-1}C_\phi\right)^2\left(1+\sqrt{1-C_\phi^2}\right)}{\rho\underbrace{(4\phi_{\max}R\hat{r}_2)^2}_{\propto U_{mean}^2}\underbrace{(2R\bar{c})}_{S}\underbrace{(C_T\sin(2\alpha))}_{C_L}(\pi^2C_\phi^2)}} & C_\theta\to\infty\end{cases}. \tag{7.13}$$

Equation 7.13 should prove useful within the design of a flapping wing vehicle as it defines the flapping frequency required to carry a certain total weight for a given wing geometry and kinematic parameters. Substitution of the above frequency relations into Equation 7.12 delivers expressions for the average power for a given weight constraint as

$$\bar{P}=\sqrt{\frac{3\pi\left(1+Hypergeom\left[\{2\},\{\frac{1}{2},\frac{5}{2}\},-\theta_{\max}^2\right]\right)^2}{32C_T\theta_{\max}^3\left(Hypergeom\left[\{2\},\{\frac{3}{2},\frac{5}{2}\},-\theta_{\max}^2\right]\right)^3}}W^{\frac{3}{2}}\sqrt{\frac{2}{\rho S}}\left(\frac{\hat{r}_3}{\hat{r}_2}\right)^3 \quad C_\phi=C_\theta=0 \tag{7.14}$$

$$\bar{P}=\left(\frac{-2\left(C_\phi\sqrt{1-C_\phi^2}-\sin^{-1}\left(C_\phi\right)\right)\left(1+\sqrt{1-C_\phi^2}\right)^{\frac{3}{2}}}{\pi C_\phi^3}\right)\frac{C_D}{C_L^{\frac{3}{2}}}W^{\frac{3}{2}}\sqrt{\frac{2}{\rho S}}\left(\frac{\hat{r}_3}{\hat{r}_2}\right)^3 \quad C_\theta\to\infty \tag{7.15}$$

Equation 7.15 shows that the average power is inversely proportional to the power factor, $PF=C_L^{3/2}/C_D$, which is a measure of the amount of weight that can be lifted per unit aerodynamic power [218]. For a C_ϕ value of 0.001 (corresponding to sinusoidal variation of the flapping angle), Equation 7.15 reduces to

$$\bar{P}=1.2W^{\frac{3}{2}}\sqrt{\frac{2}{\rho S}}\frac{C_D}{C_L^{\frac{3}{2}}}\left(\frac{\hat{r}_3}{\hat{r}_2}\right)^3. \tag{7.16}$$

Whilst for a unity C_ϕ value corresponding to constant angular velocity variation with respect to time, Equation 7.15 reduces to

$$\bar{P}=W^{\frac{3}{2}}\sqrt{\frac{2}{\rho S}}\frac{C_D}{C_L^{\frac{3}{2}}}\left(\frac{\hat{r}_3}{\hat{r}_2}\right)^3, \tag{7.17}$$

Equations 7.16 and 7.17 are consistent with the final results of reference [230]; and apart from the appearance of the term containing $\hat{r}_2$ and $\hat{r}_3$ due to the linear variation of

the sectional velocity along the wing length (i.e. $U(r) = \dot{\phi} r$), Equation 7.17 is the same as the well-know aerodynamic power relation for steady flight of fixed wing vehicles. Whilst this does not validate the model in anyway, it does provide circumstantial evidence that the analytical approach is sound.

7.3 Model Interpretation

7.3.1 Selection of flapping profile

Before progressing to evaluation of the complete aerodynamic model as a function of both flapping and pitching control parameters (C_ϕ and C_θ), it is instructive to consider the implications of changing flapping kinematics using a simple case in which the pitch change at the end of each stroke is instantaneous ($C_\theta \to \infty$) such that the geometric angle of attack is constant during each half-stroke. From inspection of Equation 7.7 it can be seen that with the flapping velocity, $\dot{\phi}$, as the only variable, the lift will be proportional to the *mean square* of the flapping velocity over the flapping cycle. Consider the two flapping profiles given by $C_\phi = 0$ and $C_\phi = 1$ corresponding to a sinusoidal and triangular motion, respectively. For a given flapping frequency and stroke amplitude the sinusoidal profile will have the higher mean square value, hence it is anticipated that solutions for high effectiveness obtained from the complete model will be biased towards sinusoidal flapping profiles. If we now consider efficiency as the goal, measured in terms of power/lift, then from dividing Equations 7.8 by 7.7 for the case of $C_\theta \to \infty$ we can see by inspection that efficiency is proportional to the ratio of *mean cube* to *mean square* of the flapping velocity. Thus for efficiency we would expect flapping kinematics to be biased towards triangular flapping profiles.

7.3.2 Selection of the pitching amplitude and the flapping amplitude

The selection of the pitching angle amplitude, $\theta_{\max}$, depends on which design criteria should be prioritised. By inspection, for maximum lift to be generated $\theta_{\max}$ should take a value which maximises the wing *lift coefficient*, which for the present aerodynamic model (see Equation 7.4) occurs at 45 degrees. This is consistent with practise adopted within the early stages of the design process in a number of previous studies [225,227,229]. On the other hand, if efficiency in terms of power for a given lift is to be minimised, then Equation 7.15 shows that to achieve this design criteria the *power*

factor, *PF*, has to be maximised which in turn is achieved by decreasing the mid-stroke angle of attack amplitude through increasing θ_{max} (see Appendix A).

With regard to selection of the flapping angle amplitude, ϕ_{max}, this should always be as large as possible: in terms of effectiveness, larger stroke amplitudes allow higher instantaneous velocity values for the same wing geometry and operational frequency (see Equation 7.2) and hence generation of higher aerodynamic forces; in terms of lift production efficiency, a larger stroke means a larger disk area and hence a lower disk loading. This leads to lower average downwash velocity and reduced induced power expenditure. Furthermore, higher velocity and larger disk area combined leads to lower inflow ratios and thus lower induced losses due to the wake periodicity effect as shown in Chapter 3.

7.4 Results

7.4.1 Effectiveness and efficiency maps

Further to the qualitative interpretation of the kinematic-aerodynamic model in Section 7.3.1, consider a numerical evaluation in the form of contour maps of effectiveness and efficiency as a function of the flapping and pitching control parameters C_ϕ and C_θ, Figure 7.3.

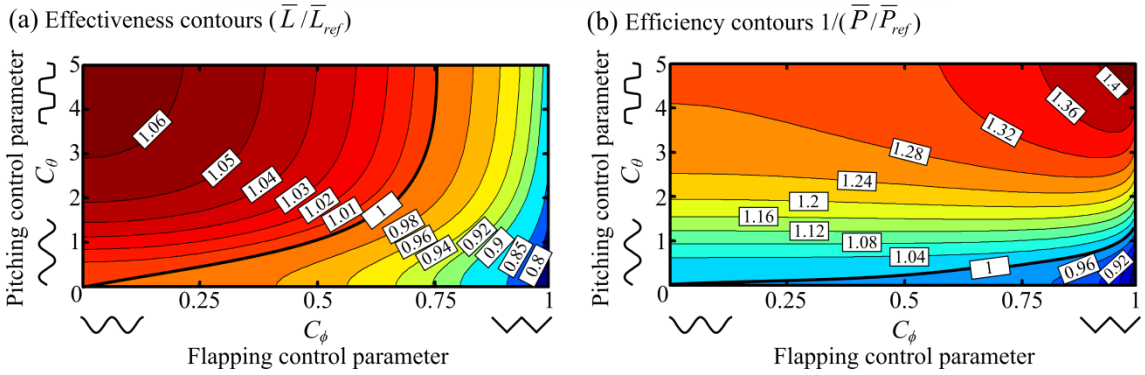

Figure 7.3 Variation of (a) normalised lift, and (b) inverse of the normalised power for a given lift for different combinations of C_ϕ and C_θ. The values are normalised with respect to the values obtained for sinusoidal flapping and pitching angle variations. Red indicates 'better' in each case. This demonstration is based on integrands numerical integration of Equations 7.7 and 7.8 with θ_{max} value of 45 degrees.

Note that lift and power values are normalised with respect to the lift and power values for sinusoidal flapping and pitching angles variations (i.e. $C_\phi = C_\theta = 0$). Sinusoidal variations of the flapping and pitching angles are used as the reference kinematics because they are simple to implement and also minimise peak acceleration in the wing motion which reduces instantaneous actuator power requirement [231]. Also, the upper bound for the C_θ parameter was set to 5 representing a practical upper bound for this control parameter. A value of 5 for C_θ is equivalent to completing of wing rotation within around 25% of the flapping cycle period, see Figure 7.2. This upper bound is consistent with observations of insects [145,171,172], and the performance of engineered flapping mechanisms [100,229].

7.4.1.1 Maximum effectiveness

Here the wing kinematics that leads to generation of the largest aerodynamic force for a given wing geometry and flapping frequency are identified, irrespective of the required power. It is a given that the wing operates at a maximum stroke amplitude and a value for θ_{max} of 45 degrees, so the task becomes that of identifying the shape of variation of flapping and pitching angles during the stroke. Lift generated for constant wing geometry, constant kinematic parameters (except C_ϕ and C_θ) and constant translation force coefficient for different combinations for C_ϕ and C_θ is shown in Figure 7.3a. It can be seen that for any flapping angle variation a step-like variation of the pitching angle (i.e. constant incidence through half-strokes) will always provide the highest lift. The best combination for highest effectiveness is to have a sinusoidal variation of the flapping angle (implying sinusoidal variation of the velocity) with the step-like pitching variation. This combination produces 6.5% more lift compared to the sinusoidal reference kinematics. This result is consistent with the discussion in Section 7.3.1 (model interpretation). On the other hand, the combination of a triangular variation of the flapping angle and a sinusoidal variation of the pitching angle is the least good with respect to aerodynamic effectiveness, producing 30% less lift compared to the sinusoidal reference kinematics.

7.4.1.2 Maximum efficiency

Here, minimum power for a given lift constraint is used as the criteria for the kinematic pattern selection. Lift is kept constant for different kinematic motions by adjusting the flapping frequency value. The efficiency contours shown in Figure 7.3b are represented

as the inverse of the power expended for a given lift for different value combinations of C_ϕ and C_θ. It can be seen that the best combination for highest efficiency (lowest power for given lift) is to have a triangular variation of the flapping angle with a step-like pitching angle variation, i.e. a constant flapping velocity and a fixed pitch angle in each half stroke. These profiles are consistent with those discussed in Section 7.3.1 (model interpretation) and are consistent with the higher order calculus of variation result obtained by Taha *et al*. [230]. They are also similar to the kinematics used by Schenato *et al*. [232]. Moreover they are compatible with optimal hovering rotor aerodynamics where, in the absence of unsteady effects, a rotor is usually operated at a constant angular speed and a constant optimal angle of attack [133].

On the other hand, the combination of a triangular variation of the flapping angle and a sinusoidal variation of the pitching angle is the least good with respect to aerodynamic efficiency. Note that the kinematics for least good effectiveness and least good efficiency are the same. Also for both best effectiveness and best efficiency the optimum pitching angle variation is the step-like variation. Therefore it remains only to choose a sinusoidal flapping angle variation for maximum effectiveness or a triangular flapping angle variation for maximum efficiency.

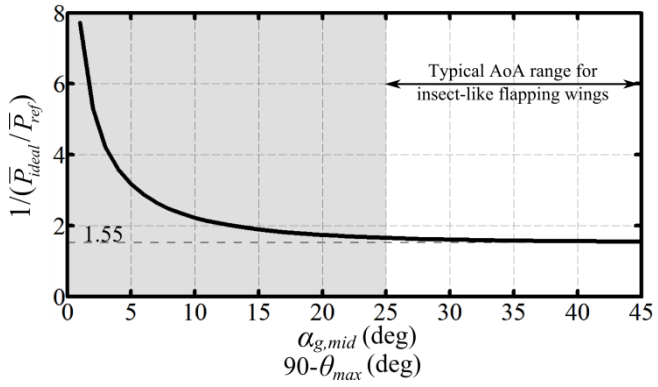

Figure 7.4 Variation of the inverse of the normalised power for a given lift for the efficiency optimum combination (C_ϕ = 1 and $C_\theta \rightarrow \infty$) with geometric angle of attack value. This demonstration is based on the quotient of the analytical expressions of Equations 7.14 and 7.17.

It is noteworthy to mention that the contour values in Figure 7.3b are based on integrand numerical evaluations with a $\theta_{\max}$ value of 45 degrees. Changing the value of $\theta_{\max}$ will only change the efficiency contour values, but does not change the conclusion that a triangular variation of the flapping angle with a step-like pitching angle variation are the most efficient motion profiles. To further demonstrate this point, Figure 7.4

compares the mean aerodynamic power for a given lift values of the ideal motion profile (C_ϕ = 1 and $C_\theta \rightarrow\infty$) with respect to the reference sinusoidal case. This evaluation is based on the quotient of Equations 7.14 and 7.17. The superiority of the efficiency-optimum combination can be directly seen from the figure and this superiority even improves as the angle of attack decreases which is consistent with the discussion of Section 7.3.2. However within the typical angle of attack operation range for insect-like wings [145], the variation of the curve shown in Figure 7.4 is not very significant.

7.4.1.3 Practical implementation of the optimum kinematic profiles

Whilst the triangular variation of the flapping angle is mathematically elegant, it is challenging from a practical point of view due to the high acceleration requirement at the end of each half-stroke. Additionally, insect-scale flapping vehicles are typically driven at resonance to achieve the large amplitude motion required for sufficient flapping; for a linear transmission system operating at resonance, the output will be sinusoidal by default regardless of the driving waveform [231].

Similarly, rectangular variation of the pitch angle to give rapid reversal of geometric angle of attack at the end of each half-stroke may be mechanically more expensive than a sinusoidal variation due to the higher actuation torque required and the fact that resonance cannot be used to amplify this motion. A number of practical flapping wing implementations have successfully used passively generated pitching kinematics in which wing hinge properties are exploited to generate a pitching motion of the correct phase to the flapping motion [100,229]. Use of a suitably nonlinear structural response, e.g. via implementation of a softening torsional stiffness, can allow passively generated pitching kinematics to more closely approximate the rectangular variation required for both maximum efficiency and maximum effectiveness.

Whilst the combination of a triangular variation of the flapping angle and a rectangular variation of the pitching angle is practically challenging for a flapping wing, it is trivial to implement using a rotary wing. Comparison of Equations 7.16 and 7.17, shows us that sinusoidal flapping expends 20% more aerodynamic power than triangular flapping for the same lift. Thus apart from practicality issues, a flapping wing becomes most efficient when it approaches the rotary wing motion. This also support the argument presented in references [9] and [142] that a rotating (spinning or revolving) wing motion is more efficient at generating lift than a flapping motion.

Using the second expression of Equation 7.11, it can be shown that sinusoidal flapping generates 23% more lift compared to triangular flapping for all other variables being the same. Given that a sinusoidal variation in velocity is the most effective solution for a flapping wing at a given frequency, why is it that we do not see this in engineered continuously rotating wings? The answer appears to be that for these systems it is easier mechanically to increase the speed by increasing the frequency than it is to introduce angular velocity variations within each cycle.

7.4.2 Selection of the flapping frequency

Table 7.1 Comparison between reported and calculated frequency for eight hovering insects. Weight, morphological and kinematic parameters are taken from reference [145]. Insects listed in order of increasing mass.

Insect	mass (mg)	R (mm)	$\bar{c}$ (mm)	$\hat{r}_2$	$\phi_{\max}$ (deg.)	$f_{reported}$ (Hz)	$f_{calculated}$ (Hz)	error (%)
FF	0.72	2.02	0.67	0.596	75	254	281	+9.6
CF	11.4	12.7	2.38	0.614	61.5	45.5	44.6	-2.11
HF	27.3	9.3	2.2	0.578	45	160	166	+3.7
LB	34.4	11.2	3.23	0.538	88.5	54	63.6	+15
DF	68.4	11.4	3.19	0.543	54.5	157	141	-11
HB	101.9	9.8	3.08	0.566	65.5	197	176	-11.9
BB	175	13.2	4.02	0.554	58	155	149	-4
HM	1648	51.9	18.26	0.525	60.5	26.3	27.8	+5.5
						Mean absolute error		7.88%
						Mean error		0.6%

The flapping frequency, f, can always be selected in order to satisfy a given weight constraint; that is, more lift can always be generated by flapping faster. For the present analysis it is assumed that the angle of attack during each half-stroke is constant (which is consistent with requirements for both efficiency and effectiveness). Thus the flapping frequency is calculated from the second formula in Equation 7.13, with $C_\theta \to \infty$. A comparison between predicted and reported flapping frequency for eight hovering insects is given in Table 7.1. Insect weight, morphological and kinematic data is from Sun and Du [145]. Calculated flapping frequency is obtained from Equation 7.13 using a C_ϕ = 0.001 and a representative value of 1.1 for the lift coefficient. The obtained results are in close agreement with the frequency values reported by Sun and Du [145] with a mean absolute error of 7.9% and mean error of 0.6% for the eight calculations. Note that accuracy in the predicted frequency can be significantly improved by using lift coefficient values specific to each wing geometry; however, the point to make with

the data is that even assuming a universal value of 1.1, the predicted results are still usefully accurate over a broad range of insect sizes and wing geometries.

7.5 Chapter Conclusions

A simple approach for optimum kinematic motion selection of hovering flapping wings has been proposed. Explicit analytical expressions for the average lift and power of the most relevant kinematic motions for hovering flapping flight are derived. These expressions are useful for the purposes of preliminary engineering design of flapping wing vehicles and prediction of flapping frequency of robotic and natural insects from weight and morphological data. Flapping and pitching angle variations are identified for achieving maximum effectiveness, and for achieving maximum efficiency.

For effectiveness, the flapping angle profile should be sinusoidal, whereas for efficiency, the flapping angle profile should be triangular, with the pitching angle being rectangular in each case. Operation at maximum effectiveness generates 23% more lift compared to optimum efficiency case, and expends 20% more aerodynamic power to produce the same lift compared to optimum efficiency case.

The use of a rectangular pitching profile and sinusoidal flapping profile increases the maximum attainable effectiveness by around 6.5% compared to the dual sinusoidal reference case. Whereas, the use of triangular flapping and rectangular pitching profiles increases the maximum attainable efficiency by at least 55% compared to the dual sinusoidal reference case.

8

Dynamic Performance of Piezoelectric Bending Actuators[3]

Previous chapters dealt with the different aspects of the wing performance. This chapter will consider the flapping vehicle actuator. The aim is to acquire improved understanding of the underlying electromechanical properties of piezoelectric actuators in dynamic operation. Here, a detailed analytical modelling treatment of the dynamic electromechanical behaviour of piezoelectric actuators with different configurations is developed. Experimental validation of the model for unimorph actuators is presented. An expression for the Electromechanical Coupling Factor (EMCF) is extracted from the analytical model and is used as the objective for parametric design studies for the different actuator configurations. Valuable insights into the selection of the configuration, the material properties and the operation variables controlling the dynamic performance of this class of actuators are delivered.

[3] This chapter is an extended version of the publication: Nabawy MRA, Parslew B, Crowther WJ. 2015 Dynamic performance of unimorph piezoelectric bending actuators. *Proc IMechE PartI: J Systems and Control Engineering* **229**: 118-129(doi 10.1177/0959651814552810)

8.1 Introduction

Piezoelectric bending actuators are a class of actuators designed to utilise the inverse piezoelectric effect to convert input electric energy to useful mechanical work, and are capable of producing relatively large bending deflections at low voltage [233]. Some common applications for this class of actuators include laser mirror alignment, ink ejection in printing, and atomic force microscopy. For these applications, operation is typically performed off-resonance in order to prioritise positional accuracy over amplitude. However, the flapping wing propulsion application has an alternative objective that is the actuator should achieve large tip displacements for flapping motion amplification. Thus, operation at resonance becomes a fundamental requirement for the concept operation. Although the concern of the current work is for insect-scale flapping wing propulsion, it should be noted that the current work is also useful for other resonant devices such as cooling fans [234-236] and micro-pumps [237]. The objective of all these engineering applications is to maximise fluid flow rate with respect to electrical power consumption. In order to properly address this challenge a detailed understanding of the underlying electromechanical properties of the actuator is necessary.

Piezoelectric actuators come in different arrangements, and are mainly classified by the type and number of layers involved. Well known examples include unimorphs (actuators with a passive elastic layer and an active piezo-layer), bimorphs (actuators with two active piezo-layers), and triple layer actuators (actuators with two active piezo-layers sandwiching a passive elastic layer), Figure 8.1. Unimorphs are often preferred for their simple structure, ease of manufacture and improved reliability compared to bimorph structures [78,111]. However, bimorphs can offer better electromechanical behaviour. Thus, a triple layer actuator combines the merits of both configurations as it can provide good electromechanical behaviour, whilst the elastic layer improves the mechanical reliability [238]. The mechanical reliability issue was indeed the main criteria for actuator selection for the different flapping wing concepts presented in Chapter 2 where most of them were either using a unimorph or a triple layer actuator.

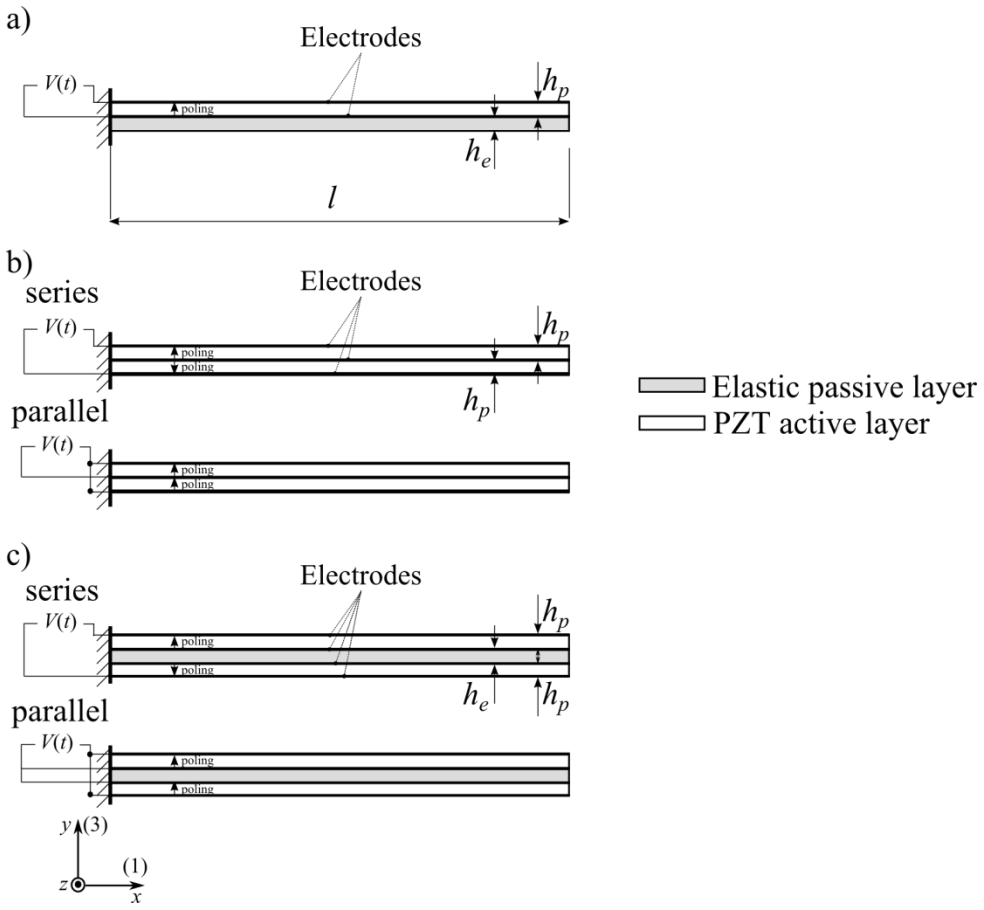

Figure 8.1 Schematic drawing of piezoelectric bending actuators. (a) Unimorph, (b) bimorph, (c) triple layer actuator.

Existing theoretical treatments of piezoelectric actuators characterisation can be broadly divided into two cases: static and dynamic actuation. Static actuation characterisation has been widely dealt with in the available literature. For static operation, the complete set of constituent equations relating the driving parameters (moment, force, uniform load and voltage) to the response parameters (deflection slope, deflection, volumetric displacement and charge) have been derived for unimorph and bimorph cantilever actuators [239] [240]. Wang *et al*. [111] used these equations to investigate actuator performance metrics as the electromechanical coupling factor and the maximum energy transmission coefficient. For unimorphs, they found that these metrics are related to the transverse coupling coefficient, k_{31}, the Young's modulus of the materials and the thickness ratio of the actuator layers, whereas for bimorphs it was found that dependency was on transverse coupling coefficient only. Note that maximum energy transmission coefficient is a direct function of the EMCF; thus, best configurations with respect to EMCF are also best with respect to the maximum energy

transmission coefficient. Static actuation constitutive equations have also been driven for the triple layer configuration [238]; however, its electromechanical performance was not assessed as for the unimorph and bimorph cases.

Dynamic actuation characterisation for piezoelectric bending actuators has been addressed at different levels but still there are significant gaps that require addressing. Smits and Ballato [241] provided the equations describing the dynamic behaviour of bimorph actuators in the form of a complete dynamic admittance matrix relating the harmonically varying driving parameters (tip moment, tip force, uniformly applied body force and voltage) to response parameters (tip rotation, tip deflection, volumetric displacement and charge). However, damping was ignored in their derivation and the work was not extended to the unimorph case. Later, dynamic structural models of unimorph actuators have been presented (e.g. [242]); however, only actuator mode shapes and natural frequencies were predicted. More recently, analytical models for actuators and harvesters have been developed by Inman and his group taking damping into account [243-247]. Actuation application models [243-245] have been provided for unimorphs whereas harvesting application models were provided for unimorphs [246] and triple layer actuators [247]. Actuation application models concentrated only on relating unimorph beam deflections to the applied voltage; whereas energy harvesting application models [246,247] provided more assessment on the relation between charge, current and voltage. Nonetheless the presented models were not extended to include a dynamic admittance matrix relating the driving parameters to response parameters for unimorphs, bimorphs or triple layer actuators, and no assessment of the actuation electromechanical coupling performance was provided.

Actuator displacement, force and resonant frequency are important extrinsic metrics for actuation characterisation; however, the intrinsic metric provided by electromechanical coupling factor provides a more fundamental insight into the actuator performance for different applications (see discussion on this issue by Wang *et al*. [111], Rodriguez *et al*. [248] and Ikeda [249]). Thus, this chapter focuses the modelling and discussion on assessment of the electromechanical coupling factor rather than the higher level outputs of force and displacement. There have been some attempts to characterise the electromechanical coupling characteristics of unimorphs in dynamic operations. Basak *et al*. [242] developed analytical and finite element models to compute the open and short circuits natural frequencies of unimorphs from which they calculated the dynamic electromechanical coupling factor using the simple ‘Mason

formula' (a discussion on methods to evaluate the electromechanical coupling will be presented in Section 8.2). A similar approach was also followed by Bidakhvidi *et al*. [250] to evaluate the dynamic electromechanical coupling factor of piezoelecric flapping wing propulsion structures. Chung *et al.* [62] demonstrated that the product of resonant frequency and vibration amplitude serves as a viable measure of unimorph performance. The same measure was applied later by Lal Kummari *et al*. [251] to the optimization of motion amplification mechanisms for flapping wing actuators. The use of the product of resonant frequency and vibration amplitude was based on an observation that this measure varies with the unimorph elastic/active layer thickness ratio in a similar fashion to the static EMCF [62]. Therefore, the discussed methods can be regarded as indicatory rather than predictive, and there remains a need to develop a more comprehensive treatment of actuator dynamic characterisation that can be used for engineering design.

In this chapter, a comprehensive extended analytical model is developed for the dynamic operation of piezoelectric actuators taking into account realistic operation conditions quantified by the damping ratio. The model is cast in the form of a matrix relating the harmonic driving parameters to response parameters allowing for the extraction of an analytical expression for the electromechanical coupling factor in dynamic operation. This allows for the first time analysis of the significant effect that damping can have on a piezoelectric actuator dynamic electromechanical coupling performance. The present work therefore provides insight into optimised selection of materials and configurations that allow high dynamic performance of actuators for use within insect-scale flapping wing vehicles (or any other resonant application). The next section will discuss the different measures of actuator performance represented through the definition of the electromechanical coupling factor. This will be followed by the development of a dynamic electromechanical model for piezoelectric actuators and its experimental verification. Finally, a comprehensive analysis of the electromechanical coupling performance based on the theoretical model will be presented.

8.2 Electromechanical Coupling Factor (EMCF)

The electromechanical coupling coefficient (EMCC) is a performance metric for a transducer; however, it is usually more meaningful to use the square of the EMCC, referred to as the electromechanical coupling factor (EMCF, k^2), which corresponds to

the ratio of the stored mechanical energy to the supplied electrical energy [111,248,249]. Whilst EMCF is not a direct measure of the transducer efficiency, it represents a measure of the unavailable or ineffective fraction of energy [249] within an actuation cycle. Therefore, it serves as a useful measure to gauge piezoelectric actuator performance.

There are a number of different ways of deriving an expression for the EMCF. For a system close to resonance, a simple expression based on Mason's formula is given as [248,252,253]

$$k^2 = \frac{f_a^2 - f_r^2}{f_a^2}, \tag{8.1}$$

where f_r is the resonant frequency and f_a is the nearest anti-resonant frequency to f_r determined from experimental measurements [248,253]. However, an alternative less restrictive expression for the EMCF can be obtained directly from the piezoelectric actuator equations according to Ikeda [249]. When the physical and electrical configuration of the piezoelectric actuator is defined, its behaviour is given by a set of constitutive equations derived in the form [111,249]

$$\begin{bmatrix} \delta \\ Q \end{bmatrix} = \begin{bmatrix} C_{11} & C_{12} \\ C_{12} & C_{22} \end{bmatrix} \begin{bmatrix} F \\ V \end{bmatrix}, \tag{8.2}$$

where δ, F, Q and V are the tip deflection, tip force, charge and voltage, respectively. The EMCF is then defined as [111,249]

$$k^2 = \frac{C_{12}^2}{C_{11}C_{22}}, \tag{8.3}$$

Here the dynamic EMCF of different piezoelectric actuators will be derived from an analytical expression of Equation 8.2 which in dynamic operation can be written as

$$\begin{bmatrix} \delta(x,t) \\ Q(x,t) \end{bmatrix} = \begin{bmatrix} D_{11}(x) & D_{12}(x) \\ D_{21}(x) & D_{22}(x) \end{bmatrix} \begin{bmatrix} Fe^{i(\omega t)} \\ Ve^{i(\omega t)} \end{bmatrix}, \tag{8.4}$$

where the real and imaginary parts of $e^{i\omega t}$ represent a cosine and sine form of excitation, respectively. Once derived, the elements of the dynamic matrix, $D_{ij}(x)$, can be used in the same sense of Equation 8.3 to evaluate the dynamic EMCF of piezoelectric

actuators. Whilst Equation 8.4 is presented in the form required for extraction of the EMCF, it also can be used to provide metrics for force and displacement using the first row that relates displacement, force and voltage, as will be used in next chapter.

8.3 Electromechanical Model

The derivation presented here builds on previous analytical treatments of bending actuators [241,243-247,254-256]. Each of these studies contributed to the foundations that the present work utilises to derive a more comprehensive model of piezoelectric actuators dynamic behaviour. Here, the bending actuator model is based on a uniform composite Euler-Bernoulli beam. The electrodes are assumed to be: (1) very thin (negligible thickness) compared to actuator layers; (2) perfectly conductive and (3) cover the entire PZT surface from top and bottom, so the electric field is uniform over the length [246]. The governing equation of motion can be written as [246,256]

$$YI\frac{\partial^4\delta(x,t)}{\partial x^4}+c_v\frac{\partial\delta(x,t)}{\partial t}+\rho A\frac{\partial^2\delta(x,t)}{\partial t^2}=f(x,t), \tag{8.5}$$

where Y is Young's modulus, I is the area moment of inertia of the composite cross section, c_v is the equivalent viscous damping coefficient that include damping sources, ρA is the mass per unit length, f is the external applied force per unit length, x is the spatial coordinate along the length of the actuator, t is time and δ is the transverse deflection.

It should be noted that Equation 8.5 does not consider the Kelvin-Voigt damping term which requires a temporal derivative of the spatial fourth derivative. Viscous damping is influential at lower vibration modes, while Kelvin-Voigt damping is influential at higher vibration modes [246,257,258]. The main concern of the current model is towards the application of flapping wing propulsion which operates at the first resonant frequency to achieve large displacements necessary for its functionality; therefore, it is appropriate to neglect the Kelvin-Voigt damping. Thus, the damping coefficient, c_v, is given by

$$c_v=\rho A\left(2\zeta_n\omega_n\right), \tag{8.6}$$

where ζ is the damping ratio and ω is the natural frequency and n indicates the nth mode.

Table 8.1 Configuration parameters for the different actuators.

Parameter	Unimorph [231,246]	Bimorph	Triple Layer Actuator [247]
$\bar{y}$	$\dfrac{\left(\dfrac{Y_e}{Y_p}\right)h_e^2 + 2h_e h_p + h_p^2}{2\left(\left(\dfrac{Y_e}{Y_p}\right)h_e + h_p\right)}$	h_p	$h_p + \dfrac{h_e}{2}$
YI	$\dfrac{b}{3}\left[\begin{array}{l} Y_e\left(\begin{array}{l}3h_e\bar{y}(\bar{y}-h_e)+\\ h_e^3\end{array}\right)+ \\ Y_p\left(\begin{array}{l}3h_p(\bar{y}-h_e)\times\\ (\bar{y}-(h_e+h_p))+\\ h_p^3\end{array}\right)\end{array}\right]$	$\dfrac{2bY_p h_p^3}{3}$	$\dfrac{2b}{3}\left[\begin{array}{l} Y_e\left(\dfrac{h_e^3}{8}\right)+ \\ Y_p\left(\left(h_p+\dfrac{h_e}{2}\right)^3 - \dfrac{h_e^3}{8}\right)\end{array}\right]$
ρA	$b(\rho_e h_e + \rho_p h_p)$	$b(2\rho_p h_p)$	$b(\rho_e h_e + 2\rho_p h_p)$
α_p	$\dfrac{d_{31}Y_p b}{2h_p}\times$ $\left(h_p^2 + 2h_e h_p - 2\bar{y}h_p\right)$	$\dfrac{d_{31}Y_p b}{2}h_p$	$\dfrac{d_{31}Y_p b}{2}\left(h_p + h_e\right)$
h_{pc}	$\dfrac{1}{2h_p}\left(h_p^2 + 2h_e h_p - 2\bar{y}h_p\right)$	$\dfrac{h_p}{2}$	$\dfrac{h_p + h_e}{2}$
h_E	h_p	$2h_p$	$2h_p$

Table 8.1 provides the configuration parameters that will be used throughout the current derivation. These include: the neutral axis position, $\bar{y}$, the rigidity, *YI*, the mass per unit length, ρA, the voltage loading parameter, α_p, the distance between the neutral axis and PZT layer centre line, h_{pc}, and the thickness defining the electric field, h_E. In the provided expressions within Table 8.1, d_{31} is the piezoelectric constant, *b* is the actuator width, *h* is the thickness, *Y* is the Young's modulus, ρ is the material density and the subscripts *e* and *p* denote the elastic and PZT layers respectively. Note that the unimorph expressions are the most complex due to its non-symmetric configuration. Also, the expressions for the bimorph case can be obtained either by substituting $h_e = h_p$ and $Y_e = Y_p$ in the unimorph expressions or by substituting $h_e = 0$ and $Y_e = 0$ in the triple layer actuator expressions.

For forced oscillations the steady state response of the beam can be obtained using modal analysis making use of the orthogonality of the mode shapes

$$\int_0^l X_n(x)X_m(x)dx = I_n = \int_0^l X_n^2(x)dx \text{ for } n = m, \text{ and is zero for } n \neq m, \tag{8.7}$$

where l is the actuator length. The integral, I_n, can be obtained numerically once the mode shape, $X_n(x)$, is defined for given boundary conditions. Using the orthogonality property, the steady-state solution of Equation 5 is given by [245,254]

$$\delta(x,t) = \sum_{n=1}^{\infty} X_n(x)T_n(t), \tag{8.8}$$

where $T_n(t)$ are determined from [254]

$$\ddot{T}_n(t) + 2\zeta_n\omega_n\dot{T}_n(t) + \omega_n^2 T_n(t) = \frac{1}{\rho A I_n}\int_0^l f(x,t)X_n(x)dx. \tag{8.9}$$

For a uniform cantilever beam the mode shapes are given by [256]

$$X_n(x) = \left(\cosh(\kappa_n x) - \cos(\kappa_n x)\right) - \upsilon_n\left(\sinh(\kappa_n x) - \sin(\kappa_n x)\right), \tag{8.10}$$

whose derivative with respect to x is given by

$$X_n'(x) = \kappa_n\left(\sinh(\kappa_n x) + \sin(\kappa_n x)\right) - \upsilon_n\kappa_n\left(\cosh(\kappa_n x) - \cos(\kappa_n x)\right), \tag{8.11}$$

where

$$\upsilon_n = \frac{\sinh(\kappa_n l) - \sin(\kappa_n l)}{\cosh(\kappa_n l) + \cos(\kappa_n l)}. \tag{8.12}$$

The clamped-free condition leads to the characteristic equation [256]

$$\cos(\kappa l)\cosh(\kappa l) = -1. \tag{8.13}$$

The first two roots of Equation 8.13 are $\kappa_1 l$ = 1.8751 and $\kappa_2 l$ = 4.6941 and the undamped natural frequency of the nth mode is given as

$$\omega_n = \frac{(\kappa_n l)^2}{l^2}\sqrt{\frac{YI}{\rho A}}, \tag{8.14}$$

which is approximately the resonant frequency for light damping.

Whilst there are several expressions available within the literature to represent the clamped-free boundary condition, the above one is chosen for the characteristic of

$$I_1 = l\,, \tag{8.15}$$

and thus the so-called 'generalised mass' [258] appearing on the right hand side of Equation 8.9 becomes the actual actuator mass at the first resonant frequency

$$mass_1 = \rho A I_1 = mass_{act}\,, \tag{8.16}$$

The 'generalised mass' will appear extensively throughout the next steps of the derivation and thus having it simplified for the current application using Equation 8.16 reduces the numerical effort involved in later calculations. Note also that the mode shape expression given by Equation 8.10 has the following useful characteristics

$$X_1(l) = 2 \text{ and } X_1'(l) = 2\kappa_1\upsilon_1\,, \tag{8.17}$$

In order to obtain an expression for $D_{11}(x)$ in Equation 8.4 the force per unit length appearing in the right hand side of Equation 8.5 is expressed to represent an equivalent concentrated harmonic force at the actuator tip [255,258]

$$f(x,t) = Fe^{i\omega t}\delta_D(x-l)\,, \tag{8.18}$$

where $\delta_D(x)$ is the *Dirac delta* function. Thus, the right hand side of Equation 8.9 becomes

$$\frac{1}{\rho A I_n}\int_0^l Fe^{i\omega t} X_n(x)\delta_D(x-l)dx\,. \tag{8.19}$$

Since $Fe^{i\omega t}$ is independent of x it is taken out of the integration and using the *Dirac delta* function property

$$\int_{x_l}^{x_u} f(x)\delta_D(x-a)dx = f(a)\,;\ \text{for } x_l \le a \le x_u\,, \tag{8.20}$$

the right hand side of Equation 8.9 becomes

$$\frac{Fe^{i\omega t} X_n(l)}{\rho A I_n} = \frac{Fe^{i\omega t}}{\rho A} g_1(\kappa_n l)\,, \tag{8.21}$$

where

$$g_1(\kappa_n l) = \frac{X_n(l)}{I_n}. \tag{8.22}$$

Substituting Equation 8.21 back into Equation 8.9 leads to

$$\ddot{T}_n(t) + 2\zeta_n \omega_n \dot{T}_n(t) + \omega_n^2 T_n(t) = F_{eq1} e^{i\omega t},\ F_{eq1} = \frac{g_1(\kappa_n l)}{\rho A} F. \tag{8.23}$$

The particular (steady state) solution of the above differential equation is well known in the vibration literature as [256]

$$\begin{gathered} T_n(t) = A e^{i(\omega t - \vartheta)}, \\ A = \frac{F_{eq1}}{\omega_n^2 \sqrt{(1-r_n^2)^2 + (2\zeta_n r_n)^2}},\ \vartheta = \tan^{-1}\frac{2\zeta_n r_n}{1-r_n^2},\ r_n = \frac{\omega}{\omega_n}. \end{gathered} \tag{8.24}$$

Hence, following Equation 8.8 the first element of the dynamic matrix, $D_{11}(x)$, is obtained as

$$D_{11}(x) = \sum_{n=1}^{\infty} X_n(x) \frac{g_1(\kappa_n l)}{\rho A} \frac{1}{\omega_n^2 \sqrt{(1-r_n^2)^2 + (2\zeta_n r_n)^2}}. \tag{8.25}$$

Now, the second element of the dynamic matrix, $D_{12}(x)$, will be derived. It can be shown that the right hand side of Equation 8.5 (i.e force per unit length) due to a voltage excitation of a bending actuator is given by [244,246,247]

$$f(x,t) = \alpha_p V e^{i\omega t}\left[\frac{d\delta_D(x-l)}{dx} - \frac{d\delta_D(x)}{dx}\right], \tag{8.26}$$

where α_p is given for the different configurations in Table 8.1.Following a similar procedure to that used to derive $D_{11}(x)$, Equation 8.26 is substituted into the right hand side of Equation 8.9 and making use of the *Dirac delta* function property

$$\int_{x_l}^{x_u} \frac{d^n \delta_D(x-a)}{dx^n} f(x)dx = (-1)^n \frac{d^n f(a)}{dx^n};\ \text{for}\ x_l \le a \le x_u, \tag{8.27}$$

the right hand side of Equation 8.9 becomes

$$-\frac{\alpha_p V e^{i\omega t}}{\rho A I_n} X_n'(l) = -\frac{\alpha_p V e^{i\omega t}}{\rho A} g_2(\kappa_n l), \tag{8.28}$$

where

$$g_2(\kappa_n l) = \frac{1}{I_n} X_n'(l) = \frac{g_1(\kappa_n l)}{X_n(l)} X_n'(l). \tag{8.29}$$

Substituting Equation 8.28 back in Equation 8.9 leads to

$$\ddot{T}_n(t) + 2\zeta_n \omega_n \dot{T}_n(t) + \omega_n^2 T_n(t) = F_{eq2} e^{i\omega t},\ F_{eq2} = -\frac{\alpha_p g_2(\kappa_n l)}{\rho A} V. \tag{8.30}$$

Again the solution of the above equation is similar to that given in Equation 8.24; thus, the second element of the dynamic matrix, $D_{12}(x)$, is obtained

$$D_{12}(x) = -\sum_{n=1}^{\infty} X_n(x) \frac{\alpha_p g_2(\kappa_n l)}{\rho A} \frac{1}{\omega_n^2 \sqrt{(1-r_n^2)^2 + (2\zeta_n r_n)^2}}. \tag{8.31}$$

In order to obtain the expression of the third element of the dynamic matrix, $D_{21}(x)$, the relationship between charge, Q, and electric transverse displacement, D_3, is used [241,246,247,255]

$$Q = \int_0^b \int_0^x D_3 dx dz. \tag{8.32}$$

An expression of the electric displacement can be obtained from the equations describing piezoelectricity [241,246,247]

$$\begin{aligned} S_1 &= \frac{1}{Y_p} T_1 + d_{31} E_3, \\ D_3 &= d_{31} T_1 + \varepsilon_{33}^T E_3, \end{aligned} \tag{8.33}$$

where T is the stress, S is the strain and E is the electric field; subscripts 1 and 3 denote the x and y directions, respectively. Using the above equations it can be shown that the electric transverse displacement, D_3, is related to the piezoelectric strain, S_1, and the transverse electric field, E_3, by

$$D_3 = Y_p d_{31} S_1 + \left(\varepsilon_{33}^T - Y_p d_{31}^2\right) E_3, \tag{8.34}$$

with

$$\varepsilon_{33}^{T} = \frac{d_{31}^{2} Y_p}{k_{31}^{2}}, \tag{8.35}$$

where k_{31} is the piezoelectric material transverse electromechanical coupling coefficient [111] (a material property). An expression for S_1 of a piezoelectric actuator can be written as [246,247]

$$S_1 = -h_{pc} \frac{\partial^2 \delta}{\partial x^2}, \tag{8.36}$$

where h_{pc} is defined for the different configurations in Table 8.1. Note that Equation 8.36 is based on the more convenient average strain and not the strain at the top of the piezoelectric layer as adopted in reference [241]. Substituting back with Equations 8.34 and 8.36 into 8.32 leads to

$$Q = \int_0^b \int_0^x \left[Y_p d_{31} \left(-h_{pc} \frac{\partial^2 \delta}{\partial x^2} \right) + \left(\varepsilon_{33}^{T} - Y_p d_{31}^{2} \right) E_3 \right] dx dz . \tag{8.37}$$

Integrating Equation 8.37 with respect to x leads to

$$Q = \int_0^b \left[Y_p d_{31} \left(-h_{pc} \frac{\partial \delta}{\partial x} \right) + \left(\varepsilon_{33}^{T} - Y_p d_{31}^{2} \right) E_3 x \right] dz . \tag{8.38}$$

Performing the remaining integration and substituting the electric field as voltage divided by h_E defined in Table 8.1 gives

$$Q = \left(-d_{31} Y_p b h_{pc} \frac{\partial \delta}{\partial x} \right) + \left(\varepsilon_{33}^{T} - Y_p d_{31}^{2} \right) \frac{V(t)}{h_E} x b . \tag{8.39}$$

It can be proved that the following relation holds for the actuators under consideration

$$\alpha_p = d_{31} Y_p b h_{pc}, \tag{8.40}$$

therefore, the electric charge is

$$Q = -\alpha_p \frac{\partial \delta}{\partial x} + \left(\varepsilon_{33}^{T} - Y_p d_{31}^{2} \right) \frac{V(t)}{h_E} x b . \tag{8.41}$$

In order to obtain the relation between tip force and charge, the displacement, δ, caused by a tip force defined through the element $D_{11}(x)$ is substituted for in the above equation while setting the voltage to zero leading to

$$Q(x,t) = -\sum_{n=1}^{\infty} X_n'(x) \frac{\alpha_p g_1(\kappa_n l)}{\rho A} \frac{1}{\omega_n^2 \sqrt{(1-r_n^2)^2 + (2\zeta_n r_n)^2}} F e^{i(\omega t - \vartheta)} . \tag{8.42}$$

Therefore, the third element of the dynamic matrix $D_{21}(x)$ is obtained as

$$D_{21}(x) = -\sum_{n=1}^{\infty} X_n'(x) \frac{\alpha_p g_1(\kappa_n l)}{\rho A} \frac{1}{\omega_n^2 \sqrt{(1-r_n^2)^2 + (2\zeta_n r_n)^2}} . \tag{8.43}$$

Note that $D_{21}(l)$ has exactly the same value as $D_{12}(l)$; this can be shown from comparing Equations 8.31 and 8.43 making use of Equation 8.29; therefore, the symmetry of the dynamic matrix is guaranteed at the tip

$$D_{12}(l) = D_{21}(l) . \tag{8.44}$$

Finally, to obtain the relationship between charge and voltage, the displacement, δ, caused by voltage defined through the element $D_{12}(x)$ is substituted into Equation 8.41 leading to

$$Q(x,t) = \left[\begin{array}{l} \displaystyle\sum_{n=1}^{\infty} X_n'(x) \frac{\alpha_p^2 g_2(\kappa_n l)}{\rho A} \frac{1}{\omega_n^2 \sqrt{(1-r_n^2)^2 + (2\zeta_n r_n)^2}} + \\ \left(\varepsilon_{33}^T - Y_p d_{31}^2\right) \dfrac{xb}{h_E} \end{array} \right] V e^{i(\omega t - \vartheta)} . \tag{8.45}$$

Therefore, the fourth element of the dynamic matrix, $D_{22}(x)$, is obtained as

$$D_{22}(x) = \sum_{n=1}^{\infty} X_n'(x) \frac{\alpha_p^2 g_2(\kappa_n l)}{\rho A} \frac{1}{\omega_n^2 \sqrt{(1-r_n^2)^2 + (2\zeta_n r_n)^2}} + \left(\varepsilon_{33}^T - Y_p d_{31}^2\right) \frac{xb}{h_E} . \tag{8.46}$$

The expressions presented for the dynamic matrix elements are in the most general form and can be used for the electromechanical behaviour evaluation of piezoelectric actuators of different configurations and subjected to different boundary conditions. However, because the main concern of the current work is towards the tip behaviour of cantilever actuators operating at the first resonant frequency, the expressions of the dynamic matrix elements reduce to

$$D_{11}(l) = X_1(l)\frac{g_1(\kappa_1 l)}{\rho A}\frac{1}{\omega_1^2\sqrt{(1-r_1^2)^2+(2\zeta_1 r_1)^2}}. \tag{8.47}$$

$$D_{12}(l) = D_{21}(l) = -X_1(l)\frac{\alpha_p g_2(\kappa_1 l)}{\rho A}\frac{1}{\omega_1^2\sqrt{(1-r_1^2)^2+(2\zeta_1 r_1)^2}}. \tag{8.48}$$

$$D_{22}(l) = X_1'(l)\frac{\alpha_p^2 g_2(\kappa_1 l)}{\rho A}\frac{1}{\omega_1^2\sqrt{(1-r_1^2)^2+(2\zeta_1 r_1)^2}} + \left(\varepsilon_{33}^T - Y_p d_{31}^2\right)\frac{lb}{h_E}. \tag{8.49}$$

Using the mode shape properties given in Equations 8.16 and 8.17, the above equations reduce to

$$D_{11}(l) = \frac{4}{mass_{act}}\frac{1}{\omega_1^2\sqrt{(1-r_1^2)^2+(2\zeta_1 r_1)^2}}. \tag{8.50}$$

$$D_{12}(l) = D_{21}(l) = -X_1'(l)\frac{2\alpha_p}{mass_{act}}\frac{1}{\omega_1^2\sqrt{(1-r_1^2)^2+(2\zeta_1 r_1)^2}}. \tag{8.51}$$

$$D_{22}(l) = \left(X_1'(l)\right)^2\frac{\alpha_p^2}{mass_{act}}\frac{1}{\omega_1^2\sqrt{(1-r_1^2)^2+(2\zeta_1 r_1)^2}} + \left(\varepsilon_{33}^T - Y_p d_{31}^2\right)\frac{lb}{h_E}. \tag{8.52}$$

Using the above expressions and following Equation 8.3, an expression for the dynamic EMCF of piezoelectric actuators at the first resonant frequency (i.e. r_1=1) can be obtained as

$$k^2 = \frac{D_{12}^2(l)}{D_{11}(l)D_{22}(l)} = \frac{B}{B+C}, \tag{8.53}$$

where

$$B = \left(X_1'(l)\right)^2\frac{\alpha_p^2}{mass_{act}}\frac{1}{\omega_1^2(2\zeta_1)}. \tag{8.54}$$

$$C = \left(\varepsilon_{33}^T - Y_p d_{31}^2\right)\frac{lb}{h_E}. \tag{8.55}$$

It is noteworthy that the presented expressions for the bimorph and triple layer actuators consider the series connection case. As for parallel connection $D_{11}(l)$ will remain the same; however, $D_{12}(l)\big|_{parallel} = 2D_{12}(l)\big|_{series}$, and $D_{22}(l)\big|_{parallel} = 4D_{22}(l)\big|_{series}$. Therefore, the expression for the EMCF in parallel connection remains the same as that given in Equation 8.53.

8.4 Experimental Verification

In this section, an experimental setup to measure the dynamic actuation of unimorphs will be presented. Only unimorph actuators will be measured due to the easiness of their preparation from commercial available diaphragms. The objectives of this experiment are to: (1) identify the level of damping ratio required within the dynamic model, (2) validate possible aspects of the dynamic model given the available measurement facilities, (3) evaluate the EMCF experimentally making use of Mason's formula (Equation 8.1) and compare with the EMCF values obtained later in Section 8.5 from the dynamic model.

The test specimens used in the current study are five unimoph actuators of the same width and thickness, but different lengths, Figure 8.2. The elastic layer is brass and the active layer is PZT (Murata PIEZOTITE ceramic, P-7 [259]). The test specimens were manufactured from commercially available diaphragms (Murata Manufacturing Co., Ltd., Part number: 7BB-35-3L0 [259], Figure 8.2a). This provides a fast and cost effective way to prepare beams of different lengths; however, it limits the ability to vary the thicknesses of the elastic and PZT layers. Table 8.2 provides typical properties of the prepared unimorph beams.

Table 8.2 Typical properties of the measured unimorph beams.

Geometric properties	
length, l (mm)	16, 18, 20, 22, 24
width, b (mm)	4.5
elastic layer thickness, h_e (mm)	0.3
active layer thickness, h_p (mm)	0.23
Elastic layer material properties	
material	Brass
Young's modulus, Y_e (GPa)	110
density, ρ_e (kg/m^3)	8600
Active layer material properties	
model	Murata PIEZOTITE ceramic
type	PZT, P-7
Young's modulus, Y_p (GPa)	63
density, ρ_p (kg/m^3)	7800
electromechanical coupling, k_{31}	0.38
piezoelectric constant, d_{31} (10^{-12} m/V)	-207
maximum voltage (V)	15

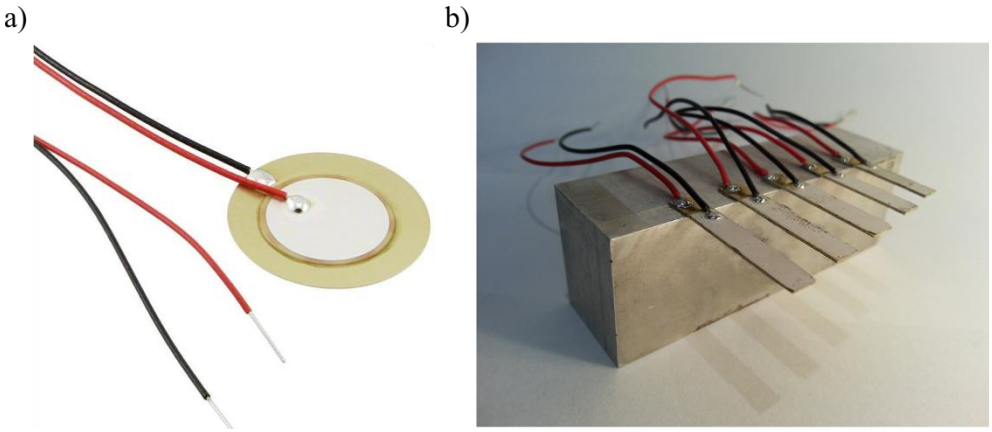

Figure 8.2 (a) Piezoelectric diaphragms used to manufacture the unimorph beams. (b) Unimorph cantilever beams used during the measurements. Each beam is 4.5 mm wide.

Figure 8.3 shows the experimental apparatus. Beam oscillation displacement was measured using a Polytec PDV-100 laser vibrometer. The input sinusoidal signal to the beams was generated using a TTi TG200 20 MHz DDS function generator amplified using a TREK PZD350 Piezo Driver/Amplifier. The measurement setup was managed through LabVIEW. Data acquisition was conducted within the frequency range appropriate for each measurement/beam combination with 1 Hz resolution.

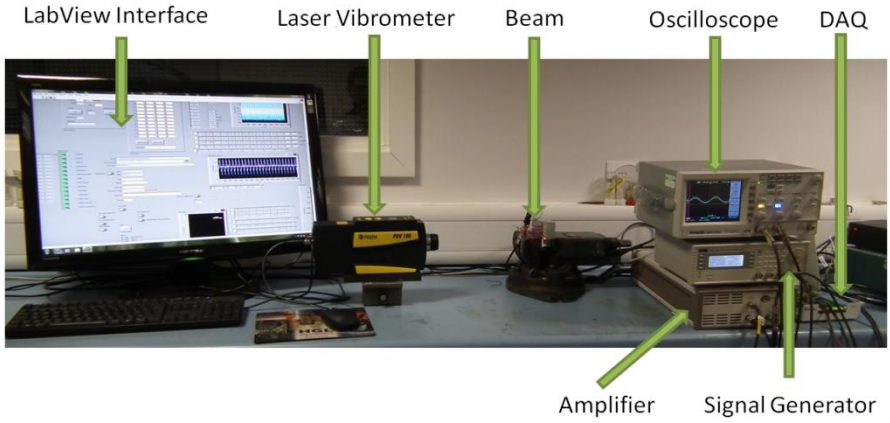

Figure 8.3 The piezoelectric unimorph actuator measurement setup.

Firstly, the fundamental frequency and associated mode shape were measured for each beam, Figure 8.4. A comparison of the measured first resonant frequency with that evaluated from the model (Equation 8.14) is shown in Figure 8.4a. Also, Figure 8.4b shows the experimental and theoretical mode shapes for the 24 mm beam. The theoretical mode shape is obtained from Equation 8.10, and the experimental mode shape is obtained by measuring the amplitude of the deflection along the beam while

operating around the first resonant frequency. Both results show good agreement between the model and the experimental measurements.

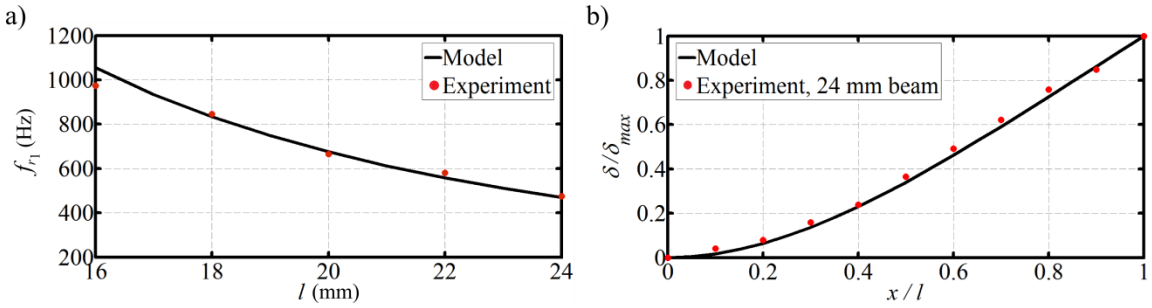

Figure 8.4 (a) Fundamental bending resonant frequency variation with the beam length having all other variables fixed. (b) Fundamental mode shape of the 24 mm beam; δ is the amplitude of deflection along the beam length and δ_{max} is the amplitude of deflection at the beam tip.

Next, measurements were conducted to characterise the damping ratio at first resonant frequency based on an evaluation of the harmonic vibration response

$$\zeta_1 = \frac{(f_2 - f_1)}{2 f_{r1}}, \tag{8.56}$$

where f_{r1} is the first resonant frequency, and f_1 and f_2 are the half-power point frequencies where the response is 0.707 of the maximum [254]. Figure 8.5a shows the measured tip velocity in the range around the first resonant frequency for the 16 mm beam at different input voltage amplitudes. The response is weakly nonlinear with voltage, with the first resonant frequency decreasing as the voltage increases. This observation was also reported by Wang *et al.* [260]. The damping ratios for the 16 mm beam were higher than those of other beams. For this reason the 16 mm beam results are used to exemplify the variation of damping ratio with voltage in Figure 8.5b. For this case, the damping ratio increases with increasing voltage, and varies between 0.011 and 0.022.

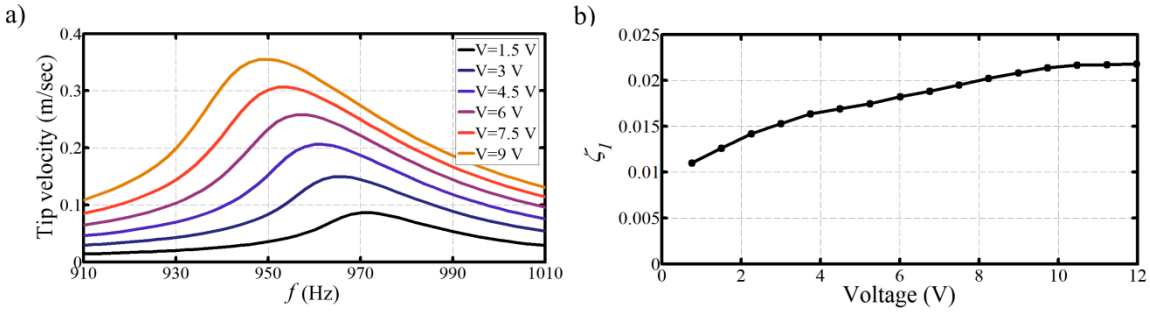

Figure 8.5 (a) Measured tip velocity of the 16 mm actuator plotted against driving frequency at several driving voltage amplitudes. (b) Variation of damping ratio with voltage amplitude for the 16 mm beam. Note that, an input signal greater than 12 V yields tip velocities higher than the measurable limits of the vibrometer.

Having obtained the damping coefficient values at the different voltage levels, the second element of the dynamic matrix, $D_{12}(x)$, can now be used to relate the driving voltage to the output displacement. Figure 8.6a compares the measured tip deflection amplitude of the 24 mm unimorph due to a 7.5 voltage amplitude signal with that evaluated from the theoretical model using the expression of $D_{12}(l)$. Over the range of frequencies considered, a very good agreement is evident. Figure 8.6b compares the measured and modelled tip deflection amplitude at the fundamental bending resonant frequency as a function of the input voltage amplitude for the 16 mm and 24 mm unimorphs. Note that the resonant frequency of the beam shifts slightly with the voltage amplitude (Figure 8.5a); thus, the experimental values in Figure 8.6b are the measured beam tip deflection values at the fundamental resonant frequency corresponding to each voltage amplitude.

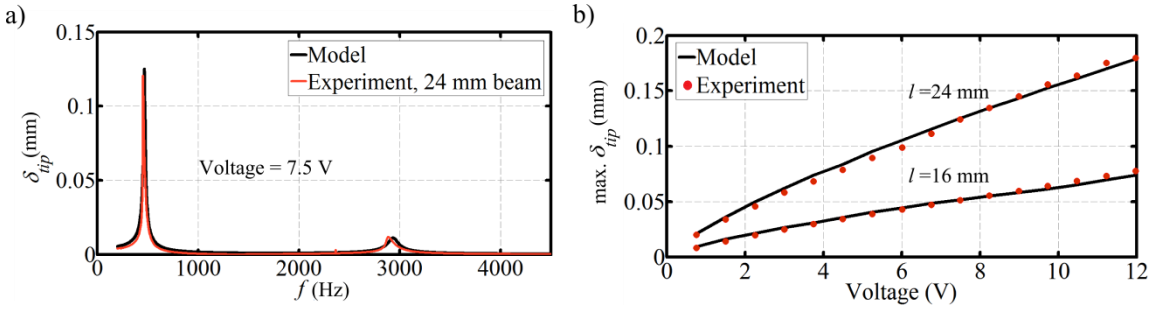

Figure 8.6 (a) Tip deflection amplitude of the 24 mm actuator for the first two modes. (b) Tip deflection amplitude of the 16 mm and 24 mm actuators at their fundamental (first) resonant frequency as a function of the input voltage amplitude.

Finally, the tip velocity to harmonic voltage excitation frequency response function (FRF) was measured for each of the five beam specimens, with the objective of

determining the anti-resonant frequencies required in Mason's formula (Equation 8.1). Figure 8.7 shows the FRF for measurements with an input voltage amplitude of 7.5V, representing a mid-range value for the input signal.

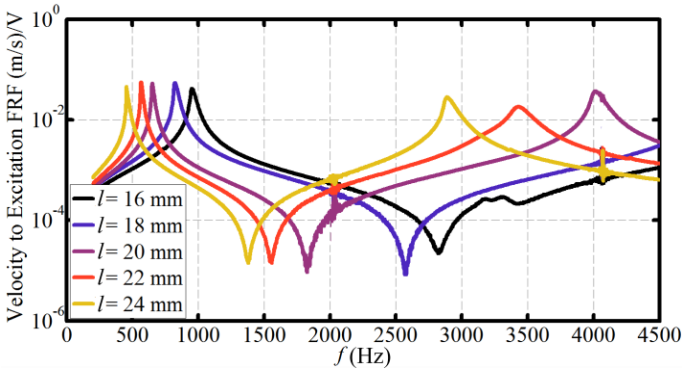

Figure 8.7 Experimental tip velocity to harmonic voltage excitation FRF of the five beams. The voltage level is 7.5 V for all beams.

Table 8.3 shows that the variation of the EMCF using Equation 8.1 for the different beam specimens is minimal and an average value of 0.88 ± 0.013 (mean ± s.d.) can be assigned for all beams. Note that varying the voltage level changes the resonant and anti-resonant frequencies slightly; however, the EMCF value from Mason's formula remains almost unchanged. The important outcome here is that the average value for the dynamic EMCF is significantly higher than that for static operation. This will be discussed in the next section, which will focus on evaluating the dynamic EMCF for unimorphs using the derived dynamic model.

Table 8.3 Unimorph actuators EMCF at excitation level of 7.5 V.

l (mm)	f_{r1} (Hz)	f_{a1} (Hz)	k^2 Eqn. 8.1
16	954	2822	0.88
18	824	2568	0.9
20	650	1826	0.87
22	566	1558	0.87
24	454	1380	0.89

8.5 Electromechanical Coupling in Dynamic Operation

The electromechanical coupling factor, k^2, was discussed comprehensively in Section 8.2 as an important measure for piezoelectric device performance. Here, the EMCF in

dynamic operation will be evaluated using the derived expression of Equation 8.53. It should be noted that the results presented in this section are all based on the theoretical model of Equation 8.53. Within this equation, the material properties and damping levels will be selected to be similar to those from the experiments. Note that, the dynamic k^2 from Equation 8.53 is evaluated at the first resonant frequency as this condition provides maximum tip deflection which is consistent with the objective of the current application.

The current analysis shows that the dynamic EMCF of piezoelectric actuators depends only on: (1) the Young's modulus of the elastic and active layers, (2) the thicknesses of the elastic and active layers, (3) the damping ratio, ζ_1 and 4) the PZT layer material transverse electromechanical coupling coefficient, k_{31} (Note that the first two factors do not apply to the bimorph case). In what follows, the influence of each of these four factors on the dynamic EMCF will be discussed in detail.

8.5.1 Young's modulus and thickness ratios effects

For the current analysis, unimorphs made of the same active layer but with different passive layer materials are considered; the active layer material properties used are Y_p=63 GPa and k_{31}=0.38. Figure 8.8a shows the unimorph dynamic EMCF plotted against elastic/piezo thickness ratio for different elastic materials for a damping ratio of 0.005 representing the lower end of damping obtained from experiments. The overall trend is a rapid increase in EMCF as the thickness ratio increases from zero, with a peak reached at an optimum thickness ratio; beyond this, the EMCF decreases slightly as the thickness ratio increases. The effect of increasing elastic material stiffness is to shift the thickness ratio for peak EMCF (optimum thickness ratio) to the left. This optimum thickness ratio is found to vary only with the Young's modulus ratio of the elastic and active layers, Figure 8.8b. Decreasing damping ratio increases the peak value of EMCF however does not affect the thickness ratio at which it occurs. Stiffer elastic material leads to higher peak EMCF values; however, at very low damping ratios, the peak EMCF for different stiffness ratio values are relatively closer.

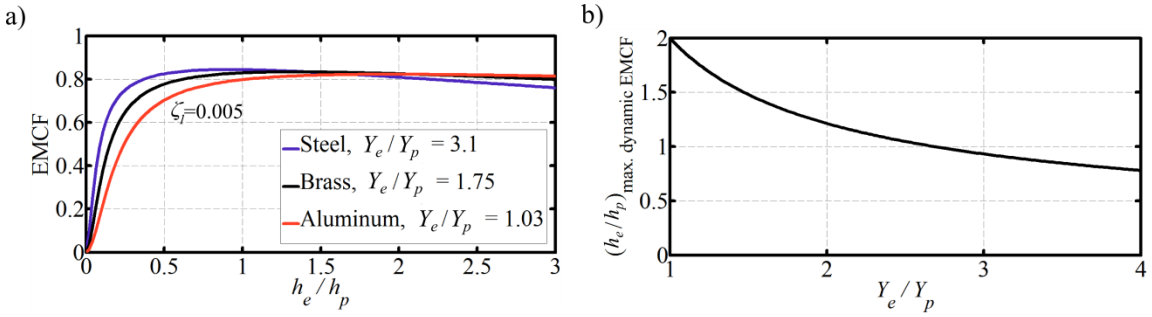

Figure 8.8 (a) Unimorph dynamic EMCF as function of (passive/active) layer thickness ratio for different passive layer materials for a damping ratio of 0.005. The active layer material properties are Y_p=63 GPa and k_{31}=0.38. (b) Dynamic operation optimum thickness ratio variation with the Young's modulus ratio for unimorphs.

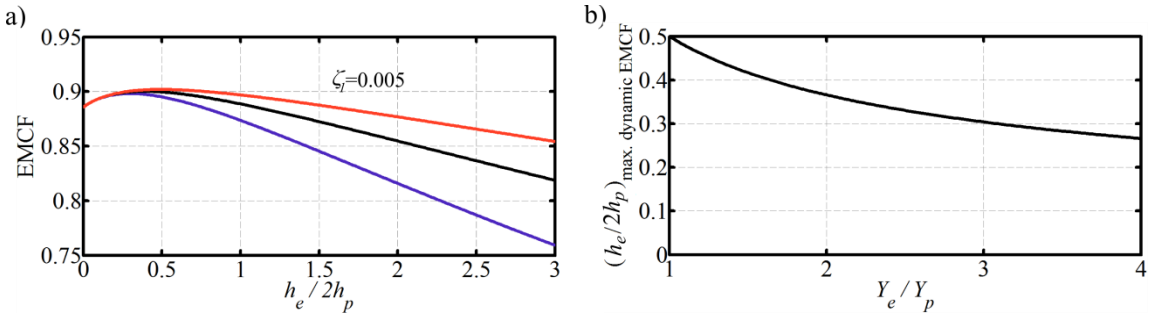

Figure 8.9 (a) Triple layer actuator dynamic EMCF as function of (passive/active) layer thickness ratio for different passive layer materials for a damping ratio of 0.005. The active layer material properties are Y_p=63 GPa and k_{31}=0.38. Blue is for a steel elastic layer, black is for brass, and red is for aluminum. (b) Dynamic operation optimum thickness ratio variation with the Young's modulus ratio for triple layer actuators. Note the difference in scales between Figure 8.8 and 8.9.

Figure 8.9a shows the triple layer actuator dynamic EMCF plotted against elastic/piezo thickness ratio for different elastic materials for a damping ratio of 0.005. Here, the thickness ratio is defined as the elastic layer thickness to the total piezo layers thickness. The same active layer properties of the unimorph case are used for performance comparison. Note that, the zero thickness ratio case represents the bimorph performance. It can be clearly seen that bimorphs can achieve better EMCF values compared to unimorphs (also see Figure 8.11a), and that there is an optimum thickness ratio for the triple layer actuator through which it can achieve higher EMCF values compared to bimorphs. Again, this optimum thickness ratio is found to vary only with the Young's modulus ratio of the elastic and active layers, Figure 8.9b. Similar to unimorphs, the effect of increasing elastic material stiffness is to shift the thickness ratio for peak EMCF (optimum thickness ratio) to the left. Decreasing damping ratio

increases the peak value of EMCF however does not affect the thickness ratio at which it occurs. Unlike unimorphs, stiffer elastic material leads to lower EMCF values; however, at very low damping ratios, the EMCF for different stiffness ratio values are relatively closer.

8.5.2 Damping ratio and k_{31} effects

The effect of the damping ratio is shown for the different actuators in Figures 8.10a, 8.11a and 8.12a. It can be seen for all cases that as the damping ratio decreases, the EMCF values increases. A similar analysis using several materials but based on the static equations showed that a typical unimorph or bimorph actuator can only achieve EMCF values up to 0.08 for unimorphs and 0.11 for bimorphs [111], which is an order of magnitude less than the peak EMCF values shown here. This highlights the important role damping plays in determining the achievable performance of such actuators in dynamic operation: piezoelectric actuators achieve high dynamic EMCF values when subjected to light damping. These high EMCF values are similar to EMCF values obtained experimentally using Mason's formula.

The effect of the PZT layer transverse electromechanical coupling coefficient on the dynamic EMCF is similar to the damping ratio effect, Figures 8.10b, 8.11b and 8.12b. It also scales the EMCF curve up (higher k_{31}) and down (lower k_{31}) without influencing the EMCF shape variation against the (elastic/active) thickness ratio. This is demonstrated for a range of values of electromechanical coupling coefficients that is typical of currently available actuators.

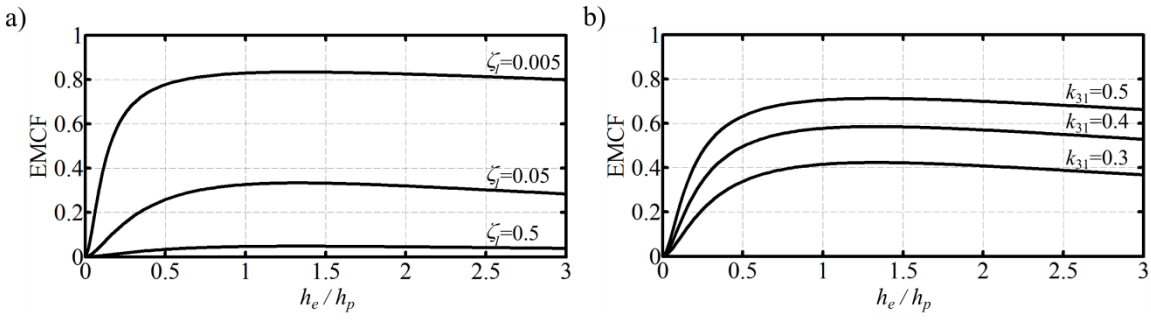

Figure 8.10 Unimorph dynamic EMCF as function of (passive/active) layer thickness ratio for a brass passive layer and an active layer of Y_p= 63 GPa. (a) Effect of damping ratio, k_{31}=0.38. (b) Effect of the PZT layer transverse electromechanical coupling coefficient, ζ_1 =0.02.

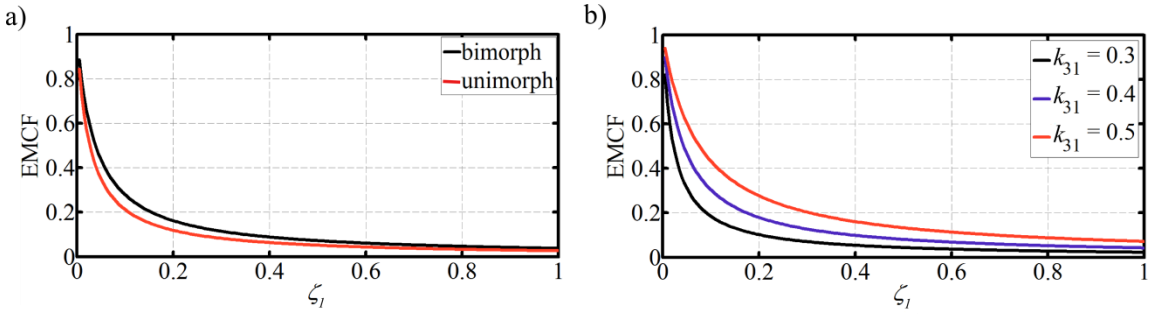

Figure 8.11 Bimorph dynamic EMCF. (a) Effect of damping ratio, k_{31}=0.38. The EMCF of an optimum thickness unimorph with steel passive layer is shown for reference. Practically, this unimorph configuration can achieve the best EMCF values; thus, the superiority of bimorphs against unimorphs is demonstrated. (b) Effect of the PZT layer transverse electromechanical coupling coefficient for bimorphs.

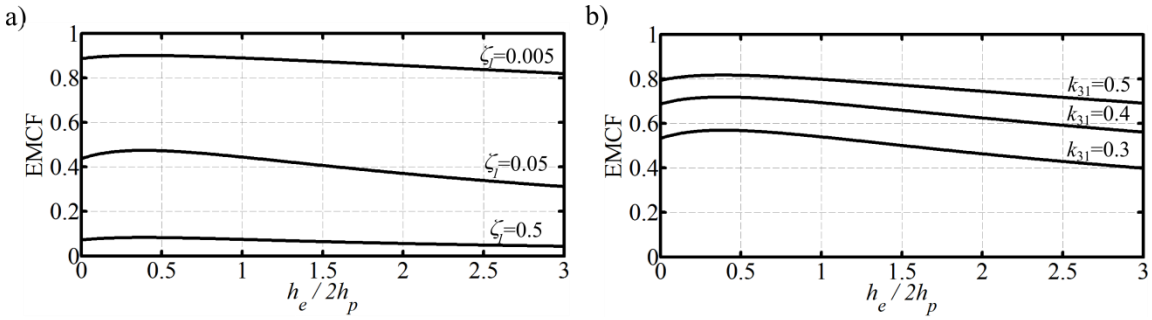

Figure 8.12 Triple layer actuator dynamic EMCF as function of (passive/active) layer thickness ratio for a brass passive layer and an active layer of Y_p= 63 GPa. (a) Effect of damping ratio, k_{31}=0.38. (b) Effect of the PZT layer transverse electromechanical coupling coefficient, ζ_1 =0.02.

8.5.3 Equivalent static EMCF

Lastly, the static and dynamic EMCF at equivalent conditions are compared. There is a damping ratio at which the piezoelectric actuator dynamic electromechanical coupling is equal to the static one. Figure 8.13 compares the static EMCF (based on equations in Appendix C) with the dynamic EMCF at a damping ratio of 0.44 and 0.425 for a unimorph and a triple layer actuator respectively. Both actuators have an elastic layer made from brass and an active layer with Y_p= 63 GPa. The static and dynamic curves are the same and have the same peak value showing that for practical purposes the optimum thickness ratio for static operation is the same as that for dynamic operation.

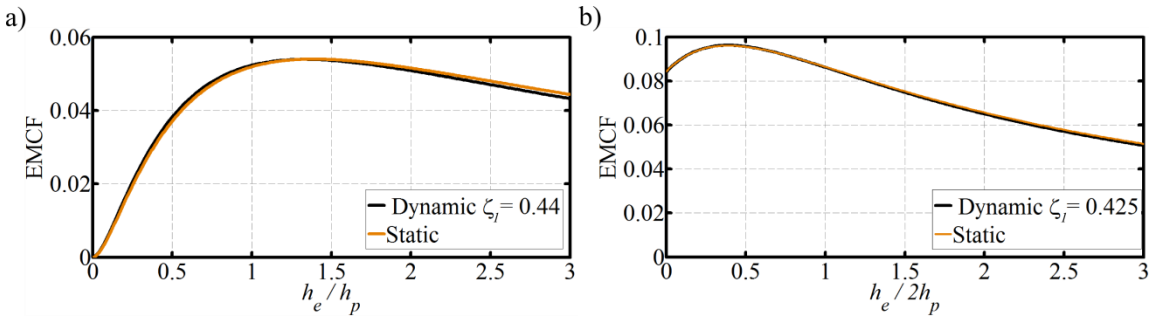

Figure 8.13 EMCF plotted for (a) a unimoph and (b) a triple layer actuator at static and equivalent dynamic condition. The elastic layer is made of brass and the active layer(s) made with material of Y_p=63 GPa and k_{31}=0.38.

8.6 Chapter Conclusions

A comprehensive analytical model of the dynamic electromechanical behaviour of a piezoceramic bending actuator has been derived and successfully validated against experimental data. The model provides a mapping between force, displacement, voltage and charge. Damping is modelled using experimental data. Experimental validation is based on measurement of mode shape and frequency response of a series of unimorph beams of varying length but of the same thickness and material. The experimental frequency response is weakly nonlinear with excitation voltage, with a reduction in natural frequency and increase in damping with increasing excitation amplitude.

An analytical expression for the EMCF extracted from the model is used as the objective for parametric design studies. It is found that the shape of variation of EMCF with thickness ratio for a given piezoelectric actuator geometry is the same for both static and dynamic operation, meaning that an actuator optimised for static operation with respect to maximising EMCF will also be optimal for dynamic operation. However, the achievable values of the EMCF for dynamic operation are dependent on damping ratio.

For unimorphs and triple layer actuators, a peak value of EMCF occurs at an optimal thickness ratio that varies only with the Young's modulus ratio of the elastic and active layers of the actuator. Increasing elastic layer material Young’s modulus shifts the optimal thickness ratio to the left (thinner elastic layer). For unimorphs, increasing the thickness ratio beyond the optimal value (increasing elastic layer thickness) has a relatively minor effect on the achievable EMCF for practical actuator configurations. However for triple layer actuators, increasing the thickness ratio beyond the optimal

value is more influential on the achievable EMCF compared to unimorphs. Thus operation at the optimal thickness ratio is more crucial for the triple layer actuator. A triple layer actuator with an optimum thickness ratio can achieve higher peak EMCF value compared to bimorphs. A bimorph, in turn, can achieve higher peak EMCF compared to optimum unimorph configurations.

For all actuators considered in this chapter, the achievable magnitude of EMCF is increased by decreasing the damping ratio and/or increasing k_{31}. However, for unimorphs and triple layer actuators, the thickness ratio for given material properties at which maximum EMCF is achieved is independent of both damping ratio and k_{31}. As the actuator damping is reduced towards zero, EMCF is decreasingly sensitive to thickness ratio for practical actuator configurations and tends towards a value of unity.

9

Sizing of Piezoelectric Actuators for Insect-Scale Flapping Wing Vehicles

In this chapter, a low order transparent design method for preliminary design of the propulsion system of insect-scale flapping wing vehicles is presented. The design method is an integration of the different models developed throughout this thesis. The propulsion system drive chain is modelled as a damped second order dynamic system operated at resonance. The design method allows designers to explore the interaction between electric, mechanical and aerodynamic domains in a single design environment. Design scaling laws and mass breakdown using the available data are presented. Data from flapping insects are used as an indicator of the feasible space whilst not considered the best. The process is illustrated using three design points based on all up weights of 50, 500 and 5000 mg. The process is also used to assess the performance of unimorph configuration against that of triple layer actuator configuration. Important insights are delivered regarding the feasible design space for such class of air vehicles.

9.1 Introduction

Integrated design of resonant flapping wing vehicles presents a particular challenge to propulsion system drive train design due to the need to match the dynamics of the actuator with the wing via a suitable mechanical transmission mechanism. Given the level of analytical challenge and the relative immaturity of micro electro mechanical systems the current focus of most piezoelectric driven flapping wing design efforts is on achieving the basic requirement of lift greater than or equal to weight in hover and establishment of basic stability and control. This situation is not dissimilar to the status for powered flight at the beginning of the 20th Century.

The aim of this chapter is to develop a low order preliminary design method for the propulsion system of piezoelectric insect-scale flapping wing vehicles. The design process is based on the developments in analytical modelling of piezoelectric bending actuators, flapping wing aerodynamics, and flapping wing kinematics presented throughout this thesis. The main design contribution is the preliminary sizing of the piezoelectric actuator that forms the heart of the propulsion system. The level of uncertainty in technology specific weight estimates is currently high due to lack of historically successful vehicles upon which mass estimation heuristics can be based. There is also considerable uncertainty associated with manufacturing. Given the absence of engineering heuristic data, both data from insects to benchmark engineered designs are used. Whilst engineering solutions may outperform biologically evolved forms in the long run, the current effort focuses on achieving weight support in hover as a primary goal.

A visualisation of an insect-scale flapping wing vehicle of the same weight and wing loading as a bumble bee based on the design process that will be presented in this chapter is shown in Figure 9.1. Note that for this class of vehicles at current technology levels the wing design in term of planform and kinematics is very similar to that of insects whereas the actuation and power systems are very different.

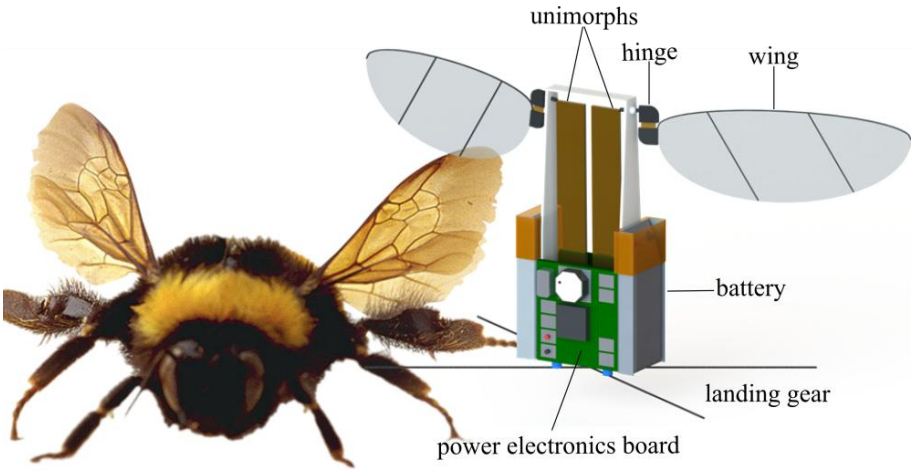

Figure 9.1 (a) Illustration of the general arrangement of a piezoelectric flapping wing vehicle concept. The vehicle all up weight, wing loading and kinematic parameters are set to that of a bumble bee [145]. Primary design constraint is $L=W$. Primary design output is actuator sizing. The power electronics board shown is a scaled model of the board presented in [261,262]. The batteries are an illustration based on scaling of existing LiPo batteries.

Two requirements are asked of the design process here: (1) that it is fully physics based for the actuator sizing, and (2) the underlying equations are cast in dimensionless form to facilitate understanding of the underlying laws.

In what follows, Section 9.2 defines the general arrangement, the expected mass ratios of the different vehicle components, the general configuration of the vehicle and the operational kinematics. Section 9.3 provides details of the major design models of the process including aerodynamics, system dynamics simulation, actuator sizing and electromechanical performance estimation. Section 9.4 explores the design space through a sensitivity analysis to demonstrate the influence of the main design variables on the outputs of the design process. Finally, conclusions are provided in Section 9.5.

9.2 Design Problem Setup

9.2.1 General arrangement description

The vehicle propulsion system is based on the provision of a separate piezoelectric actuator for each wing. As part of the design selection process both unimorphs and triple layer actuators are considered in this work, Figure 9.2. These actuator configurations provide a good balance between performance, ease of fabrication and reliability for the proposed application at current technology levels.

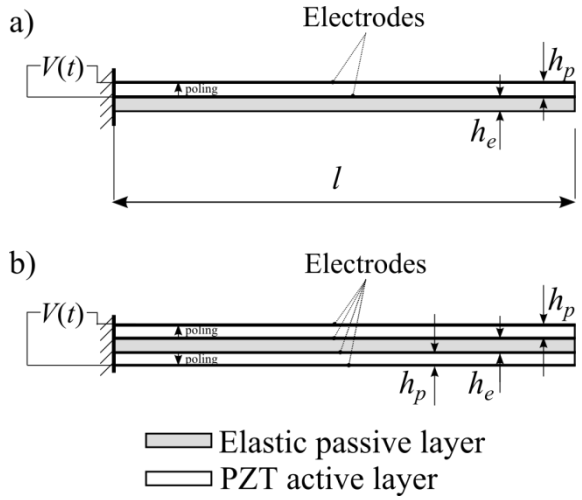

Figure 9.2 Schematic drawing of piezoelectric bending actuators considered for the design process; (a) unimorph and (b) triple layer actuator.

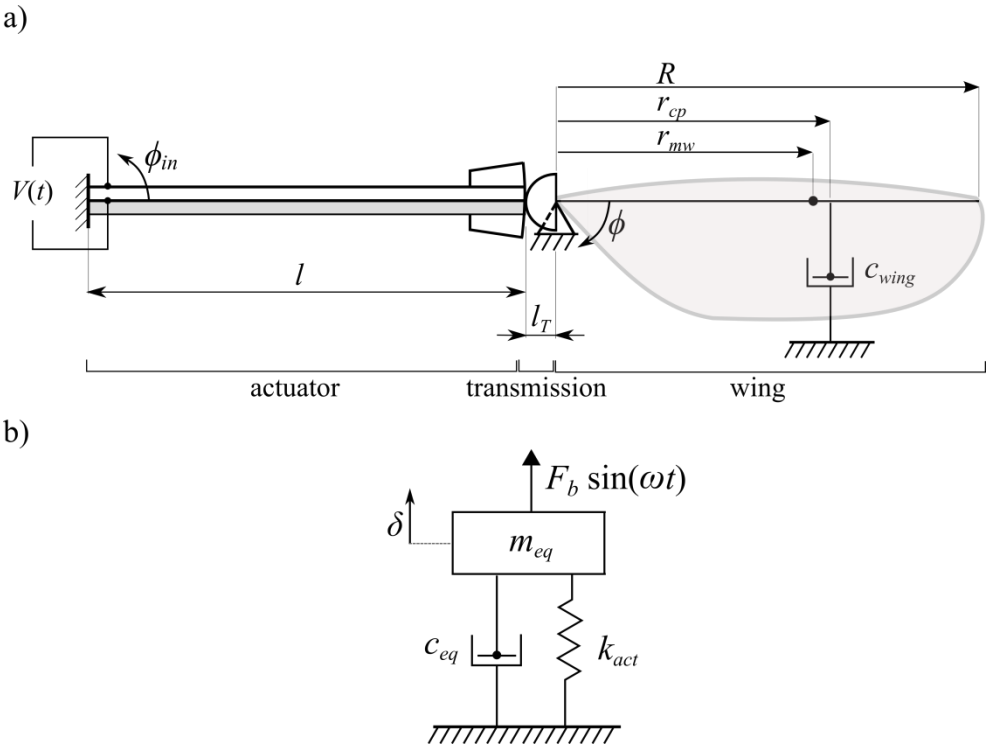

Figure 9.3 (a) Schematic drawing of the propulsion system. The actuator shown is a unimorph, the transmission is assumed to have a constant transmission ratio, and the wing contribution is represented as inertial and damping elements. (b) Linear, single degree of freedom, lumped parameter model for systems dynamics simulation.

The transmission element is required for efficient matching of the low impedance load (wing) with high impedance source (piezoelectric actuator/muscle). In biological systems (insects), the transmission between muscle and wing is through a relatively complex system of flexures. By their nature, flexure systems are non-linear at the high

output angle displacements (± 90°) required for aerodynamically efficient flapping flight as discussed in Chapter 3. For the present work, the transmission is modelled as a linear system with constant transmission/gear ratio. The transmission is illustrated as a geared system in Figure 9.3a for clarity. The work can be extended to accommodate non-linear transmission designs through appropriate linearisation, e.g. as undertaken in [91,229].

The geared transmission is assumed to be mass-less and loss-less. The flapping angle, ϕ, can be related to the actuator tip displacement, δ using

$$\phi(t) = G\phi_{in}(t) \cong G\hat{\delta}(t), \tag{9.1}$$

where,

$$G = \frac{l}{l_T} \text{ and } \hat{\delta}(t) \cong \frac{\delta(t)}{l}, \tag{9.2}$$

where, G is the gain of the transmission, l_T is the transmission output radius, and l is the transmission input radius equivalent to the actuator length. Note that in practice the actuator tip does not follow an exactly circular path; however due to the small actuator deflection compared to the actuator length, deviations are small enough to ignore.

It is useful to define two non-dimensional quantities to support the current modelling approach. First is the wing mechanical advantage, *MA*, which appears within the system dynamics expressions for wing inertia and damping. It is defined as

$$MA = \frac{R}{l_T}, \tag{9.3}$$

where R is the wing length. The second non-dimensional quantity is a ratio named *Actuator Length Ratio* denoted by *ALR* and defined as

$$ALR = \frac{l}{R}. \tag{9.4}$$

Thus, based on the above definitions the following relations can be written

$$G = ALR \times MA, \tag{9.5}$$

and

$$\phi(t) \cong MA\frac{\delta(t)}{R} \text{ and } \delta(t) \cong \frac{\phi(t)R}{MA}. \tag{9.6}$$

In this work, it is chosen to constrain the design space by setting the *ALR* to unity. This decision is based on a practicality argument: increasing the length of the actuator helps in terms of increasing the available tip displacement for a given thickness of the piezoelectric layer [231]; however, as the actuator becomes long compared to the wing length, it starts to become the limiting factor on vehicle overall compactness. A dimensionless *ALR* of around unity appears to be a good compromise based on existing successful designs (see for example [87,100]: the Harvard Microrobotic Fly had an actuator length of 13 mm and a wing length around 12 mm). Within insects, it is found that the average body length to wing length is around unity (see Table 2 of [141]). As an incidental outcome, the choice of a unity *ALR* leads to some simplification of the mathematics in that *G* becomes equal to *MA*.

9.2.2 Mass breakdown

An aircraft conceptual design process requires an estimate of the all up (total takeoff) weight as well as the main weight fractions contributing to this takeoff weight [263]. Here, it is chosen to use the following mass breakdown developed by Whitney and Wood [229]

$$m_{total} = m_{bats} + m_{acts} + m_{other}, \tag{9.7}$$

where m_{total} is the total vehicle mass, m_{bats} refers to the mass of the batteries, m_{acts} is the mass of the two piezoelectric actuators and m_{other} includes the payload mass, the wing mass, the airframe mass or any sensor mass, etc. The mass fraction, μ_{other} ($\mu_{other}=m_{other}/m_{tot}$) is chosen to be one of the design variables in the current design process and it typically takes a value in the range $0.25 \le \mu_{other} \le 0.35$ [10,229]. Following [10,229], the remaining mass is assumed to split equally between the batteries and the actuators

$$\mu_{bats} = \mu_{acts} = \frac{(1-\mu_{other})}{2}, \tag{9.8}$$

and thus the mass fraction of a single actuator is

$$\mu_{act} = \frac{\mu_{acts}}{2} = \frac{(1-\mu_{other})}{4}. \tag{9.9}$$

The above mass breakdown is based on current practice, however should be considered as a place holder till more data from successful designs is present.

9.2.3 Design scaling laws

It is useful to obtain scaling laws that allow insight into how the design space varies with physical scale. Figure 9.4 shows a log-log plot for the wing length, *R*, against the weight for different insect species as well as for available resonant flapping wing concepts. The insect data are based on [145] and were given in Table 3.1, whereas those of insect-like flapping wing concepts are based on the collected data in Table 2.3. It is important to note that all resonant flapping wing concepts were tether powered and thus the weight shown in Figure 9.4 is based on the empty mass

$$m_{empty} = m_{total} - m_{bats} = m_{acts} + m_{other}\,. \tag{9.10}$$

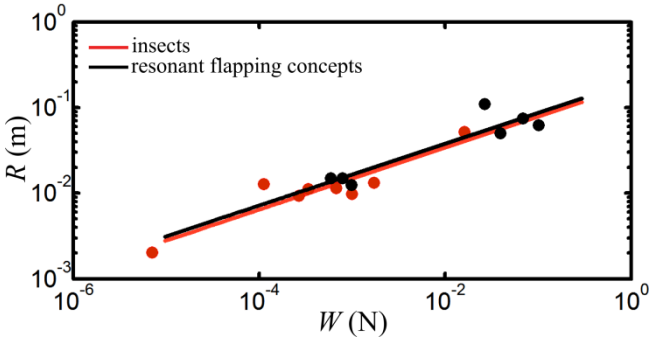

Figure 9.4 Scaling of size with weight for insects and resonant flapping wing concepts. Weight of flapping wing concepts is based on empty weight (all up weight minus batteries weight).

Based on the data shown in Figure 9.4, the following scaling laws are obtained

$$R_{ins} = 0.1794 W_{ins}^{0.3617},\ n = 8,\ R^2 = 0.85 \tag{9.11}$$

$$W_{ins} = 17.902 R_{ins}^{2.3519},\ n = 8,\ R^2 = 0.85 \tag{9.12}$$

$$R_{NAV} = 0.1977 W_{empty,NAV}^{0.3599},\ n = 7,\ R^2 = 0.845 \tag{9.13}$$

Note that, the exponent of the wing length in Equation 9.12 is slightly less than 3, where 3 is the volume exponent if the scaling constant is the effective density. It is important again to mention that the derived scaling laws here should be considered as place holders within the design process till more data for flapping wing nano air vehicles (NAVs) are available.

9.2.4 Wing configuration

For the purpose of design, the wing is considered as a thin, rigid plate mounted on a fulcrum via a single rotational degree of freedom along the flapping axis. The wing has a second rotary degree of freedom in pitch along the wing spanwise axis. In the present model, it is assumed that this latter degree of freedom is passive (unactuated), however is free to move in response to wing aerodynamic and inertial forces generated through the flapping motion. The dynamics of the pitch degree of freedom are not included within the overall system model. However, the underlying physics is captured through constraint of pitch motion kinematics to that possible with a passive hinge.

The wing has an effective mass m_{wing} located at the wing structure radius of gyration r_{mw} giving a moment of inertia I_{wing} about the flapping axis of

$$I_{wing} = m_{wing} r_{mw}^2 . \tag{9.14}$$

The wing effective mass fraction of a single wing is constrained to be within the range $0.01 \le \mu_{wing} \le 0.03$ based on observed values from insects [145]. The wing effective mass contains the effects of wing structural inertia, $m_{w,s}$, and wing aerodynamic inertia, $m_{w,a}$, [86] such that: $m_{wing} = \left(m_{w,s} + m_{w,a} r_{mw,a}^2 / r_{mw}^2\right)$, with $m_{w,a} = \rho_{air} \frac{\pi}{4} \bar{c}^2 R$, where ρ_{air} is the air density, $\bar{c}$ is the mean geometric chord and $r_{mw,a}^2 = R^2 \int_0^1 \left(c(\hat{r})/\bar{c}\right)^2 \hat{r}^2 d\hat{r}$, where $\hat{r} = r/R$.

Note that the wing aerodynamic inertia is usually neglected within the literature e.g. [56,91,229,264] since it is typically much smaller compared to the structural wing inertia.

Regarding the wing radius of gyration, if the wing structural mass is assumed to be distributed uniformly along the spanwise axis then $r_{mw} = R/\sqrt{3} = 0.5774R$. As a reference point, the Harvard Microrobotic Fly (HMF) wing has a R equal to 11.95 mm and m_{wing} equal 0.91 mg [100]. The estimated value of I_{wing} calculated from Equation 9.14 is 43.32 mg.mm^2, which compares acceptably well with the reported wing inertia of 45.3 mg.mm^2 [91]. Additionally Roll *et al.* [265] experimentally measured the radius of gyration of 16 wing candidates made of mylar film spanned over unidirectional carbon fibre frame. They measured the wing inertia based on the undamped compound pendulum formula as proposed by Ellington [141]. The obtained non-dimensional

radius of gyration values ranged between 0.47 to 0.61with an average value of 0.56 which again compares well with the assumed value of 0.577.

The wing planform shape is defined using Ellington's beta function representation [141]. Three variables are required for the chord distribution definition: the wing length, *R*, the wing aspect ratio, *AR* (which defines the mean chord, $AR = R/\bar{c}$) and the non-dimensional radial location of the wing centre of area, $\hat{r}_1$. The chord distribution is thus given by

$$c(r) = \bar{c}\left(\frac{\hat{r}^{\,p-1}(1-\hat{r})^{q-1}}{\int_0^1 \hat{r}^{\,p-1}(1-\hat{r})^{q-1} d\hat{r}} \right),\ \hat{r} = \frac{r}{R}, \tag{9.15}$$

where the parameters are chosen as

$$p = \hat{r}_1\left(\frac{\hat{r}_1(1-\hat{r}_1)}{\hat{r}_2^2 - \hat{r}_1^2} - 1 \right), q = p\frac{(1-\hat{r}_1)}{\hat{r}_1}, \hat{r}_2 = 0.929(\hat{r}_1)^{0.732}, \hat{r}_3 = 0.9(\hat{r}_1)^{0.581} \tag{9.16}$$

where $\hat{r}_1$, $\hat{r}_2$ and $\hat{r}_3$ are the non-dimensional radii of first, second and third moments of wing area respectively. The value of $\hat{r}_1$ is selected as a design variable within the current design process whose value ranges between 0.4 and 0.6. As discussed in Chapter 5, from an aerodynamic point of view, a wing with $\hat{r}_1$ of 0.4 allows higher *lift coefficient* values whereas a wing with $\hat{r}_1$ of 0.6 produces a higher lift force due to the more area towards the tip where the velocity is higher.

Higher values of the wing aspect ratio are known to improve the aerodynamic induced effects. However as the aspect ratio increases there can be insufficient chord length to allow smooth flow reattachment on the wing upper surface necessary to prevent shedding of the LEV, and thus the wing losses its ability to generate sufficient flight lift coefficients. Also structurally, higher aspect ratio leads to higher moment of inertia which directly influences the system resonance frequency. These are probably the main reasons why insect wing aspect ratios are most clustered between 3 and 4 [141,214]. Thus, a typical constant value of 3.5 will be used for the aspect ratio in the current model (Note that this value was recommended by Ellington for MAV candidates [214] and was the wing aspect ratio value of the HMF [100]).

Finally, an important aerodynamic wing characteristic that will be required within the system dynamics simulation is the non-dimensional spanwise location of the wing centre of pressure, $\hat{r}_{cp}$. The centre of pressure location determines the lever arm for aerodynamic moment calculation around the wing root, and is calculated here based on: $\hat{r}_3^3 / \hat{r}_2^2$.

9.2.5 Operational kinematics

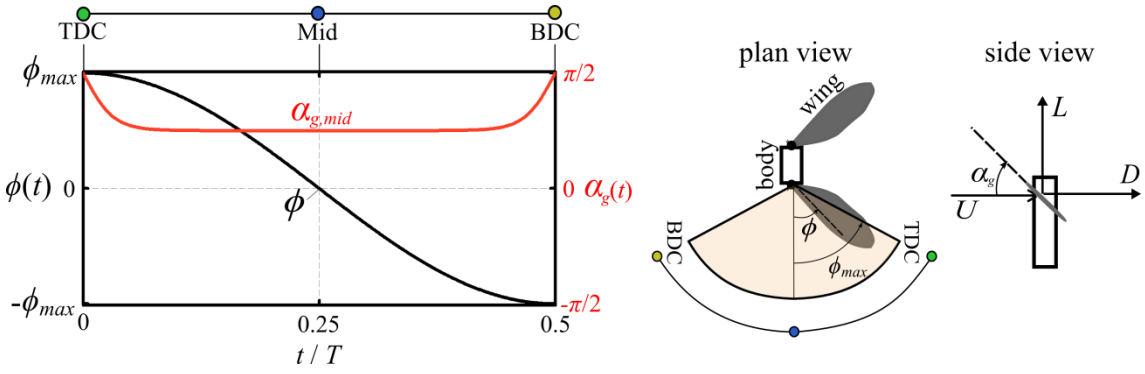

Figure 9.5 Wing kinematics used within the design process. Owing to the symmetry of half-strokes, only the down-stroke is shown. Value of $\alpha_{g,mid}$ set by physical end stops within the wing passive pitch mechanism.

The current process assumes symmetric normal hovering flight with the wings moving along the horizontal stroke plane with symmetrical half strokes and no deviation from the original stroke plane. It is assumed that the flapping angle time variation is sinusoidal and the pitching angle variation (defining the geometric angle of attack variation) is trapezoidal-like, Figure 9.5. This model is similar to that found in insects [145,171,172,266] and similar waveforms have been successfully implemented on insect-scale flapping wing vehicles using passive control of wing pitch [100]. These kinematics have also been shown to be approaching the optimum variations for aerodynamic effectiveness as shown in Chapter 7.

9.3 The Design Process

9.3.1 Aerodynamic model

The current study only focuses on the aerodynamics of hovering flight for several reasons: (1) hovering flight is necessary for takeoff and landing of flapping wing

vehicles and is typically the main driver for propulsion system sizing. (2) Relatively simple expressions for the lift and power requirements can be derived owing to the absence of the forward speed component. (3) Several forward flight performance characteristics such as the maximum speed and range can be estimated once the hovering requirements are identified [214,229]. The aerodynamic model adopted here is based on a quasi-steady treatment which provides an appropriate balance between accuracy and simplicity for preliminary design. The instantaneous lift and drag forces on a single flapping wing are given by

$$L = \frac{1}{2}\rho_{air}\left(\dot{\phi}(t)\hat{r}_2 R\right)^2 (R^2/AR) C_L(\alpha_g(t)), \tag{9.17}$$

$$D = \frac{1}{2}\rho_{air}\left(\dot{\phi}(t)\hat{r}_2 R\right)^2 (R^2/AR) C_D(\alpha_g(t)), \tag{9.18}$$

where the lift and drag coefficients, C_L and C_D, are defined in terms of the geometric angle of attack, α_g, based on the well-established non-linear expressions

$$C_L(\alpha_g(t)) = C_T \sin(2\alpha_g(t)) \cong C_T \sin(2\alpha_{g,mid}), \tag{9.19}$$

$$C_D(\alpha_g(t)) = 2C_T \sin^2(\alpha_g(t)) \cong 2C_T \sin^2(\alpha_{g,mid}), \tag{9.20}$$

where C_T is the translational lift coefficient which depends primarily on the wing shape and Reynolds number. The value of C_T is evaluated based on the method proposed in Chapter 4 as

$$C_T = \left(\frac{0.5 C_{l\alpha,2d}}{E + \frac{k C_{l\alpha,2d}}{\pi AR}} \right). \tag{9.21}$$

The two dimensional aerofoil lift curve slope, $C_{l\alpha,2d}$, takes the value 0.09 deg^{-1} for flat plate wings at typical insect Reynolds numbers [195]. The parameter E is the quotient of the wing semi perimeter to its length. The parameter k is the induced power factor included to correct for the difference in efficiency between assumed ideal uniform downwash distribution and real downwash distribution, and is evaluated based on the method proposed in Chapter 3. Thus unlike previous efforts [100,229], the current model accounts for the induced effects of the insect-like wing flows.

It is important to mention that the above aerodynamic relations are most accurate within the Reynolds number range $1000 \le \mathrm{Re} \le 15000$ [142]. Aerodynamics at higher

Reynolds numbers can be dominated by turbulent mixing which may cause the LEV to be unstable with periodic shedding limiting the maximum achievable lift coefficients [154,215]. On the other hand, if the Reynolds number is significantly lower than this range, viscous effects may play a role that cannot be neglected [148] (see also discussion of Appendix A).

For the given kinematics and using the method developed in Chapter 7, an analytical expression can be obtained for the average lift produced by the two wings as

$$\bar{L} = \rho(R^2\hat{r}_2^2)(2R\bar{c})(C_T \sin(2\alpha_{g,mid}))\left(\phi_{\max}^2 \pi^2 f^2\right). \tag{9.22}$$

Using the above equation, the required flapping frequency, *f*, can be calculated to satisfy a weight ($W=m_{tot}g$) requirement as

$$f = \sqrt{\frac{16W}{\rho\pi^2 \underbrace{(4\phi_{\max} R\hat{r}_2)^2}_{\propto U_{mean}^2} \underbrace{(2R^2/AR)}_{S} \underbrace{(C_T \sin(2\alpha_{g,mid}))}_{C_L}}}. \tag{9.23}$$

Use of Equation 9.23 to predict the flapping frequency of the Harvard Microrobotic Fly described in [98] (mass = 80 mg, $\phi_{\max}$ =55°) gives a flapping frequency of 119.7 Hz, which is very close to the actual frequency of 120 Hz.

Given the relationship between weight and wing size for insects identified in Equation 9.12, the relationship in 9.23 can be used to provide an estimate of the likely flapping frequency as a function of insect size (*R*) only. This frequency can then be used as a comparator for the flapping frequency calculated as part of the design process for a vehicle at the same scale. This is not to say that the insect derived value of frequency is the correct one, rather it informs the designer how close a candidate solution is to existing viable solutions.

To enumerate the reference frequency, the following parameter values are used: $\hat{r}_2$ =0.56, *AR*=3.5, C_L=1.1 and $\phi_{\max}$ =90°. Values for $\hat{r}_2$, *AR* and C_L are insect average values from [145]. The 90° value for $\phi_{\max}$ is only attained by few insects, however it represents an aerodynamic optimum, useful for comparison purposes. Thus, the obtained relation for the reference frequency, f_{ref} is

$$f_{ref} = 1.7448R^{-0.82405}, \tag{9.24}$$

where *R* is in meters.

9.3.2 System dynamics simulation

The actuator output is represented as a force, F_{act}, acting at the free end (tip) of the actuator that gives the equivalent torque to that produced by the inverse piezoelectric effect [91,235]. Thus,

$$F_{act} = F_b \sin(\omega_{res} t) = F_b \sin(2\pi f t), \tag{9.25}$$

where F_b is the actuator blocking force. It is assumed here that the actuator viscous damping is minor compared to the aerodynamic damping generated from the wing. Thus the system governing equation can be written as

$$m_{eq}\ddot{\delta} + c_{eq}\dot{\delta} + k_{act}\delta = F_b \sin(2\pi f t). \tag{9.26}$$

The actuator stiffness, k_{act}, can be calculated from the beam relation [267]

$$k_{act} = \frac{3(YI)_{act}}{l^3}, \tag{9.27}$$

where $(YI)_{act}$ is the actuator rigidity which for a unimorph configuration is given by

$$(YI)_{act} = \frac{b}{3}\left[Y_e\left(3h_e\bar{y}(\bar{y}-h_e)+h_e^3\right)+Y_p\left(3h_p(\bar{y}-h_e)(\bar{y}-(h_e+h_p))+h_p^3\right)\right], \tag{9.28}$$

where b is the actuator width, Y is the Young's modulus, h is the thickness and the subscripts e and p denote the elastic and PZT layers respectively and for unimorphs the neutral axis position, $\bar{y}$, is given by

$$\bar{y} = \frac{\left(\frac{Y_e}{Y_p}\right)h_e^2 + 2h_e h_p + h_p^2}{2\left(\left(\frac{Y_e}{Y_p}\right)h_e + h_p\right)}. \tag{9.29}$$

Furthermore, the mass of the unimorph actuator is given by

$$m_{act} = lb(\rho_e h_e + \rho_p h_p), \tag{9.30}$$

where ρ is the material density. For a triple layer actuator configuration the rigidity is given by

$$(YI)_{act} = \frac{2b}{3}\left[Y_e\left(\frac{h_e^3}{8}\right) + Y_p\left(\left(h_p + \frac{h_e}{2}\right)^3 - \frac{h_e^3}{8}\right)\right], \tag{9.31}$$

and the actuator mass is given by

$$m_{act} = lb(\rho_e h_e + 2\rho_p h_p)\,. \tag{9.32}$$

However, the effective actuator mass, $m_{act,ef}$, at the actuator tip within the lumped parameter system, as given by Lord Rayleigh, is [267]

$$m_{act,ef} = \frac{33}{140} m_{act}\,. \tag{9.33}$$

Thus, the equivalent system mass, m_{eq}, that also takes into account the wing effective inertia [229] can be written as

$$m_{eq} = m_{act,ef} + \left(\tfrac{1}{3} m_{wing} MA^2\right). \tag{9.34}$$

Finally, an expression for the equivalent system damping, c_{eq}, is derived. Taking the moment around the fulcrum point [229] it can be shown that the damping force on the actuator is given by

$$F_{damp} = D\hat{r}_{cp} MA\,, \tag{9.35}$$

where, the drag force, D, is given by Equation 9.18. By substituting Equation 9.6 into 9.18, the drag force on a single wing can be expressed as a function of the actuator displacement, δ, as

$$D = \left(\frac{1}{2}\rho_{air}\hat{r}_2^2\left(R^2/AR\right)C_D(\alpha_{g,mid})MA^2\right)\mathrm{sgn}(\dot{\delta})\dot{\delta}^2\,. \tag{9.36}$$

Therefore the actuator damping force can be expressed as

$$F_{damp} = \underbrace{\left(\frac{1}{2}\rho_{air}\hat{r}_2^2\hat{r}_{cp}\left(R^2/AR\right)C_D(\alpha_{g,mid})MA^3\right)}_{K_D}\mathrm{sgn}(\dot{\delta})\dot{\delta}^2\,, \tag{9.37}$$

where K_D is the damping constant. Clearly, Equation 9.37 is nonlinear; however, a linearised expression for the equivalent damping can be obtained following the equivalent viscous-damping method [256] where an approximation to the steady state

oscillation can be made. This is achieved by equating the aerodynamic energy dissipated per cycle to that of an equivalent linear viscous damping leading to

$$c_{eq} = \frac{8}{3\pi} K_D \omega_{res} \delta_{\max}, \tag{9.38}$$

where δ_{max} can be obtained using

$$\delta_{\max} \cong \frac{\phi_{\max} R}{MA}. \tag{9.39}$$

The above expressions thus allow a direct evaluation of the required blocking force magnitude, F_b, to achieve δ_{max} while operating at system resonance:

$$F_b = \frac{8}{3\pi} K_D (2\pi f)^2 \delta_{\max}^2. \tag{9.40}$$

9.3.3 Actuator sizing and electromechanical coupling characteristics

An important aspect of the design process is the selection of the actuator materials and dimensions. In Chapter 8, it has been shown that a peak value of the electromechanical coupling factor (EMCF) occurs at an optimal thickness ratio, and this optimal thickness ratio varies only with the Young's modulus ratio of the elastic and active layers for the actuator. Increasing the elastic layer material Young's modulus allows higher peak EMCF values and thus higher energy transmission coefficient (ratio of output mechanical energy to input electrical energy) for a unimorph actuator. Polynomial fitting has been applied to the optimum thickness ratio curve in Figure 8.8b, and for a unimorph actuator the following quartic polynomial is obtained

$$h_e = h_p \left(0.0278 \left(\frac{Y_e}{Y_p} \right)^4 - 0.3411 \left(\frac{Y_e}{Y_p} \right)^3 + 1.6035 \left(\frac{Y_e}{Y_p} \right)^2 - 3.615 \left(\frac{Y_e}{Y_p} \right) + 4.3084 \right). \tag{9.41}$$

For a triple layer actuator, the curve fitting was applied to Figure 8.9b and the following polynomial was obtained

$$h_e = h_p \left(0.006 \left(\frac{Y_e}{Y_p} \right)^4 - 0.075 \left(\frac{Y_e}{Y_p} \right)^3 + 0.3748 \left(\frac{Y_e}{Y_p} \right)^2 - 0.9534 \left(\frac{Y_e}{Y_p} \right) + 1.645 \right). \tag{9.42}$$

Both relations have an R^2 value of 1 over the (Y_e/Y_p) range between 1 and 4, and thus are excellent fits for the obtained theoretical results of Chapter 8.

Recall that the actuator length with respect to wing size is fixed a priori. In order to obtain the values of the actuator width and thicknesses, two other equations in addition to Equation 9.41 or 9.42 have to be satisfied. The first is the actuator mass equation, either Equation 9.30 for unimorphs or Equation 9.32 for triple layer actuators. The second is for the system resonance frequency:

$$\omega_{res} = 2\pi f = \sqrt{\frac{k_{act}}{m_{eq}}}\,. \tag{9.43}$$

Satisfaction of equations for the optimum thickness ratio, actuator mass and system resonance frequency thus determines the values of the actuator width, the PZT active layer thickness and the elastic layer thickness simultaneously. These equations are non-linear algebric equations in three variables, and were solved using a custom non-linear solver developed in Matlab®. The solver error was consistently of the order ~ 10^{-12} confirming that the problem was well posed and solutions were accurate.

For piezoelectric bending actuators, the admittance matrix relating the driving parameters (force and voltage) to the response parameters (deflection and charge) was derived in Chapter 8. The first row of this matrix relates blocking force magnitude to the voltage magnitude. After some simplification the following result is obtained

$$F_b = d_{31} Y_p b h_{pc} \left(\frac{1.37651}{l}\right) V_{\max} \tag{9.44}$$

where d_{31} is the piezoelectric constant and h_{pc} is the distance between the neutral axis and PZT layer centre line which for unimorphs is given as

$$h_{pc} = \frac{1}{2h_p}\left(h_p^2 + 2h_e h_p - 2\bar{y}h_p\right), \tag{9.45}$$

whereas for triple layer actuators is given as

$$h_{pc} = \frac{h_p + h_e}{2}\,. \tag{9.46}$$

Now that the required actuator drive voltage is known, preliminary design of the vehicle power electronics system can be undertaken. Related to this, the designer also

needs to assess the actuator field strength at the calculated design point. Increasing field strength enables greater output from the actuator, but ultimately there is a technology dependent limit due to dielectric breakdown and/or piezoelectric depolarisation. The limit to the maximum electric field strength is dependent on the PZT material, the duration of application and operating temperature. Manufacturers usually provide typical operating limits of 1000 V/mm [268]; however, there are some piezoelectric actuators that can sustain up to 2500 V/mm [77]. For unimorphs, the field strength is given by

$$E_3 = \frac{V_{\max}}{h_p}, \tag{9.47}$$

whereas for a triple layer actuator is calculated from

$$E_3 = \frac{V_{\max}}{2h_p}. \tag{9.48}$$

Finally, the system *Q* factor can be estimated from

$$Q = \frac{1}{2\zeta_{eq}}, \tag{9.49}$$

where

$$2\zeta_{eq} = \frac{c_{eq}}{m_{eq}\omega_{res}}, \tag{9.50}$$

9.3.4 The calculation process

Here, both design parameters and design variables within the design process are referred to. Design parameters are those values that are constant within the design process as material physical constants or fundamental constants as the gravitational acceleration. A summary of the parameters used within the design process and their nominal values is provided in Table 9.1. Design variables are model states that change with inputs or varying parameters. For the current problem in hand, six design variables are used. Their lower and upper bounds as well as their nominal values are given in Table 9.2.

Table 9.1 Design parameters included within the design process and their available nominal values.

Parameter	Sym.	Type	Value	Comment
Actuator Length Ratio	*ALR*	geometric	1	Driven by vehicle form factor requirement
Wing aspect ratio	*AR*	geometric	3.5	For LEV attachment, and is an average value for biological and robotic insects
Mid half-stoke geometric angle of attack	$\alpha_{g,mid}$	kinematic	45 (deg)	For maximum *lift* effectiveness
Piezo-layer Young's modulus	Y_p	material	63 (GPa)	Based on PZT typical characteristics [111,231]
Piezo-layer density	ρ_p	material	7800 ($kg.m^{-3}$)	Based on PZT typical characteristics [111,231]
Piezoelectric constant	d_{31}	material	-320 (10^{-12} m/V)	Based on PZT typical characteristics [77,111]
elastic-layer Young's modulus	Y_e	material	195 (GPa)	Based on steel characteristics
elastic-layer density	ρ_e	material	7800 ($kg.m^{-3}$)	Based on steel characteristics

Table 9.2 Design variables included within the design process with their lower, upper and nominal values.

Variable	Sym.	Type	Lower bound	Nominal value	Upper bound
Takeoff mass	m_{total}	inertia	50 (mg)	500 (mg)	5000 (mg)
Other components mass fraction	μ_{other}	inertia	0.25	0.3	0.35
Wing effective mass fraction	μ_{wing}	inertia	0.01	0.02	0.03
Wing centre of area	$\hat{r}_1$	geometric	0.4	0.5	0.6
Flapping angle amplitude	ϕ_{max}	kinematic	20 (deg)	45 (deg)	70 (deg)
Transmission gain	*G*	Transmission	5	10	15

A summary of the design process in a form similar to that of a preliminary design diagram [263] is shown in Figure 9.6.

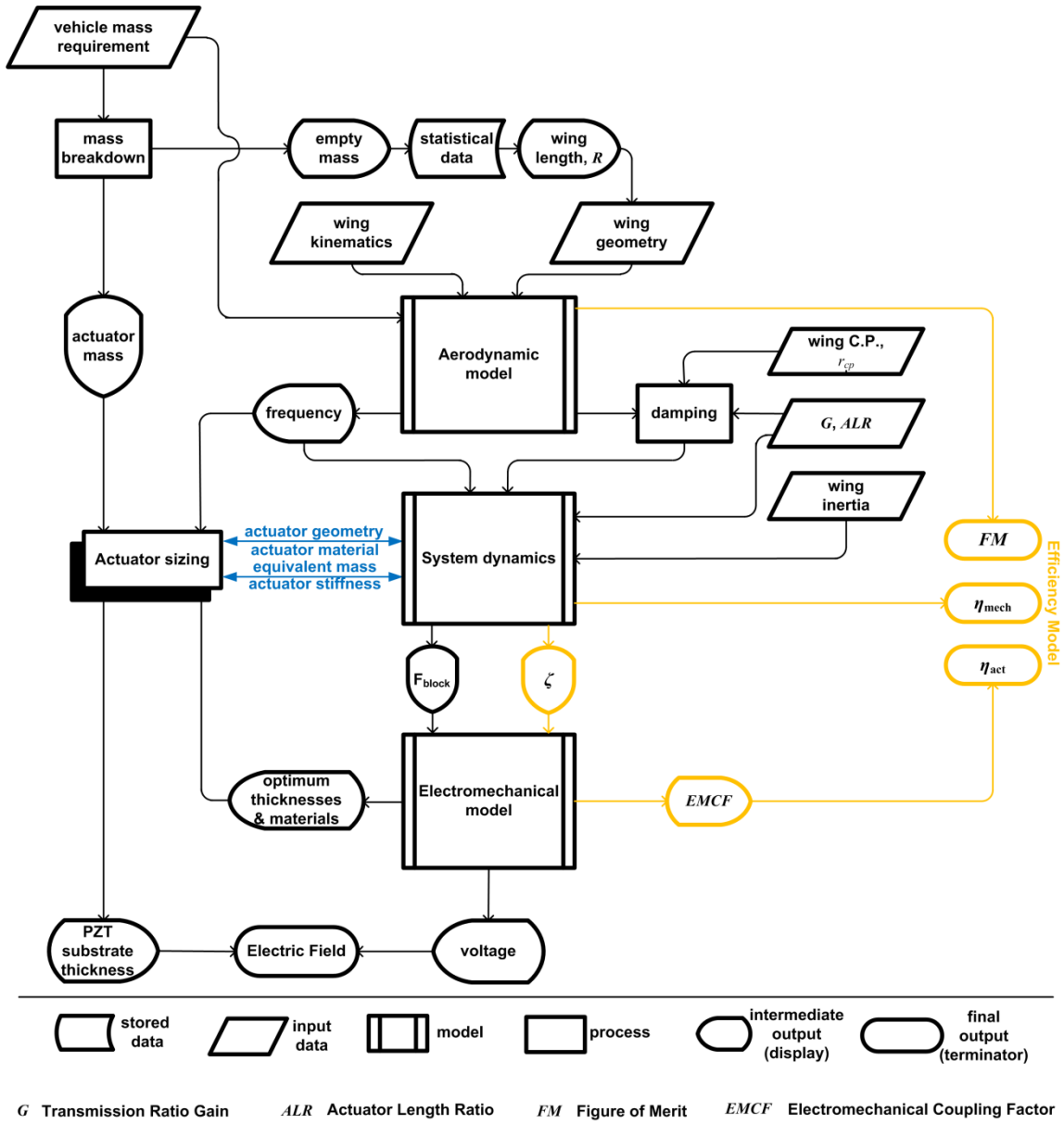

Figure 9.6 Insect-scale flapping wing vehicle design process. The processes shown in orange are not considered in the current framework. The main output of the process is sizing of the piezoelectric actuator.

The design process starts with input of a total takeoff mass requirement. Based on the mass breakdown explained in Section 9.2.2, the actuator mass budget and the vehicle empty mass are determined. The empty weight is then used within the developed statistical relation (Equation 9.13) to determine the wing length, *R*. This is then fed together with total vehicle mass, wing kinematics and wing geometry variables and parameters into the aerodynamic model. The main two outputs of the aerodynamic model are the value of the system resonance frequency that would allow weight support and the damping constant, K_D. Given the actuator length ratio, *ALR* and the transmission

gain, G, the wing mechanical advantage, MA, is determined. The value of the maximum tip actuator displacement, δ_{max}, is then evaluated and consequently the required blocking force, F_b. The actuator sizing process is then undertaken to evaluate the actuator dimensions. Finally, the required voltage amplitude is evaluated and subsequently the electric field strength, E_3.

It is important to recognise that the current design process is driven by the weight support requirement without consideration of the efficiency of the system components. Whilst this would be overly simplistic for design of existing classes of fixed and rotary wing flight vehicles, this is believed to be appropriate for current technology flapping wing vehicles for two reasons: (1) the primary goal at the current time is to build methods and procedures that will allow self supported hovering flapping flight from piezoelectric actuated flapping robotic insects. (2) The efficiency of flappers at this scale is low anyhow. For example, in Chapter 8, the EMCF values were shown to decrease significantly as the damping ratio increases. Given the expected operational damping ratios, the EMCF is expected to be low and thus piezoelectric actuation efficiency will be even lower [111,231] with an expected electrical to mechanical efficiency of the actuator including power electronics to be around 10% [229]. Therefore, given the problem in hand, detailed consideration of efficiency at this design stage becomes less critical.

9.4 Results

In this section, a sensitivity analysis is used to develop an understanding of the relationships between design variables and main outputs of the design process, Figure 9.7. Within this figure, the design variables are presented on the x-axis and the design outputs are on the y-axis. Design variables and outputs are given in dimensionless form (apart from the field strength for which there is no convenient value to normalise against). Recognising the importance of choice of all up weight (and hence, according to inbuilt scaling relationships, physical scale and flapping frequency) the sensitivity analysis is run for three different mass values (50, 500 and 5000 mg). The results in each column of the sensitivity analysis are obtained by variation of the design variable for that column alone whilst all other variables are fixed to their nominal values given in Table 9.2.

There are a number of points that need to be checked before interpretation of the results in Figure 9.7. First the Reynolds number, Re, should be within the range of validity of the aerodynamic model. In the present case, the Re is in the range $1000 \leq \mathrm{Re} \leq 15000$ which is acceptable based on the discussion in Section 9.3.1.

The second check point is the actuator aspect ratio (beam length to thickness) which is favourable to be greater than 30 [269] in the Euler-Bernoulli formulation for the actuator electromechanical characterisation model. In the present analysis (judged from Figure 9.7iv), the actuator aspect ratio satisfies this requirement for the different variations of the design variables.

The third check point of this demonstration is the values of the Q factor which at the nominal design variables values has a value of the order of 10 or lower. This means a system damping ratio, ζ_{eq}, of 0.05 or higher. These values are an order of magnitude higher than a typical actuator viscous damping which is around 0.005 (see Chapter 8 experimental results); thus, the assumption of neglecting the actuator viscous damping within the lumped parameter representation is quite justified. Ellington [214] provided *Quality factor* values for some insects calculated based on the ratio of the peak kinetic energy of the oscillator to the energy dissipated per cycle. The obtained values for Q were 6.5 for the fruit fly, 10 for the hawkmoth and 19 for the bumble bee. These values are in quite good agreement with the demonstrated values here.

The fourth check point is the computed electric field strength. At nominal design variables values, the maximum electric field is of the order 1000 V/mm or less which is acceptable based on the discussion in Section 9.3.3.

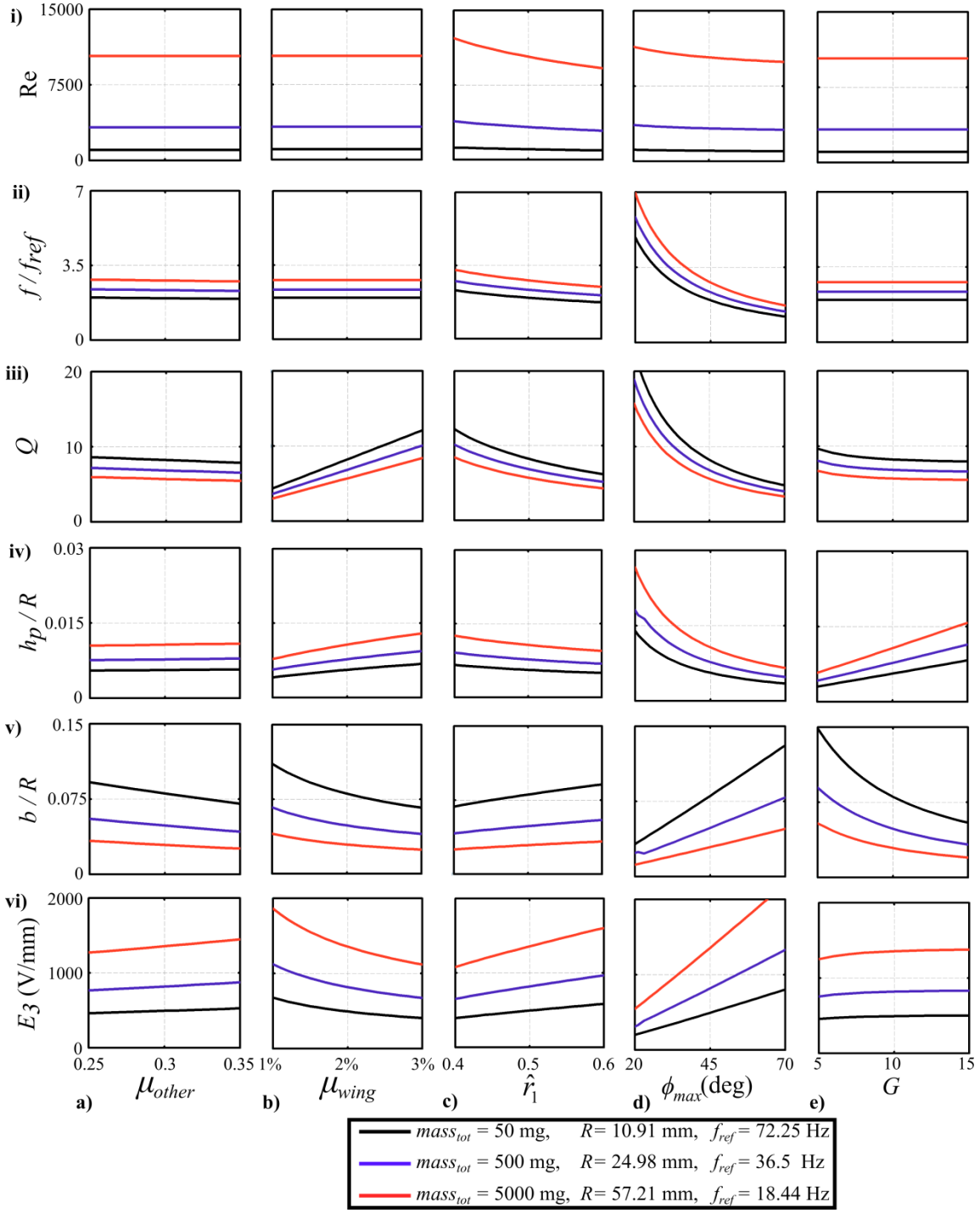

Figure 9.7 Sensitivity analysis of (i) Reynolds number, (ii) flapping frequency, (iii) *Q* factor, (iv) PZT substrate thickness, (v) actuator width and (vi) electric field against (a) components other than batteries and actuators mass fraction, (b) wing mass fraction, (c) wing area centroid, (d) flapping angle amplitude, (e) transmission ratio gain. The actuator configuration in this demonstration is a unimorph configuration. Note that the value of *R* changes as μ_{other} changes and is constant elsewhere. Because the *ALR* is unity, actuator dimensions are normalised with respect to *R*. Mid values of the design variables are the nominal values of variables in Table 9.2

Now turning to investigate the outcomes of the sensitivity analysis; first, flapping frequency, *f*, is considered which represents a main output of the aerodynamic model. Note that μ_{wing} and *G* do not contribute to the aerodynamic model and thus do not affect the frequency values. Generally, the f/f_{ref} ratios are larger than unity; i.e., the vehicle flapping frequencies are higher than the biological reference frequencies. It is seen that for the range of ϕ_{max} considered (20°-70°) there is a large impact on flapping frequency: At low amplitudes the wing has to flap faster to achieve the same lift, everything else being equal. As ϕ_{max} approaches 90°, the flapping frequency ratio approaches 1, as expected from the definitions used. However, if the effect of flapping amplitude on the piezoelectric field strength is considered, subfigure (6,4), it can be seen that reduced flapping frequency is achieved at the expense of increased field strength. Thus, it may be necessary to flap at a higher frequency in order to work within the technological limits of available piezoelectric material.

With regards to the assumed weight fractions of the vehicle, the effect of the effective wing mass ratio, μ_{wing}, is much greater than the mass fraction μ_{other} for the variable ranges considered, despite the wing mass fraction being very small. The reason for this is the comparatively large inertial load the wing presents to the actuator via the transmission system. This result captures one of the unique design challenges for flapping wing vehicles in that the wing inertia has a significant effect on the propulsion system design, which is not the case for rotary or fixed wing design.

Variable $\hat{r}_1$ has a similar effect to ϕ_{max}, and both taken together define the 'aerodynamic effectiveness' of the wing. Note that increasing the aerodynamic effectiveness leads to a decreased *Q*-factor (subfigures (3,3-4)) consistent with more power per cycle being absorbed by the aerodynamic load.

An important outcome of Figure 9.7 is what we can learn from scaling the configuration to different weights. It can be seen that system performance monitors become less favourable as the all up vehicle mass increases, e.g. E_3 increases, and the *Q*-factor decreases. This supports established engineering practice in that piezoelectric actuation becomes less practical as the length scale increases. In terms of the configuration dimensions, the actuator length ratio stays the same as the all up mass increases. On the other hand, as the all up mass increases the actuator cross section aspect ratio (*b*/*h*) decreases; i.e. the actuator cross section tends to be more of a square shape rather than a rectangle shape.

An assessment of the influence of the actuator configuration selection on the actuator sizing process is shown in Figure 9.8. The results shown are for an all up weight of 500 mg, and to allow a meaningful comparison, the same material properties are used for both actuator configurations. A variable *PTT* is introduced equal to the total thickness of the PZT layers. Hence, for a unimorph *PTT* is equal to h_p whereas for a triple layer actuator it is equal to $2h_p$; however, it should be noted that the h_p value of a unimorph is not necessarily equal to h_p value of a triple layer actuator. Also remember that from comparison of Equations 9.41 and 9.42, it is evident that for a given h_p value the h_e value of a triple layer actuator is smaller compared to that of a unimorph.

The obtained results shows that a triple layer actuator designed for the same inputs as a unimoph will have a slightly smaller width and larger thickness. More importantly, it requires a reduced electric field strength, which is favourable. Note that the lower electric field strength is not just because of the larger total PZT thickness but also because of the lower voltage required for a triple layer actuator.

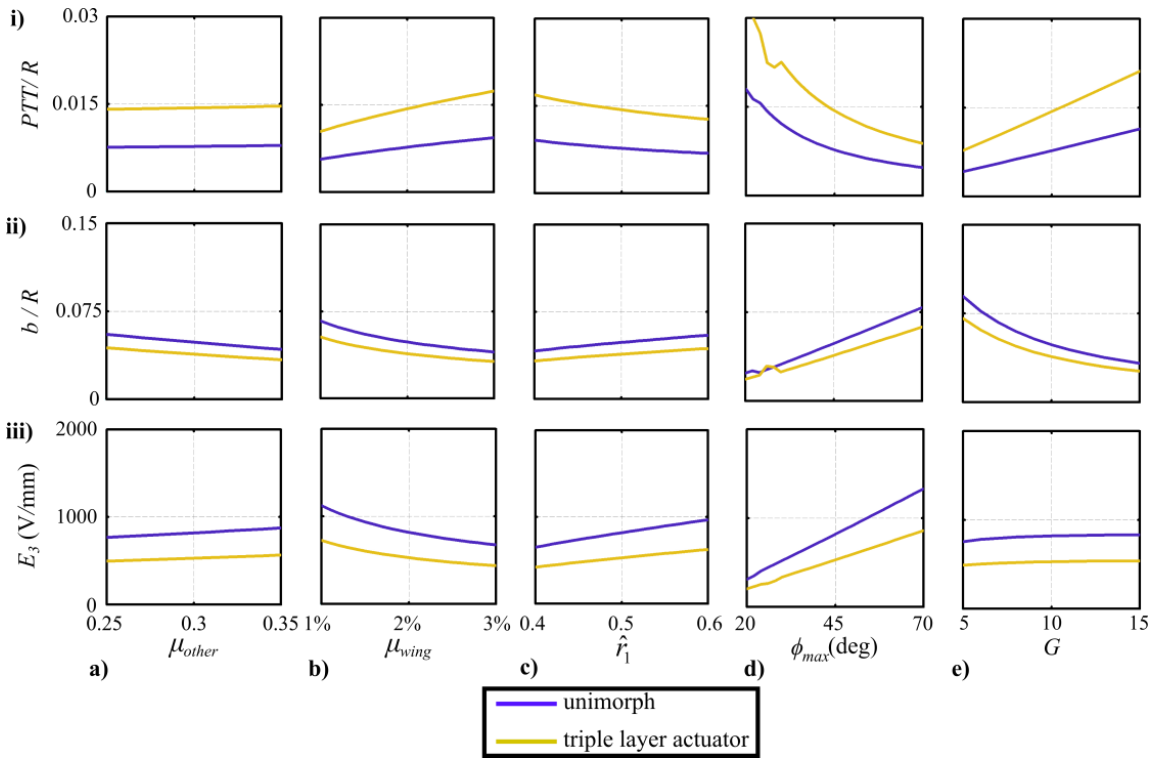

Figure 9.8 Sensitivity analysis comparisons for unimorphs and triple layer actuators. All demonstrations are for an all up mass of 500 mg. *PTT* denotes PZT Total Thickness and for a unimorph is equivalent to h_p whereas for a triple layer actuator is equivalent to $2h_p$. Active and elastic layers material properties are the same for both cases.

9.5 Chapter Conclusions

This chapter presented a theoretical framework for the design of piezoelectric insect-scale flapping wing vehicles that exploit resonance as a means for motion amplification. A multi-physics modelling approach spanning electrical, mechanical and aerodynamic domains is presented that allows designers to explore interactions between domains in a single transparent design environment. The work specifically considered unimorph and triple layer actuator as candidate piezoelectric actuator configurations within the process. However, the developed models are cast in a generic fashion allowing easy adaptation to other configurations, as required. The developed methodology assumes a generic conserving mechanical transmission mechanism between the actuator and the wing with a constant transmission ratio, allowing simple theoretical representations for both kinematics and kinetics of the system. Non-dimensional variables are used throughout to facilitate intuitive investigation of the available design space over a wide range of design mass.

The current work considered quasi-steady treatments for the wing aerodynamics and assumed simple but realistic wing kinematics, allowing the solution procedure to begin with an explicit evaluation of the flapping frequency for weight support based on supplied wing kinematics and geometric data. From the other side the actuator design is constrained by specifying the actuator length based on compactness considerations as well as specifying the actuator material properties based on optimum electromechanical coupling performance. At the heart of the process lies the system dynamics simulation module which interfaces the aerodynamics to the electromechanics and facilitates design iteration of the actuator breadth, thicknesses and operating voltage to achieve the required flapping frequency and blocking force within the upper weight limit set for the actuator.

An important feature of the current air vehicle design problem is the aero-mechanical coupling that leads to unique aspects of the design problem. The design process needs to find the operational frequency at the start which is similar to finding the head speed in rotary vehicles design. However because the system is resonant, actuator physical sizing comes into play. Also, a fixed or a rotary wing vehicle design does not include acceleration considerations; however, for a flapping wing inertial loads become part of the design of the propulsion system.

The design process outputs a number of design performance metrics that enables the designer to evaluate the solution against higher level trades within the overall vehicle design loop. Clear scope limitations are also provided including the feasible Reynolds number range for applying the aerodynamic module as well as field strength feasible range to avoid piezoceramic breakdown. The developed design process was tested through conducting a sensitivity analysis for the influence of the design variables on the design process outcomes allowing undertaking a design trade within a fast and robust computational environment. Several important outcomes were obtained from the conducted sensitivity study including: (1) demonstration of the primary effect of the flapping angle amplitude selection on the air vehicle operation, and that the current technological limits of piezoelectric materials constrain operation to lower flapping angle-higher frequency compared to biological reference. (2) Demonstration of deterioration of piezoelectric actuated concepts as the mass scale increases and thus defines the feasible design space for piezoelectic actuated insect-scale flapping wing vehicles. (3) Demonstration of the superiority of triple layer actuators over unimorph actuators in terms of the electromechanical performance.

An important issue with the proposed design process is that it is based on the satisfaction of an effectiveness criterion (i.e. lift $\geq$ weight) without consideration of efficiency. However, this is an acceptable limitation at the current state of technology and given that the primary goal at present is to achieve self supported hovering flapping flight at insect scale from piezoelectric driven propulsion systems. Thus future work should include more detailed modules for evaluating the total system efficiency including aerodynamic losses, losses within the transmission system, electromechanical actuator deficiency in parallel with limitations to charge recovery circuits, efficiency of power electronics circuits, and available power sources efficiency levels. Another issue to recognise within the proposed design process is the development of design scaling laws based on the current available heuristic data as well as relying on very limited past experience for the mass breakdown of the vehicle. However, the level of uncertainty in technology specific weight estimates and uncertainty associated with manufacturing are currently high due to the lack of historical successful vehicles upon which estimation heuristics can be based. Therefore it is necessary to note that the current design process should always be updated with reliable vehicle data when released.

10

Conclusions and Future Work

This chapter is divided into two main sections. The first summarises the main conclusions from this dissertation whereas the second provides directions for future research. Both sections are presented as a series of statements each followed by a brief supporting summary.

10.1 Conclusions

A comprehensive literature review of the state of the art for hover-capable micro and nano air vehicles is conducted.

A thorough literature review of the designs presented in the pursuit of providing an engineering solution to develop miniature air vehicles has been provided. A taxonomy based on wing and actuator kinematics has been proposed to classify the different vehicles under development. The air vehicles were classified into three main groups including rotary wing, flapping wings with rotary actuation and flapping wings with reciprocating actuation. More focus was directed towards the last class of designs, and a detailed assessment of the main subsystems constituting these vehicles has been provided. Comprehensive discussions have been presented on the strengths and weaknesses of the presented designs; additionally potential design challenges were identified to improve efficiency, effectiveness and performance.

Flapping flight is aerodynamically much less efficient than previously thought.

An analytical treatment to quantify the losses captured in the induced power factor, k, has been provided for flapping wings in normal hover including the effects of non uniform downwash, wake periodicity and finite flapping amplitude. The method is based on a novel combination of actuator disc and lifting line blade theories that also takes into account the effect of advance ratio. The model has been validated against available experimental results. An evaluation of the contributions to induced power factor showed that for some insects the induced power can be twice the ideal value in hover. The figure of merit has been evaluated for eight hovering insects giving values between 15% and 28%. Compared to rotary and fixed wing flight modes, flapping flight not only has higher or at least equal levels with respect to common aerodynamic deficiency sources, but also has further deficiency sources characteristic to its operation. Specific outcomes for the induced power factor evaluation showed that the induced power factor due to the non-uniform downwash effect, k_{ind}, can attain values up to 1.25 in hovering for realistic insect wing planforms defined based on a beta function. The

induced power factor due to the wake periodicity effect, k_{per}, can reach to a value of 1.15 for typical insect-like normal hovering. The induced power factor due to effective flapping disk area, k_{flap}, attained a maximum value of 1.4 for real hovering insects. The evaluation of the figure of merit of eight hovering insects showed the prevalence of the profile component in determining the aerodynamic efficiency owing to the typical high angles of attack operation associated with hovering flapping flight.

The leading-edge vortex (LEV) on revolving/flapping wings eliminates wing stall in a similar manner to a '*slat effect*' in classical aerodynamics.

It is well established that the presence of a stable leading-edge vortex (LEV) on steadily revolving wings enables significantly higher lift coefficients at high angles of attack, yet there is no clear mechanism to explain how the additional lift is generated. Three analytical treatments for modelling revolving/flapping wings at low Reynolds numbers consistent with insect-scale hovering flight have been discussed with the aim of providing a theoretical argument for attributing the observed lift enhancement and in particular the role of the LEV in lift production. The three analytical models investigated were based on (1) potential flow theory, (2) the so-called normal force model, and (3) the Polhamus leading edge suction analogy. These models were derived in a form that exposes the contribution of the LEV and enables model closure based on analytical estimation of the lift curve slope at small angles of attack. Models have been evaluated against available experimental data and for the potential flow model, it was shown that the best fit with experimental data is with the LEV strength set to zero. The normal force model was shown to be equivalent to the potential flow model resolved in the lift direction with the LEV circulation set to zero. The potential lift term of the Polhamus model was shown to have a structure similar to the normal force model, but with an additional multiplier that attenuates the potential lift. It has been found that the normal force model is the most accurate model over the whole first quadrant of angle of attack and it is also the simplest of the models and does not explicitly include any aerodynamic force contribution from the LEV. Hence it was concluded that the LEV does not have a direct effect on lift by increasing circulation or generating increased local suction; rather, it has an indirect effect on high lift by preventing flow separation in the same manner as a slat in classical aerodynamics.

Quasi-Steady aerodynamic models of normal hovering flight are no longer semi-empirical.

Generic, transparent and compact models for evaluation of the aerodynamic performance of insect-like flapping wings in hovering flight have been presented. The models are generic in that it can be applied to wings of arbitrary morphology and kinematics without use of experimental data, are transparent in that the aerodynamic components of the model are linked directly to morphology and kinematics via physical relationships, and are compact in the sense that they can be efficiently evaluated for use within a design optimisation environment. An important aspect of the developed models in Chapters 4 and 5 is the method by which translational force coefficients for the aerodynamic model are obtained from first principles, however important insights were also provided for the morphological and kinematic treatments that improve the clarity and efficiency of the overall model. The full models have been evaluated against experimental data for revolving wings and good agreement is obtained for lift and drag up to 90 degrees incidence. Comparison of the models output with data from CFD studies on a range of different insect species also showed good agreement with predicted weight support ratio and specific power. The validated model was used to evaluate the relative impact of different contributors to the induced power factor, and it was shown that assumption of an ideal induced power factor (k=1) for a normal hovering hoverfly can lead to a 23% overestimation of the generated force due to flapping.

The novel concept of the equivalent angle of attack is a powerful modelling treatment that enables the linear lifting line theory to capture the steady nonlinear aerodynamics of wings at high angles of attack.

A novel lifting line formulation has been proposed for the aerodynamic evaluation of insect-like wings in hovering flight. The main adaptation is the introduction of the concept of the equivalent angle of attack, which enables the linear LLT formulation to capture the steady nonlinear aerodynamics of wings at high angles of attack using a simple analytical correction term. Additionally, simplified methodologies to include the non-ideal effects including wake periodicity, effective flapping disk area, low Reynolds

number effect as well as the well-known edge velocity correction within the lifting line theory have been presented. The validation of the developed lifting line theory for hovering wings (LLT_{hw}) against available measurements from revolving wing experiments showed very good agreement with respect to both the shape of variation of the lift coefficient with incidence as well as the magnitude. Comparison of the results against CFD simulations showed that the mean lift to weight ratio results are on average within +4% accuracy. The developed model has been used to assess the relative impact of the proposed adaptations on the LLT_{hw} for the investigated insects. Excluding these adaptations leads on average to a 60% over estimation in the mean lift force required for weight support, and most of this discrepancy is due to the nonlinear aerodynamic effect.

In normal hovering flight, the induced drag contributes 22% of the total drag.

The developed LLT_{hw} allowed for a first time explicit evaluation of the induced drag component of insect wings. On average for the eight insects investigated based on their reported kinematic profiles, the induced drag is shown to contribute 22% of the total drag based on the mean cycle values and 29% of the total drag based on the mid half-stroke values. For insects operating with high mid-stroke angles of attack (such as the ladybird and the fruit fly) this ratio decreases below 20% which is consistent with the expected prevalence of profile drag as the angle of attack increases.

A theoretical solution is derived for the optimum revolving wing planform.

An optimum planform for wings performing continuous rotary motion or within the steady translational phase of the flapping motion capable of producing an elliptic circulation distribution has been derived. The obtained expression is proportional to $\sqrt{\frac{1}{\hat{r}}-1}$, where $\hat{r}$ is the non dimensional location along the wing length. A wing planform defined by this relation whilst prescribing the correct twist distribution will be able to minimise both induced and profile powers expenditure. Nevertheless without applying any twist distribution, the derived optimum chord distribution produces a downwash distribution very near to the constant distribution and thus the induced power expenditure is still significantly reduced.

A hummingbird-like wing is the most efficient realistic planform with respect to induced losses.

The derived optimum chord distribution requires a very broad root region; however the beta chord distribution provides a less optimal performance in terms of downwash distribution but with a more practical planform shape. An untwisted wing planform, similar to a hummingbird, whose centre of area is at forty percent of the wing length provides the minimum induced power factor due to non-uniform downwash with a value of 1.07.

A revolving elliptic wing planform is capable of minimising profile losses.

This work has revealed the unique aerodynamic advantage of elliptic wings performing continuous rotary motion or within the steady translational phase of the flapping motion. It has been shown that for any aspect ratio, an untwisted elliptic revolving wing can allow all wing sections to operate at the same optimum effective angle of attack for a minimum profile power requirement.

For maximum effectiveness, the flapping angle kinematic profile should be sinusoidal, whereas for maximum efficiency, it should be triangular, with the pitching angle being rectangular in both cases.

A compact analytical aero-kinematic model has been developed and was shown to be useful for the optimisation of flapping wing kinematics against aerodynamic criteria of effectiveness (maximum lift) and efficiency (minimum power for a given amount of lift), as well as for making predictions of the required flapping frequency for a given geometry and basic aerodynamic parameters. The kinematic treatment is based on a consolidation of an existing formulation that allows explicit derivation of flapping velocity for complex motions whereas the aerodynamic model is based on the quasi-steady analysis. The combined aero-kinematic model provided novel explicit analytical expressions for both lift and power of a hovering wing in a compact form that enable exploration of a rich kinematic design space. Good agreement was found between model predictions of flapping frequency and observed results for a number of insects

and optimal hovering kinematics identified using the model were consistent with results from studies using higher order computational models. It was found that for effectiveness, the flapping angle profile should be sinusoidal, whereas for efficiency, the flapping angle profile should be triangular, with the pitching angle being rectangular in each case. The optimum effectiveness kinematics generate 23% more lift and expend 20% more aerodynamic power to produce the same lift compared to optimum efficiency kinematics. Compared to the dual sinusoidal kinematics, the use of a rectangular pitching profile and sinusoidal flapping profile increases the maximum attainable effectiveness by around 6.5%, whilst, the use of triangular flapping and rectangular pitching profiles increases the maximum attainable efficiency by at least 55%.

Electromechanical coupling performance of piezoelectric bending actuators in dynamic operation is the same as that of static operation; however for light damping, the electromechanical coupling factor is typically an order of magnitude higher than that of static operation.

A comprehensive analytical model of the dynamic electromechanical behaviour of piezoelectric actuators has been developed and successfully validated against experimental data. The model provides a mapping between force, displacement, voltage and charge. Damping is modelled using experimental data. Experimental validation was based on measurement of mode shape and frequency response of a series of unimorph beams of varying length but of the same thickness and material. The experimental frequency response was found to be weakly nonlinear with excitation voltage, with a reduction in natural frequency and increase in damping with increasing excitation amplitude. An expression for the ElectroMechanical Coupling Factor (EMCF) has been extracted from the analytical model and was used as the objective for parametric design studies. The design parameters are thickness ratio and Young's modulus ratio of the elastic and piezoceramic layers, and the piezoelectric constant k_{31}. The operational design point is defined by the damping ratio. It was found that the relative variation of the EMCF with the design parameters for dynamic operation is the same as that of static operation; however, for light damping the magnitude of the peak EMCF will typically be an order of magnitude greater than that of static operation. For the actuator configuration considered in this work, it was shown that the absolute variation of EMCF

with thickness ratio for dynamic operation is same as that for static operation when the damping ratio is 0.44 for unimorphs and 0.425 for triple layer actuators.

Triple layer actuators have the best electromechanical characteristics.

A triple layer actuator with an optimum thickness ratio can achieve higher peak EMCF value compared to bimorphs which in turn can achieve higher peak EMCF compared to optimum unimorph configurations. For unimorphs and triple layer actuators, a peak value of EMCF occurs at an optimal thickness ratio that varies only with the Young's modulus ratio of the elastic and active layers of the actuator. Increasing elastic layer material Young's modulus leads to thinner elastic layer for both cases. The relations defining the optimum thickness ratio as function of the Young's modulus ratio have been derived as simple polynomials suitable for designing the propulsion system. Triple layer actuators have also shown superiority when implemented within flapping wing designs in the sense that they require lower operational electric field strength and thus allow improved reliability of the piezoceramic.

The design process for piezoelectric actuated robotic flying insects is conceptually different from rotary and fixed wing air vehicles.

A design process for sizing piezoelectric propulsion system actuators for insect-scale flapping wing vehicles has been developed. Multi-physics modelling of the combined electrical, mechanical and aerodynamic domains was presented. Compared to fixed and rotary wing air vehicles, the design problem is unique due to the aero-mechanical coupling involved. Owing to the system resonance the actuator sizing is directly connected to the aerodynamic flapping frequency required for sufficient lift generation; also owing to acceleration considerations, inertial loads become a major player within the design of the propulsion system.

Piezoelectric propulsion performance deteriorates beyond the insect scale, and at the current state of technology robotic insects are less efficient compared to their biological counterparts.

The design process presented in this work demonstrated that engineered solutions tend to be driven to higher frequency operation than biological equivalents at the same scale. It also showed the performance deterioration of piezoelectric actuated concepts as the mass scale increases: as the mass increases, engineered solutions tend to have lower Q factor, and they require higher electric field which is usually beyond the available piezoceramic technology. Moreover, as the mass increases the vehicle has to operate at higher Reynolds number where there is more chance for leading-edge vortex shedding. Thus, it can be argued that piezoelectric propulsion with flapping wings is most suited for the insect-scale and becomes a less efficient concept as the scale increases.

10.2 Recommendations for Future Work

Investigate the aerodynamic performance of flapping wings over the extended range of advance ratios.

The current work concentrated on hovering flight as a first step; however, it is important to extend the aerodynamic treatment to forward flight as well. The aim is to provide a full investigation for the effect of the advance ratio on the flapping aerodynamics. Chapter 3 laid the foundation for including the advance ratio into the aerodynamic characterisation; however, further work is still required. The problem is non-trivial because other aspects such as the LEV stability and the change of stroke-plane angle inclination must be accounted for. A particular aim is to identify the so-called '*critical advance ratio*' for insect-like flappers which defines the limits of aerodynamic performance in terms of the maximum achievable speed, as well as the lift generation effectiveness and efficiency variations with the forward speed build up.

Conduct aerodynamic experiments to fully characterise the wing planform effects on the aerodynamic performance and efficiency.

Dedicated experiments towards full characterisation of the wing geometry effects on the aerodynamic performance of revolving/flapping wings are a calling requirement. The aim here is to investigate the effect of chord distribution and aspect ratio on the lift, drag, wing regions of flow separation, and aerodynamic efficiency measured in terms of the figure of merit. This would allow a full and comprehensive comparison with the developed theoretical models. Indeed, some experiments have been started to characterise the lift and figure of merit of available propellers as that used within the Nano-Hubsan quad-rotor and the initial results indicate very low figure of merit values matching with the conclusions derived from the developed analytical treatments.

Develop detailed theoretical models for the rotational, added mass, and wake capture effects for non-symmetric half-stroke kinematics.

The current work concentrated on symmetric half-stroke kinematics for weight support. However for the vehicle to manoeuvre, different sorts of non-symmetry must be introduced to the kinematics. For this case the net forces due to rotational and added mass effects are no longer zero and can play an important role in control and manoeuvrability. Thus to approach the control problem, robust theoretical modelling treatments for the associated aerodynamic phenomena have to be developed taking into account the effect of the wing pitch axis location and the detailed profile distribution of the wing leading-edge.

Investigate experimentally the efficiency of elastic storage within engineering designs.

The current work has always assumed a perfect elastic storage for the flapping motion. This is an appropriate practice for most of engineering designs where an elastic spring element can be used in theory to recover the energy. Though it will be instructive to conduct experimental measurements on the possible elastic element options for insect-scale flapping wing vehicles to assess the degree of validity of this assumption and provide either empirical or theoretical models for any evident elastic storage deficiency.

Develop theoretical models for the dynamic electromechanical characterisation of piezoelectric actuators with generic configurations.

There is currently some evidence showing that actuator width tapering provides better electromechanical performance for static actuation. It is instructive to extend the dynamic model presented here to investigate the width tapering value for dynamic operation. The developed analysis in this thesis also considered beams with the piezoelectric layer fully covering the entire beam. Thus, a model extension to investigate the effect of partial coverage may be beneficial.

Characterise the non-ideal operation effects on the performance of piezoelectric actuators.

The current work investigated the primary design variables on the electromechanical performance of piezoelectric actuators including material properties, geometry and damping effects. Some of the effects associated with piezoelectric actuation were characterised based on the conducted experiments such as the variation of the resonance frequency and damping with the excitation amplitude. However, a theoretical method for their inclusion within the developed models should be developed. Some other sources of losses such as actuator saturation and temperature increase are also expected at a high driving field operation. The influence of these effects on the actuator operation should also be investigated experimentally and theoretically.

Update the developed design process of robotic insects with successful design data as soon as they are released to improve design scaling laws, and encounter system efficiency modules within the design process.

It is important to always improve the design capabilities of the developed design process through updating it with mass and scale data from successful insect-scale flapping wing vehicles as soon as they appear. This will decrease the level of current uncertainty in technology specific weight estimates and uncertainty associated within manufacturing of these types of vehicles. Additionally, it is highly recommended to include more detailed modules for evaluating the total system efficiency particularly models for friction losses within the transmission system, losses within charge recovery circuits, losses within power electronics circuits and losses within available battery technology.

Provide an insect-scale flapping wing vehicle demonstrator.

An ultimate goal of this work is to develop a battery powered insect-scale flapping wing vehicle. Several milestones in the pursuit of achieving this goal have been provided in this thesis mainly in developing the foundation and the understanding required for this longstanding target. Indeed the next-step is to make use of these foundations to provide

an un-tethered insect-scale flapping wing vehicle demonstration; however, this task is not an easy one. Several design iterations are required to refine the transmission mechanism design and fabrication. Full simulation and experimental validation of the passive pitching properties of different hinge configurations are required. Addressing the different manufacturing challenges should then come as a final step.

Investigate 'Manufacturing' challenges.

Our ability to change the ongoing 'robotic-insect' dream to a full truth lies to a great extent in our success to provide robust and cheap micro-manufacturing techniques. There have been intense efforts, including the current work, to understand what needs to be done. This is not to say that no more focused research into the physical aspects is required, but probably what has been achieved is sufficient to provide guide lines for an operating concept. However without manufacturing facilities, these concepts are just ink on papers or routines awaiting execution on simulation software.

Appendix A

Evaluation of the Effect of Skin Friction Drag on the Aerodynamic Performance of Flapping Wings at Insect Scales

Experimental measurements for insect-like model wings at Reynolds number of $O(10^3)$ or higher have shown that at zero angle of attack the drag coefficient can be sensibly approximated as zero [142,146,213]. However at lower Reynolds number of $O(10^2)$, experiments on fruit fly model wings showed that C_{D0} may be more significant as the Reynolds number decreases [142,154,164]. To evaluate the effect of the friction tangential force within the lift and drag coefficient relations, the following equations are used for the wing lift and drag coefficients following reference [8]

$$C_L(\alpha_g) = C_T \sin(2\alpha_g) - C_{D0} \cos^2(2\alpha_g) \sin(\alpha_g), \quad \text{(A.1)}$$

$$C_D(\alpha_g) = 2C_T \sin^2(\alpha_g) + C_{D0} \cos^2(2\alpha_g) \cos(\alpha_g), \quad \text{(A.2)}$$

where C_{D0} is the drag coefficient at zero geometric angle of attack. Figure A.1 shows the variation of the relevant aerodynamic indices: the *power factor* $C_L^{3/2}/C_D$ (*PF*) and the *glide number*, C_L/C_D (*GN*) against geometric angle of attack for a range of C_{D0} values, and a fixed C_T value of 1.5. Note that variations of the C_T values within its typical range do not change the general conclusions from this analysis.

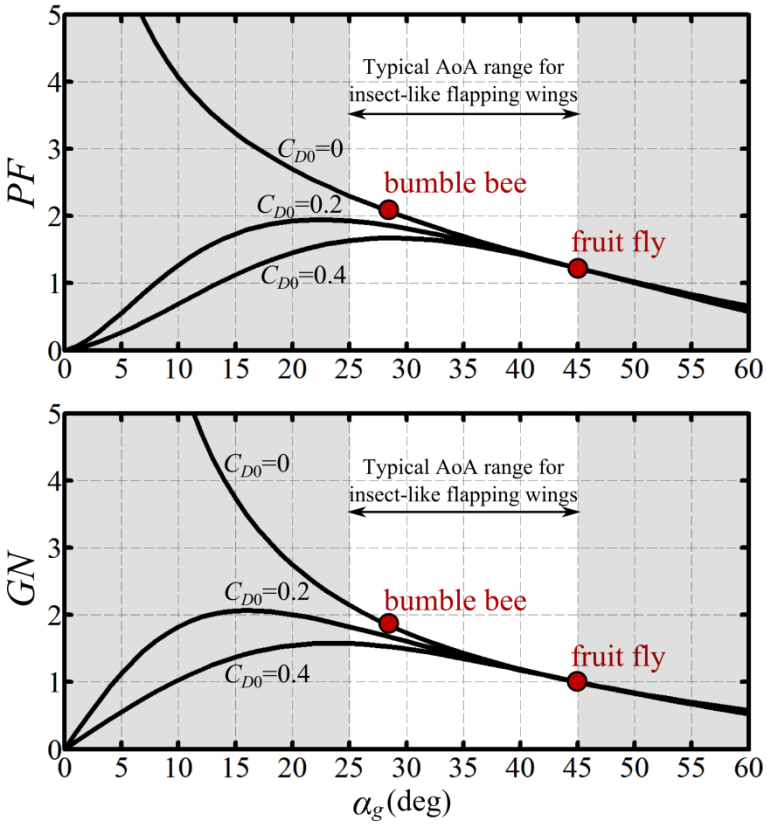

Figure A.1 Variation of the *power factor* and *glide number* against angle of attack for a range of skin friction drag values. The highlighted part represents the operating mid-stroke angle of attack range for most insects between 25 to 45 degrees.

The main outcomes from Figure A.1 are: (1) the *power factor* and *glide number* increase as the geometric angle of attack decreases within the insect-like flapping operation range; thus to achieve higher efficiency the operational geometric angle of attack should be biased towards low values. (2) As the geometric angle of attack increases, the influence of C_{D0} becomes less significant. Thus for the fruit fly, which operates at a typical mid-stroke geometric angle of attack of 44 degrees [145], the effect of having a high C_{D0} does not affect the flight performance. On the other hand, insects such as the honey bee and bumble bee employ mid-stroke geometric angle of attack values around 25 degrees [145]. However, they operate at Reynolds number of $O(10^3)$ and above where the skin friction drag is negligible [146,164].

Appendix B

Lift Augmentation Mechanisms

Following classical aeronautics, a wing can achieve higher lift coefficient values if one (or a combination) of three effects is adopted, Figure B.1. The first is known as the *flap effect* which is to have a positive offset in C_L-α_g curve allowing an increased lift coefficient, C_L, value for the same angle of attack, α_g. The second approach is to increase the possible achievable maximum lift coefficient value by delaying (or elimination) of the angle of attack at which stall occur, α_{stall} without shifting the angle of zero lift and is known as the *slat effect* [270]. Instead of following the first approach that offsets the C_L-α_g curve by a constant value which is independent of α_g, the third approach is to increase the lift curve slope and thus allowing a higher lift coefficient value but here the added lift increment is dependent on α_g.

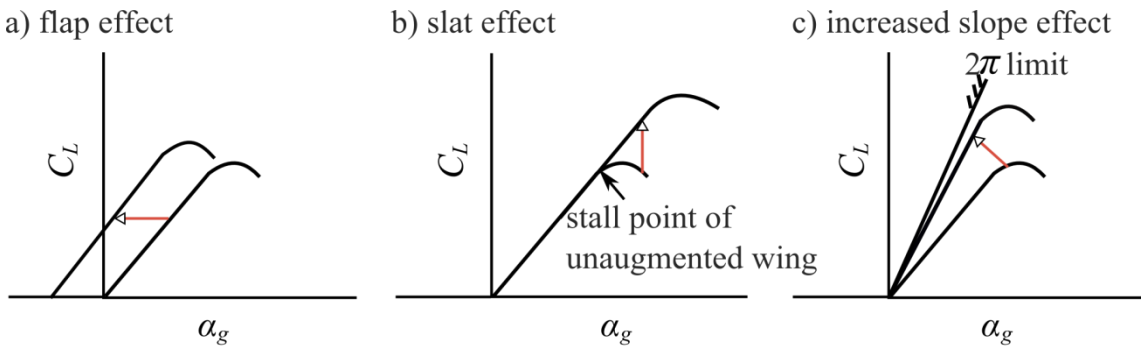

Figure B.1 Different approaches adopted to achieve higher lift coefficient values.

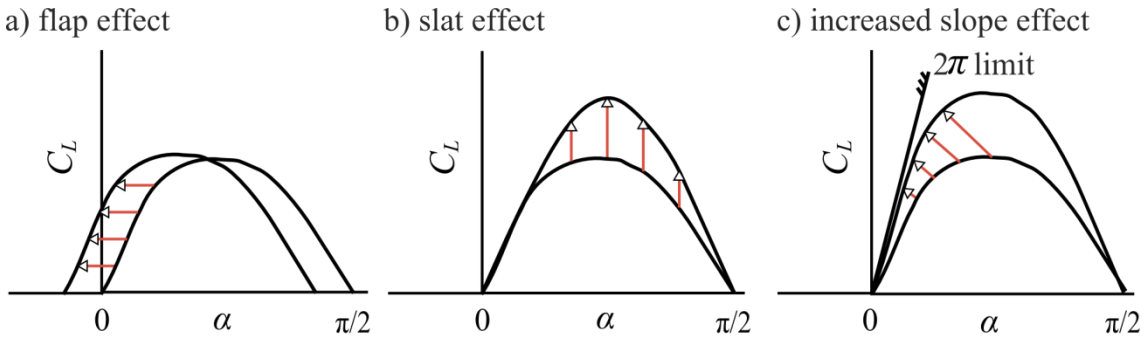

Figure B.2 Different approaches adopted to achieve higher lift coefficient values extended to the first positive quadrant aerodynamics. Abrupt stall characteristics of the original lift curve are removed for better clarity of the concept.

Now the above three effects are extended to the complete first positive quadrant aerodynamics relevant for revolving and flapping wings where operation is at high angles of attack, Figure B.2. Despite that this extension goes outside normal practice, it remains consistent with physical observations. As shown in Figure B.2, the *flap effect* allows the same C_L to be achieved at reduced α_g with $C_{L,max}$ being almost unchanged whilst the *slat effect* enables the recovery of lift lost due to leading edge stall and hence allows the increase of C_L at post-stall α_g. Therefore from a modelling point of view, the *flap effect* is consistent with provision of an increment in circulation at all angles of attack whilst the *slat effect* is consistent with an increase in circulation at angles of attack where the maximum lift coefficient, $C_{L,max}$, is limited by stall. Therefore, the *flap effect* is consistent with the potential flow model results, the *slat effect* is consistent with the 'normal force' model results, and the increased slope effect is consistent (within $0 \le \alpha_g \le 45^\circ$) with the leading edge suction analogy.

Appendix C

Static Actuation Constituent Equations

The static actuation constituent equations governing piezoelectric actuators are written as

$$\begin{bmatrix} \delta \\ Q \end{bmatrix} = \begin{bmatrix} S_{11} & S_{12} \\ S_{21} & S_{22} \end{bmatrix} \begin{bmatrix} F \\ V \end{bmatrix}. \tag{C.1}$$

The elements of the static matrix that were used for the evaluation of the EMCF static curve of the unimorph actuator in Figure 8.13a are given as [111,239]

$$S_{11} = \frac{4s_{11}^{p} l^3}{bh_p^3} \frac{AB+1}{1+4AB+6AB^2+4AB^3+A^2B^4},$$

$$S_{12} = S_{21} = \frac{3d_{31} l^2}{h_p^2} \frac{AB(B+1)}{1+4AB+6AB^2+4AB^3+A^2B^4}, \tag{C.2}$$

$$S_{22} = \frac{\varepsilon_{33}^{T} lb}{h_p} \left(1 - k_{31}^2 \frac{AB(1+AB^3)}{1+4AB+6AB^2+4AB^3+A^2B^4} \right)$$

$$A = \frac{s_{11}^{p}}{s_{11}^{e}} = \frac{Y_e}{Y_p}, \; B = \frac{h_e}{h_p}.$$

The elements of the static matrix that were used for the evaluation of the EMCF static curve of the triple layer actuator in Figure 8.13b are given as [238]

$$S_{11} = \frac{4 s_{11}^{e} s_{11}^{p} l^{3}}{Db},$$

$$S_{12} = S_{21} = \frac{3 s_{11}^{e} d_{31} \left(h_e + h_p\right) l^{2}}{D}, \tag{C.3}$$

$$S_{22} = \frac{\varepsilon_{33}^{T} l b}{2 h_p} \left(1 - k_{31}^{2} \frac{D - 6 s_{11}^{e} h_p \left(h_e + h_p\right)^{2}}{D} \right)$$

$$s_{11}^{p} = \frac{1}{Y_p},\ s_{11}^{e} = \frac{1}{Y_e},\ D = 2 s_{11}^{e} \left(3 h_e^{2} h_p + 6 h_e h_p^{2} + 4 h_p^{3}\right) + s_{11}^{p} h_e^{3}.$$

Appendix D

Thesis Publications

The following are the papers published by the time of the thesis submission:

- Nabawy, M. R. A., Crowther, W. J. 2014 On the quasi-steady aerodynamics of normal hovering flight part I: the induced power factor. *J. R. Soc. Interface* **11**: 20131196. (doi 10.1098/rsif.2013.1196)
- Nabawy, M. R. A., Crowther, W. J. 2014 On the quasi-steady aerodynamics of normal hovering flight part II: model implementation and evaluation. *J. R. Soc. Interface* **11**: 20131197. (doi 10.1098/rsif.2013.1197)
- Nabawy, M. R. A., Parslew, B., Crowther, W. J. 2015 Dynamic performance of unimorph piezoelectric bending actuators. *Proc. Inst. Mech. Eng. I J. Syst. Control Eng.* **229**(2), 118-129. (doi 10.1177/0959651814552810)
- Nabawy, M.R.A., Crowther, W.J. Is flapping flight aerodynamically efficient? 32nd AIAA Applied Aerodynamics Conference, AIAA Aviation and Aeronautics Forum and Exposition, 16 - 20 June 2014, Atlanta, Georgia. (doi 10.2514/6.2014-2277)

The following are the papers either submitted or in preparation for journal publication:

- Nabawy, M. R. A., Crowther, W. J. Optimum revolving wing planform.
- Nabawy, M. R. A., Crowther, W. J. Aero-optimum hovering kinematics.
- Nabawy, M. R. A., Crowther, W. J. A quasi-steady lifting line theory for insect-like hovering flight.
- Nabawy, M.R.A., Crowther, W.J. Electromechanical coupling of piezoelectric bending actuators in dynamic operation.

- Nabawy, M.R.A., Crowther, W.J. Sizing of piezoelectric actuators for insect scale flapping wing vehicles.
- Nabawy, M.R.A., Crowther, W.J. Towards an insect-scale air vehicle: a review of design concepts, system components and development challenges.

The following are the presentations given by the time of thesis submission:

- An aerodynamic evaluation of insect wing shapes and kinematics optimised for efficiency or effectiveness, Society for Experimental Biology Annual meeting, 1-4 July 2014, Manchester, UK.

References

1. Ansari, S. A., Zbikowski, R., & Knowles, K. (2006). Aerodynamic modelling of insect-like flapping flight for Micro Air Vehicles. *Progress in Aerospace Sciences*, *42*, 129-172. (doi: 10.1016/j.paerosci.2006.07.001)
2. Pines, D. J., & Bohorquez, F. (2006). Challenges facing future micro-air-vehicle development. *Journal of Aircraft*, *43*(2), 290-305.
3. Wood, R. J., Finio, B., Karpelson, M., Ma, K., Pérez-Arancibia, N. O., Sreetharan, P. S., ... & Whitney, J. P. (2012). Progress on 'pico' air vehicles. *The International Journal of Robotics Research*, *31*(11), 1292-1302. (doi: 10.1177/0278364912455073)
4. Hylton, T., Martin, C., Tun, R., & Castelli, V. (2012, January). The DARPA Nano Air Vehicle Program. In *50th AIAA Aerospace Science Meeting*, Nashville, TN, January, 6-12.
5. Shyy, W., Lian, Y., Tang, J., Viteru, D., & Liu, H. (2008). *Aerodynamics of low Reynolds number flyers*, Cambridge, UK: Cambridge University Press
6. Pitt Ford, C. W., & Babinsky, H. (2013). Lift and the leading-edge vortex. *Journal of Fluid Mechanics*, *720*, 280-313. (doi: 10.1017/jfm.2013.28)
7. Gerdes, J. W., Gupta, S. K., & Wilkerson, S. A. (2012). A review of bird-inspired flapping wing miniature air vehicle designs. *ASME Journal of Mechanisms and Robotics*, *4*, 021003. (doi: 10.1115/1.4005525)
8. Wood, R. J., Whitney, J. P., & Finio, B. M. (2010). Mechanics and actuation for flapping-wing robotic insects. *Encyclopedia of Aerospace Engineering*, Chapter 357, John Wiley & Sons, Ltd., 4393-4405.
9. Lentink, D., Jongerius, S. R., & Bradshaw, N. L. (2009). The scalable design of flapping micro-air vehicles inspired by insect flight. *Flying Insects and Robots*, Chapter 14, Springer Berlin Heidelberg, 185-205. (doi: 10.1007/978-3-540-89393-6_14)
10. Fearing, R. S., & Wood, R. J. (2009). Challenges for 100 milligram flapping flight. *Flying Insects and Robots*, Chapter 16, Springer Berlin Heidelberg, 219-229. (doi: 10.1007/978-3-540-89393-6_16)
11. Tanaka, H., Finio, B. M., Karpelson, M., Pérez-Arancibia, N. O., Sreetharan, P. S., Whitney, J. P., & Wood, R. J. (2012). Insect flight and micro air vehicles (MAVs). *Encyclopedia of Nanotechnology*, Springer Netherlands, 1096-1109.
12. Jones, K. D., & Platzer, M. F., (2010). Flapping-wing propelled micro air vehicles. *Encyclopedia of Aerospace Engineering*, Chapter 356, John Wiley & Sons, Ltd., 4385-4391.

13. Bohorquez, F., Samuel, P., Sirohi, J., Pines, D., Rudd, L., & Perel, R. (2003). Design, analysis and hover performance of a rotary wing micro air vehicle. *Journal of the Amererican Helicopter Society*, *48*(2), 80-90.
14. http://en.wikipedia.org/wiki/Seiko_Epson_Micro_flying_robot
15. Wang, W., Song, G., Nonami, K., Hirata, M., & Miyazawa, O. (2006, October). Autonomous control for micro-flying robot and small wireless helicopter xrb. In *IEEE/RSJ International Conference on Intelligent Robots and Systems*, Beijing, 9-15 October, 2906-2911. (doi: 10.1109/IROS.2006.282142)
16. Bouabdallah, S., Siegwart, R., & Caprari, G. (2006, October). Design and control of an indoor coaxial helicopter. In *IEEE/RSJ International Conference on Intelligent Robots and Systems*, Beijing, 9-15 October, 2930-2935. (doi: 10.1109/IROS.2006.282146)
17. http://www.hubsan.com/products/HELICOPTER/H111.htm
18. Kroo, I., & Kunz, P. (2000). Development of the mesicopter: a miniature autonomous rotorcraft, In the *American Helicopter Society International Vertical Lift Aircraft Design Specialists' Meeting*, San Francisco, CA.
19. Kroo, I., & Kunz, P. (2001). Mesoscale flight and miniature rotorcraft development. *Fixed and Flapping Wing Aerodynamics for Micro Air Vehicle Applications*, *Progress in Astronautics and Aeronautics*, *195*, (edited by Mueller, T. J.), Chapter 23, AIAA Reston, USA.
20. Kunz, P., & Kroo, I. (2001). Analysis, design, and testing of airfoils for use at ultra-low Reynolds numbers. *Fixed and Flapping Wing Aerodynamics for Micro Air Vehicle Applications*, *Progress in Astronautics and Aeronautics*, *195*, (edited by Mueller, T. J.), Chapter 3, AIAA, Reston, USA.
21. http://www.proxdynamics.com/
22. https://www.gov.uk/government/news/miniature-surveillance-helicopters-help-protect-front-line-troops
23. Lentink, D., Dickson, W. B., Van Leeuwen, J. L., & Dickinson, M. H. (2009). Leading-edge vortices elevate lift of autorotating plant seeds. *Science*, *324*(5933), 1438-1440. (doi: 10.1126/science.1174196)
24. Ulrich, E. R., Pines, D. J., & Gerardi, S. (2009). Autonomous flight of a samara MAV. In *American Helicopter Society AHS 65th Annual Forum and Technology Display*, Grapevine, TX.
25. Ulrich, E. R., Pines, D. J., & Humbert, J. S. (2010). From falling to flying: the path to powered flight of a robotic samara nano air vehicle. *Bioinspiration & Biomimetics*, *5*(4), 045009. (doi: 10.1088/1748-3182/5/4/045009)
26. Ulrich, E. R., Humbert, J. S., & Pines, D. J. (2010). Pitch and heave control of robotic samara micro air vehicles. *Journal of Aircraft*, *47*(4), 1290-1299. (doi: 10.2514/1.47197)
27. Pines, D. J., Humbert, J. S., Hubbard, J. E., Ulrich, E. R., Faruque, I., & Grauer, J. (2010). Control model for robotic samara: Dynamics about a coordinated helical turn. *Journal of guidance, control, and dynamics*, *33*(6), 1921-1927. (doi: 10.2514/1.50878)
28. Kim, G. B., Goo, N. S., Yoon, K. J., Park, H. C., & Yu, Y. H. (2006). Design, fabrication, and performance test of a rotary-wing micro aerial vehicle. *Journal of Aircraft*, *43*(2), 564-566.
29. Shkarayev, S., Moschetta, J. M., & Bataille, B. (2008). Aerodynamic design of micro air vehicles for vertical flight. *Journal of Aircraft*, *45*(5), 1715-1724. (doi: 10.2514/1.35573)

30. Benedict, M., Jarugumilli, T., & Chopra, I. (2013). Effect of rotor geometry and blade kinematics on cycloidal rotor hover performance. *Journal of Aircraft*, *50*(5), 1340-1352. (doi: 10.2514/1.C031461)
31. Benedict, M., Mattaboni, M., Chopra, I., & Masarati, P. (2011). Aeroelastic analysis of a micro-air-vehicle-scale cycloidal rotor in hover. *AIAA Journal*, *49*(11) , 2430-2443. (doi: 10.2514/1.J050756)
32. Benedict, M., Ramasamy, M., & Chopra, I. (2010). Improving the aerodynamic performance of micro-air-vehicle-scale cycloidal rotor: an experimental approach. *Journal of Aircraft*, *47*(4), 1117-1125. (doi: 10.2514/1.45791)
33. Guo, S., Li, D., & Wu, J. (2011). Theoretical and experimental study of a piezoelectric flapping wing rotor for micro aerial vehicle. *Aerospace Science and Technology*, *23*(1), 429-438. (doi: 10.1016/j.ast.2011.10.002)
34. Pornsin-Sirirak, T. N., Tai, Y. C., Nassef, H., & Ho, C. M. (2001). Titanium-alloy MEMS wing technology for a micro aerial vehicle application. *Sensors and Actuators A: Physical*, *89*(1), 95-103. (doi: 10.1016/S0924-4247(00)00527-6)
35. Pornsin-Sirirak, T. N., Lee, S. W., Nassef, H., Grasmeyer, J., Tai, Y. C., Ho, C. M., & Keennon, M. (2000, January). MEMS wing technology for a battery-powered ornithopter. In *IEEE* 13th *Annual International Conference on Micro Electro Mechanical Systems, MEMS*, Miyazaki, 23-27 January, 799-804. (doi: 10.1109/MEMSYS.2000.838620)
36. Yang, L. J., Hsu, C. K., Ho, J. Y., & Feng, C. K. (2007). Flapping wings with PVDF sensors to modify the aerodynamic forces of a micro aerial vehicle. *Sensors and Actuators A: Physical*, *139*(1), 95-103. (doi: 10.1016/j.sna.2007.03.026)
37. Yang, L. J., Hsu, C. K., Han, H. C., & Miao, J. M. (2009). Light flapping micro aerial vehicle using electrical-discharge wire-cutting technique. *Journal of Aircraft*, *46*(6), 1866-1874. (doi: 10.2514/1.38862)
38. Tsai, B. J., & Fu, Y. C. (2009). Design and aerodynamic analysis of a flapping-wing micro aerial vehicle. *Aerospace Science and Technology*, *13*(7), 383-392. (doi: 10.1016/j.ast.2009.07.007)
39. http://www.proxdynamics.com/r_d/micro_helicopters_and_ornithopters/
40. http://www.avinc.com/nano/
41. Richter, C., & Lipson, H. (2011). Untethered hovering flapping flight of a 3D-printed mechanical insect. *Artificial life*, *17*(2), 73-86. (doi: 10.1162/artl_a_00020)
42. Festo AG & C0. KG. Lightweight design with intelligent kinematics. http://www.festo.com/cms/en_corp/13165.htm
43. Weis-Fogh, T. (1973). Quick estimates of flight fitness in hovering animals, including novel mechanisms for lift production. *Journal of Experimental Biology*, *59*(1), 169-230.
44. Zdunich, P., Bilyk, D., MacMaster, M., Loewen, D., DeLaurier, J., Kornbluh, R., ... & Holeman, D. (2007). Development and testing of the mentor flapping-wing micro air vehicle. *Journal of Aircraft*, *44*(5), 1701-1711.
45. Delfly, Aerospace Software and Technologies Institute, Delft University of Technology, Delft, The Netherlands, http://www.delfly.nl/micro.html.
46. Kawamura, Y., Souda, S., Nishimoto, S., & Ellington, C. P. (2008). Clapping-wing micro air vehicle of insect size. *Bio-mechanisms of Swimming and Flying*, Chapter 26, Springer Japan, 319-330.
47. van Breugel, F., Teoh, Z. E., & Lipson, H. (2009). A passively stable hovering flapping micro-air vehicle. *Flying insects and robots*, Chapter 13, Springer Berlin Heidelberg, 171-184. (doi: 10.1007/978-3-540-89393-6_13)

48. Jones, K. D., & Platzer, M. F. (2009). Flow control using flapping wings for an efficient low-speed micro-air vehicle. *Flying insects and robots*, Chapter 12, Springer Berlin Heidelberg, 159-169. (doi: 10.1007/978-3-540-89393-6_12)
49. Tanaka, H., Hoshino, K., Matsumoto, K., & Shimoyama, I. (2005, August). Flight dynamics of a butterfly-type ornithopter. In *IEEE/RSJ International Conference on Intelligent Robots and Systems*, 2-6 August, 2706-2711. (doi: 10.1109/IROS.2005.1544999)
50. Ristroph, L., & Childress, S. (2014). Stable hovering of a jellyfish-like flying machine. *Journal of The Royal Society Interface*, 11(92), 20130992. (doi: 10.1098/rsif.2013.0992)
51. Flynn, A. M. (1987). Gnat robots (and how they will change robotics). IEEE MicroRobots and Teleperators Workshop, Hyannis, MA, November 1987.
52. Shimoyama, I., Miura, H., Suzuki, K., & Ezura, Y. (1993). Insect-like microrobots with external skeletons. *IEEE Control Systems Magazine*, *13*(1), 37-41.
53. Kubo, Y., Shinoyama, I., Kaneda, T., & Miura, H. (1994, May). Study on wings of flying microrobots. In *IEEE International Conference on Robotics and Automation*, 8-13 May, 834-839. (doi: 10.1109/ROBOT.1994.351385)
54. Bolsman, C. T., Goosen, J. F., & van Keulen, F. (2008, March). Insect-inspired wing actuation structures based on ring-type resonators. In *Proc. of SPIE* Vol. 6928, March 2008, 69281I-1.
55. Bolsman, C. T., Goosen, J. F. L., & van Keulen, F. (2009). Design overview of a resonant wing actuation mechanism for application in flapping wing MAVs. *International Journal of Micro Air Vehicles*, *1*(4), 263-272.
56. Bolsman, C. T., Goosen, J. F. L., & van Keulen, F. (2009, July). Design and realization of resonant mechanisms for wing actuation in flapping wing micro air vehicles. In *3rd International Conference on Integrity, Reliability and Failure (IRF), Porto, Portugal*, July 2009.
57. Hines, L., Campolo, D., & Sitti, M. (2014). Liftoff of a motor-driven, flapping-wing microaerial vehicle capable of resonance. *IEEE Transactions on Robotics, 30*(1), 220-232. (doi: 10.1109/TRO.2013.2280057)
58. Campolo, D., Azhar, M., Lau, G., & Sitti, M. (2014). Can DC motors directly drive flapping wings at high frequency and large wing strokes? *IEEE/ASME Transactions on Mechatronics*, *19*(1), 109-120. (doi: 10.1109/TMECH.2012.2222432)
59. Azhar, M., Campolo, D., Lau, G. K., Hines, L., & Sitti, M. (2013, May). Flapping wings via direct-driving by DC motors. In *IEEE International Conference on Robotics and Automation (ICRA)*, Karlsruhe, 6-10 May 2013, 1397-1402. (doi: 10.1109/ICRA.2013.6630753)
60. http://nanolab.me.cmu.edu/projects/FlappingRobot/
61. Chung, H. C., Kummari, K. L., Croucher, S. J., Lawson, N. J., Guo, S., & Huang, Z. (2008). Coupled piezoelectric fans with two degree of freedom motion for the application of flapping wing micro aerial vehicles. *Sensors and Actuators A: Physical*, *147*(2), 607-612. (doi: 10.1016/j.sna.2008.06.017)
62. Chung, H. C., Kummari, K. L., Croucher, S. J., Lawson, N. J., Guo, S., Whatmore, R. W., & Huang, Z. (2009). Development of piezoelectric fans for flapping wing application. *Sensors and Actuators A: Physical*, *149*(1), 136-142. (doi: 10.1016/j.sna.2008.10.004)

63. Mukherjee, S., & Ganguli, R. (2010). Non-linear dynamic analysis of a piezoelectrically actuated flapping wing. *Journal of Intelligent Material Systems and Structures, 21*(12), 1157-1167. (doi: 10.1177/1045389X10378776)
64. Nima Mahmoodi, S., & Jalili, N. (2007). Non-linear vibrations and frequency response analysis of piezoelectrically driven microcantilevers. *International Journal of Non-Linear Mechanics, 42*(4), 577-587. (doi: 10.1016/j.ijnonlinmec.2007.01.019)
65. DeLaurier, J. D. (1993). An aerodynamic model for flapping-wing flight. *Aeronautical Journal, 97*(964), 125-130.
66. Mukherjee, S., & Ganguli, R. (2012). Nonlinear dynamic analysis of dragonfly-inspired piezoelectric unimorph actuated flapping and twisting wing. *International Journal of Smart and Nano Materials, 3*(2), 103-122. (doi: 10.1080/19475411.2011.649804)
67. Mukherjee, S., & Ganguli, R. (2012). A comparative study of dragonfly inspired flapping wings actuated by single crystal piezoceramic. *Smart Structures and Systems*. *10*(1), 67-87.
68. Cox, A., Monopoli, D., Goldfarb, M. & Garcia, E. (1999, September). The development of piezoelectrically actuated micro air vehicles. Part of *SPIE Conference on Microrobotics and Microassembly*, SPIE Vol. 3834, Boston, Massachusetts, September 1999, 101–108.
69. Cox, A., Monopoli, D., Cveticanin, D., Goldfarb, M., & Garcia, E. (2002). The development of elastodynamic components for piezoelectrically actuated flapping micro-air vehicles. *Journal of Intelligent Material Systems and Structures, 13*(9), 611-615. (doi: 10.1106/104538902032463)
70. Fearing, R. S., Chiang, K. H., Dickinson, M. H., Pick, D. L., Sitti, M., & Yan, J. (2000, April). Wing transmission for a micromechanical flying insect. In *IEEE International Conference on Robotics and Automation*, San Francisco, CA , 24-28 April, 1509-1516. (doi: 10.1109/ROBOT.2000.844811)
71. Sitti, M. (2001). PZT actuated four-bar mechanism with two flexible links for micromechanical flying insect thorax. In *IEEE International Conference on Robotics and Automation*, 3893-3900. (doi: 10.1109/ROBOT.2001.933224)
72. Yan, J., Wood, R. J., Avadhanula, S., Sitti, M., & Fearing, R. S. (2001). Towards flapping wing control for a micromechanical flying insect. In *IEEE International Conference on Robotics and Automation*, 3901-3908. (doi: 10.1109/ROBOT.2001.933225)
73. Wood, R. J., & Fearing, R. S. (2001, October). Flight force measurements for a micromechanical flying insect. In *IEEE/RSJ International Conference on Intelligent Robots and Systems*, Maui, HI, 29 October - 3 November, 355-362. (doi: 10.1109/IROS.2001.973383)
74. Avadhanula, S., Wood, R. J., Campolo, D., & Fearing, R. S. (2002). Dynamically tuned design of the MFI thorax. In *IEEE International Conference on Robotics and Automation*, 52-59. (doi: 10.1109/ROBOT.2002.1013338)
75. Avadhanula, S., Wood, R. J., Steltz, E., Yan, J., & Fearing, R. S. (2003, October). Lift force improvements for the micromechanical flying insect. In *IEEE/RSJ International Conference on Intelligent Robots and Systems*, 27-31 October, 1350-1356. (doi: 10.1109/IROS.2003.1248832)
76. Steltz, E., Avadhanula, S., & Fearing, R. S. (2007, October). High lift force with 275 Hz wing beat in MFI. In *IEEE/RSJ International Conference on Intelligent Robots and Systems*, San Diego, CA, 29 October - 2 November, 3987-3992. (doi: 10.1109/IROS.2007.4399068)

77. Wood, R. J., Steltz, E., & Fearing, R. S. (2005). Optimal energy density piezoelectric bending actuators. *Sensors and Actuators A: Physical*. *119*(2), 476-488. (doi: 10.1016/j.sna.2004.10.024)
78. Sitti, M., Campolo, D., Yan, J., & Fearing, R. S. (2001). Development of PZT and PZN-PT based unimorph actuators for micromechanical flapping mechanisms. In *IEEE International Conference on Robotics and Automation*, 3839-3846. (doi: 10.1109/ROBOT.2001.933216)
79. Campolo, D., Sitti, M., & Fearing, R. S. (2003). Efficient charge recovery method for driving piezoelectric actuators with quasi-square waves. *IEEE Transactions on Ultrasonics, Ferroelectrics and Frequency Control*, *50*(3), 237-244. (doi: 10.1109/TUFFC.2003.1193617)
80. Campolo, D., Sahai, R., & Fearing, R. S. (2003, September). Development of piezoelectric bending actuators with embedded piezoelectric sensors for micromechanical flapping mechanisms. In *IEEE International Conference on Robotics and Automation*, 14-19 September, 3339-3346. (doi: 10.1109/ROBOT.2003.1242106)
81. Steltz, E., Seeman, M., Avadhanula, S., & Fearing, R. S. (2006, October). Power electronics design choice for piezoelectric microrobots. In *IEEE/RSJ International Conference on Intelligent Robots and Systems*, Beijing, 9-15 October, 1322-1328. (doi: 10.1109/IROS.2006.281897)
82. Steltz, E., & Fearing, R. S. (2007, October). Dynamometer power output measurements of piezoelectric actuators. In *IEEE/RSJ International Conference on Intelligent Robots and Systems*, San Diego, CA, 29 October - 2 November, 3980-3986. (doi: 10.1109/IROS.2007.4399067)
83. Syaifuddin, M., Park, H. C., & Goo, N. S. (2006). Design and evaluation of a LIPCA-actuated flapping device. *Smart Materials and Structures*, *15*(5), 1225. (doi: 10.1088/0964-1726/15/5/009)
84. Nguyen, V. Q., Syaifuddin, M., Park, H. C., Byun, D. Y., Goo, N. S., & Yoon, K. J. (2008). Characteristics of an insect-mimicking flapping system actuated by a unimorph piezoceramic actuator. *Journal of Intelligent Material Systems and Structures*, *19*(10), 1185-1193. (doi: 10.1177/1045389X07084203)
85. Nguyen, Q. V., Park, H. C., Goo, N. S., & Byun, D. (2009). An insect-like flapping-wing device actuated by a compressed unimorph piezoelectric composite actuator. *Intelligent Unmanned Systems: Theory and Applications*, 101-117, Springer Berlin Heidelberg.
86. Wood, R. J. (2007, October). Design, fabrication, and analysis of a 3DOF, 3cm flapping-wing MAV. In *IEEE/RSJ International Conference on Intelligent Robots and Systems*, San Diego, CA, 29 October - 2 November, 1576-1581. (doi: 10.1109/IROS.2007.4399495)
87. Wood, R. J. (2007, October). Liftoff of a 60mg flapping-wing MAV. In *IEEE/RSJ International Conference on Intelligent Robots and Systems*, San Diego, CA, 29 October - 2 November, 1889-1894. (doi: 10.1109/IROS.2007.4399502)
88. Wood, R. J. (2008). The first takeoff of a biologically inspired at-scale robotic insect. *IEEE Transactions on Robotics*, *24*(2), 341-347. (doi: 10.1109/TRO.2008.916997)
89. Karpelson, M., Whitney, J. P., Wei, G. Y., & Wood, R. J. (2010, October). Energetics of flapping-wing robotic insects: Towards autonomous hovering flight. In *IEEE/RSJ International Conference on Intelligent Robots and Systems*, Taipei, 18-22 October, 1630-1637. (doi: 10.1109/IROS.2010.5650269)

90. Pérez-Arancibia, N. O., Ma, K. Y., Galloway, K. C., Greenberg, J. D., & Wood, R. J. (2011). First controlled vertical flight of a biologically inspired microrobot. *Bioinspiration and Biomimetics*, *6*(3), 036009. (doi: 10.1088/1748-3182/6/3/036009)
91. Finio, B. M., Pérez-Arancibia, N. O., & Wood, R. J. (2011, September). System identification and linear time-invariant modeling of an insect-sized flapping-wing micro air vehicle. In *IEEE/RSJ International Conference on Intelligent Robots and Systems*, San Francisco, CA, 25-30 September, 1107-1114. (doi: 10.1109/IROS.2011.6094421)
92. Finio, B. M., Shang, J. K., & Wood, R. J. (2009, May). Body torque modulation for a microrobotic fly. In *IEEE International Conference on Robotics and Automation*, Kobe, 12-17 May, 3449-3456. (doi: 10.1109/ROBOT.2009.5152582)
93. Finio, B. M., Whitney, J. P., & Wood, R. J. (2010, October). Stroke plane deviation for a microrobotic fly. In *IEEE/RSJ International Conference on Intelligent Robots and Systems*, Taipei, 18-22 October, 3378-3385. (doi: 10.1109/IROS.2010.5650812)
94. Finio, B. M., & Wood, R. J. (2012, October). Open-loop roll, pitch and yaw torques for a robotic bee. In *IEEE/RSJ International Conference on Intelligent Robots and Systems*, Vilamoura, 7-12 October, 113-119. (doi: 10.1109/IROS.2012.6385519)
95. Finio, B. M., Eum, B., Oland, C., & Wood, R. J. (2009, October). Asymmetric flapping for a robotic fly using a hybrid power-control actuator. In *IEEE/RSJ International Conference on Intelligent Robots and Systems*, St. Louis, MO, 10-15 October 2009, 2755-2762. (doi: 10.1109/IROS.2009.5354424)
96. Finio, B. M., & Wood, R. J. (2010). Distributed power and control actuation in the thoracic mechanics of a robotic insect. *Bioinspiration and Biomimetics*, *5*(4), 045006. (doi: 10.1088/1748-3182/5/4/045006)
97. Ma, K. Y., Felton, S. M., & Wood, R. J. (2012, October). Design, fabrication, and modeling of the split actuator microrobotic bee. In *IEEE/RSJ International Conference on Intelligent Robots and System*, Vilamoura, 7-12 October, 1133-1140. (doi: 10.1109/IROS.2012.6386192)
98. Ma, K. Y., Chirarattananon, P., Fuller, S. B., & Wood, R. J. (2013). Controlled flight of a biologically inspired, insect-scale robot. *Science*, *340*(6132), 603-607. (doi: 10.1126/science.1231806)
99. http://micro.seas.harvard.edu/
100. Whitney, J. P., & Wood, R. J. (2010). Aeromechanics of passive rotation in flapping flight. *Journal of Fluid Mechanics*, *660*, 197-220. (doi: 10.1017/S002211201000265X)
101. Karpelson, M., Wei, G. Y., & Wood, R. J. (2009, May). Milligram-scale high-voltage power electronics for piezoelectric microrobots. In *IEEE International Conference on Robotics and Automation*, Kobe, 12-17 May, 2217-2224. (doi: 10.1109/ROBOT.2009.5152319)
102. Karpelson, M., Whitney, J. P., Wei, G. Y., & Wood, R. J. (2011, March). Design and fabrication of ultralight high-voltage power circuits for flapping-wing robotic insects. In *Twenty-Sixth Annual IEEE Applied Power Electronics Conference and Exposition*, Fort Worth, TX, 6-11 March, 2070-2077. (doi: 10.1109/APEC.2011.5744882)
103. Karpelson, M., Wei, G. Y., & Wood, R. J. (2012). Driving high voltage piezoelectric actuators in microrobotic applications. *Sensors and Actuators A: Physical*, *176*, 78-89. (doi: 10.1016/j.sna.2011.11.035)

104. Wood, R. J., Steltz, E., & Fearing, R. S. (2005, April). Nonlinear performance limits for high energy density piezoelectric bending actuators. In *IEEE International Conference on Robotics and Automation*, 18-22 April, 3633-3640. (doi: 10.1109/ROBOT.2005.1570673)
105. Tanaka, H., Whitney, J. P., & Wood, R. J. (2011). Effect of flexural and torsional wing flexibility on lift generation in hoverfly flight. *Integrative and Comparative Biology*, *51*(1), 142-150. (doi: 10.1093/icb/icr051)
106. Fuller, S. B., Karpelson, M., Censi, A., Ma, K. Y., & Wood, R. J. (2014). Controlling free flight of a robotic fly using an onboard vision sensor inspired by insect ocelli. *Journal of The Royal Society Interface*, *11*(97), 20140281. (doi: 10.1098/rsif.2014.0281)
107. http://www.atomicworkshop.co.uk/catalog/index.php?main_page=index&cPath=65
108. Stux, A. M., & Swider-Lyons, K. (2007). *Survey of commercial small lithium polymer batteries* (No. NRL/MR/6110--07-9073). NAVAL RESEARCH LAB WASHINGTON DC.
109. Karpelson, M., Wei, G. Y., & Wood, R. J. (2008, May). A review of actuation and power electronics options for flapping-wing robotic insects. In *IEEE International Conference on Robotics and Automation*, Pasadena, CA, 19-23 May, 779-786. (doi: 10.1109/ROBOT.2008.4543300)
110. Petricca, L., Ohlckers, P., & Grinde, C. (2011). Micro-and nano-air vehicles: State of the art. *International Journal of Aerospace Engineering*, *2011*, 214549. (doi: 10.1155/2011/214549)
111. Wang, Q., Du, X., Xu, B. & Cross, L. (1999). Electromechanical coupling and output efficiency of piezoelectric bending actuators. *IEEE Transactions on Ultrasonics, Ferroelectrics, and Frequency Control*, *46*(3), 638-646. (doi: 10.1109/58.764850)
112. Yoon, K. J., Park, K. H., Lee, S. K., Goo, N. S., & Park, H. C. (2004). Analytical design model for a piezo-composite unimorph actuator and its verification using lightweight piezo-composite curved actuators. *Smart Materials and Structures*, *13*(3), 459-467. (doi: 10.1088/0964-1726/13/3/002)
113. Wood, R. J., Avadhanula, S., Sahai, R., Steltz, E., & Fearing, R. S. (2008). Microrobot design using fiber reinforced composites. *Journal of Mechanical Design*, *130*(5), 052304. (doi: 10.1115/1.2885509)
114. Whitney, J. P., Sreetharan, P. S., Ma, K. Y., & Wood, R. J. (2011). Pop-up book MEMS. *Journal of Micromechanics and Microengineering*, *21*(11), 115021. (doi: 10.1088/0960-1317/21/11/115021)
115. Sreetharan, P. S., Whitney, J. P., Strauss, M. D., & Wood, R. J. (2012). Monolithic fabrication of millimeter-scale machines. *Journal of Micromechanics and Microengineering*, *22*(5), 055027. (doi: 10.1088/0960-1317/22/5/055027)
116. Shang, J. K., Combes, S. A., Finio, B. M., & Wood, R. J. (2009). Artificial insect wings of diverse morphology for flapping-wing micro air vehicles. *Bioinspiration and Biomimetics*, *4*(3), 036002. (doi: 10.1088/1748-3182/4/3/036002)
117. Tanaka, H., & Wood, R. J. (2010). Fabrication of corrugated artificial insect wings using laser micromachined molds. *Journal of Micromechanics and Microengineering*, *20*(7), 075008. (doi: 10.1088/0960-1317/20/7/075008)
118. Luo, G., & Sun, M. (2005). The effects of corrugation and wing planform on the aerodynamic force production of sweeping model insect wings. *Acta Mechanica Sinica*, *21*(6), 531-541. (doi: 10.1007/s10409-005-0072-4)

119. Bomphrey, R. J., Taylor, G. K., Lawson, N. J., & Thomas, A. L. R. (2006). Digital particle image velocimetry measurements of the downwash distribution of a desert locust *Schistocerca gregaria*. *Journal of The Royal Society Interface*, *3*(7), 311-317. (doi: 10.1098/rsif.2005.0090)
120. Spedding, G. R., & McArthur, J. (2010). Span efficiencies of wings at low Reynolds numbers. *Journal of Aircraft*, *47*(1), 120-128. (doi: 10.2514/1.44247)
121. Pennycuik, C. J. (2008). *Modelling the flying bird*, Oxford, UK: Elsevier.
122. Ellington, C. P. (1984). The aerodynamics of hovering insect flight: V. A vortex theory. *Philosophical Transactions of The Royal Society of London. B, Biological Sciences*, *305*(1122), 115-144. (doi: 10.1098/rstb.1984.0053)
123. Sunada, S., & Ellington, C. P. (2000). Approximate added-mass method for estimating induced power for flapping flight. *AIAA Journal*, *38*(8), 1313-1321.
124. Henningsson, P., & Bomphrey, R. J. (2012). Time-varying span efficiency through the wingbeat of desert Locust. *Journal of The Royal Society Interface*, *9*, 1177-1186. (doi: 10.1098/rsif.2011.0749)
125. Henningsson, P., & Bomphrey, R. J. (2013). Span efficiency in hawkmoths. *Journal of The Royal Society Interface*, *10*(84), 20130099. (doi: 10.1098/ rsif.2013.0099)
126. Henningsson, P., Hedenström, A., & Bomphrey, R. J. (2014). Efficiency of lift production in flapping and gliding flight of swifts. *PloS one*, *9*(2), e90170. (doi: 10.1371/journal.pone.0090170)
127. Muijres, F. T., Spedding, G. R., Winter, Y., & Hedenstrom, A. (2011). Actuator disk model and span efficiency of flapping flight in bats based on time-resolved PIV measurements. *Experiments in Fluids*, *51*(2), 511-525. (doi: 10.1007/s00348-011-1067-5)
128. Muijres, F. T., Bowlin, M. S., Johansson, L. C., & Hedenstrom, A. (2012). Vortex wake, downwash distribution, aerodynamic performance and wingbeat kinematics in slow-flying pied flycatchers. *Journal of The Royal Society Interface*, *9*(67), 292-303. (doi: 10.1098/rsif.2011.0238)
129. Johansson, L. C., Engel, S., Baird, E., Dacke, M., Muijres, F. T., & Hedenstrom, A. (2012). Elytra boost lift, but reduce aerodynamic efficiency in flying beetles. *Journal of The Royal Society Interface*, *9*(75), 2745-2748. (doi: 10.1098/rsif.2012.0053)
130. Stepniewski, W. Z., & Keys, C. N. (1984). *Rotary-wing aerodynamics*, New York NY: Dover Publications, Inc.
131. Mayo, D.B., & Leishman, J.G. (2010). Comparison of the hovering efficiency of rotating wing and flapping wing micro air vehicles. *Journal of the American Helicopter Society*, *55*(2), 025001. (doi: 10.4050/JAHS.55.025001)
132. Sane S. P. (2006). Induced air flow in flying insects. I. A theoretical model of the induced flow. *Journal of Experimental Biology*, *209*(1), 32-42. (doi: 10.1242/jeb.01957)
133. Leishman, J. G. (2006). *Principles of helicopter aerodynamics*, 2nd edition, Cambridge, UK: Cambridge University Press.
134. Dickson, W. B., & Dickinson, M. H. (2004). The effect of advance ratio on the aerodynamics of revolving wings. *Journal of Experimental Biology*, *207*(24), 4269-4281. (doi: 10.1242/jeb.01266)
135. Glauert, H. (1948). *The elements of aerofoil & airscrew theory*, 2nd edition, Cambridge, UK: Cambridge University Press.
136. Pope, A. (1951). *Basic wing and airfoil theory*, New York, NY: McGraw-Hill, Inc.

137. Schlichting, H., & Trunckenbrodt, E. (1979). *Aerodynamics of the airplane*, New York, NY: McGraw-Hill, Inc.
138. Grădinaru, S. (2011). Pairs of Glauert integrals. *Analele Universităţii Spiru Haret-Seria Matematică-Informatică*, *7*(2), 19-24.
139. Okamoto, M., Yasuda, K., & Azuma, A. (1996). Aerodynamic characteristics of the wings and body of a dragonfly. *Journal of Experimental Biology*, *199*(2), 281-294.
140. Johnson, W. (1980). *Helicopter theory*, Princeton, NJ: Princeton University Press.
141. Ellington, C.P. (1984). The aerodynamics of hovering insect flight: II. Morphological parameters. *Philosophical Transactions of The Royal Society of London. B, Biological Sciences*, *305*(1122), 17-40. (doi: 10.1098/rstb.1984.0050)
142. Lentink, D., & Dickinson, M. H. (2009). Rotational accelerations stabilize leading edge vortices on revolving fly wings. *Journal of Experimental Biology*, *212*(16), 2705-2719. (doi: 10.1242/jeb.022269)
143. Harbig, R. R., Sheridan J., & Thompson, M. C. (2014). The role of advance ratio and aspect ratio in determining leading-edge vortex stability for flapping flight. *Journal of Fluid Mech*anics, *751*, 71-105. (doi: 10.1017/jfm.2014.262)
144. Birch, J. M., Dickson, W. B., & Dickinson, M. H. (2004). Force production and flow structure of the leading edge vortex on flapping wings at high and low Reynolds numbers. *Journal of Experimental Biology*, *207*(7), 1063-1072. (doi: 10.1242/jeb.00848)
145. Sun, M., & Du, G. (2003). Lift and power requirements of hovering insect flight, *Acta Mechanica Sinica*, *19*(5), 458-469. (doi: 10.1007/BF02484580)
146. Usherwood, J. R., & Ellington, C. P. (2002). The aerodynamics of revolving wings: I. Model hawkmoth wings. *Journal of Experimental Biology*, *205*(11), 1547-1564.
147. Usherwood, J. R., & Ellington, C. P. (2002). The aerodynamics of revolving wings: II. Propeller force coefficients from mayfly to quail. *Journal of Experimental Biology*, *205*(11), 1565-1576.
148. Sane, S. P. (2003). The aerodynamics of insect flight. *Journal of Experimental Biology*, *206*(23), 4191-4208. (doi: 10.1242/jeb.00663)
149. Zhao, L., Huang, Q., Xinyan, D., & Sane, S. P. (2010). Aerodynamic effects of flexibility in flapping wings. *Journal of The Royal Society Interface*, *7*(44), 485-497. (doi: 10.1098/rsif.2009.0200)
150. Sane, S. P., & Dickinson, M. H. (2002). The aerodynamic effects of wing rotation and a revised quasi-steady model of flapping flight. *Journal of Experimental Biology*, *205*(8), 1087-1096.
151. Ellington, C. P. (1984). The aerodynamics of hovering insect flight: VI. Lift and power requirements. *Philosophical Transactions of The Royal Society of London. B, Biological Sciences*, *305*(1122), 145-181. (doi: 10.1098/rstb.1984.0054)
152. Wu, J. H., & Sun, M. (2004). Unsteady aerodynamic forces of a flapping wing. *Journal of Experimental Biology*, *207*(7), 1137-1150. (doi: 10.1242/jeb.00868)
153. Ramasamy, M., Lee, T. E., & Gordon Leishman, J. (2007). Flowfield of a rotating-wing micro air vehicle. *Journal of Aircraft*, *44*(4), 1236-1244. (doi: 10.2514/1.26415)
154. Ellington, C. P. (2006, January). Insects versus birds: the great divide. In *44th AIAA aerospace sciences meeting and exhibit*, January 2006, AIAA 2006-35.
155. Bohorquez, F., Pines, D., & Samuel, P. D. (2010). Small rotor design optimization using blade element momentum theory and hover tests. *Journal of Aircraft*, *47*(1), 268-283. (doi: 10.2514/1.45301)

156. Sicard, J., & Sirohi, J. (2012). Experimental study of an extremely flexible rotor for microhelicopters. *Journal of Aircraft*, *49*(5), 1306-1314. (doi: 10.2514/1.C031643)
157. Minotti, F. (2002). Unsteady two-dimensional theory of a flapping wing. *Physical Review E*, *66*(5), 051907. (doi: 10.1103/PhysRevE.66.051907)
158. Ansari, S. A., Żbikowski, R., & Knowles, K. (2006). Non-linear unsteady aerodynamic model for insect-like flapping wings in the hover. Part 1: methodology and analysis. *Proceedings of the Institution of Mechanical Engineers, Part G: Journal of Aerospace Engineering*, *220*(2), 61-83. (doi: 10.1243/09544100JAERO49)
159. Ansari, S. A., Żbikowski, R., & Knowles, K. (2006). Non-linear unsteady aerodynamic model for insect-like flapping wings in the hover. Part 2: implementation and validation. *Proceedings of the Institution of Mechanical Engineers, Part G: Journal of Aerospace Engineering*, *220*(3), 169-186. (doi: 10.1243/09544100JAERO50)
160. Fritz, T. E., & Long, L. N. (2004). Object-oriented unsteady vortex lattice method for flapping flight. *Journal of Aircraft*, *41*(6), 1275-1290. (doi: 10.2514/1.7357)
161. Roccia, B. A., Preidikman, S., Massa, J. C., & Mook, D. T. (2013). Modified unsteady vortex-lattice method to study flapping wings in hover flight. *AIAA Journal*, *51*(11), 2628-2642. (doi: 10.2514/1.J052262)
162. Dickinson, M. H., Lehmann, F. O., & Sane, S. P. (1999). Wing rotation and the aerodynamic basis of insect flight. *Science 284*(5422), 1954-1960. (doi: 10.1126/science.284.5422.1954)
163. Walker, J. A., & Westneat, M. W. (2000). Mechanical performance of aquatic rowing and flying. *Proceedings of the Royal Society of London. Series B: Biological Sciences*, *267*(1455), 1875-1881. (doi 10.1098/rspb.2000.1224)
164. Berman, G. J., & Wang, Z. J. (2007). Energy-minimizing kinematics in hovering insect flight. *Journal of Fluid Mech*anics, *582*, 153-168. (doi 10.1017/S0022112007006209)
165. Khan, Z. A., & Agrawal, S. K. (2011). Optimal hovering kinematics of flapping wings for micro air vehicles. *AIAA Journal*, *49*(2), 257-268. (doi: 10.2514/1.J050057)
166. Ellington, C. P. (1984). The aerodynamics of hovering insect flight. I. The quasi-steady analysis. *Philosophical Transactions of the Royal Society of London. B, Biological Sciences*, *305*(1122), 1-15. (doi: 10.1098/rstb.1984.0049)
167. Taha, H. E., Hajj, M. R., & Nayfeh, A. H. (2012). Flight dynamics and control of flapping-wing MAVs: a review. *Nonlinear Dynamics*, *70*(2), 907-939 (doi: 10.1007/s11071-012-0529-5)
168. Liu, H., Ellington, C. P., Kawachi, K., van den Berg, C., & Wilmott, A. P. (1998). A computational fluid dynamic study of hawkmoth hovering. *Journal of Experimental Biology*, *201*(4), 461-477.
169. Ramamurti, R., & Sandberg, W. C. (2002). A three-dimensional computational study of the aerodynamic mechanisms of insect flight. *Journal of Experimental Biology*, *205*(10), 1507-1518.
170. Sun, M., & Tang, J. (2002). Unsteady aerodynamic force generation by a model fruitfly wing in flapping motion. *Journal of Experimental Biology*, *205*(1), 55-70.
171. Liu, Y., & Sun, M. (2008). Wing kinematics measurement and aerodynamics of hovering droneflies. *Journal of Experimental Biology*, *211*(13), 2014-2025. (doi 10.1242/jeb.016931)

172. Altshuler, D. L., Dickson, W. B., Vance, J. T., Roberts, S. P., & Dickinson, M. H. (2005). Short-amplitude high-frequency wing strokes determine the aerodynamics of honeybee flight. *Proceedings of the National Academy of Sciences of the United States of America*, *102*(50), 18213-18218. (doi: 10.1073/pnas.050690102)
173. Nagai H, Isogai K, & Hayase T. (2008, September). Measurement of unsteady aerodynamic forces of 3D flapping wing in hovering to forward flight. In *26th Congress of International Council of the Aeronautical Sciences and 8th AIAA Aviation Technology, Integration, and Operations (ATIO) Conference*, Anchorage, AK, 14–19 September, paper ICAS 2008-3.4.3.
174. Ellington, C. P., van den Berg, C., Willmott, A. P., & Thomas, A. L. R. (1996). Leading-edge vortices in insect flight. *Nature 384*, 626-630. (doi: 10.1038/384626a0)
175. Birch, J. M., & Dickinson, M. H. (2001). Spanwise flow and the attachment of the leading edge vortex on insect wings. *Nature 412*(6848), 729-733. (doi: 10.1038/35089071)
176. Wang, Z. J. (2005). Dissecting insect flight. *Annual Review of Fluid Mechanics*, *37*, 183-210. (doi: 10.1146/annurev.fluid.36.050802.121940)
177. Wang, Z. J., Brich, J. M., & Dickinson, M. H. (2004). Unsteady forces and flows in low Reynolds number hovering flight: two-dimensional computations vs robotic wing experiments. *Journal of Experimental Biology*, *207*(3), 449-460. (doi: 10.1242/jeb.00739)
178. Hewes, D. E. (1978). *Development of a nonlinear switching function and its application to static lift characteristics of straight wings*, NACA Technical Memorandum 78737.
179. Roskam, J., & Lan C-T. E. (1997). *Airplane aerodynamics and performance*, Lawrence, KS: Design, Analysis and research Corporation.
180. Brandt, S. A., Stiles, R. J., Bertin, J. J. & Whitford, R. (2004). *Introduction to aeronautics: A design perspective*, 2nd edition, AIAA Educational Series, Reston, VA: AIAA.
181. Bomphery, R. J., Taylor, G. K., & Thomas, A. L. R. (2009). Smoke visualization of free-flying bumblebees indicates independent leading edge vortices on each wing pair. *Experiments in Fluids*, *46*(5), 811-821. (doi: 10.1007/s00348-009-0631-8)
182. Ormiston, R. A. (2004, June). Induced power of the helicopter rotor. In *American Helicopter Society 60th Annual Forum and Technology Display*, Baltimore, MD, 8-10 June, 33-53.
183. Chattot, J. J. (2004). Analysis and design of wings and wing/winglet combinations at low speeds. AIAA Paper: AIAA-2004-220.
184. Azuma. A. (2006). *The biokinetics of flying and swimming*, 2nd edition , AIAA Educational Series, Reston, VA: AIAA.
185. Jones, R. T. (1941). *Correction of the lifting line theory for the effect of the chord*, NACA Technical Note 817.
186. Abbott, I. H., & Von Doenhoff, E. (1959). *Theory of wing sections*, 2nd edition, New York NY: Dover Publications, Inc.
187. Ahmed, M. R., Abdelrahman, M. M., ElBayoumi, G. M., & ElNomrossy, M. M. (2011). Optimal wing twist distribution for roll control of MAVs. *Aeronautical Journal*, *115*(1172), 641- 649.
188. Nabawy, M. R. A., & Crowther, W. J. (2014). On the quasi-steady aerodynamics of normal hovering flight part I: the induced power factor. *Journal of The Royal Society Interface*, *11*(93), 20131196. (doi 10.1098/rsif.2013.1196)

189. Ellington, C. P. (1984). The aerodynamics of hovering insect flight: III. Kinematics. *Philosophical Transactions of The Royal Society of London. B, Biological Sciences*, *305*(1122), 41-78. (doi: 10.1098/rstb.1984.0051)
190. Shyy, W., & Liu, H. (2007). Flapping wings and aerodynamic lift: the role of leading-edge vortices. *AIAA Journal*, *45*(12), 2817-2819. (doi 10.2514/1.33205)
191. Saffman, P. G., & Sheffield, J. S. (1977). Flow over a wing with an attached free vortex. *Studies in Applied Mathematics*, *57*, 107-117.
192. Huang, M. K., & Chow, C. Y. (1982). Trapping of a free vortex by Joukowski airfoils. *AIAA Journal*, *20*(3), 292-298.
193. Polhamus, E. C. (1966). *A concept of the vortex lift of sharp-edge delta wings based on a leading-edge-suction analogy*, NACA Technical Note D-3767.
194. Zbikowski, R., Knowles, K., Pedersen, C. B., & Galinski, C. (2004). Some aeromechanical aspects of insect-like flapping wings in hover. *Proceedings of the Institution of Mechanical Engineers, Part G: Journal of Aerospace Engineering*, *218*(6), 389-398. (doi: 10.1243/0954410042794948)
195. Traub, L. W. (2004). Analysis and estimation of the lift components of hovering insects. *Journal of Aircraft*, *41*(2), 284–289. (doi: 10.2514/1.9323)
196. Thielicke, W., Kesel, A. B., & Stamhuis, E. J. (2011). Reliable force predictions for a flapping-wing micro air vehicle: A 'vortex-lift' approach. *International Journal of Micro Air Vehicles*, *3*(4), 201-215. (doi: 10.1260/1756-8293.3.4.201)
197. Polhamus, E. C. (1968). *Application of the leading-edge-suction analogy of vortex lift to the drag due to lift of sharp-edge delta wings*, NASA Technical Note D-4739.
198. Prandtl, L. (1918). Tragflügel-Theorie, *Nachrichten von der Gesellschaft der Wissenschaften zu Gottingen, Geschaeftliche Mitteilungen, Klasse*, 451-477.
199. Prandtl, L. (1923). *Applications of modern hydrodynamics to aeronautics*, NACA 116.
200. Tietjens, O. G. (1957). *Applied hydro-and aeromechanics: based on lectures of L. Prandtl*, New York, NY: Dover Publications Inc.
201. Phillips, W. F., Fugal, S. R., & Spall, R. E. (2006). Minimizing induced drag with wing twist, computational-fluid-dynamics validation. *Journal of Aircraft*, *43*(2), 437-444
202. Nabawy, M. R. A., ElNomrossy, M. M., Abdelrahman, M. M., & ElBayoumi, G. M. (2012). Aerodynamic shape optimisation, wind tunnel measurements and CFD analysis of a MAV wing. *Aeronautical J*ournal, *116*(1181), 685- 708.
203. Rasmussen, M. L., & Smith, D. E. (1999). Lifting-line theory for arbitrarily shaped wings. *Journal of Aircraft*, *36*(2), 340-348.
204. Phillips, W. F., & Snyder, D. O. (2000). Modern adaptation of Prandtl's classic lifting-line theory. *Journal of Aircraft*, *37*(4), 662-670.
205. Sclavounos, P. D. (1987). An unsteady lifting-line theory. *Journal of Engineering Mathematics*, *21*(3), 201-226.
206. Mehrle, A. H. (2009). Extension of Multhopp's quadrature method to cyclic periodic lifting systems. *Acta mechanica*, *202*, 135-144. (doi: 10.1007/s00707-008-0017-7)
207. Anderson, J. D. (2011). *Fundamentals of aerodynamics*, 5th edition, New York, NY: McGraw-Hill.
208. Conlisk, A. T. (2001). Modern helicopter rotor aerodynamics. *Progress in Aerospace Sciences*, *37*(5), 419-476.

209. Rayner, J. M. V. (2001). Mathematical modelling of the avian flight power curve. *Mathematical Methods in the Applied Sciences*, *24*, 17-18, 1485-1514. (doi: 10.1002/mma.196)
210. Phlips, P. J., East, R. A., & Pratt, N. H. (1981). An unsteady lifting line theory of flapping wings with application to the forward flight of birds. *Journal of Fluid Mech*anics, *112*, 97-125.
211. Smith, M., Wilkin, P., & Williams, M. (1996). The advantages of an unsteady panel method in modelling the aerodynamic forces on rigid flapping wings. *Journal of Experimental Biology*, *199*(5), 1073-1083.
212. Zhao, L., Deng, X., & Sane, S. P. (2011). Modulation of leading edge vorticity and aerodynamic forces in flexible flapping wings. *Bioinspiration & Biomimetics*, *6*(3), 036007. (doi: 10.1088/1748-3182/6/3/036007)
213. Nabawy, M. R. A., & Crowther, W. J. (2014). On the quasi-steady aerodynamics of normal hovering flight part II: model implementation and evaluation. *Journal of The Royal Society Interface*, *11*(94), 20131197. (doi: 10.1098/rsif.2013.1197)
214. Ellington, C. P. (1999). The novel aerodynamics of insect flight: applications to micro-air vehicles. *Journal of Experimental Biology*, *202*(23), 3439-3448.
215. Ellington, C. P., & Usherwood, J. R. (2001). Lift and drag characteristics of rotary and flapping wings. *Fixed and Flapping Wing Aerodynamics for Micro Air Vehicle Applications*, *Progress in Astronautics and Aeronautics*, *195*, (edited by Mueller, T. J.), Chapter 12, AIAA, Reston, USA.
216. Usherwood, J. R. (2009). The aerodynamic forces and pressure distribution of a revolving pigeon wing. *Experiments in Fluids*, *46*(5), 991-1003. (doi: 10.1007/s00348-008-0596-z)
217. Altshuler, D. L., Dudley, R., & Ellington, C. P. (2004). Aerodynamic forces of revolving hummingbird wings and wing models. *Journal of zoology*, *264*(4), 327-332. (doi: 10.1017/S0952836904005813)
218. Kruyt, J. W., Quicazan-Rubio, E. M., van Heijst, G. J. F., Altshuler, D. L., & Lentink, D. (2014). Hummingbird wing efficacy depends on aspect ratio and compares with helicopter rotors. *Journal of The Royal Society Interface*, *11*(99), 20140585. (doi: 10.1098/rsif.2014.0585)
219. Walker, J. A. (2002). Rotational lift: something different or more of the same. *Journal of Experimental Biology*, *205*(24), 3783-3792.
220. Taha, H. E., Hajj, M. R., & Beran, P. S. (2014). State-space representation of the unsteady aerodynamics of flapping flight. *Aerospace Science and Technology*, *34*, 1-11. (doi: 10.1016/j.ast.2014.01.011)
221. Nabawy, M. R. A., & Crowther, W. J. (2014, June). Is flapping flight aerodynamically efficient? In *32nd AIAA Applied Aerodynamics Conference, AIAA Aviation and Aeronautics Forum and Exposition*, Atlanta, Georgia, 16-20 June. (doi: 10.2514/6.2014-2277)
222. Wang, Z. J. (2004). The role of drag in insect hovering. *Journal of Experimental Biology*, *207*(23), 4147-4155. (doi: 10.1242/jeb.01239)
223. Ansari, S. A., Knowles, K., & Zbikowski, R. (2008). Insectlike flapping wings in the hover part II: effect of wing geometry. *Journal of Aircraft*, *45*(6), 1976-1990. (doi 10.2514/1.35697)
224. Gessow, A. (1948). *Effect of rotor-blade twist and plan-form taper on helicopter hovering performance*, NACA Technical Note No. 1542.
225. Wang, Z. J. (2008). Aerodynamic efficiency of flapping flight: analysis of a two-stroke model. *Journal of Experimental Biology*, *211*(2), 234-238. (doi: 10.1242/jeb.013797)

226. Pesaveno, U., & Wang, Z. J. (2009). Flapping wing flight can save aerodynamic power compared to steady flight. *Physical Review Letters*, *103*(11), 118102. (doi: 10.1103/PhysRevLett.103.118102)
227. Ansari, S. A., Knowles, K., & Zbikowski, R. (2008). Insectlike flapping wings in the hover part 1: effect of wing kinematics. *Journal of Aircraft*, *45*(6), 1945-1954. (doi: 10.2514/1.35311)
228. Lau, G. K., Chin, Y. W., Goh, J. W., & Wood, R. J. (2014). Dipteran-insect-inspired thoracic mechanism with nonlinear stiffness to save inertial power of flapping-wing flight. *IEEE Transactions on Robotics*. (doi: 10.1109/TRO.2014.2333112)
229. Whitney, J. P., & Wood, R. J. (2012). Conceptual design of flapping-wing micro air vehicles. *Bioinspiration & Biomimetics*, *7*(3), 036001. (doi: 10.1017/S002211201000265X)
230. Taha, H. E., Hajj, M. R., & Nayfeh, A. H. (2013). Wing kinematics optimization for hovering micro air vehicles using calculus of variation. *Journal of Aircraft*, *50*(2), 610-614. (doi: 10.2514/1.C031969)
231. Nabawy, M. R., Parslew, B., & Crowther, W. J. (2014). Dynamic performance of unimorph piezoelectric bending actuators. *Proceedings of the Institution of Mechanical Engineers, Part I: Journal of Systems and Control Engineering*, *229*(2), 118-129 (doi: 10.1177/0959651814552810)
232. Schenato, L., Campolo, D., & Sastry, S. (2003, December). Controllability issues in flapping flight for biomimetic micro air vehicles (MAVs). In *42nd IEEE Conference on Decision and Control*, Maui, HI, 9–12 December, 6441-6447. (doi: 10.1109/CDC.2003.1272361)
233. Wang, Q., Du, X., Xu, B., & Cross, L. (1999). Theoretical analysis of the sensor effect of cantilever piezoelectric benders. *Journal of Applied Physics*, *85*(3), 1702-1712. (doi: 10.1063/1.369314)
234. Yoo, J., Hong, J., & Cao, W. (2000). Piezoelectric ceramic bimorph coupled to thin metal plate as cooling fan for electronic devices. *Sensors and Actuators A: Physical*, *79*(1), 8-12. (doi: 10.1016/S0924-4247(99)00249-6)
235. Yao, K., & Uchino, K. (2001). Analysis on a composite cantilever beam coupling a piezoelectric bimorph to an elastic blade. *Sensors and Actuators A: Physical*, *89*(3), 215-221. (doi: 10.1016/S0924-4247(00)00552-5)
236. Wu, T., Ro, P. I., Kingon, A. I., & Mulling, J. F. (2003). Piezoelectric resonating structures for microelectronic cooling. *Smart materials and structures*, *12*(2), 181.
237. de Lima, C. R., Vatanabe, S. L., Choi, A., Nakasone, P. H., Pires, R. F., & Nelli Silva, E. C. (2009). A biomimetic piezoelectric pump: Computational and experimental characterization. *Sensors and Actuators A: Physical*, *152*(1), 110-118. (doi: 10.1016/j.sna.2009.02.038)
238. Wang, Q. M., & Eric Cross, L. (1999). Constitutive equations of symmetrical triple layer piezoelectric benders. *IEEE Transactions on Ultrasonics, Ferroelectrics and Frequency Control*, *46*(6), 1343-1351. (doi: 10.1109/58.808857)
239. Smits, J. G., & Choi, W. S. (1991). The constituent equations of piezoelectric heterogeneous bimorphs. *IEEE Transactions on Ultrasonics, Ferroelectrics and Frequency Control*, *38*(3), 256-270. (doi: 10.1109/58.79611)
240. Smits, J. G., Dalke, S. I., & Cooney, T. K. (1991). The constituent equations of piezoelectric bimorphs. *Sensors and Actuators A: Physical*, *28*(1), 41-61. (doi: 10.1016/0924-4247(91)80007-C)

241. Smits, J. G., & Ballato, A. (1994). Dynamic admittance matrix of piezoelectric cantilever bimorphs. *Journal of Microelectromechanical Systems*, *3*(3), 105-112. (doi: 10.1109/84.311560)
242. Basak, S., Raman, A., & Garimella, S. V. (2005). Dynamic response optimization of piezoelectrically excited thin resonant beams. *Journal of Vibration and Acoustics*, *127*(1), 18-27. (doi: 10.1115/1.1857921)
243. Bilgen, O., Erturk, A., & Inman, D. J. (2010). Analytical and experimental characterization of macro-fiber composite actuated thin clamped-free unimorph benders. *Journal of Vibration and Acoustics*, *132*(5), 051005. (doi: 10.1115/1.4001504)
244. Bilgen, O., Karami, M. A., Inman, D. J., & Friswell, M. I. (2011). The actuation characterization of cantilevered unimorph beams with single crystal piezoelectric materials. *Smart Materials and Structures*, *20*(5), 055024. (doi: 10.1088/0964-1726/20/5/055024)
245. Bilgen, O., Wang, Y., & Inman, D. J. (2012). Electromechanical comparison of cantilevered beams with multifunctional piezoceramic devices. *Mechanical Systems and Signal Processing*, *27*, 763-777. (doi: 10.1016/j.ymssp.2011.09.002)
246. Erturk, A., & Inman, D. J. (2008). A distributed parameter electromechanical model for cantilevered piezoelectric energy harvesters. *Journal of Vibration and Acoustics*, *130*(4), 041002. (doi: 10.1115/1.2890402)
247. Erturk, A., & Inman, D. J. (2009). An experimentally validated bimorph cantilever model for piezoelectric energy harvesting from base excitations. *Smart Materials and Structures*, *18*(2), 025009. (doi: 10.1088/0964-1726/18/2/025009)
248. Rodríguez, H., Ceres Ruíz, R., Calderón Estévez, L., & Pons Rovira, J. L. (2004). Modelling of the travelling wave piezoelectric motor stator: an integrated review and new perspective. *Boletín de la Sociedad Española de Cerámica y Vidrio*, *43*(3), 698-705.
249. Ikeda T. (1996). *Fundamentals of piezoelectricity*, Oxford, UK: Oxford University Press.
250. Bidakhvidi, M. A., Vucinic, D., & Vanlanduit, S. (2012, July). Multiphysics optimization of the piezoelectric flapping wing propulsion. In *International Conference on Engineering Optimization*. Rio de Janeiro, 1-5 July. (Website: engopt.org)
251. Lal Kummari, K., Li, D., Guo, S., & Huang, Z. (2010). Development of piezoelectric actuated mechanism for flapping wing micro-aerial vehicle applications. *Advances in Applied Ceramics*, *109*(3), 175-179. (doi: 10.1179/174367509X12447975734357)
252. Mason, W. P. (1950). *Piezoelecric crystals and their application to ultrasonics*, New York, NY: Van Nostrand.
253. Chang, S. H., Rogacheva, N. N., & Chou, C. C. (1995). Analysis of methods for determining electromechanical coupling coefficients of piezoelectric elements. *IEEE Transactions on Ultrasonics, Ferroelectrics and Frequency Control*, *42*(4), 630-640. (doi: 10.1109/58.393106)
254. Braun, S., Ewins, D., & Rao, S. S. (2002). *Encyclopedia of vibration*, Vol. 1, Academic Press, San Diego, CA: A division of Harcourt Inc.
255. Ballas, R. G. (2007). *Piezoelectric multilayer beam bending actuators: static and dynamic behavior and aspects of sensor integration*. Berlin, Heidelberg: Springer.
256. Inman, D. J. (2009). *Engineering vibrations*, 3rd edition, Pearson International Edition, Upper Saddle River, NJ: Prentice Hall.

257. Renardy, M. (2004). On localized Kelvin-Voigt damping. *ZAMM-Journal of Applied Mathematics and Mechanics/Zeitschrift für Angewandte Mathematik und Mechanik*, *84*(4), 280-283. (doi: 10.1002/zamm.200310100)
258. Abu-Hilal, M. (2003). Forced vibration of Euler–Bernoulli beams by means of dynamic Green functions. *Journal of Sound and Vibration*, *267*(2), 191-207. (doi: 10.1016/S0022-460X(03)00178-0)
259. Piezoelectric Ceramic Sensors (PIZOTITE®), Catalog No. P19E-6, Murata Manufacturing Co., Ltd.
260. Wang, Q. M., Zhang, Q., Xu, B., Liu, R., & Cross, L. E. (1999). Nonlinear piezoelectric behavior of ceramic bending mode actuators under strong electric fields. *Journal of Applied Physics*, *86*(6), 3352-3360. (doi: 10.1063/1.371213)
261. Yong, Y. K., & Fleming, A. J. (2014). Piezoelectric actuators with integrated high-voltage power electronics. *IEEE/ASME Transactions on Mechatronics*. (doi: 10.1109/TMECH.2014.2311040)
262. http://www.piezodrive.com/product-pdu100.html
263. Abdelrahman, M. M., Elnomrossy, M. M., & Ahmed, M. R. (2009, May). Development of mini unmanned air vehicles. In *13th International Conference on Aerospace Sciences & Aviation Technology*, Cairo, May 2009, ASAT-13-US-02.
264. Cheng, B., Roll, J. A., & Deng, X. (2013, May). Modelling and optimization of an electromagnetic actuator for flapping wing micro air vehicle. In *IEEE International Conference on Robotics and Automation (ICRA)*, Karlsruhe, 6-10 May, 4035-4041. (doi: 10.1109/ICRA.2013.6631146)
265. Roll, J. A., Cheng, B., & Deng, X. (2013, May). Design, fabrication, and experiments of an electromagnetic actuator for flapping wing micro air vehicles. In *IEEE International Conference on Robotics and Automation (ICRA)*, Karlsruhe, 6-10 May, 809-815. (doi: 10.1109/ICRA.2013.6630666)
266. Mou, X. L., Liu, Y. P., & Sun, M. (2011). Wing motion measurement and aerodynamics of hovering true hoverflies. *Journal of Experimental Biology*, *214*(17), 2832-2844. (doi: 10.1242/jeb.054874)
267. Erturk, A., & Inman, D. J. (2011). *Piezoelectric energy harvesting*, John Wiley & Sons Ltd, West Sussex: John Wiley & Sons.
268. http://www.morganelectroceramics.com/resources/piezo-ceramic-tutorials/limitations/
269. Aldraihem, O. J., Wetherhold, R. C., & Singh, T. (1997). Distributed control of laminated beams: Timoshenko theory vs. Euler-Bernoulli theory. *Journal of intelligent material systems and structures*, *8*(2), 149-157. (doi: 10.1177/1045389X9700800205)
270. Smith, A. M. O. (1975). High-lift aerodynamics. *Journal of Aircraft*, *12*(6), 501-530.